NANOSCOPIC EXPLORATION OF THE NUCLEUS

DISSERTATION AN DER FAKULTÄT FÜR BIOLOGIE

DER LUDWIG-MAXIMILIANS-UNIVERSITÄT MÜNCHEN

CLEMENS STEINEK

MÜNCHEN, 2024

Diese Dissertation wurde angefertigt
unter der Leitung von Prof. Dr. Heinrich Leonhardt
im Bereich Humanbiologie und BioImaging
an der Ludwig-Maximilians-Universität München

Erstgutachter: Prof. Dr. Heinrich Leonhardt
Zweitgutachter: Prof. Dr. Ralf Jungmann
Tag der Abgabe: 30.09.2024
Tag der mündlichen Prüfung: 16.01.2025

EIDESSTATTLICHE ERKLÄRUNG

Ich versichere hiermit an Eides statt, dass die vorgelegte Dissertation von mir selbstständig und ohne unerlaubte Hilfe angefertigt wurde.

München, den 30.09.2024

Clemens Steinek

ERKLÄRUNG

Hiermit erkläre ich, dass die vorliegende Dissertation weder ganz, noch teilweise bei einer anderen Prüfungskommission vorgelegt wurde.
Ich habe noch zu keinem früheren Zeitpunkt versucht, eine Dissertation einzureichen oder an einer Doktorprüfung teilzunehmen.

München, den 30.09.2024

Clemens Steinek

LIST OF PUBLICATIONS

Parts of this thesis have been published elsewhere:

Brandstetter, K. et al. (Mar. 2022). "Differences in nanoscale organization of regulatory active and inactive human chromatin." *Biophysical Journal* 121, pp. 977–990. DOI: `10.1016/j.bpj.2022.02.009`.

Steinek, C., M. Guirao Ortiz, G. Stumberger, A. J. Toelke, D. Hoerl, T. Carell, H. Harz, and H. Leonhardt (Aug. 2024). "Generation of densely labeled oligonucleotides for the detection of small genomic elements." *Cell Reports Methods* 4, p. 100840. DOI: `10.1016/j.crmeth.2024.100840`.

Weichenhan, D. et al. (Oct. 2024). "Altered enhancer-promoter interaction leads to MNX1 expression in pediatric acute myeloid leukemia with t(7;12)(q36;p13)." *Blood Advances* 8, 5100–5111. DOI: `10.1182/bloodadvances.2023012161`.

DECLARATION OF CONTRIBUTIONS

GENERATION OF DENSELY LABELED OLIGONUCLEOTIDES FOR THE DETECTION OF SMALL GENOMIC ELEMENTS

Clemens Steinek, Heinrich Leonhardt, and Hartmann Harz conceived the study. Clemens Steinek synthesized NOVA probes, conducted FISH experiments, acquired microscopy images, and prepared the figures. David Hörl acquired 3D STED images of telomeres and automated STED acquisition. Clemens Steinek, Miguel Guirao Ortiz, Gabriela Stumberger and David Hörl analyzed the data. Annika J. Tölke purified NOVA-probes using HPLC. Clemens Steinek, Heinrich Leonhardt and Hartmann Harz wrote the manuscript and prepared figures. All authors read, discussed, and approved the manuscript.

ALTERED ENHANCER-PROMOTER INTERACTION LEADS TO MNX1 EXPRESSION IN PEDIATRIC ACUTE MYELOID LEUKEMIA WITH T(7;12)(Q36;P13)

Dieter Weichenhan, Anna Riedel, Etienne Sollier and Umut H. Toprak conceived the study. Clemens Steinek designed and synthesized probesets, conducted FISH experiments and contributed to Figure 3. Clemens Steinek discussed and proofread the manuscript.

DIFFERENCES IN NANOSCALE ORGANIZATION OF REGULATORY ACTIVE AND INACTIVE HUMAN CHROMATIN

Katharina Brandstetter conceived the study. Clemens Steinek cloned, labeled and imaged the Widom 601 construct and contributed to Supplementary Figure S3. Clemens Steinek discussed and proofread the manuscript.

München, den 30.09.2024

_____

Clemens Steinek

_____

Prof. Dr. Heinrich Leonhardt

CONTENTS

ABBREVIATIONS

3C	Chromatin conformation capture
4C	Capture or chromosome conformation capture-on-chip
5C	Chromosome conformation capture carbon copy
ABL	Abelson murine leukemia viral oncogene homolog
Act-seq	Activated cell population sequencing
AML	Acute myeloid leukemia
ATAC-seq	Assay for transposase-accessible chromatin with sequencing
BAC	Bacterial artificial chromosome
BCR	Breakpoint cluster region protein
BLAST	Basic local alignment search tool
bp	Base pair
ChIP	Chromatin immunoprecipitation
CTCF	CCCTC-binding factor
DNA	Deoxyribonucleic acid
EDN1	Endothelin 1
eRNA	Enhancer RNA
ETV6	ETS variant transcription factor 6
FISH	Fluorescence in situ hybridization
FRAP	Fluorescence recovery after photobleaching
FRET	Förster resonance energy transfer
GFI1	Growth factor independent 1 transcriptional repressor
GOLD-FISH	Genome oligopaint via local denaturation FISH
HOXD	Homeobox D
IGF2	Insulin-like growth factor II
IGH	Immunoglobulin heavy chain
LAD	Lamina-associated domain
MNase-seq	Micrococcal nuclease digestion with deep sequencing
MNX1	Motor neuron and pancreas homeobox 1
MYC	Myelocytomatosis
NIPBL	Nipped-B-like protein
NOVA	Nanoscopy-compatible oligonucleotides with dyes in variable arrays
oligoFISH	oligonucleotide-based FISH
ORCA	Optical reconstruction of chromatin architecture

PAINT	Point accumulation in nanoscale topography
PALM	Photoactivated localization microscopy
PCR	Polymerase chain reaction
PHACTR1	Phosphatase and actin regulator 1
PML	Promyelocytic leukemia protein
PNA	Peptide-nucleic acid
RARA	Retinoic Acid Receptor Alpha
RASER-FISH	Resolution after single-strand exonuclease resection FISH
RESI	Resolution enhancement by sequential imaging
RESOLFT	Reversible saturable optical fluorescence transitions
RNA	Ribonucleic acid
RNA Pol II	RNA polymerase II
SABER	Signal amplification by exchange reaction
SIM	Structured illumination microscopy
SMC	Structural maintenance of chromosomes
SMLM	Single molecule localization microscopy
SPRITE	Split-pool recognition of interactions by tag extension
STED	Stimulated emission depletion
STORM	Stochastic optical reconstruction microscopy
SV40	Simian virus 40
TAD	Topologically associated domain
TF	Transcription factor
TSA	Tyramide signal amplification
WAPL	Wings apart-like protein homolog
YAC	Yeast artificial chromosome

SUMMARY

A somatic human cell contains 23 pairs of chromosomes, which are condensed by several orders of magnitude to fit into the confined space of the nucleus. This compaction follows a hierarchical order known as "chromatin architecture" and involves the positioning of chromosomes in the nucleus, formation of compartments, and interactions between regulatory elements. Computational, biochemical, sequencing, and imaging methods have delineated local or genome-wide DNA-DNA interaction patterns, but mapping complex spatial arrangements of regulatory elements in single cells remains challenging.

A primary goal of this thesis was to establish a simple, quick, and cost-effective workflow for the generation of FISH probes optimized for the detection of small genomic elements. To this end, we screened polymerases for their ability to incorporate dye-labeled nucleotides and systematically analyzed distance-dependent dye-dye quenching to yield densely labeled, bright FISH probes. We demonstrate that our densely labeled probes are well-suited for the detection of genomic targets down to the sub-kilobase level.

We used our densely labeled FISH probes to detect enhancer hijacking events in cancer. It is widely accepted that genetic rearrangements impact cancer development through gene amplification, truncation, deletion, or fusion. However, whole-genome sequencing and expression profiles suggest that three-dimensional chromatin reconfigurations may also represent a common, yet poorly understood, process in cancer formation. Using FISH, we probe spatial relationships between the oncogene MNX1 and regulatory elements in AML cells carrying recurrent chromosomal translocations and confirm enhancer hijacking events.

Lastly, we complemented super-resolution microscopy with simulation models to characterize the organization of kilobase genomic loci. While population-averaged mapping methods suggest a defined pattern of nucleosomes across the genome, single-cell methods reveal cell-to-cell variability in the placement of individual nucleosomes. We systematically measured end-to-end distances of regulatory active or inactive regions and attributed variability in chromatin compaction to internucleosomal interactions, differences in nucleosome occupancy, and binding of histone H1. In summary, we employ a microscopy-based approach to explore the nanoscopic organization of the nucleus.

2

ZUSAMMENFASSUNG

Eine somatische menschliche Zelle enthält 23 Chromosomenpaare, die dicht verpackt werden müssen, um in den begrenzten Raum des Zellkerns zu passen. Diese Verpackung folgt einer hierarchischen Ordnung, die als 'Chromatinarchitektur' bekannt ist und umfasst die Positionierung der Chromosomen im Zellkern, die Bildung von Kompartimenten und Interaktionen zwischen regulatorischen Elementen. Computergestützte, biochemische, sequenzbasierte und bildgebende Methoden haben lokale und genomweite DNA-DNA-Interaktionsmuster aufgedeckt, aber die Detektion komplexer räumlicher Anordnungen von regulatorischen Elementen bleibt eine Herausforderung.

Ein Ziel dieser Arbeit war es, ein einfaches, schnelles und kosteneffizientes Protokoll zu entwickeln, um FISH-Sonden zu generieren, die für die Erfassung kleiner regulatorischer Elemente geeignet sind. Wir haben Polymerasen auf ihre Fähigkeit getestet, farbstoffmarkierte Nukleotide in Proben einzubauen und abstandsabhängiges 'quenching' von Farbstoffen systematisch analysiert, um dicht markierte, helle FISH-Sonden zu erzeugen. Wir zeigen, dass unsere FISH-Sonden gut geeignet sind, um kleine Genomregionen zu detektieren.

Wir verwendeten unsere FISH-Sonden, um 'enhancer hijacking events' in Krebszellen nachzuweisen. Es ist allgemein bekannt, dass genetische Translokationen die Krebsentwicklung durch Genamplifikation, Trunkierung, Deletion oder Fusion beeinflussen. Sequenzierungsdaten und Expressionsprofile deuten jedoch darauf hin, dass Chromatin-Rekonfigurationen ebenfalls erheblich zur Krebsentstehung beitragen könnten. Mittels FISH untersuchten wir die räumlichen Beziehungen zwischen dem Onkogen MNX1 und regulatorischen Elementen in AML-Zellen mit einer prominenten chromosomalen Translokation und detektierten 'enhancer hijacking events'.

Schließlich kombinierten wir hochauflösende Mikroskopie mit Simulationen, um die nanoskopische Organisation von Genomregionen zu charakterisieren. Während gemittelte Datensätze ein definiertes Muster von Nukleosomen über das gesamte Genom hinweg suggerieren, zeigen Einzelzellmethoden eine Variabilität in der Positionierung einzelner Nukleosomen. Wir haben die End-zu-End-Distanzen von regulatorisch aktiven und inaktiven Regionen systematisch gemessen und konnten die Variabilität in der Chromatinkompaktierung auf internukleosomale Interaktionen, unterschiedliche Nukleosompositionierung und die Bindung von Histon H1 zurückführen. Diese Arbeit beschreibt, wie hochauflösende Mikroskopie genutzt werden kann, um die nanoskopische Organisation des Zellkerns zu untersuchen.

INTRODUCTION

3.1 A BRIEF HISTORY OF THE NUCLEUS

Since the emergence of life on Earth over four billion years ago, all organisms have stored, retrieved, and propagated genetic information. While the origins, evolution, and physiology of early organisms remain subjects of debate, first cells likely used ribonucleic acid (RNA) to store genetic information (Weiss et al., 2018). As cells evolved and became more complex, their genetic information expanded, and RNA was replaced with deoxyribonucleic acid (DNA) as the carrier of hereditary information (Di Giulio, 2021). DNA molecules are double-stranded polymers, each strand containing a unique series of nucleotides with one of four nitrogenous bases: adenine, cytosine, guanine, and thymine. The nitrogenous bases of two DNA strands are stacked and connected by hydrogen bonds, while sugar-phosphate backbones remain on the outside of the molecule (Watson and Crick, 1953). Because of its biochemical properties, DNA is stable, energy-efficient, and stores information 1.000.000 more effectively than the most advanced magnetic tape storage systems (Ceze et al., 2019; Gervasio et al., 2024). However, DNA needs to be compacted by orders-of-magnitude to fit inside the cells of an organism. For this reason, protists, plants, fungi, and animals have developed a structure that confines DNA within its boundaries: the nucleus. The nucleus is a membrane-enclosed organelle that protects genetic information from physical insults, provides a chemically distinct environment, concentrates DNA-binding proteins, and regulates gene activity (Baum and Spang, 2023). While the biochemical properties of DNA have been extensively characterized, the regulation of genetic information in the three-dimensional context of the nucleus remains an active area of investigation (Bonev and Cavalli, 2016; Zheng and Xie, 2019).

FINDING THE STORAGE UNIT   For over 300 years, the nucleus has captivated generations of scientists who have devoted their careers to characterizing its structure and function (figure 1). The invention of light microscopy in the 18th century enabled the first independent observations of the nucleus by Antony van Leeuwenhoek, Felice Fontana, Franz Bauer, Jan Purkyně, and Robert Brown (Pederson, 2011). These studies did not assign any function to the nucleus but acknowledged its presence in various cell types and organisms. Besides observations made through microscopy, the development of chemical assays enabled the first detailed analysis of nuclear contents. In the late 1860s,

Friedrich Miescher isolated nuclei using the pus from surgical bandages and observed a substance that precipitated from the solution when acid was added (Miescher, 1871). Miescher named the precipitate "nuclein" and realized it contained an unknown macromolecule with a high phosphorus content (Dahm, 2005, 2008). Later, this macromolecule would come to be known as DNA. Miescher's studies on "nuclein" influenced Albrecht Kossel, who further characterized "nuclein" and identified an unknown class of peptides, which he named histones (Kossel, 1884). As nuclei were documented in an increasing number of cell types and organisms, it became apparent that the nucleus plays a significant role in the physiology of the cell. However, it would take several decades before the function of the nucleus was uncovered.
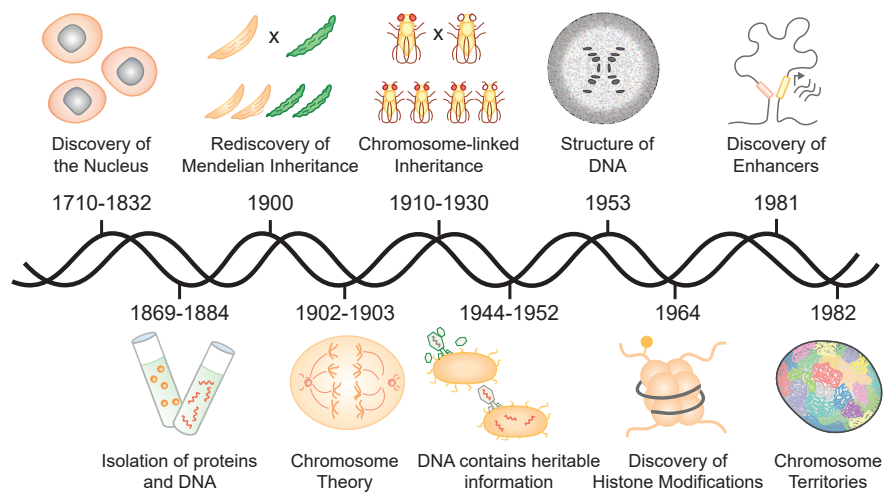

Figure 1: Timeline of milestones in chromatin research (1710-1982).

The groundwork for the functional characterization of the nucleus was laid in a monastery in Brünn (today Brno), located in the eastern part of the Czech Republic. Augustinian friar and abbot Gregor Mendel conducted breeding studies in plants and observed that traits are often inherited as distinct units that segregate during gametogenesis (Mendel, 1866). Mendel's discoveries initially went unnoticed but were rediscovered in 1900 by Hugo de Vries, Carl Erich Correns, and Eric Tschermak-Seysenegg, who independently obtained similar results (Correns, 1900; De Vries, 1900; Tschermak, 1900). During that period, the development of DNA staining methods further provided insights into the structure and inheritance of nuclear components. Walther Flemming analyzed DNA compaction during cell division and coined the terms "chromatin" and "mitosis" and Wilhelm Waldeyer introduced the term "chromosome" (Flemming, 1882; Waldeyer, 1888). Robert Feulgen developed a semi-quantitative DNA staining method and discovered that germ cells (n) contained half the DNA content of somatic cells (2n), while some somatic cells contained quadruple

the amount of DNA (4n) (Mello and Vidal, 2017). In 1902, Walter Sutton observed that the segregation of chromosomes during meiosis closely resembles the segregation patterns described by Mendel. Based on these observations, Edmund Wilson, Walter Sutton, Theodor Boveri, and August Weismann proposed the chromosome theory of inheritance, which states that genetic information is encoded by chromosomes in the nucleus (O'Connor and Miko, 2008). In 1910, Thomas Hunt Morgan provided conclusive evidence for the chromosome theory of inheritance by demonstrating X chromosome linked inheritance of eye color in fruit flies (Morgan, 1910). Subsequently, H.J. Muller observed that X-rays can provoke chromosomal rearrangements that relocate genes to a locus where they are silenced (Elgin and Reuter, 2013; Muller, 1927). This phenomenon, known as position-effect variegation, occurs when genes are positioned in dense genomic regions called heterochromatin (Schultz, 1936).

The rediscovery of the Mendelian rules and chromosome theory of inheritance led to the widespread acceptance that the nucleus is the repository of genetic information. However, most scientists assumed that proteins encode genetic information based on works by Phoebus Levene (Frixione and Ruiz-Zamarripa, 2019). Although Levene correctly identified that the building blocks of DNA contain sugars, phosphate groups, and nitrogenous bases, he wrongly assumed that DNA is a repeating tetramer consisting of all four nucleotides (Levene and Mandel, 1908). As a result of Levene's tetranucleotide hypothesis, DNA was believed to be incapable of encoding genetic information and instead served structural purposes. However, a series of experiments have disproven this hypothesis and demonstrated that DNA is the carrier of genes. Oswald T. Avery, Colin MacLeod, and Maclyn McCarty observed that bacteria become pathogenic when incubated with purified DNA from heat-inactivated pathogenic strains (Avery et al., 1943). However, the scientific community was initially hesitant to draw conclusions from this experiment. Alfred Hershey and Martha Chase ultimately confirmed that DNA is the carrier of genetic information (Hershey and Chase, 1952). They labeled the proteins of bacteriophages with sulfur-35 or the DNA with phosphorus-32 and incubated the labeled bacteriophages with bacteria. Since bacteria infected with phosphorus-32-labeled bacteriophages became radioactive, Hershey and Chase concluded that DNA is used to propagate genetic information.

While the function of DNA became apparent, its structure had yet to be solved. Building on Levene's work, Erwin Chargaff analyzed nucleobase composition and made two fundamental discoveries: The proportions of the four nucleobases vary between species and the ratios of cytosine to guanine and thymine to adenine are always 1:1 (Chargaff, 1950). Chargaff's research, along with X-ray diffraction images generated by Rosalind Franklin, enabled James Watson and

Francis Crick to solve the structure of DNA in 1953 (Franklin and Gosling, 1953; Watson and Crick, 1953; Wilkins et al., 1953). DNA forms a three-dimensional double helix that is stabilized by interactions between complementary base pairs.

Following discoveries about the process of protein synthesis, it became apparent that genetic information encoded in DNA is transcribed into RNAs, which can be translated into proteins (Crick, 1970; Crick, 1958). However, nearly all cells of an organism contain the same genetic information, yet they exhibit different morphologies and functions. Therefore, mechanisms in the cell must exist that regulate gene activity and establish cellular identity. Early evidence for possible mechanisms of gene regulation was provided by Rollin Hotchkiss, who found a modified form of cytosine known as 5-methylcytosine in calf thymus (Hotchkiss, 1948). A role of 5-methylcytosine in gene regulation was proposed following a series of findings showing its non-random distribution in the genome, enrichment at silent genes, and abnormal levels observed in cancer (Ehrlich et al., 1982; Holliday and Pugh, 1975; Mattei et al., 2022). In addition to DNA methylation, post-translational modifications of histones have been implicated in gene activity and DNA compaction (Allfrey et al., 1964; Peng et al., 2021).

Shortly after DNA methylation and histone modifications were implicated in gene regulation, it was discovered that gene activity is also controlled by short sequences in the genome. In 1981, Julian Banerji, Sandro Rusconi, and Walter Schaffner identified the first enhancer through transient expression of a cloned beta-globin gene (Banerji et al., 1981). Banerji, Rusconi, and Schaffner observed that inserting a viral 72 bp SV40 sequence motif into a plasmid containing beta-globin upregulated its expression several hundred-fold. Since overexpression was achieved regardless of the location of the SV40 sequence in the construct, the authors concluded that enhancers could impact gene activity from remote locations. The identification of regulatory elements, along with the discovery of chromosome territories a year later, paved the way for a new field of study known as chromatin architecture.

3.2   FUNDAMENTALS OF 3D GENOME ARCHITECTURE

3.2.1   *From Chromosomes to Nucleosomes*

A somatic human cell contains 23 pairs of chromosomes spanning 6 billion base pairs of DNA. Given that each base-pair is 3.4 Å long, the DNA content of one cell would extend to 2 meters if stretched end-to-end (Piovesan et al., 2019). Therefore, DNA needs to be condensed by several orders of magnitude to fit into the confined space of the nucleus. This compaction is not random and instead follows a hierarchical order known as "chromatin architecture" (figure 2) (Elimelech and Birnbaum, 2020; Finn et al., 2019; Zheng and Xie, 2019). Chromatin is organized on multiple levels, including the positioning of chromosomes in the nucleus (chromosome territories), regions of self-interacting DNA (A/B compartments, TADs), proximity of genes and regulatory elements (enhancer-promoter interactions), and arrangement of nucleosomes (nucleosome occupancy).
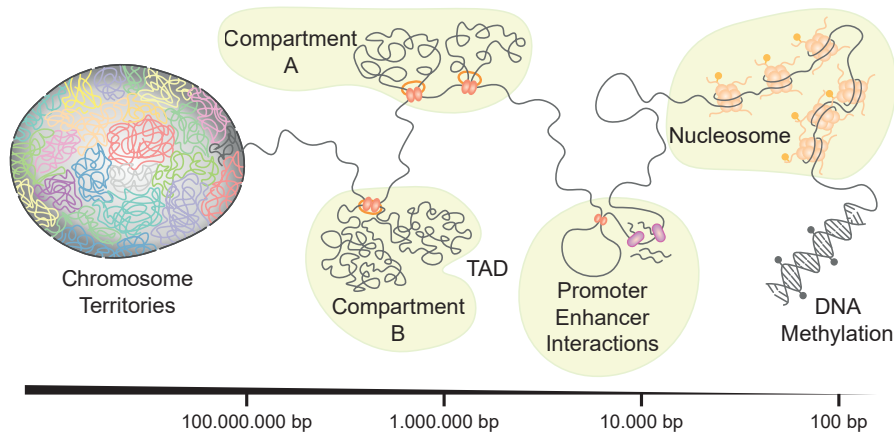

Figure 2: Hierarchical organization of chromatin. Chromosomes occupy distinct regions within the nucleus (chromosome territories) that can intermingle at their boundaries. Chromosome territories are divided into dense (compartment B) and less compacted segments (compartment A) which primarily interact with compartments of the same type. Areas within A/B compartments, known as TADs, form DNA loops that facilitate enhancer-promoter interactions. At the kilobase and sub-kilobase scale, nucleosome occupancy, histone modifications, and DNA methylation impact gene expression.

A fundamental characteristic of chromatin architecture is the occurrence of transient DNA-DNA interactions that allow adjustments in gene regulation during cell maintenance, division, and differentiation (Dupont and Wickstrom, 2022). Consequently, cells within the same population exhibit variability in spatiotemporal chromatin contacts and three-dimensional genome organization. Moreover, large chromatin configurations often contain smaller structures and disruptions in one layer of organization may have only a moderate effect on gene

expression. This complicates the interpretation of experimental results and questions the importance of individual regulatory elements, DNA-binding proteins, and post-translational histone modifications in gene regulation. The following chapters discuss fundamental features of each level of chromatin organization and dissect their role in gene expression.

CHROMOSOME TERRITORIES: WHERE CHROMOSOMES RESIDE

Throughout the late 19th century and the first half of the 20th century, two conflicting models described the spatial organization of chromatin in interphase nuclei. The first model was proposed by Carl Rabl and stated that chromosomes exist in specific conformations across cell divisions (Rabl, 1885). Expanding on that theory, Theodor Boveri suggested that individual chromosomes occupy specific parts of the nucleus and coined the term "chromosome territory" (Boveri, 1909). Another model proposed that interphase chromosomes randomly intermingle in the nucleus, comparable to "a bowl of spaghetti". Nearly 100 years after Carl Rabl's proposal, a series of experiments confirmed the existence of chromosome territories. In the 1970s, Stephen Stack, David Brown, and William Dewey treated Chinese hamster ovary cells with acetic acid and air-dried and stained them (Stack et al., 1977). The treatment caused shrinking and swelling of chromatin, which became visible as stained patches. Stack, Brown, and Dewey interpreted that each individual patch corresponded to a single chromosome and concluded that chromatin is not randomly dispersed in the nucleus. However, it was not entirely clear whether the results were reliable, or if the harsh treatment had artificially provoked the observed patches (Fritz et al., 2019). It was not until 1982 that Thomas Cremer and colleagues provided conclusive evidence for the existence of chromosome territories (Cremer et al., 1982). In an elegant experiment, Cremer et al. induced DNA damage in small parts of interphase nuclei using laser micro-irradiation. Radiolabeled thymidine was then added to the medium and incorporated into the newly synthesized DNA at irradiated regions. When distinct radioactive spots were still detected after cell division, Cremer et al. concluded that chromosomes are confined to certain areas of the nucleus (Cremer et al., 1981).

In the forty years after the pioneering experiment by Cremer et al., chromosome territories have been identified in many higher eukaryotes (Meaburn and Misteli, 2007). The distribution of chromosomes in the nucleus follows a loose radial pattern, with gene-rich and small chromosomes often located near the center and gene-poor and large chromosomes positioned towards the periphery (Cremer and Cremer, 2010; Tanabe et al., 2002). For example, imaging studies have located inactive X chromosomes in the periphery (Zhang et al., 2007) and gene-rich Alu sequences in the center of the nucleus (Bolzer et al., 2005). However, radial genome positioning is not universally applica-

ble, as chromocenters, the Y chromosome, and regions enriched for H3K27me3 or H3K9me3 are found in the periphery and the center of the nucleus (Belmont, 2022). While chromosome territories typically remain stable throughout interphase, their positions in the nucleus can permanently change during mitosis or cell differentiation (Clowney et al., 2012; Gerlich et al., 2003; Kosak et al., 2002; Pichugin et al., 2017; Solovei et al., 2009; Thomson et al., 2004; Walter et al., 2003). A striking example of chromosome territory reorganization occurs during the terminal differentiation of rod cells in nocturnal mammals. The differentiation of nocturnal photoreceptors involves the relocation of heterochromatin to the center of the nucleus to facilitate the collection of light in rod cells (Solovei et al., 2009). Furthermore, the differentiation of olfactory sensory neurons is marked by the relocation of olfactory receptor alleles to a repressive gene zone and their subsequent inactivation (Clowney et al., 2012). B lymphocyte development is accompanied by the activation of immunoglobulin genes and their rearrangement in the nucleus (Kosak et al., 2002; Pichugin et al., 2017). Although these examples directly link large-scale genomic reorganization to cellular function, chromosome territories generally remain stable during interphase. However, small genomic loci may undergo continuous, dynamic, and transient movements to regulate gene expression (Kurz et al., 1996; Wegel and Shaw, 2005). The development of 3C-based methods (chapter 3.3.1) has enabled the identification of genome-wide chromatin contacts and identified chromatin compartments.

A/B COMPARTMENTS: INTERACTING MEGA-DOMAINS   Early evidence for the existence of chromatin compartments was derived from two imaging studies. Zink et al. injected a fluorescent nucleotide analog into nuclei and observed distinct foci within labeled regions after S-phase (Zink et al., 1998). Notably, these chromatin compartments persisted through several cell cycles, remained mobile during interphase, and exhibited diameters between 400 and 800 nm. Shopland et al. used FISH to label neighboring regions on chromosome 14 and observed separate clusters with gene-rich or gene-poor foci (Shopland et al., 2006). They concluded that megabase genomic loci organize into three-dimensional structures that may facilitate transcription. Although these findings provided early evidence of chromatin organization at the megabase scale, the role and significance of chromatin compartments in the nucleus remained unclear. In 2009, Lieberman-Aiden et al. developed Hi-C to identify genome-wide DNA-DNA interaction patterns and discovered two classes of spatial compartments (A/B compartments) across the genome (Lieberman-Aiden et al., 2009). A compartments typically interact with other A compartments and are associated with euchromatin, while B compartments are more likely to engage with other B compartments and are linked to a tran-

scriptionally repressed state. Consequently, A compartments exhibit higher gene density, active histone modifications and open chromatin, whereas B compartments contain a high content of silenced genes, repressive histone modifications and condensed chromatin (Zheng and Xie, 2019). Improvements in the sensitivity of Hi-C and ChIP-seq have enabled detailed characterization of chromatin compartments. Rao et al. systematically investigated chromatin marks across the genome and classified compartments A and B into five subcompartments (A1-A2, B1-B3) (Rao et al., 2014). Interestingly, B1 compartments overlap with polycomb silencing, whereas the B2 and B3 subcompartments correspond to lamina-associated domains (LADs). Features of A/B compartments, such as spatial positioning and function, are often linked to other hierarchical levels of chromatin organization. A/B compartments exhibit a loose form of radial organization, comparable to chromosome territories. While A compartments are frequently found in the central region of the nucleus, B compartments often localize to the periphery (Buchwalter et al., 2019; Magana-Acosta and Valadez-Graham, 2020). Using a combined approach of nuclear speckle and lamin TSA-seq, Chen et al. found that A1 and A2 subcompartments are located close to or near nuclear speckles (Chen et al., 2018b). Furthermore, B compartments overlap with LADs and are often demarcated by CTCF (Guelen et al., 2008). Predicting the location of chromatin subcompartments beyond these associations can be challenging, as organizational patterns vary between cell types and nuclear shapes (Crosetto and Bienko, 2020; Kind et al., 2015). Moreover, the isolated role of chromatin compartments in gene regulation remains elusive, as their properties are deeply interconnected with TADs and histone modifications.

TOPOLOGICALLY ASSOCIATED DOMAINS   Recent advances in microscopy, genome sequencing, and bioinformatics have enabled extensive characterization of genome-wide DNA-DNA contacts (see chapter 3.3.1 and 3.3.3). In 2012, two independent studies identified self-interacting regions in the mammalian genome and named them topologically associated domains (TADs). Nora et al. used FISH and 5C to characterize the spatial organization of a 4.5 megabase segment in the X-inactivation center and detected frequent DNA-DNA interactions within 0.2-1.0 megabase regions (Nora et al., 2012). In the same year, Dixon et al. used Hi-C to probe genome-wide DNA-DNA interactions and identified TADs across the entire genomes of mouse and human embryonic stem cells and differentiated cells (Dixon et al., 2012). Subsequent studies have confirmed the presence of TADs in the genomes of various mammals, zebrafish, drosophila, and yeast (Dixon et al., 2012; Mizuguchi et al., 2014; Rudan et al., 2015; Sexton et al., 2012).

Precise mapping and annotation of TADs depend on the resolution of contact maps and may vary between studies (Eres and Gilad, 2021). However, TADs share several features in their structure, associated proteins, and function. Regions within TADs typically exhibit 2- to 3-fold more interactions among themselves than with neighboring regions (Goel and Hansen, 2021). This increased contact frequency within TADs is proposed to facilitate enhancer-promoter interactions, as active regulatory elements of genes are often located in the same TAD (Symmons et al., 2014). TADs are restricted by TAD boundaries, with gene-rich regions and replication domains often located near these boundaries (Pope et al., 2014; Shah et al., 2018). 75 percent of TAD boundaries contain CCCTC-binding factor (CTCF)-sites and are enriched in CTCF, cohesin and the mediator complex (Dixon et al., 2012; Phillips-Cremins et al., 2013). LADs represent a distinct type of TAD that is characterized by low gene density and enrichment of H3K9m2/3 and H2K27me3 (Meuleman et al., 2013; Steensel and Belmont, 2017).

Biochemical reconstitution, single-molecule imaging, genetic perturbation, and polymer models have provided evidence for the formation of TADs through cohesin-dependent loop extrusion (Banigan and Mirny, 2020; Davidson et al., 2019; Fudenberg et al., 2016; Haarhuis et al., 2017; Kim et al., 2019; Nora et al., 2017; Rao et al., 2017; Schwarzer et al., 2017; Wutz et al., 2017). Cohesin is a complex composed of RAD21, SMC1, and SMC3 that is continuously recruited to the chromatin fiber by nipped-B-like protein (NIPBL, also known as SCC2) (Ciosk et al., 2000; Tedeschi et al., 2013). According to the loop extrusion model, cohesin moves along chromatin and forms progressively larger loops until it is unloaded by Wapl or encounters chromatin barriers that are composed of CTCF proteins (Gandhi et al., 2006; Ganji et al., 2018; Haarhuis et al., 2017; Sanborn et al., 2015). The stalling of cohesin at CTCF sites then facilitates the formation of DNA-DNA contacts within TADs. Mechanistical insights into ATP–dependent extrusion of DNA by cohesin were provided by in vitro and in vivo studies (Davidson et al., 2019; Kim et al., 2019; Schwarzer et al., 2017). Moreover, TADs disintegrate upon depletion of CTCF, cohesin, or Nipbl1, whereas Wapl depletion increases the contact strength at TAD borders (Haarhuis et al., 2017; Nora et al., 2017; Rao et al., 2017; Wutz et al., 2017).

Contact maps suggest that most TADs and LADs are conserved across cell types in mammals (Dixon et al., 2012; Meuleman et al., 2013; Rao et al., 2014). The evolutionary conservation of TADs, along with the preferential occurrence of enhancer-promoter interactions within TADs, indicate an important role in gene regulation. Indeed, Fabre et al. introduced genetic perturbations in the HoxD locus and directly linked TAD disruption to altered transcription of HoxD genes (Fabre et al., 2017). Rodríguez-Carballo et al. gradually removed a

boundary region between two TADs and observed a progressive increase in novel enhancer-promoter interactions across the boundary (Rodríguez-Carballo et al., 2017). Moreover, human limb malformations were linked to deletions, inversions, or duplications of specific TADs that rewire long-range regulatory architecture (Lupianez et al., 2015). Therefore, TADs seem to be crucial for facilitating enhancer-promoter interactions, and their disruption should inevitably lead to irreversible changes in gene expression. However, global depletion of cohesin or CTCF has provided conflicting evidence. Auxin-inducible degradation of cohesin causes only moderate changes in gene expression, and cohesin-depleted cells partially rebuild compartments after S-phase (Cremer et al., 2020; Rao et al., 2017). Induced depletion of CTCF further correlated with changes in the expression of approximately 2000 genes across a diverse set of tissues, while many gene expression patterns remained unchanged (Kubo et al., 2021). These observations suggest that TADs might not be essential for the expression of most genes and instead provide a framework for enhancer-promoter interactions. However, it is also worth considering that the effects of short-term TAD loss on gene regulation may be partially offset by other layers of genome organization that remain intact.

PROMOTER-ENHANCER INTERACTIONS: LET'S KEEP IN TOUCH? Since the discovery of the first enhancer over 40 years ago, more than a million enhancers have been identified in the human genome (Consortium et al., 2020). Enhancers are DNA sequences that amplify gene expression through direct or indirect interactions with promoters, which are often located several hundred kb away (Lettice et al., 2003; Nelson et al., 2004). The identification of specific enhancers is often context-dependent, as genome-wide analyses have shown that some enhancers may function as promoters and vice versa (Dao et al., 2017; De Santa et al., 2010; Engreitz et al., 2016; Kim et al., 2010; Rajagopal et al., 2016). Active enhancers are also often transcribed and may share properties with promoters, including sequence similarities or enriched DNA-binding proteins (Andersson and Sandelin, 2020; Core et al., 2014; Kim et al., 2015). Therefore, the definitions of promoters and enhancers are context-dependent and should be examined on a case-by-case basis. The following paragraphs outline general mechanisms of enhancer-promoter interactions.

Human enhancers are typically 100-1000 bp long, contain transcription factor binding motifs, and are enriched in p300, RNA polymerase II (RNA Pol II), the mediator complex, eRNAs, and epigenetic marks such as H3K4me1 and H3K27ac (Creyghton et al., 2010; Rada-Iglesias et al., 2011). It is widely accepted that active enhancers support RNA Pol II activation and the assembly of the pre-initiation complex at the core promoter (Allen and Taatjes, 2015; Haberle and Stark, 2018). However, multiple mechanistic models have been proposed to describe

enhancer selectivity of proximal or distal regulatory elements (figure 3) (Kolovos et al., 2012; Uyehara and Apostolou, 2023). The first class of models describes enhancer-promoter interactions that are independent of the three-dimensional arrangement of regulatory elements. The "sliding" model posits that RNA Pol II is loaded at the enhancer and moves along chromatin until it encounters a promoter and initiates transcription (Moreau et al., 1981). A related model involves the recruitment of chromatin remodelers to the enhancer, which then spread histone modifications towards the promoter ("tracking" model) (Travers, 1999). Alternatively, enhancers may recruit proteins that drive the polymerization of transcription factors and co-activators, forming a bridge between the enhancer and promoter ("bridging" model) (Bulger and Groudine, 1999). All three models share a simplistic one-dimensional view of the genome, where enhancers preferentially interact with the nearest promoters (Yang and Hansen, 2024). While interactions frequently occur between proximal regulatory elements, enhancers occasionally bypass nearby promoters or activate genes located over 100 kb away (Gasperini et al., 2019). Therefore, additional enhancer-promoter models have been proposed that emphasize spatial arrangements of regulatory elements in the three-dimensional context of the nucleus.
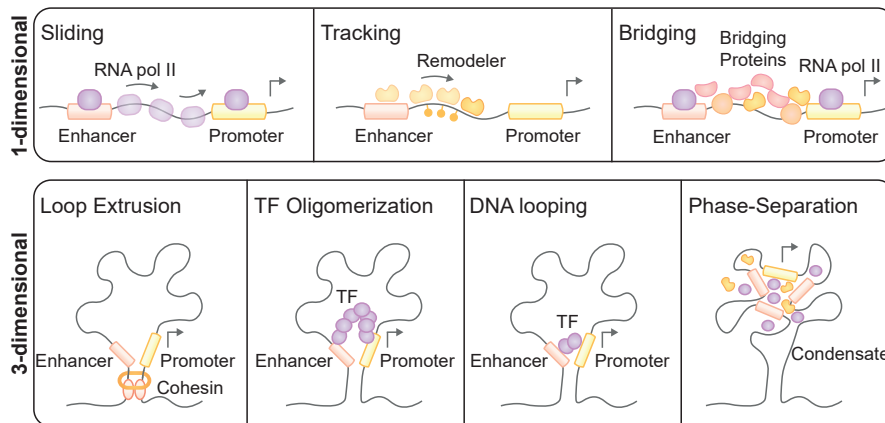
Figure 3: Proposed enhancer-promoter interaction models. Enhancers can activate proximal genes through the recruitment of (i) RNA pol II (sliding), (ii) chromatin remodelers that deposit histone marks (tracking), and (iii) transcription factors that form bridges between enhancers and promoters (bridging). Three-dimensional enhancer-promoter interaction models describe (i) cohesin-dependent or (ii) independent DNA looping, (iii) the oligomerization of transcription factors (TFs), or (iv) the assembly of liquid-liquid phase-separated condensates. Please note that there are alternative or similar enhancer-promoter interaction models that are not depicted in this graph.

Loop extrusion is one of the most well-described mechanisms for long-range enhancer-promoter interactions (Dekker and Mirny, 2016; Doyle et al., 2014). As described before, loop extrusion involves the orchestrated action of cohesin, CTCF, NIPBL, and the mediator complex to bring distant regulatory elements into spatial proximity (demonstrated in (Deng et al., 2014; Deng et al., 2012)). Despite its recent popularity, the importance of cohesin-dependent loop extrusion in gene regulation remains unclear, as global loss of cohesin does not affect the expression of most genes (Hsieh et al., 2020; Kane et al., 2022; Nora et al., 2017). An alternative model proposes that transient DNA looping may occur through interactions between transcription factors bound at the enhancer and the promoter (DNA looping) (Monfils and Barakat, 2021). Loop extrusion and DNA looping models are supported by forced chromatin looping experiments that induce gene expression by bringing enhancers and promoters into close proximity (Bartman et al., 2016; Deng et al., 2014; Deng et al., 2012). Another model describes the formation of transcription factor oligomers that facilitate enhancer-promoter interactions (TF oligomerization). For example, Nanog has been shown to facilitate enhancer-promoter interactions through the assembly of oligomers that simultaneously bind multiple DNA molecules (Choi et al., 2022). Similarly, the transcription factor YY1 enables enhancer-promoter interactions through self-dimerization (Weintraub et al., 2017). A recent model has also highlighted that gene activation might be driven by the formation of liquid-liquid phase-separated condensates induced by transcription factors and coactivators (Di Giammartino et al., 2020; Stadhouders et al., 2019). Multiple in vitro and in vivo experiments have demonstrated that transcription factors can form condensates with the mediator complex via their intrinsically disordered domains (Boija et al., 2018; Sabari et al., 2018; Zamudio et al., 2019). Given that RNA pol II exhibits dynamic clustering in living cells, it is plausible to assume that enhancers serve as scaffolds to assemble condensates and transcriptional hubs (Cisse et al., 2013; Du et al., 2024). This model is compatible with observations that enhancers can activate multiple genes simultaneously, super-enhancers can target the same promoter, and some genes can be activated independently of increased contact frequency (Alexander et al., 2019; Benabdallah et al., 2019; Fukaya et al., 2016; Halfon, 2020). However, the role of phase-separated condensates as the primary driver of gene expression remains a subject of debate, as other studies have found that phase-separated condensates negatively correlate with gene expression (Chong et al., 2022; Trojanowski et al., 2022).

While many models for enhancer-promoter interactions have been proposed, gene regulation may ideally be understood through the integration of multiple models. For example, sliding of transcription factors might facilitate DNA looping, or loop extrusion may relocate

regulatory elements into transcriptional hubs. Therefore, a holistic view of gene regulation that includes regulatory elements, transcription factors, chromatin remodelers, RNA pol II, protein oligomers, and phase-separated condensates in the three-dimensional space may accurately describe transcription in cells.

NUCLEOSOME OCCUPANCY   The nucleosome is the basic unit of chromatin compaction in eukaryotic cells and consists of 145-147 bp of DNA wrapped around an octamer of histone proteins H2A, H2B, H3, and H4 (Kornberg, 1974; Luger et al., 1997). Neighboring nucleosomes are connected by 10-80 bp linker DNA, which is bound and stabilized by H1-linker histones (Izzo and Schneider, 2016; Woodcock et al., 2006). The term "nucleosome occupancy" describes how often a given base pair is situated within a nucleosome in a specific cell type or species (Baldi et al., 2020). The placement and sliding of nucleosomes are controlled by ATP-dependent remodeling enzymes that create heterogeneous clutches and fibers (Baldi et al., 2020; Chen et al., 2021; Narlikar et al., 2013; Ricci et al., 2015; Segal and Widom, 2009). Since ATP-dependent remodeling enzymes are recruited by transcription factors to their targets, nucleosome density within clutches can vary among promoters in different cell types (Singh and Mueller-Planitz, 2021).

In addition to their role in compaction, nucleosomes modulate interactions with nuclear proteins through post-translational modifications (Zhang et al., 2021b). Over the years, a diverse set of post-translational histone modifications has been identified, which is established by epigenetic writers and removed by erasers (reviewed in (Rothbart and Strahl, 2014)). Active genes are enriched in H3K4me3, H3K9ac, and H3K27ac marks at the transcriptional start sites, while active enhancers exhibit higher levels of H3K4me1 and H3K27ac, and less often, H4K16ac, H3 globular acetylation, H3K122ac, and H3K64ac (Creyghton et al., 2010; Gates et al., 2017; Pradeepa, 2017; Shogren-Knaak et al., 2006). Post-translational modifications are established by epigenetic writers to change local chromatin properties. For example, histone acetyltransferases establish acetylation marks at promoters and enhancers following interactions with transcription factors, the basal transcription machinery, or modified histone residues (Voss and Thomas, 2018). Histone acetylation marks then neutralize positive charges on lysines, destabilize histone-DNA interactions, mobilize nucleosomes, and promote DNA accessibility (Talbert and Henikoff, 2021). Multiple studies have established a direct link between post-translational histone modifications and gene expression. Crump et al. chemically inhibited the acetyl transferase p300/CBP to disrupt the association of RNA pol II with chromatin and gene expression (Crump et al., 2011). Hilton et al. fused p300 with nuclease-null dCas9 to establish H3K27ac marks at target genes and induce their expression

(Hilton et al., 2015). However, some studies challenge the role of local histone modifications in gene regulation. Dorighi et al. demonstrated that the loss of H3K4me1 at active enhancers only modestly impacts the activity of nearby genes (Dorighi et al., 2017). Zhang et al. mutated lysine 27 in histone variant H3.3 and only detected mild changes in chromatin accessibility and enhancer activity (Zhang et al., 2020a). Histone modifications are part of a complex regulatory system that controls genes expression. Therefore, the loss of individual histone modifications might be partially compensated by other regulatory mechanisms, leading to minor changes in enhancer activity and gene expression.

3.2.2 *Consequences of altered 3D Chromatin Organization in Cancer*

The spatiotemporal control of gene expression is essential for cell function and dysregulated transcription has been linked to many diseases including cancer (Baylin and Jones, 2016; Krijger and Laat, 2016). Over the past decades, several mechanisms have been implicated in abnormal expression patterns that drive cancer growth, replicative immortality, immune evasion, metastasis, or therapeutic resistance (reviewed in (Hanahan, 2022)). One of these "hallmarks of cancer" involves chromosomal rearrangements that result in the production of fusion proteins or dysregulated gene activity. Deep sequencing has identified thousands of fusion transcripts and proteins that may dysregulate transcription, cell signaling, cell division, or DNA repair (Mertens et al., 2015). Fusion proteins can arise from the reciprocal translocation of two chromosomes that are spatially close in the 3D context of the nucleus. For instance, chronic myeloid leukemia and adult acute lymphoblastic leukemia often exhibit reciprocal translocation of neighboring chromosomes 9 and 22, resulting in the production of BCR-ABL (Fritz et al., 2019; Neves et al., 1999). Similar observations have been made for translocations between chromosomes 15 and 17 (PML-RARA) or chromosomes 8 and 14 (MYC-IGH) in hematopoietic precursors and lymphoid cells (Canoy et al., 2022; Neves et al., 1999; Roix et al., 2003). In all three examples, specific genomic rearrangements lead to the production of fusion proteins with abnormal functions or activities.

Recent advancements in high-throughput sequencing technologies has dramatically accelerated the characterization of chromosomal rearrangements (Spielmann et al., 2018). Remarkably, sequencing analyses have revealed that structural rearrangements often result in altered gene expression in regions near the breakpoints, rather than the production of fusion proteins (Claringbould and Zaugg, 2021; Helmsauer et al., 2020; Northcott et al., 2014, 2017). In these cases, chromosomal duplication, inversion, deletion, or translocation may lead to TAD reconfiguration and novel enhancer-promoter interactions ("en-

hancer hijacking"). It is hypothesized that enhancer hijacking events represent a common process in cancer development comparable to in-frame gene fusions (Claringbould and Zaugg, 2021). In 2014, Northcott et al. identified chromosomal rearrangements that juxtapose GFI1 family oncogenes with active enhancers, leading to their activation (Northcott et al., 2014). Kloetgen et al. analyzed in situ Hi-C, RNA-seq, and ChIP–seq datasets and found that TAD fusion events can induce novel interactions between enhancers and oncogenes in T cell acute lymphoblastic leukemia (Kloetgen et al., 2020). Weischenfeldt et al. identified tandem duplications that intersect with a TAD boundary and facilitate novel interactions between the oncogene IGF2 and a super-enhancer in colorectal cancers (Weischenfeldt et al., 2017). Furthermore, whole-genome sequencing profiles in over 1200 cancer genomes identified aberrant expression of hundreds of genes close to the breakpoint (Zhang et al., 2020b). As enhancer hijacking emerges as a common phenomenon in cancer formation, several questions arise: Are enhancer hijacking events a byproduct of chromosomal rearrangements, or do they actively drive cancer evolution? Can we identify enhancer hijacking events that are found in multiple types of cancer? What is the clinical relevance of enhancer hijacking events? Given the complexity of enhancer-promoter interactions (chapter 3.2.1), addressing these questions requires sensitive methods that identify suitable enhancer candidates, probe spatial proximity, and quantify changes in gene expression.

3.3 METHODS TO STUDY GENOME ARCHITECTURE

An intricate interplay of chromosome territories, TADs, regulatory elements, nucleosomes, and histone and DNA modifications defines cellular identity in development and disease. Over the past decades, computational, biochemical, sequencing, and imaging methods have been developed to characterize 3D genome organization and identify local or genome-wide DNA-DNA or DNA-protein interaction patterns (Kempfer and Pombo, 2020). This thesis highlights two methodologies (chromatin conformation capture, imaging-based approaches) that have made substantial contributions to our understanding of chromatin architecture and its role in gene regulation.

3.3.1 *Chromatin Conformation Capture*

Chromatin conformation capture (3C) techniques are biochemical assays that detect pairwise contacts between genomic loci in the three-dimensional space. Today, various 3C-based techniques are available to map spatial relationships between specific genomic regions or genome-wide interaction patterns (figure 4). In 2002, Dekker et al. developed the first 3C technique to probe population-averaged contact

frequencies between two genomic loci (Dekker et al., 2002). 3C involves crosslinking of DNA, restriction digestion, and proximity ligation to generate DNA fragments from spatially close genomic loci. Fragments that contain sequences from two loci of interest are amplified through polymerase chain reaction (PCR) using region-specific primers and detected by gel electrophoresis ("one versus one"). Using 3C, dynamic changes in chromatin conformation were observed across the cell cycle (Dekker et al., 2002). However, time-consuming primer design and the low throughput of 3C hindered extensive characterization of chromatin architecture and prompted the development of two refined 3C-based methods in 2006 (Dostie et al., 2006; Simonis et al., 2006). Chromosome conformation capture-on-chip (4C) includes circularization of ligated fragments to enable amplification with single primers. This approach enables the detection of all regions that are spatially close to the region of interest ("one versus all") (Simonis et al., 2006). In the initial application, Zhao et al. used 4C to detect long-range interactions between methylated regions and the H19 imprinting control region (Zhao et al., 2006). Chromosome conformation capture carbon copy (5C) involves the generation of a library from ligated fragments using sets of primer pairs followed by sequencing or microarray analysis (Dostie et al., 2006). 5C detects pairwise interactions within a large genomic locus ("many versus all") and, together with FISH, has been used to identify self-interacting regions in the X chromosome (Nora et al., 2012).
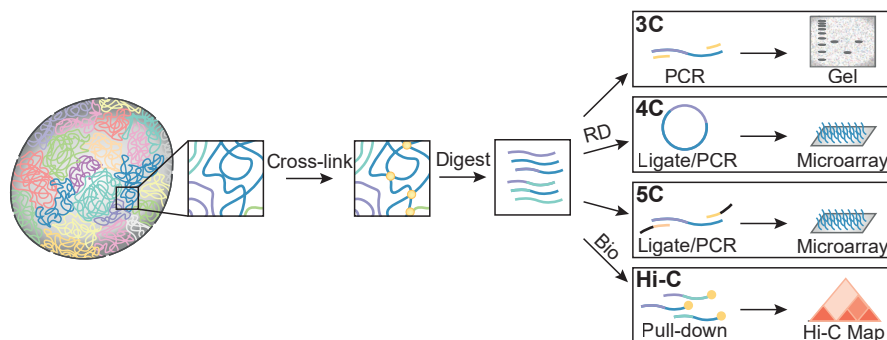
Figure 4: Workflow of common 3C-based techniques. 3C-based methods involve cross-linking, digestion, and ligation of chromatin. Generated fragments may then be amplified with primer pairs (3C), circularized and amplified with one primer (4C), amplified with many primer pairs (5C) or biotinylated and sequenced (Hi-C).

Although 3C, 4C, and 5C delineate regional chromatin conformations, the reliance on primers for amplification restricts the view of the genome. The development of Hi-C has overcome this limitation and allows detection of genome-wide interaction patterns through adapter ligation followed by high-throughput sequencing (Lieberman-Aiden et al., 2009). Early Hi-C experiments have identified A/B compartments and TADs across the genomes of different species (Dixon et

al., 2012; Lieberman-Aiden et al., 2009). Refined Hi-C methods, such as tethered conformation capture, DNase Hi-C, micro-C, and in situ Hi-C have increased resolution and captured fine-scale features of chromatin organization (Hsieh et al., 2015; Kalhor et al., 2012; Ma et al., 2015; Rao et al., 2014). Rao et al. adapted Hi-C protocols to detect pairwise interactions across the genome with a resolution of 1 kb (Rao et al., 2014). The authors further correlated Hi-C datasets with ChIP-seq analyses and found that 86 percent of loop domains are bound by CTCF proteins. Bonev et al. characterized rewiring of active and inactive TADs during neural differentiation and detected the establishment or disintegration of enhancer-promoter interactions (Bonev et al., 2017). Another biochemical method, known as split-pool recognition of interactions by tag extension (SPRITE), detects multi-way chromatin contacts across short and long distances through the separation of cross-linked chromatin fragments, followed by ligation and sequencing (Quinodoz et al., 2018). While SPRITE has been used to probe long-range interactions within gene-rich and gene-poor genomic loci, its protocol is laborious, which restricts its applications (Fiorillo et al., 2021).

3C-based methods use the average contact frequency between pairs of genomic loci in cell populations to detect chromatin contacts. Although generated contact maps are highly reproducible across cell types and related species, increasing evidence suggests that they might underrepresent transient and dynamic phenomena in the nucleus (Cattoni et al., 2017; Finn and Misteli, 2019). Using DNA standards that enable absolute quantification of 3C fragments, Gavrilov et al. estimated that chromatin contacts in the highly active beta-globin locus occur in only 1 percent of cells at a given time (Gavrilov et al., 2013). FISH and live-cell imaging experiments have confirmed the dynamic and transient nature of chromatin contacts. Bintu et al. combined Oligopaint with 3D stochastic optical reconstruction microscopy (STORM) for chromatin tracing of 30 kb regions on chromosome 21. Although the authors were able to reconstruct contact frequency maps by combining measurements in a cell population, chromatin contacts and three-dimensional conformation exhibited cell-to-cell heterogeneity (Bintu et al., 2018). Similar observations have been made in two studies that characterized the physical features of chromosomal domains using Hi-C, FISH, and polymer modeling and found cell-to-cell variability in intra-TAD and inter-TAD conformations (Szabo et al., 2020, 2018). Live-cell imaging has further revealed that contacts between enhancers, promoters and TAD boundaries may last only for several minutes (Chen et al., 2018a; Gabriele et al., 2022). Therefore, substantial effort has been put into the development of single-cell 3C-based methods. Single-cell Hi-C involves cross-linking, digestion, and biotinylation in intact nuclei followed by separation of single nuclei for pulldown and library preparation (Nagano et al., 2013). Although early

forms of single-cell Hi-C had a resolution limited to several hundred kb, they enabled the characterization of chromosome territories and verified cell-to-cell variations in intra- and inter-chromosomal domains. (Nagano et al., 2013). Moreover, Nagano et al. combined single-cell Hi-C with in-silico cell cycle phasing and detected dynamic changes in TAD insulation depending on the cell cycle phase (Nagano et al., 2017). Improvements in single-cell Hi-C have enabled the detection of a greater number of chromatin contacts and confirmed cell-to-cell variability of TADs (Flyamer et al., 2017; Stevens et al., 2017). However, the genomic resolution of single-cell Hi-C remains orders of magnitude lower than the resolution of bulk 3C-based methods or FISH. Thus, complementing 3C-based methods with imaging-based approaches is essential for accurately characterizing the nature of dynamic and transient chromatin contacts.

3.3.2 *Imaging-based Approaches*

Microscopy provides spatial information about DNA, RNA, or protein within the three-dimensional context of single cells. Since the advent of light microscopy in the 18th century, substantial progress has been made in image acquisition, processing, and analysis. The development of novel imaging agents and super-resolution microscopy has enabled the visualization of any cellular structure of interest with unprecedented detail (Schermelleh et al., 2019; Terai and Nagano, 2013). Multiplexed imaging has delineated dozens of targets and allowed the exploration of complex spatial conformations (Chen et al., 2015b; Nir et al., 2018). High-content analysis extracts features from thousands of raw images and enables an unbiased view of biological phenomena (Sailem et al., 2016). As a result of these innovations, modern microscopy can map the location of numerous targets in single cells or tissue. The following chapters discuss the principles of fluorescence microscopy and fluorescence in situ hybridization.

FUNDAMENTALS OF FLUORESCENCE MICROSCOPY   Cells contain numerous DNA, RNA, and protein molecules that cannot be individually distinguished with light microscopy. Fluorescence microscopy uses the optical properties of fluorescent imaging agents that are covalently or transiently bound to the structure of interest. The simplified process of fluorescence can be depicted using the Perrin–Jablonski diagram (figure 5A) (Jabłoński, 1935). Electrons absorb light at a specific wavelength and are excited to a higher electronic state. Following absorption, energy is dissipating during vibrational relaxation and electrons transition into the first singlet state (S1). Electrons then revert from S1 into their ground state and emit light of a longer wavelength (emission) (Murphy and Davidson, 2012). Since vibrational relaxation

and dissipation cause energy loss, the excitation and emission maxima of fluorophores are usually shifted (Stokes shift).

Fluorescence imaging agents include fluorescent proteins, organic fluorophores, quantum dots or metal-ion complexes (Hickey et al., 2021). Organic fluorophores are especially popular in biological research due to their size, good photostability, and biocompatibility (Yang et al., 2022). In practice, different organic fluorophores can be conjugated to DNA, RNA, or protein targets and visualized using specific combinations of lasers and filters. However, only a few dyes (typically 4-6) can be clearly distinguished in one experiment, as absorption and emission spectra may overlap with an increasing number of fluorophores (figure 5B) (Grimm and Lavis, 2022). Spectral imaging or spectral unmixing enable the use of a greater number of different fluorophores by acquiring spectra for each pixel or separating overlapping emission spectra (Garini et al., 2006; Keshava and Mustard, 2002). Imaging throughput can also be increased by implementing several rounds of binding, imaging, and unbinding of target-specific fluorescent probes (see chapter 3.3.3) (Chen et al., 2015b).
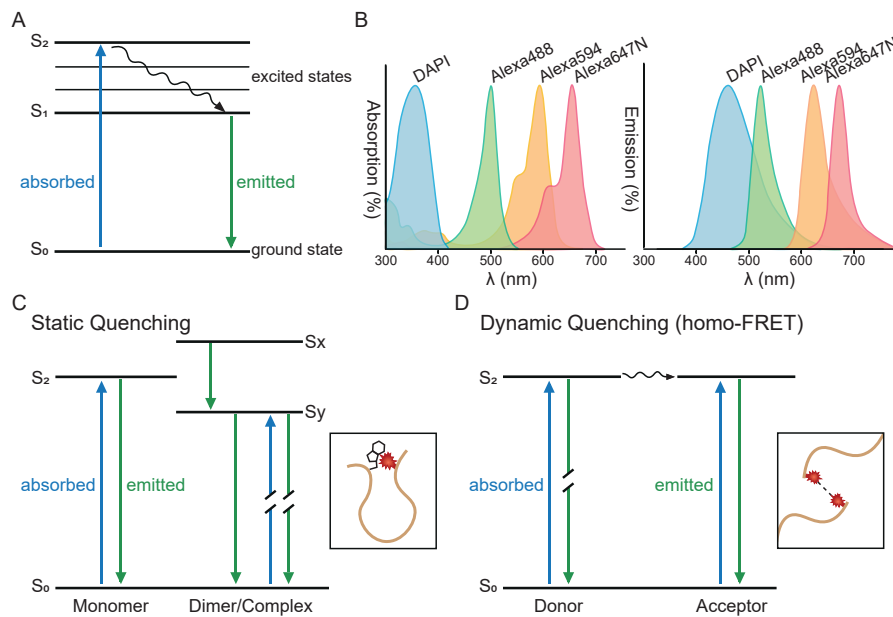
Figure 5: Absorption and emission of Fluorophores. A: Simplified Perrin–Jablonski Diagram. When fluorophores absorb light, electrons transition from the ground state into excited states (S1-S2). Fluorescence is detected when electrons revert into the ground state. The singlet electronic states are denoted S0, S1, and S2. B: Absorption and emission spectra of DAPI and Alexa-dyes. The x-axis depicts the wavelength (nm), the y-axis depicts the relative absorption or emission. C: Static quenching causes loss of fluorescence through complex formation. D: Dynamic quenching reduces fluorescence through photon transfer between donor and acceptor molecules.

In theory, fluorophores can undergo indefinite cycles of excitation and relaxation. However, photochemical stability and photobleaching restrict fluorescence time and impact imaging quality (Rost, 1991). Photobleaching is defined as the permanent loss of fluorescence in a fluorophore due to exposure to light. The rate of photobleaching depends on laser intensity, exposure time, chemical properties of the dye and the mounting medium of the specimen (Jonkman et al., 2020). Prolonged illumination and a high laser intensity can generate reactive oxygen species or radical dye intermediates that irreversibly modify and damage fluorophores (Demchenko, 2020). Extensive research has aimed to increase the half-life of fluorophores through chemical modifications that introduce electron-withdrawing groups, or hinder reactions with reactive oxygen species (Jiang et al., 2024). Anti-fading media reduce photobleaching by scavenging reactive oxygen species, thereby enabling longer imaging sessions (Demchenko, 2020; Wurm et al., 2010). Avoiding photobleaching is essential in standard imaging to ensure high-quality data sets. However, fluorescence recovery after photobleaching (FRAP) exploits photobleaching to study the kinetics and movements of molecules. FRAP is a live-cell imaging technique that involves selective bleaching of a labeled region and the subsequent detection of signal recovery (Axelrod et al., 1976; Lorén et al., 2015). Since the signal recovery of a molecule depends on diffusion, binding, and interactions with other molecules, FRAP enables quantitative analysis of molecular dynamics in living cells. Therefore, FRAP has been extensively used to characterize membrane proteins, receptor signaling, intracellular trafficking, and cytosolic or nuclear proteins (Deschout et al., 2014; Goehring et al., 2010; Lorén et al., 2015; Luu and Maurel, 2013; Schermelleh et al., 2007; Schlessinger et al., 1976; Schneider et al., 2013).

In contrast to photobleaching, quenching is a reversible, non-emissive loss of excitation energy from a fluorophore through interaction with another molecule (quencher). Quenching can be categorized into two types: static and dynamic quenching. Static quenching involves the reversible formation of a non-fluorescent complex between fluorophore and quencher (figure 5C) (Valeur and Berberan-Santos, 2013). Moreover, static quenching may occur when the fluorophore and quencher cannot change their spatial positions relative to each other. Static quenching usually does not influence fluorescence lifetime but changes the absorption spectrum of the fluorophore by causing peak broadening and the appearance of a second band (H-band) (Kang et al., 2010; Kasha et al., 1965; Valeur and Berberan-Santos, 2013; Zhegalova et al., 2014).

Dynamic quenching is a photophysical phenomenon where excited fluorophores return to the ground state due to collisions with quencher molecules (figure 5D). In contrast to static quenching, dynamic quenching does not impact the absorption spectrum of fluorophores, but it

reduces fluorophore lifetime. Förster resonance energy transfer (FRET) is a form of dynamic quenching where the excited donor transfers electronic energy to the acceptor molecule without emitting a photon (Sahoo, 2011). As FRET occurs only when donor and acceptor molecules are within 1-10 nm of each other, FRET pairs can be coupled to two proteins to detect their co-localization. In this manner, FRET microscopy has been utilized for various biological applications including protein-protein interactions, nucleic acid studies, Ca2+ signaling, or intracellular signaling (Jares-Erijman and Jovin, 2003; Sahoo, 2011; Sekar and Periasamy, 2003). While FRET is traditionally described between two molecules with different absorption spectra, two identical fluorophores may also transfer energy from one to another (homo-FRET) (Bader et al., 2011). A prerequisite for homo-FRET is a small Stokes shift and substantial overlap between the emission and absorption spectra of the fluorophore (Jun et al., 2020). While homo-FRET can lead to an undesired decrease in signal strength, it has also been used to quantify distances between fluorophores and determine the sizes of fluorophore clusters (Bader et al., 2009; Bader et al., 2011).

BREAKING THE DIFFRACTION LIMIT   Every microscope setup faces the same fundamental challenge: How can we capture specific signals of molecules of interest while minimizing nonspecific background signals? In other words, how can we achieve a satisfactory signal-to-noise ratio? Fluorescent microscopes employ lasers, mirrors, filters, and an objective lens to capture bright signals that are produced by labeled molecules at the focal point (figure 6). Although this approach enables the detection of signals produced by labeled molecules, lasers excite any dye in the field of view, including those in out-of-focus planes (Elliott, 2020). Consequently, wide-field fluorescence microscopes acquire images with low contrast in thick samples and require deconvolution to improve image quality (Schermelleh et al., 2010). Confocal microscopes block unfocused light from the imaging plane using pinholes in front of the light source and detector. Spinning-disk microscopes are precise and fast scanning confocal microscopes that use a pinhole disk to generate an array of focused laser beams (Oreopoulos et al., 2014). Despite these technical advances, the resolution of confocal microscopy remains restricted by the wavelength of emitted light and the numerical aperture of the microscope, as stated by Abbe's law (Abbe, 1873). If, for example, an excitation wavelength of 530 nm is used, a resolution of about 265 nm can practically be achieved.

For decades, the diffraction limit was considered an impenetrable physical barrier that restricts the optical resolution to roughly 250 nm (Schermelleh et al., 2019). However, the advent of super-resolution microscopy has enabled the acquisition of biological phenomena at spatial resolutions far beyond the diffraction limit of light microscopy

(Boettiger and Murphy, 2020; Sahl et al., 2017). To achieve this, super-resolution methods modulate the spatial (RESOLFT) or temporal (SMLM) excitation of fluorophores (Chen et al., 2015a; Galbraith and Galbraith, 2011; Hell, 2007; Hess et al., 2006; Kner et al., 2009; Rust et al., 2006; Schnitzbauer et al., 2017; York et al., 2012). The following paragraphs highlight the principles of commonly used RESOLFT (STED) and SMLM (STORM, PALM, PAINT) techniques.
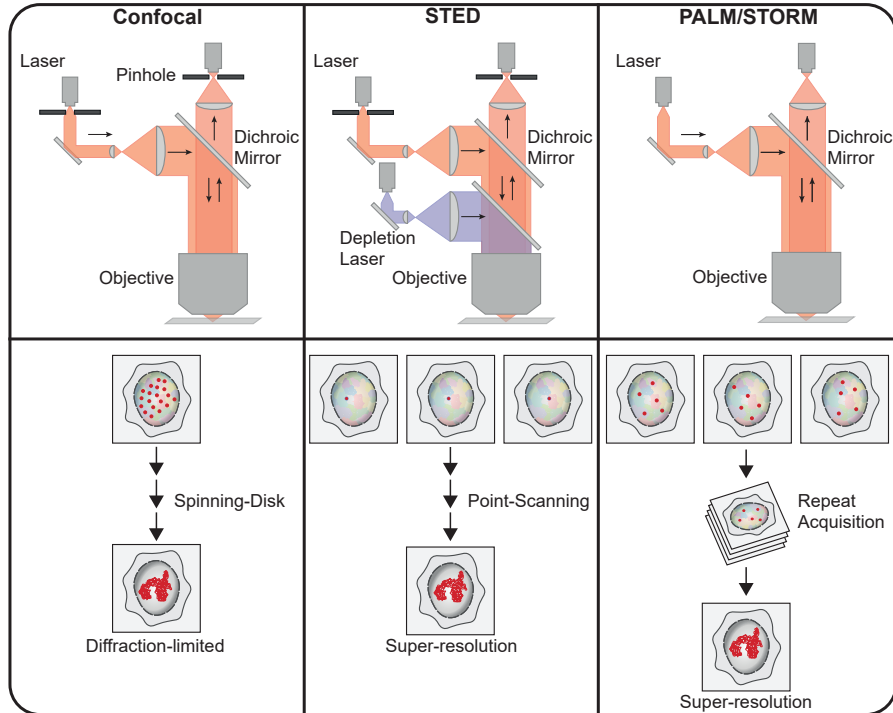

Figure 6: Schematic of diffraction-limited and super-resolution microscopy. Confocal microscopes use point illumination and pinholes to acquire diffraction-limited images and remove out-of-focus light. STED microscopes use a doughnut-shaped depletion beam that surrounds the excitation laser to surpass the diffraction limit. PALM/STORM acquires multiple wide-field images of stochastically blinking fluorophores, which are then reconstructed to produce a high-resolution image. Note that other super-resolution microscopy techniques, such as structured illumination microscopy, are not shown in this figure (Gustafsson, 2000; Kner et al., 2009; York et al., 2012).

STED microscopy overcomes the diffraction limit by confining fluorescence within the nanoscale area (Hell, 2007; Hell and Kroug, 1995). To achieve this, STED microscopy involves an excitation beam and a doughnut-shaped, red-shifted depletion beam. While the excitation beam excites fluorophores at the center, the surrounding depletion beam provokes fluorophores to emit red-shifted fluorescence, which is then filtered out by optical filters. As a consequence of this setup, the size of the fluorescent spot is reduced, and high spatial and temporal information is acquired without the need for post-processing

(Schermelleh et al., 2019). However, the high laser power required for STED microscopy results in high phototoxicity and requires bright, photostable STED-compatible dyes that absorb red light (594 nm / 638 nm) and can be depleted at 775 nm. As a result, STED is usually restricted to 2-color imaging but has provided valuable insights into gene regulation, DNA repair, meiosis, and nuclear senescence (Brown et al., 2018; Hernandez et al., 2018; Palikyras et al., 2024; Reindl et al., 2017).

The second type of super-resolution microscopy, namely SMLM, utilizes stochastic and transient on- and off-states of fluorophores. There are different variations of SMLM, including stochastic optical reconstruction microscopy (STORM) and fluorescence photoactivated localization microscopy (PALM) (Hess et al., 2006; Rust et al., 2006). In both microscopy setups, thousands of wide-field images of the same plane are acquired, and blinking fluorophores detected. Photons emitted from the fluorophores are then analyzed through image-processing algorithms and individual fluorophores localized. The resolution of the reconstructed image depends on the number of detected photons in a single fluorescence spot and can reach 20 nm laterally and 50 nm axially (Schermelleh et al., 2019). A specific form of SMLM named point accumulation in nanoscale topography (PAINT) does not strictly require the on- and off-state of fluorophores but detects transient binding events of labeled molecules to the target (Schnitzbauer et al., 2017). PAINT has recently been adapted into a DNA-barcoding method named resolution enhancement by sequential imaging (RESI), which distinguishes labeled proteins with Ångström-resolution (Reinhardt et al., 2023). Although SMLM variations allow for the detection of theoretically unlimited targets with high precision, the number of detectable targets is currently restricted by imaging speed. The development of fast, accurate, and sensitive microscopes, combined with advances in biochemical and molecular methodologies, will facilitate comprehensive characterization of nuclear architecture.

3.3.3 *The Art of FISH*

Fluorescence in situ hybridization (FISH) is a powerful technique to probe the spatial organization of nucleic acids in cells or tissue (Bantignies et al., 2011; Bauman et al., 1980; Bolzer et al., 2005; Chambeyron and Bickmore, 2004; Eskeland et al., 2010; Gall and Pardue, 1969; McGinnis et al., 1984; Pardue and Gall, 1969; Zink et al., 1998). While early FISH experiments often delineated large or repetitive genomic regions, advancements in microscopy, synthetic DNA production, and whole-genome sequencing have enabled extensive characterization of three-dimensional chromatin conformations (Beliveau et al., 2012; Bintu et al., 2018; Consortium, 2001; Finn and Misteli, 2019; Hughes and Ellington, 2017; Nora et al., 2012; Raj et al., 2008; Schermelleh

et al., 2019). A primary advantage of FISH is its ability to visualize chromatin in single cells, allowing the detection of rare biological phenomena that may be obscured in bulk data sets. Nonetheless, FISH requires careful planning in probe design, sample preparation, image acquisition and data analysis to facilitate accurate data acquisition and interpretation (figure 7).
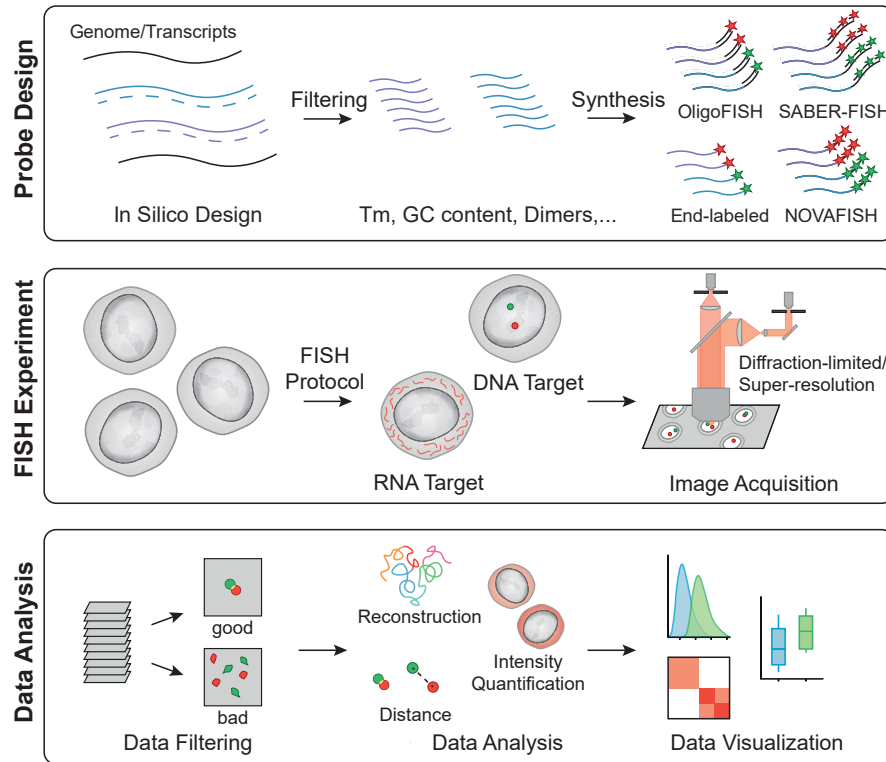
Figure 7: Overview of the FISH workflow. FISH probes are designed in silico and filtered based on criteria such as length, melting temperature, GC content, and secondary structure probability. Multiplexed imaging can be achieved using barcoded probes (OligoFISH, SABER-FISH), while small genomic targets may be visualized with labeled probes (end-labeled, NOVAFISH). Please note that there are other FISH probes not depicted in this graph. Sample preparation typically involves chemical fixation and permeabilization, and DNA or RNA targets are visualized using diffraction-limited or super-resolution microscopy. The data is then analyzed to remove false-positive or false-negative signals, and distances, intensities, or three-dimensional chromatin configurations are visualized.

FISH PROBE DESIGN   A successful FISH experiment requires probes that bind to the region of interest without interacting with themselves or other parts of the genome. In early FISH experiments, repetitive sequences were the target of choice as they could be easily detected with single FISH probes (Lansdorp et al., 1996; Matsuda and Chapman, 1995; Wiegant et al., 1991). While the advent of cloning facilitated the production of FISH probes that target single loci, unspecific binding and strong background signals restricted the minimal target size to 10s of thousands of base pairs (Liu and Zhang, 2021). Advances in bioinformatics and the availability of whole genome datasets have enabled customized probe design and synthesis of FISH probes with optimized specificity (Beliveau et al., 2018; Yilmaz et al., 2011). These FISH probes have several key characteristics: (i) high affinity for binding to the region of interest (on-target), (ii) low affinity for interacting with themselves or other genomic regions (off-target), (iii) meeting thermodynamic criteria, and (iv) a low tendency to form secondary structures.

Today, probes are routinely designed in silico using bioinformatics tools that select, filter, and analyze candidate probes (Aguilar et al., 2024; Beliveau et al., 2018; Gelali et al., 2019; Hershberg et al., 2021; Hu et al., 2020; Rouillard et al., 2003). First, target sequences are scanned using a sliding window approach to identify candidate probes with a set length of 32-40 bases to optimize for genome coverage and mismatch tolerance (Beliveau et al., 2012; Gelali et al., 2019). The probes are then filtered by GC content, melting temperature, and the likelihood of forming secondary structures to yield probes with similar binding characteristics (Kucho et al., 2004). For this purpose, various prediction models have been developed that estimate melting temperature and the probability of hairpin formation under different buffer conditions (Allawi and SantaLucia, 1997; Bommarito et al., 2000; Breslauer et al., 1986; Freier et al., 1986; Peyret et al., 1999; Sugimoto et al., 1996; Znosko et al., 2002). Alignment programs such as BLAST or Bowtie2 are used with Jellyfish to identify and filter out probes that may bind to other regions of the genome (Altschul et al., 1990; Langmead and Salzberg, 2012; Marcais and Kingsford, 2011). A final list containing all probe sequences is then retrieved and the probes are synthesized.

Most in silico probe design tools are freely available and have been optimized for user-friendliness, probe type, and target size. OligoArray 2.0 is a popular in silico FISH probe design tool that has been adapted for Oligopaint and hosts probes for six species, including human, mouse, zebrafish, and fruit fly (Beliveau et al., 2015; Rouillard et al., 2002, 2003). Oligominer and PaintSHOP are streamlined, user-friendly bioinformatics tools that filter probes based on length and various biochemical characteristics in relatively short timeframes (Beliveau et al., 2018; Hershberg et al., 2021; Passaro et al., 2020). iFISH4U

selects probe pools from a pre-designed genome-wide probe set that densely covers the human genome (Gelali et al., 2019). ProbeDealer has been specialized for chromatin tracing and RNA FISH experiments in mouse or human cells but it also allows for the integration of other genomes (Hu et al., 2020). TigerFISH is a notable exception among probe design tools, as it has been developed to detect chromosome-specific intervals of repetitive DNA (Aguilar et al., 2024).

FISH PROBE SYNTHESIS   In recent decades, FISH has evolved from a low-throughput, laborious, and expensive method to a versatile tool capable of probing complex multi-way contacts in the genome. At the center of this development is the synthesis of optimized FISH probes that produce bright signals for any target of interest. The first in situ hybridization experiments used tritium-labeled RNA or DNA to detect rDNA in Xenopus laevis and required autoradiography for detection (Gall and Pardue, 1969; Pardue and Gall, 1969). While radioisotope labeling is sensitive, visualization requires long exposure times (over a week for tritium-labeled probes) and acquired images exhibit high background signals (Huber et al., 2018). The transition from radioactively labeled probes to fluorescent probes reduced acquisition time and facilitated the widespread application of FISH (Bauman et al., 1980; Rudkin and Stollar, 1977). From the 1980s onwards, gene cloning and new labeling strategies yielded probes that can target individual regions on chromosomes (Burke et al., 1987; Deaven et al., 1986; Lu et al., 2009; Shizuya et al., 1992; Wiegant et al., 1991). In particular, bacterial artificial chromosomes (BACs), yeast artificial chromosomes (YACs), fosmids, and cosmids became popular platforms to produce and propagate FISH probes (Burke et al., 1987; Nath and Johnson, 1998; Shizuya et al., 1992). The generated FISH probes can detect regions ranging from tens of kb to several megabases, but their size renders the visualization of smaller regions unfeasible.

Advances in bioinformatics, the availability of whole-genome datasets, and the chemical synthesis of nucleic acids have enabled the production of short synthetic oligonucleotide libraries (Consortium, 2001; Hughes and Ellington, 2017; Liu and Zhang, 2021). These probes are designed in silico and optimized to quantify RNA molecules or visualize genomic loci ranging from 5 kb to 1 megabase (Beliveau et al., 2012; Kishi et al., 2019; Rouhanifard et al., 2019; Wang et al., 2021). Variations of oligonucleotide-based FISH (oligoFISH) involve barcoded primary pools and fluorescent secondary readout probes for target visualization (Bintu et al., 2018; Su et al., 2020; Takei et al., 2021). This approach enables multiplexed imaging of many genomic targets, facilitates chromatin tracing, and maps complex multi-way contacts (Bintu et al., 2018; Mateo et al., 2019; Nir et al., 2018). Nonetheless, the use of single-labeled secondary probes and the need for multiple hybridization rounds limit the detectable target size and spatial resolu-

tion. Chemical or enzymatic FISH-probe synthesis strategies enhance signal strength through serial ligation of circular DNA (Dardani et al., 2022; Rouhanifard et al., 2019), rolling circle amplification (Lizardi et al., 1998), hybridization chain reaction (Choi et al., 2014; Dirks and Pierce, 2004), branched DNA configurations (Xie et al., 2018), or primer exchange reaction (Kishi et al., 2019). These methods have become particularly popular for the quantification of RNA and allow the detection of low-abundant transcripts.

In addition to optimized probe design, various strategies have been developed to reduce nonspecific signals in the nucleus. In early FISH experiments, repetitive elements were masked with salmon sperm to decrease nonspecific background signals (Sealey et al., 1985). More recently, molecular beacon probes have been developed that provoke fluorescence quenching in the unbound state of the probe (Ni et al., 2017). Peptide nucleic acids (PNAs) are artificial oligonucleotides with an uncharged peptidic backbone that can stably bind to DNA (Nielsen et al., 1991). Compared to DNA-DNA interactions, DNA-PNA duplexes are more stable, have higher melting temperatures and exhibit lower background signals (Pellestor et al., 2003).

ENZYMATIC SYNTHESIS OF PROBES   Synthesis of FISH probes has been accomplished through biological, chemical, and enzymatic approaches. In early works, Gall et al. supplemented cell culture medium with uridine-H3 to purify radioactively labeled RNA FISH probes (Gall, 1968; Gall and Pardue, 1969; Pardue and Gall, 1969). While this strategy is sufficient for the detection of rDNA and rRNA, the generated RNA pools are not suited for detecting less abundant DNA or RNA sequences. Chemical synthesis of FISH probes often involves the conjugation of dyes to the 3'-end of chemically modified oligonucleotides through NHS ester conjugation or click-chemistry (Ishizuka et al., 2016; Kolb et al., 2001; Raddaoui et al., 2020; Raj et al., 2008; Raj and Tyagi, 2010). NHS ester conjugation is particularly effective for the generation of a limited number of labeled probes, but the production of diverse probe sets is expensive and requires laborious HPLC purification. Different strategies have been developed for the enzymatic synthesis of labeled or barcoded probes (figure 8). The construction of BAC and YAC libraries has facilitated physical mapping of the human genome and enabled the production of genome-region specific FISH probes through nick-translation (Anand et al., 1989; Osoegawa et al., 2001). Nick translation involves the introduction of single-strand breaks into BACs by DNAse 1 followed by polI-mediated excision and incorporation of modified nucleotides (Bolland et al., 2013; Garimberti and Tosi, 2010). This process typically yields pools of biotin-, digoxigenin-, or dye-labeled DNA fragments that span hundreds of bases each. BAC- and YAC-derived probes have been instrumental for chromosome painting or the visualization of megabase regions, but

their size limits their ability to bind smaller structures. Alternative approaches include the use of short, non-specific primers (random priming) or size-specific PCR to generate probes from cloned genomic regions or flow-sorted chromosomes (Nath and Johnson, 1998). However, probe design in this strategy is restricted by the availability of cloned genomic sequences, and the produced probes often generate high background signals.

The advent of synthetic oligonucleotide library production has enabled the amplification of barcoded FISH probe sets from large pools (figure 8) (Beliveau et al., 2012; Murgha et al., 2014). Several variations of selective probe amplification have been established, but the combination of PCR, in vitro transcription, reverse transcription, and RNA degradation offers several advantages: (i) different primer combinations can be used for PCR to selectively amplify distinct probe sets, (ii) probe barcodes can be adapted by changing primer overhangs used for PCR, (iii) in vitro transcription increases the yield by up to 100-fold (Moffitt and Zhuang, 2016).

Nick-Translation
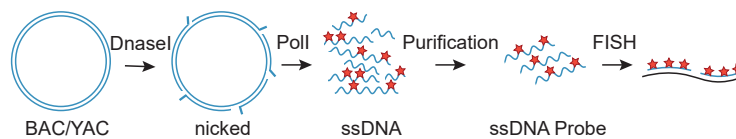
Oligopool Synthesis
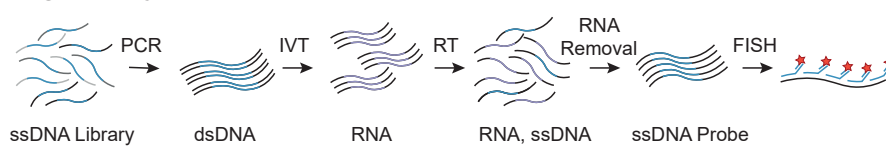
Figure 8: Enzymatic synthesis of labeled and barcoded FISH probes. Nick-translation creates labeled probes from BACs or YACs that span hundreds of bases. Oligonucleotide probe sets are synthesized from a complex single-stranded DNA library through PCR, in vitro transcription (IVT), reverse transcription (RT) and RNA removal.

3.3.4 *Limitations of FISH*

FISH provides spatial information about chromatin conformation, but several discrepancies complicate interpretations in the broader context of 3D genome organization. These limitations include potential chromatin disruption during sample preparation, low throughput in the number of detectable targets, and target size (Kempfer and Pombo, 2020). Despite substantial progress in the development of gentle, efficient, and sensitive FISH protocols, some discrepancies persist, which are addressed in the following paragraphs.

FISH sample preparation involves fixation, permeabilization, denaturation, hybridization, and washing to produce signals at the locus of interest (figure 9). However, harsh fixation treatments, aggressive permeabilization reagents, and prolonged denaturation may disrupt fine chromatin structures and lower data quality. Common fixation protocols use organic solvents or aldehyde solutions to immobilize and preserve cellular structures (Schnell et al., 2012). Methanol is an organic solvent that causes dehydration of the specimen, denaturation of proteins, and extraction of lipids (Humbel et al., 2019). While methanol treatment simultaneously induces fixation and permeabilization, the extraction of nuclear proteins causes cell shrinkage and can disrupt fine chromatin structures (Hoetelmans et al., 2001; Vielkind and Swierenga, 1989). Aldehyde-based fixation involves treatment with formaldehyde, paraformaldehyde, or glutaraldehyde and preserves cellular structures by chemical cross-linking of proteins and DNA (Thavarajah et al., 2012). Formaldehyde is a widely used fixative that requires subsequent incubation with Triton X-100, Tween 20, digitonin, or saponin to permeabilize cell membranes (Jamur and Oliver, 2010). The use of Triton X-100 for permeabilization is often preferred in FISH protocols because it renders the nucleus accessible for probe binding while preserving nuclear components (Schnell et al., 2012).
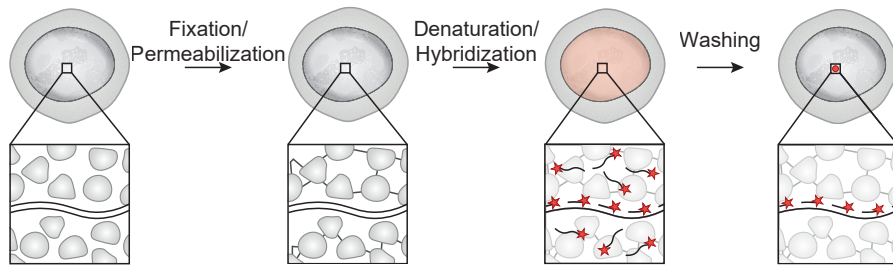
Figure 9: Workflow of DNA FISH. Fixation involves the chemical cross-linking of proteins and DNA, while permeabilization uses detergents to remove membrane lipids and facilitate the entry of FISH probes into the cell. FISH probes are added before heat denaturation and allowed to hybridize with the genomic target overnight. Unbound probes are removed during multiple temperature-dependent washing steps.

Another major concern in FISH protocols is potential chromatin swelling or dispersal that may occur during heat denaturation (Markaki et al., 2012; Solovei et al., 2002). As mentioned in chapter 3.3.3, specimens are heated prior to hybridization to denature genomic DNA and facilitate binding of probes to target sequences. However, there is debate over the impact of heat denaturation on chromatin (Markaki et al., 2012). Kim et al. immobilized GFP at lac operons in transgenic cell lines and found that GFP signals captured before heat denaturation co-localized with FISH signals (Kim et al., 2007). Using 3D-sim, Markaki et al. demonstrated that chromatin structures larger than

100 nm remain largely unchanged following heat treatment. However, Solovei et al. detected alterations in the ultrastructure of the nucleus upon heat treatment using electron microscopy (Solovei et al., 2002). Therefore, it is not entirely clear to what degree smaller structures are preserved after heat treatment.

Computational and enzymatic approaches have been developed to facilitate FISH probe hybridization without the need for prior heat treatment. COMBO-FISH involves bioinformatic searches in sequence databases to select probe sets that form triple helices with double-stranded DNA at low-temperatures (Hausmann et al., 2003). To date, applications of COMBO-FISH have been restricted to highly repetitive DNA sequences, such as transposable elements or trinucleotide repeats (Krufczik et al., 2017). Other FISH protocols involve nucleases that unwind, melt, or digest double-stranded genomic DNA and facilitate probe binding. CASFISH recruits labeled Cas9 proteins to the genomic target of interest using a set of gRNAs (Deng et al., 2015). Genome oligopaint via local denaturation (GOLD)-FISH involves the generation of Cas9-mediated nicks at the locus of interest and Rep-X helicase-mediated unwinding of DNA to enable probe binding (Wang et al., 2021). Resolution after single-strand exonuclease resection (RASER)-FISH uses UV-light and exonuclease III-mediated digestion to create ssDNA that is accessible for labeled probes (Brown et al., 2022). While these methods circumvent potential chromatin disruption caused by heat treatment, they involve enzymatic digestion of DNA and fixation with methanol-acetic acid. Therefore, the extent to which chromatin is preserved after these treatments has yet to be determined.

In addition to the implementation of gentle FISH protocols, major efforts have been made to increase the throughput and sensitivity of FISH. As discussed in chapter 3.3.3, the number of FISH targets that can be visualized is limited by the number of distinguishable fluorophores. The development of barcoded FISH probes and microfluidics has addressed this limitation by enabling high-throughput multiplexed imaging (Beliveau et al., 2012; Huber et al., 2018). Remarkable examples of multiplex FISH include chromosome tracing, which involves dozens of genomic targets, and the quantification of hundreds of RNA species in cells or tissue (Chen et al., 2015b; Nguyen et al., 2020; Nir et al., 2018; Zhang et al., 2021a). Despite these methodological advancements, probe consumption and imaging time restrict the number of hybridization rounds and make multiplexed genome-wide FISH experiments unfeasible (Huber et al., 2018). The transition from large BAC- or YAC-derived probes to short, synthetic FISH probes has increased flexibility in probe design and reduced the minimum target size from tens of kb to 5-20 kb (Kempfer and Pombo, 2020). While signal amplification methods (chapter 3.3.3) involve multiple hybridization rounds to increase signal strength, the detection of kb genomic elements may still be complicated by DNA accessibility and

nonspecific amplification (Choi et al., 2014; Dardani et al., 2022; Dirks and Pierce, 2004; Kishi et al., 2019; Lizardi et al., 1998; Rouhanifard et al., 2019; Xie et al., 2018). Therefore, optimizing experimental setups and the development of bright, specific FISH probes are necessary to increase throughput, reduce target size, and map complex spatial arrangements of small genomic elements.

3.3.5 *Complementing 3C-based Methods with FISH*

Over the past decades, 3C-based methods and FISH have emerged as powerful techniques to characterize spatial relationships between genomic regions. The interpretation of 3C-based contact maps and FISH datasets requires a thorough understanding of sample preparation, the specific distances captured, and data analysis (figure 10).

Common variations of Hi-C use cross-linking, digestion, biotinylation, ligation, pulldown, and sequencing to detect pairwise contacts across the genome. "Contacts" can be defined as distances smaller than the radius of crosslinking and proximity ligation, which is roughly 10-100 nm (Maslova and Krasikova, 2021). In this manner, contact maps provide a comprehensive view of genome-wide chromatin interactions and feature TADs and enhancer-promoter interactions. However, rare events, such as TAD-like domains observed in single-cell datasets, might not be detected by 3C-based methods (Bintu et al., 2018; Goel and Hansen, 2021). FISH involves cross-linking, denaturation, hybridization, and washing to probe all conformations between a selected number of targets (Kempfer and Pombo, 2020). Unlike 3C-based methods, FISH captures all possible conformations in single cells, detects cell-to-cell variation, and identifies rare events such as transient DNA-DNA interactions (Bintu et al., 2018). Moreover, multiplexed FISH and chromatin tracing uncover complex spatial relationships between dozens of genomic loci (Bintu et al., 2018; Cardozo Gizzi et al., 2019; Liu et al., 2020; Mateo et al., 2019; Nir et al., 2018; Wang et al., 2017). Nonetheless, the view of the genome is restricted to the number of genetic loci targeted in the FISH experiment. This may be problematic if, for example, multiple unknown regulatory elements impact the expression of a target gene. Therefore, Hi-C contact maps and ChIP datasets are frequently used for target selection and FISH probe design.

3C-based methods and FISH detect proximity between genomic loci and often produce complementary data sets. Indeed, merging single-cell chromatin tracing datasets from a cell population yields population-averaged FISH distance matrices comparable to those obtained from Hi-C (Bintu et al., 2018; Cardozo Gizzi et al., 2019). Moreover, data from 3C-based methods nearly perfectly coincide with FISH measurements when spatial thresholds between 120–150 nm are imposed on distance distributions (Bintu et al., 2018; Wang et al.,

Chromatin Conformation Capture **Fluorescence In Situ Hybridization**

Principle

Cross-link → Digest

Biotinylate Ligate → Sheer Pull-down →

Proximity Ligation

Cross-link → Denature

Hybridize → Wash →

Hybridization

Captured Distances

Probability | r | Distance

Conformations < r

Probability | Distance

All Conformations

Throughput

Interaction Map

Genome-wide

Distance

Reconstruction

Restricted

Figure 10: Comparison of 3C-based methods and FISH. 3C-based methods are biochemical approaches that capture local or genome-wide interaction patterns with distances smaller than the cross-linking and proximity ligation radius. FISH is a microscopy-based method that detects all possible conformations of a set number of defined genomic loci. Note that the first row depicts schematics of Hi-C or DNA-FISH protocols.

2017). However, several studies have revealed occasional discrepancies between data obtained from 3C-based methods and FISH (Finn and Misteli, 2019; Wang et al., 2017). These inconsistencies may arise from technical differences between the techniques, as the proximity ligation radius in 3C-based methods is poorly defined and FISH distance thresholds are often adjusted arbitrarily (Giorgetti and Heard, 2016; McCord et al., 2020). Alternatively, genomic loci may exhibit bimodal distance distributions that are difficult to detect with 3C-based methods (Giorgetti and Heard, 2016).

In conclusion, 3C-based methods provide a comprehensive view of pairwise DNA-DNA contacts across the genome, whereas FISH captures all possible conformations of a selected set of targets. Single-cell Hi-C and FISH can detect rare DNA-DNA contacts that may be masked in population-averaged datasets, but mapping complex multi-way interactions among small genomic elements remains challenging. In this thesis, we established a versatile workflow to synthesize FISH probes that allow the detection of small genomic elements with high precision (chapter 4.1). These probes were then used to map enhancer hijacking events in AML cells with recurrent chromosomal transloca-

tions (chapter 4.2). Lastly, we systematically measured the compaction of regulatory active and inactive genomic regions with FISH and attributed cell-to-cell variability to internucleosomal interactions, nucleosome occupancy, and the binding of histone H1 (chapter 4.3).

4

RESULTS

4.1 GENERATION OF DENSELY LABELED OLIGONUCLEOTIDES FOR THE DETECTION OF SMALL GENOMIC ELEMENTS

Cell Reports
Methods

Generation of densely labeled oligonucleotides for the detection of small genomic elements

Graphical abstract
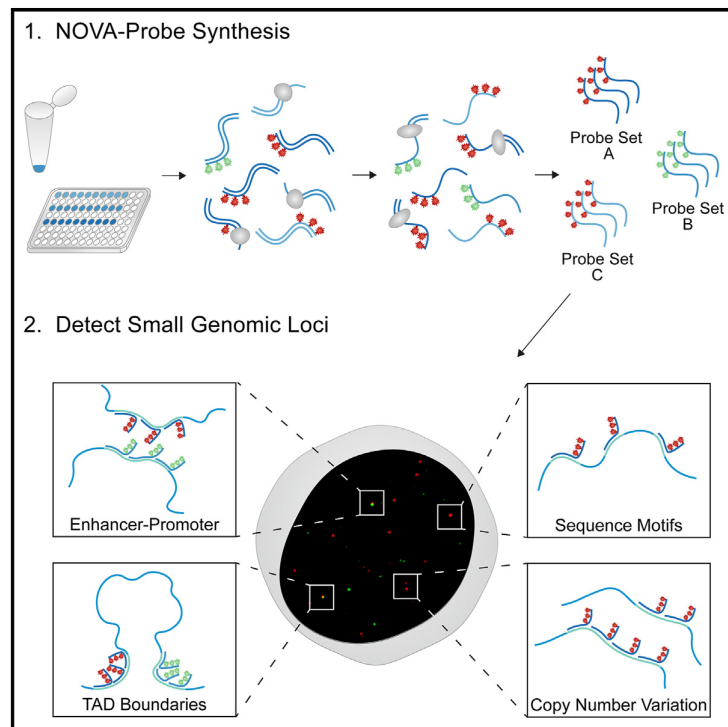
Authors

Clemens Steinek, Miguel Guirao-Ortiz, Gabriela Stumberger, ..., Thomas Carell, Hartmann Harz, Heinrich Leonhardt

Correspondence

steinek@biologie.uni-muenchen.de (C.S.),
harz@biologie.uni-muenchen.de (H.H.),
h.leonhardt@lmu.de (H.L.)

In brief

Steinek et al. develop a simple workflow for the enzymatic synthesis of densely labeled oligonucleotides. The described approach allows for free choice of fluorophores and flexible adjustment of labeling density to optimize signal detection. NOVA probes enable the detection of sub-kilobase genomic loci using confocal or super-resolution microscopy.

Highlights

- Rapid, flexible, and cost-effective synthesis of densely labeled oligonucleotides

- Systematic analysis of distance-dependent dye-dye interactions

- The NOVA workflow selectively yields labeled probe sets from complex probe pools

- NOVA-FISH enables the visualization of sub-kilobase genomic loci

CellPress

Cell Reports Methods

CellPress

Article

Generation of densely labeled oligonucleotides for the detection of small genomic elements

Clemens Steinek,[1,*] Miguel Guirao-Ortiz,[1] Gabriela Stumberger,[1] Annika J. Tölke,[2] David Hörl,[1] Thomas Carell,[2] Hartmann Harz,[1,*] and Heinrich Leonhardt[1,3,*]
[1]Faculty of Biology and Center for Molecular Biosystems (BioSysM), Human Biology and BioImaging, Ludwig-Maximilians-Universität München, 81377 Munich, Germany
[2]Department of Chemistry, Ludwig-Maximilians-Universität München, 81377 Munich, Germany
[3]Lead contact
*Correspondence: steinek@biologie.uni-muenchen.de (C.S.), harz@biologie.uni-muenchen.de (H.H.), h.leonhardt@lmu.de (H.L.)
https://doi.org/10.1016/j.crmeth.2024.100840

MOTIVATION While three-dimensional chromatin conformations can be explored with fluorescence *in situ* hybridization (FISH), the visualization of small genomic loci with high spatial resolution remains challenging. For such applications, programmable oligonucleotides with high brightness are required. To further improve precision and sensitivity, secondary hybridization steps should be omitted. Here, we present a simple, quick, and inexpensive approach to generate labeled FISH probes that carry several fluorophores. Our workflow allows for the free choice of fluorophores, flexible adjustment of labeling density, and selective probe synthesis from large probe pools. With our probes, we reliably detect genomic loci below the kilobase level and examine their topological relationships.

SUMMARY

The genome contains numerous regulatory elements that may undergo complex interactions and contribute to the establishment, maintenance, and change of cellular identity. Three-dimensional genome organization can be explored with fluorescence *in situ* hybridization (FISH) at the single-cell level, but the detection of small genomic loci remains challenging. Here, we provide a rapid and simple protocol for the generation of bright FISH probes suited for the detection of small genomic elements. We systematically optimized probe design and synthesis, screened polymerases for their ability to incorporate dye-labeled nucleotides, and streamlined purification conditions to yield nanoscopy-compatible oligonucleotides with dyes in variable arrays (NOVA probes). With these probes, we detect genomic loci ranging from genome-wide repetitive regions down to non-repetitive loci below the kilobase scale. In conclusion, we introduce a simple workflow to generate densely labeled oligonucleotide pools that facilitate detection and nanoscopic measurements of small genomic elements in single cells.

INTRODUCTION

In recent years, multiple layers of mammalian genome organization ranging from preferential positions of chromosomes in the nucleus to active and inactive compartments and small-scale interactions between individual loci have been uncovered.[1–5] An intricate interplay of chromosome territories, topologically associated domains, and regulatory elements defines cellular identity in development and disease.[6–10] While current methodologies reliably probe pairwise and multi-contact DNA-DNA interactions, deciphering complex 3D chromatin organization in single cells remains challenging, particularly in the kilobase range.[11,12] Thus, there is a growing demand for increased sensitivity to detect and study DNA elements in the 3D context of individual nuclei.

The state of the art for mapping chromatin contacts is chromatin capture assays.[13–17] These methods are especially powerful, as they detect contacts within large-scale genomic regions with a resolution ranging from 1 kb down to the nucleosome level, but typically rely on population averages.[18–20] However, early efforts to probe chromatin contacts in single cells using chromatin capture assays have revealed extensive cell-to-cell variations within the same population.[21–23] Intercell variation of 3D chromatin structures has been observed in multiple imaging studies, which is consistent with the transient nature of chromatin contacts revealed by live-cell imaging.[11,12,24–30] Therefore,

Cell Reports Methods
Article
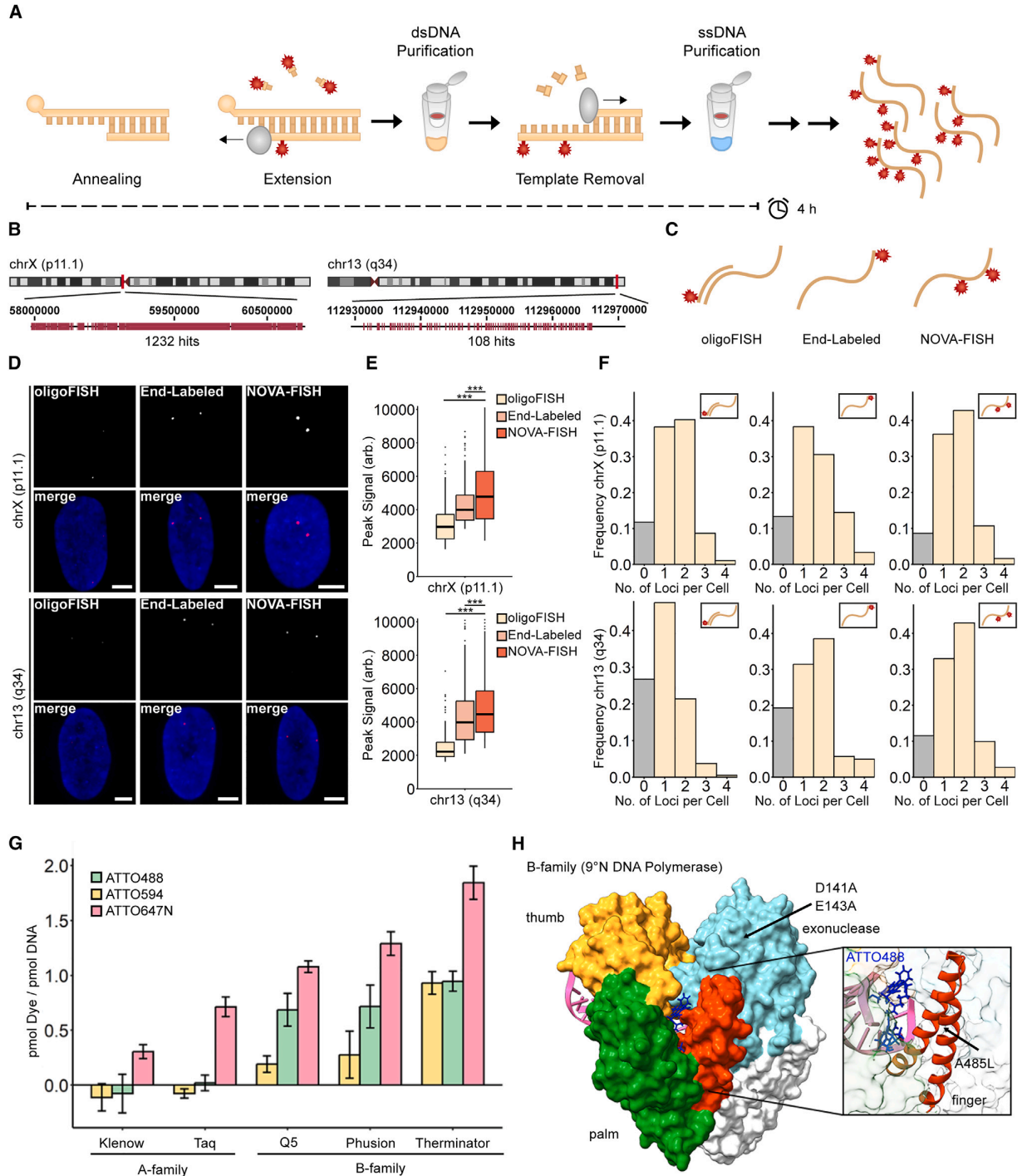
Figure 1. Generating oligonucleotides that carry multiple fluorophores

(A) Schematic workflow of the protocol. Primers are annealed to 5′ phosphorylated template strands, and dye-labeled nucleotides are incorporated in a one-step extension reaction. Template strands are then enzymatically removed, and the product is purified.

(B) Depiction of the target regions. The target regions contain a unique series of repeats (pink) in chrX (p11.1) or chr13 (q34). Human reference GRCh37/hg19 was used to retrieve coordinates.

(legend continued on next page)

Cell Reports Methods
Article

chromatin capture assays need to be complemented with sensitive imaging methods to comprehensively address the dynamics and function of chromatin conformations.

Since their advent, microscopy and fluorescence *in situ* hybridization (FISH) have shed light on the spatial distribution of chromatin in single cells and identified chromosomal abnormalities in malignant cells and tissues.[31–35] Although fluorescence microscopy has facilitated studies on large-scale chromatin structures, the detection and resolution of small regulatory elements with traditional FISH methods remains challenging.[24,36] In past works, FISH probes have often been generated from bacterial artificial chromosomes (BACs) or yeast artificial chromosomes (YACs) using polymerases in random priming or nick translation reactions.[37–40] However, the size of BAC or YAC probes limits the genomic resolution and is, therefore, not suitable for the detection of short regulatory DNA sequences.[41] Recent advances in synthetic DNA production and the availability of whole-genome datasets have ushered in a new era of oligonucleotide-based FISH (oligoFISH) methodologies.[28,42–47] Variations of oligoFISH utilize barcoded primary pools and fluorescent secondary readout probes to sequentially detect genomic loci. Although this approach has enabled considerable advancements in understanding chromatin architecture, the usage of single-labeled secondary probes limits the detectable target size and spatial resolution. Signal amplification has been achieved through rolling circle amplification,[48] hybridization chain reaction,[49,50] serial ligation of circular DNA (clamp-FISH[51,52]), branched DNA configurations,[53] or primer exchange reaction (SABER-FISH[54]). These techniques typically involve multiple hybridization rounds and enable detection of multiple targets, but DNA accessibility and an increased risk of non-specific amplification may complicate the visualization of small genomic elements. We hypothesized that the direct coupling of multiple fluorophores to primary oligonucleotides in combination with the elimination of secondary hybridization steps improves the signal-to-noise ratio at DNA loci of interest.

Here, we introduce a protocol to generate nanoscopy-compatible oligonucleotides with dyes in variable arrays (NOVA probes). Multiple fluorophores are attached to oligonucleotides in a one-step biochemical reaction, thereby considerably shortening the time required for probe generation. The protocol has further been optimized to allow precise control of the labeling density and does not require demanding amplification or purification steps. We applied our probes to detect a variety of genomic loci ranging from large-scale repetitive regions to sub-kilobase single loci using FISH (NOVA-FISH). Compared to previous methods, NOVA-FISH probes can efficiently be produced and allow free choice of fluorophores and flexible adjustment of labeling density to optimize signal detection in super-resolution microscopy.

RESULTS

Design and synthesis of NOVA probes

OligoFISH methods have proven valuable in visualizing genomic regions, but the necessity of multiple hybridization steps and/or the use of expensive, end-labeled probes limit their widespread application in nanoscopy. We reasoned that densely labeled oligonucleotide probe sets could be generated with an enzymatic approach in an efficient and cost-effective manner (Figure 1A). To this goal, we hybridized 5′ phosphate-labeled template strands with short primers followed by primer extension and lambda-exonuclease-mediated template degradation. We synthesized two probes that target a series of repeats on chromosome X (chrX; p11.1) or chr13 (q34) (Figure 1B). Compared with barcoded oligonucleotides and end-labeled probes, our densely labeled oligonucleotides (NOVA probes) significantly improve signal strength (Figures 1C–1E). Moreover, NOVA-FISH exhibits a significant improvement in detectability of the smaller target on chr13 (q34) ($p < 0.001$, Wilcoxon rank-sum test) but not chrX (p11.1). Therefore, NOVA probes are well suited for detecting small genomic loci (Figure 1F).

As our approach depends on the enzymatic incorporation of modified nucleotides into short primers, we compared commonly available DNA polymerases. We measured the incorporation of different dye-labeled nucleotides during extension using commonly available family A (Klenow exo-, Taq) and family B (Q5, Phusion, Terminator) DNA polymerases. Photometric measurements of synthetized probes showed that the highest labeling rates were obtained for all tested modified nucleotides with Terminator DNA polymerase (Figures 1G and S1A–S1C).

(C) Comparing three FISH strategies to tag genomic loci. While oligoFISH uses labeled readout strands for detection, end-labeled and NOVA-FISH probes carry fluorophores in their primary sequences.

(D) Representative images of both targets detected with oligoFISH, end-labeled probes, or NOVA-FISH. FISH was conducted in IMR-90 cells. Scale bars, 5 μm.

(E) NOVA-FISH yields bright FISH signals. Number of detected signals: chrX (p11.1): oligoFISH ($n = 430$), end-labeled ($n = 420$), and NOVA-FISH ($n = 548$); chr13 (q34): oligoFISH ($n = 292$), end-labeled ($n = 354$), and NOVA-FISH ($n = 413$). Datasets were tested for significance using the Wilcoxon rank-sum test with Bonferroni's correction for multiple testing (***$p < 0.001$).

(F) NOVA-FISH improves detectability in small genomic loci. Histograms depict the relative number (no.) of chrX (p11.1) or chr13 (q34) foci detected. NOVA-FISH exhibits a significant improvement in the detectability of chr13 (q34) ($p < 0.001$ for NOVA-FISH vs. oligoFISH and NOVA-FISH vs. end labeled, Wilcoxon rank-sum test). Nuclei that have been entirely imaged were included in the analysis. Number of cells analyzed: chrX (p11.1): oligoFISH ($n = 196$), end labeled ($n = 180$), and NOVA-FISH ($n = 243$); chr13 (q34): oligoFISH ($n = 187$), end labeled ($n = 157$), and NOVA-FISH ($n = 182$).

(G) Screening substrate preferences of selected DNA polymerases. Polymerases (Klenow exo-, Taq, Q5, Phusion, Terminator) incorporated dCTP-ATTO488, dCTP-ATTO594, or dCTP-ATTO647N into oligonucleotides using a 1:4 molar ratio of dye-labeled to unlabeled nucleotides. Data are represented as mean ± SD. See also Figure S1A.

(H) Crystal structure of the 9°N DNA polymerase in complex with DNA and dCTP-ATTO488. The protein is shown in white with highlighted palm (green), thumb (yellow), finger (orange), and exonuclease (cyan) domains. dCTP-ATTO488 was superimposed on the incorporated nucleotide in the complex. The magnified image depicts dCTP-ATTO488 in the binding pocket. See also Figure S2. The figure was generated with UCSF Chimera (v.1.17.3, RRID: SCR_015872) accessing 5OMV.[55,56]
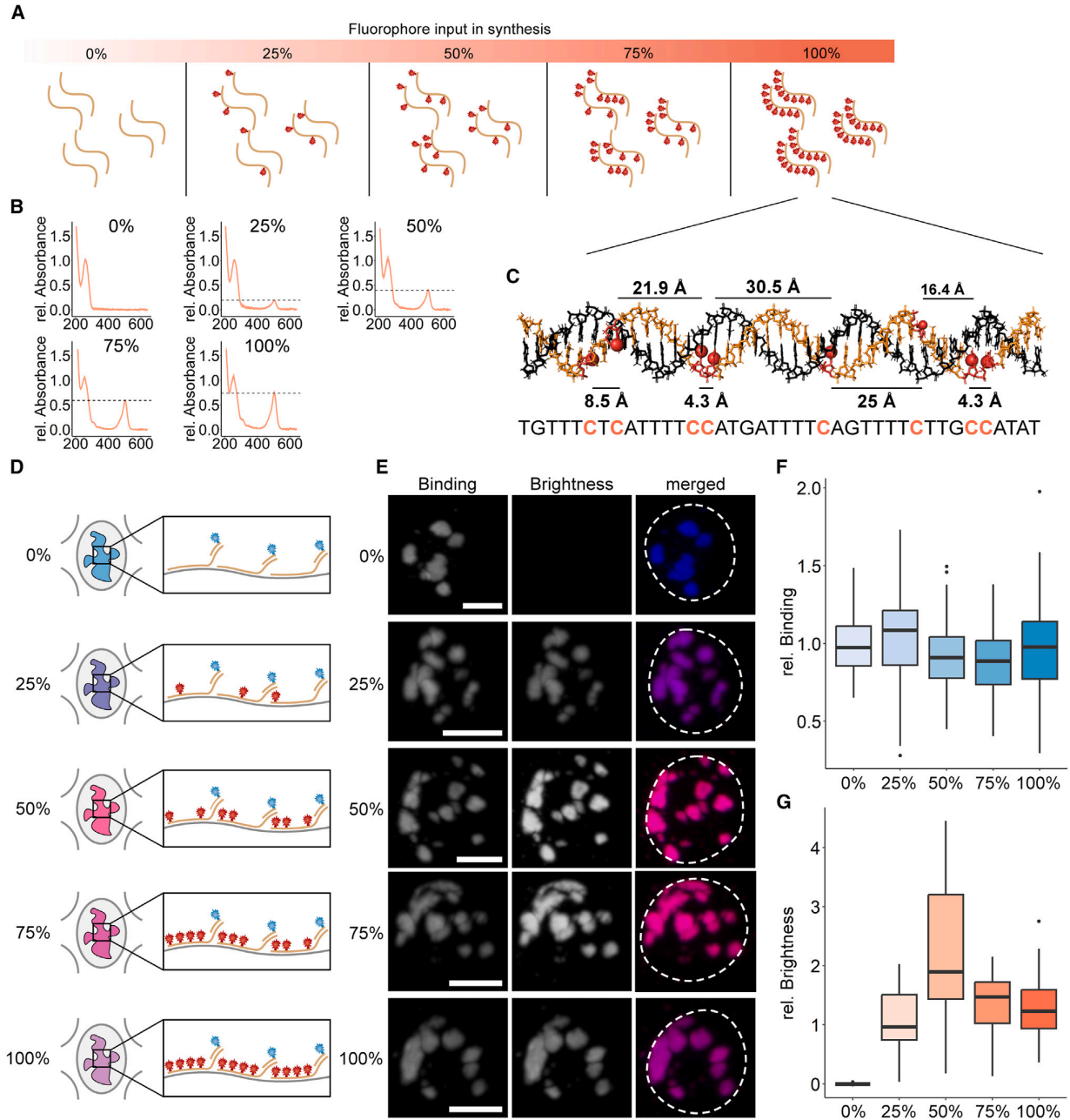
Figure 2. Binding efficiency and brightness of densely labeled probes

(A) Modulating labeling densities during NOVA probe synthesis. The labeling density is controlled through the ratio of labeled to unlabeled nucleotide (0%, 25%, 50%, 75%, 100%) in the synthesis reaction.

(B) Absorption spectra of probes with increasing labeling density. The absorbance was normalized by the absorption peak at 260 nm. The dotted lines indicate the absorption maximum of the fluorophore.

(C) Modeling fluorophore spacing in NOVA-FISH probes bound to major satellites. The B-form duplex formed by a NOVA-FISH probe (beige) and the genomic target (black) is shown. Red nucleotides indicate the locations of modified cytosines, and fluorophores are depicted as red knobs. The normal distance between neighboring fluorophores in the helix is depicted. The figure was created in Pymol v.2.5.5 (RRID: SCR_000305).[66]

(D) Assay to determine the impact of fluorophore number in the probe on hybridization efficiency. NOVA-FISH probes carrying increasing numbers of fluorophores (red) are hybridized with a locus of interest, and dye-labeled secondary strands (blue) are used as a reference.

(legend continued on next page)

Cell Reports Methods
Article

Therminator DNA polymerase is a DNA polymerase that has been derived from the euryarchaeon *Thermococcus* sp. 9°N and carries mutations in its exonuclease domain (D141A, E143A) and finger domain (A485L)[57] (Figure 1H). As a result of these modifications, Therminator DNA polymerase exhibits decreased discrimination for modified nucleotides and has been used to synthesize a variety of unnatural nucleic acids.[58–61] To investigate the molecular basis for the observed variations in incorporation efficiencies among our candidates, we modeled dye-labeled nucleotides in different conformations in conjunction with finger domains of family A and B polymerases (Figure S2). We noted possible steric clashes between dye-labeled nucleotides and finger domains of family A members, whereas no such clashes were observed with family B polymerases. Using Therminator DNA polymerase, we determined that probes are robustly generated within an hour (Figure S1D). In addition, our approach allows free choice of fluorophore and flexible adjustment of labeling density (Figure S1E).

FISH probes require a high degree of purity since complementary or unlabeled strands will compete with the labeled probe during hybridization and, thus, reduce signal intensity. To remove unbound primers, free nucleotides, and enzymes, we adapted the buffer conditions to selectively yield double-stranded oligonucleotides after extension (Figures S3A–S3C). Also, unlabeled template DNA might block the synthesized probes and thereby prevent their hybridization with the locus of interest. Therefore, we have introduced phosphate groups at the 5′ ends of template strands to mark them for lambda-exonuclease-mediated degradation (Figure S3D). Using this approach, template DNA was effectively degraded within 30 min (Figure S3E). We then used ethanol-based purification to obtain the single-stranded probe (Figures S3A and S3C). This simple purification strategy yielded all NOVA probes used for microscopic measurements in this work.

After establishing a robust workflow, we assessed the number of incorporated fluorophores in NOVA probes. High-performance liquid chromatography (HPLC) analysis revealed that using a low ratio of modified to unmodified nucleotides (25%) in the synthesis reaction yields distinct elution peaks corresponding to the incorporation of increasing numbers of fluorophores (Figures S3F and S3G).

Visualizing telomere clustering below the diffraction limit

Next, we sought to utilize the brightness of NOVA probes to visualize telomeres below the diffraction limit. We tagged telomeres with telomere-specific NOVA probes and acquired images using confocal or stimulated emission depletion (STED) microscopy (Figure S1F). We observed clustered telomeres using STED microscopy, which appear as single entities in confocal images. We then applied 3D STED microscopy to gain further insights into the degree of telomere clustering (Figure S1G). Telomeres

in the same cells exhibited considerable heterogeneity in their size, and clusters containing multiple telomeres were observed, consistent with previous works.[62–65] Next, we analyzed the number of detectable telomeres using confocal or STED microscopy (Figure S1G). In comparison to confocal images, STED microscopy detected, on average, 1.31 times more telomeres (±SD = 0.21), corresponding to clustered telomeres that are only resolved with super-resolution microscopy. Hence, the brightness of NOVA probes supports demanding super-resolution microscopy to visualize nuanced details of genomic loci with high optical resolution.

Dense labeling does not affect hybridization efficiency but reduces signal strength

As our workflow yields densely labeled probes, we next tested how the presence of multiple dyes in the probe affects hybridization efficiency. To address this, we generated barcoded probes with increasing labeling densities (Figures 2A–2C and S1E). These probes contain dye-labeled sequences that bind to the genome and unlabeled barcodes that hybridize with secondary probes carrying another dye. Using this approach, we can evaluate the brightness of the NOVA probe signal (green) and the relative number of probes localized at the target region (red) (Figures 2D and 2E). We found that increasing the number of dye-labeled nucleotides in the probe did not affect the number of bound probes at the locus of interest, as no notable drop in red signal was observed (Figure 2F). However, the brightness of our probes decreases at high labeling densities (Figure 2G). Consequently, densely labeled probes still bind to the region of interest, but short intermolecular distances between fluorophores impede signal strength (Figure 2C).

We next characterized the impact of dye-dye distances on probe fluorescence. We incorporated two dye molecules into overhangs of probes and increased the distances in between (1, 3, 5, 7, or 10 bases) (Figure 3A). Then, we measured the intensity of probes carrying two ATTO488 or ATTO647N molecules at the FISH spot (Figure 3B). The fluorescence of ATTO488- and ATTO647N-labeled probes increases with greater dye-dye distances (Figure 3C). Therefore, we hypothesize that distance-dependent fluorescence quenching impacts the brightness of densely labeled probes.

Establishing densely labeled probes with regularly spaced fluorophores

Our previous strategy yields labeled oligonucleotides in an efficient and cost-effective manner but depends on the occurrence of cytosines in the synthesized sequence. Therefore, we modified our workflow to generate extended probes (xNOVA probes) that carry fluorophores in a protruding sequence that does not bind to the genome (Figure 3D).[44,67] In this design, fluorophores are regularly spaced in the invariable sequence to avoid distance-dependent fluorescence quenching that might diminish

(E) Representative images of major satellites in mouse embryonic stem cells detected with NOVA-FISH probes containing increasing numbers of fluorophores. Scale bars, 5 μm.

(F) Binding efficiency is unaffected by dense labeling. The normalized intensity of dye-labeled secondary strands (blue) is depicted.

(G) Densely labeled probes exhibit a decrease in fluorescence. Related to (F). The normalized intensity of NOVA-FISH probes (red) is depicted. Number of cells analyzed: 0% (n = 149), 25% (n = 146), 50% (n = 172), 75% (n = 147), and 100% (n = 165).
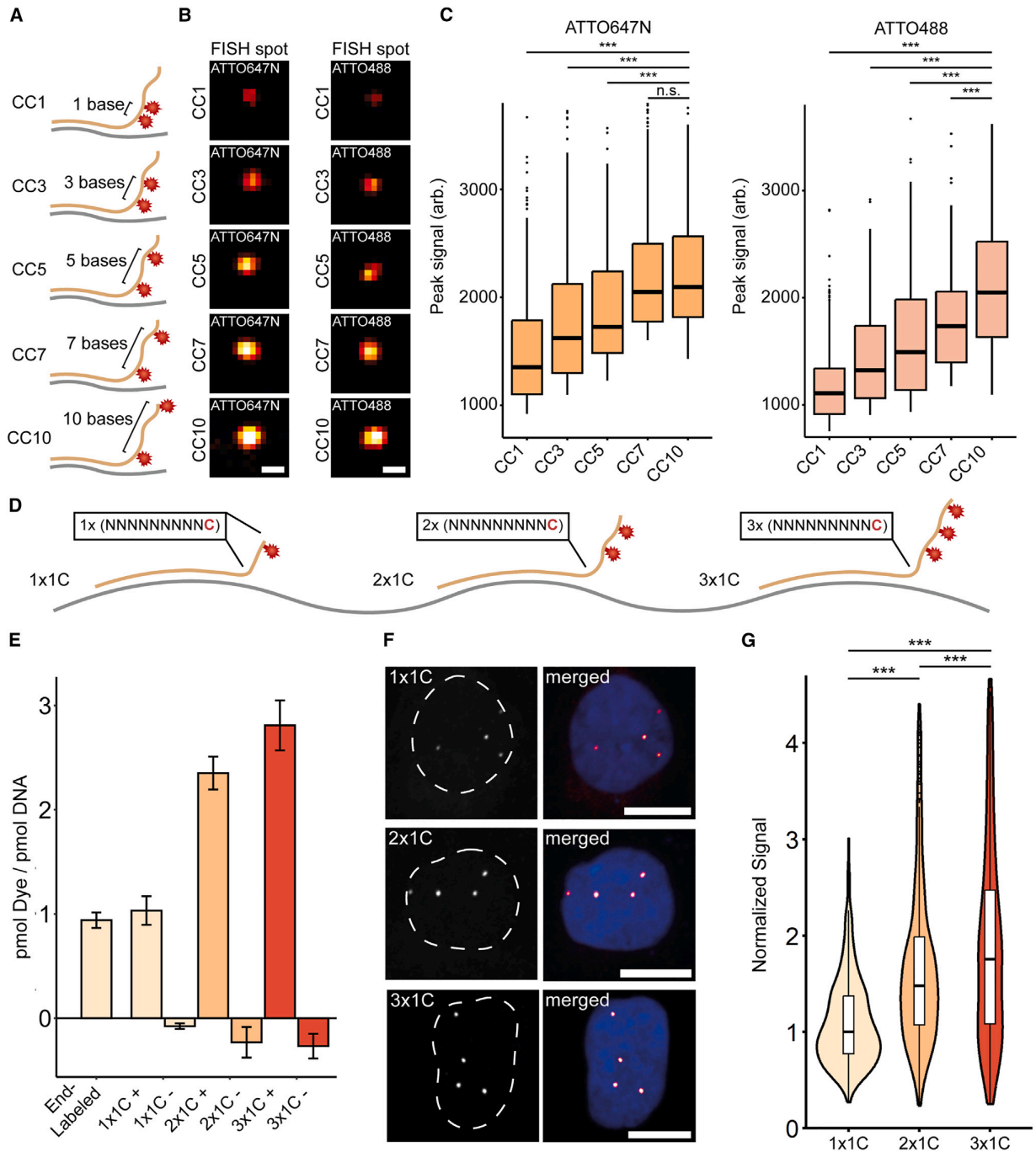
Figure 3. Designing xNOVA probes

(A) Design of probes to determine distance-dependent fluorescence quenching. NOVA probes are synthesized to carry two fluorophores with increasing distance in between (1, 3, 5, 7, or 10 bases).

(B) Representative images of chr13 (q34) targeted in IMR-90 cells. NOVA probes contain two ATTO488 or ATTO647N molecules. Scale bars, 500 nm.

(C) Dye-dye distances impact probe fluorescence. Datasets were tested for significance using the Wilcoxon rank-sum test with Bonferroni's correction for multiple testing (***$p < 0.001$).

(D) Design of extended NOVA-FISH (xNOVA) probes. xNOVA probes are extended by labeled 10-mers (NNNNNNNNNC) at their 3′ ends.

(legend continued on next page)

Cell Reports Methods
Article

the specific brightness. We synthesized probes that either carried one (1 × 1C), two (2 × 1C), or three (3 × 1C) fluorophores and measured their fluorescence signals at the locus of interest (Figures 3E, 3F, and S4A). The addition of longer sequences (2 × 1C, 3 × 1C) resulted in stronger signals (Figure 3G). With this approach, we observed a steady increase in signal strength at higher labeling densities, arguing against substantial distance-dependent quenching in 3 × 1C sequences (Figures S4B and S4C).

NOVA-FISH detects non-repetitive genomic loci with kilobase resolution

Finally, we tested the limits of NOVA-FISH by detecting small non-repetitive genomic loci with nanoscale precision using STED microscopy (Figure 4A). We designed probe sets to detect non-repetitive neighboring regions on chr11 termed "A" and "B" that have been established in past works.[24] Probe sets against "A" contained 60, 50, 40, 30, 20, or 10 individual oligonucleotides, while "B" was targeted with 60 probes. The probe sets span 6.1, 4.8, 3.7, 1.7, or 0.5 kb for "A" and 4.8 kb for "B" and yield two adjacent spots (Figure 4B). A characteristic of the NOVA technology is the complete flexibility in probe synthesis, as probes can be selectively amplified from a large pool by adding appropriate primer combinations (Figure 4C). This allows the cost-effective repeated use of one oligonucleotide pool to generate probes against different target regions. Then, we targeted "A" with decreasing numbers of individual probes, maintaining the same set of probes for "B" (Figure 4D). Despite observing a decline in detection frequency with the reduced number of probes detecting "A," we were still able to detect genomic loci as small as 0.5 kb. The ratio of co-localizing spots to total number of spots is in the range of 38%–63% for A and 29%–54% for B. Furthermore, we used STED microscopy to robustly measure distances in all "A" and "B" probe pairs (Figures 4E and 4F). Thus, NOVA-FISH is a reliable tool to detect non-repetitive regions below the kilobase level.

DISCUSSION

Over the past decade, it became clear that the 3D genome organization contributes to the establishment, maintenance, and change of gene activity.[68,69] Chromatin capture assays have identified genome-wide interactions of regulatory elements and have delineated topologically associating domains (TADs).[20,70] These findings have traditionally been complemented by FISH-based imaging methods detecting entire genomes and individual chromosomes down to single genomic loci.[28,47,71] However, the optical detection of small genetic elements and the resolution of their spatial relationships at the nanoscale level remains challenging. Here, we developed a simple, rapid, flexible, and cost-effective protocol for the generation of FISH probe sets that are suited for nanoscopic measurements with kilobase resolu-

tion. In a recent study, we applied this technique to probe enhancer hijacking events upon tumorigenic translocations.[72]

Small genetic elements are ideally detected with multiple synthetic oligonucleotides that may either be directly labeled or hybridized with secondary, labeled probes. Whereas end-labeled commercial probes are expensive if large and diverse probe pools are used, enzyme-based synthesis is cost effective and flexible but requires the subsequent removal of template strands. While previously, RNA templates were reverse transcribed and subsequently degraded by RNases, we simply removed 5′ phosphorylated DNA templates using lambda exonuclease.[73] This enzymatic synthesis, including two purification steps, takes under 4 h and yields sets with hundreds of probes for less than 10 €. A detailed cost estimate of oligoFISH, end-labeled, and NOVA probes can be found in Tables S2–S4.

For enzymatic incorporation of dye-labeled nucleotides, we tested commonly available DNA polymerases. We found that B-family DNA polymerases incorporate all used modified nucleotides more effectively than A-family DNA polymerases, such as the Klenow fragment or Taq DNA polymerase. This is consistent with previous structural data of B-family polymerases, attributing their ability to incorporate dye-labeled nucleotides to a larger channel volume, the presence of B-form DNA, and phosphate backbone-mediated protein-DNA interactions.[55,74–76] Among the tested B-family polymerases, Therminator DNA polymerase, having mutations in its exonuclease domain (D141A, E143A) and finger domain (A485L), was best suited for the incorporation of dye-labeled nucleotides.[57]

As even minor FISH projects involve dozens of probes with different dye labels, we used inexpensive, commercially synthesized template pools in combination with plates of bioinformatically optimized, target-specific primers. This approach allows the flexible generation of small to large probe sets coupled with variable dyes. We demonstrate that regions as small as 500 base pairs can be detected and genomic distances of a few kilobases can be measured.

We found that the brightness of probes can be easily adjusted with the ratio of labeled to unlabeled nucleotides in the synthesis reaction. However, the brightness did not linearly increase, due to distance-dependent effects at high labeling densities. To become independent of probe-specific sequences and ensure incorporation of the same numbers of fluorescent nucleotides, we generated extended probes with overhanging, identical sequences (xNOVA). We successfully incorporated fluorophores with a spacing of ten nucleotides but note that distances down to seven nucleotides might be permissible. Our systematic analysis of distance-dependent dye-dye quenching is consistent with a previous study that measured dye-dye interactions in DNA origami.[77]

While current FISH techniques can sequentially label multiple targets, the use of end-labeled probes for secondary hybridization steps reduces signal strength. To enhance signal strength,

(E) Synthesizing xNOVA probes with specific fluorophore numbers (1 × 1C, 2 × 1C, 3 × 1C). xNOVA probes were synthesized with a 0% (−ATTO488) or 100% (+ATTO488) ratio of labeled to unlabeled nucleotides. Data are represented as mean ± SD. See also Figure S4A.

(F) Representative images of xNOVA probes detecting chr13 (q34) in U2OS cells. Scale bars, 10 μm.

(G) Quantification of xNOVA probe signals. Related to (F). The plot depicts the two brightest signals for each cell. Number of foci analyzed: 1C (n = 513), 2 × 1C (n = 634), and 3 × 1C (n = 566). Datasets were tested for significance using the Wilcoxon rank-sum test with Bonferroni's correction for multiple testing (***p < 0.001).

(legend on next page)
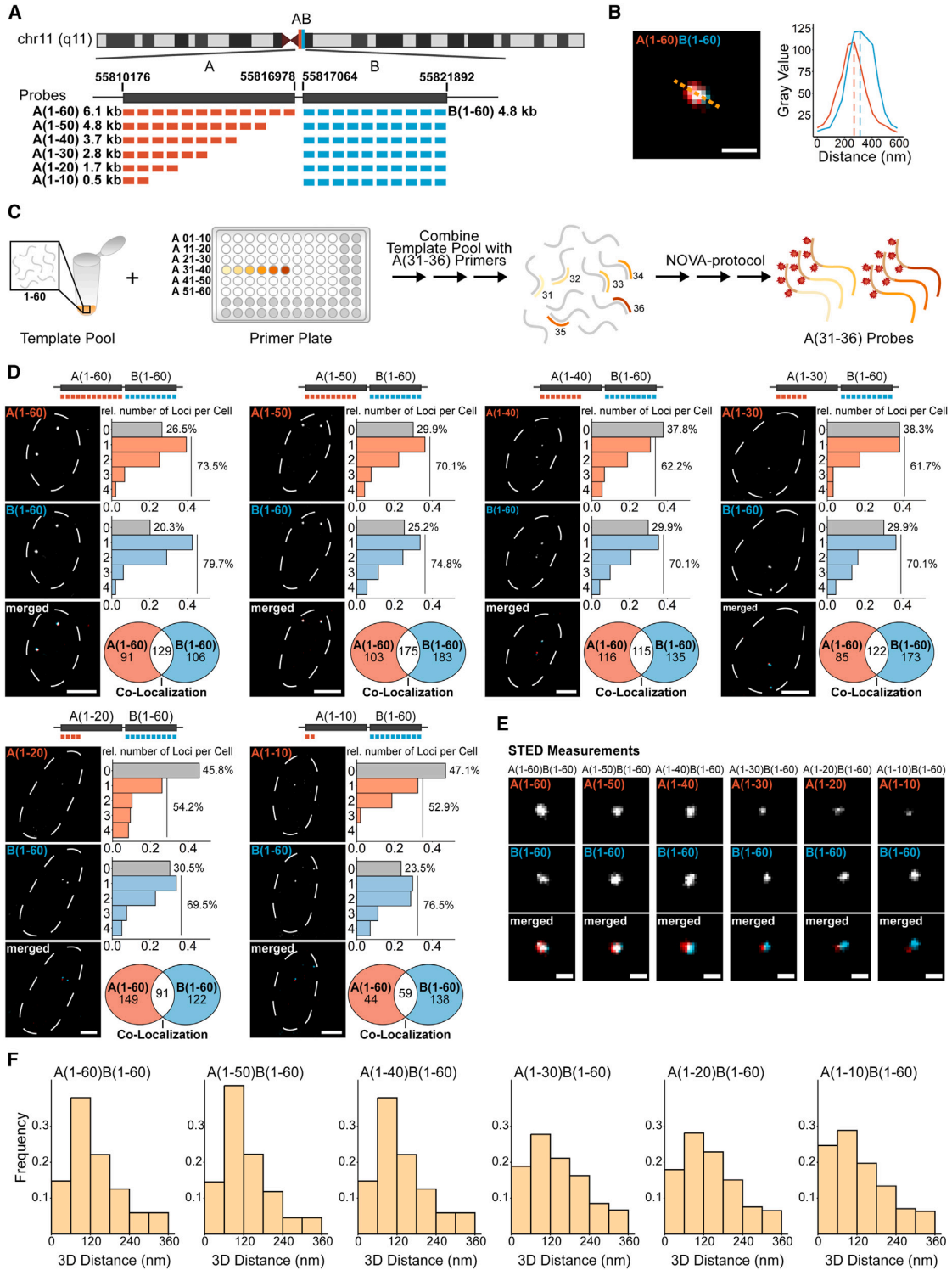
Cell Reports Methods
Article

NOVA probes carrying multiple fluorophores could be employed for secondary hybridization. Moreover, we hypothesize that our workflow is suitable for applications beyond the detection of small genomic loci. Given that oligonucleotides carrying any number of desired fluorophores can be generated, opportunities in the fields of DNA-PAINT, DNA origami, or immunostainings emerge.[78,79] In summary, we present a simple, quick, and inexpensive approach to explore the spatial relationships of genetic elements governing the activity of clusters of genes.

Limitations of study

While NOVA probes enable the detection of sub-kilobase genomic loci, the number of detectable targets is currently limited by the number of distinguishable colors in the microscopy setup. Barcoded probes circumvent this limitation by sequentially binding and releasing labeled readout probes, which, however, leads to a reduction in sensitivity. NOVA probes are not compatible with multiplexed imaging techniques, as they carry fluorophores in their primary sequence. Probing the spatial relationships of a larger number of regulatory elements requires barcoded probes, which could use NOVA probes for readout.

Furthermore, NOVA probes are used for FISH experiments and therefore subject to the same general limitations of hybridization-based methods.[36,80] In particular, the same basic trade-offs between the preservation of fine structural details and hybridization penetrance apply.

STAR★METHODS

Detailed methods are provided in the online version of this paper and include the following:

- KEY RESOURCES TABLE
- RESOURCE AVAILABILITY
  - Lead contact
  - Materials availability
  - Data and code availability
- METHOD DETAILS
  - Cell culture
  - Probe design
  - NOVA-FISH Probe synthesis
  - Quality control and purification
  - Polymerase Screens
  - HPLC
  - Sample preparation and fluorescence *in situ* hybridization
  - Image acquisition
  - 3D STED microscopy of telomers using adaptive illumination
  - Automated STED microscopy for two-color NOVA-FISH
  - Image analysis
- QUANTIFICATION AND STATISTICAL ANALYSIS

AUTHOR CONTRIBUTIONS

C.S., H.L., and H.H. conceptualized the study and wrote the manuscript. C.S. synthesized NOVA probes, conducted FISH experiments, acquired microscopy images, and prepared the figures. D.H. acquired 3D STED images of telomeres and automated STED acquisition. M.G.O., G.S., and D.H. analyzed the data. A.J.T. performed HPLC purifications. H.L. and H.H. supervised the study, and H.L., H.H., and T.C. secured funding. All authors reviewed the manuscript and agreed to the published version.

DECLARATION OF INTERESTS

The authors declare no competing interests.

REFERENCES

1. Cremer, T., and Cremer, M. (2010). Chromosome territories. Cold Spring Harb. Perspect. Biol. 2, a003889. https://doi.org/10.1101/cshperspect.a003889.

2. Rao, S.S.P., Huntley, M.H., Durand, N.C., Stamenova, E.K., Bochkov, I.D., Robinson, J.T., Sanborn, A.L., Machol, I., Omer, A.D., Lander, E.S., and Aiden, E.L. (2014). A 3D map of the human genome at kilobase resolution reveals principles of chromatin looping. Cell 159, 1665–1680. https://doi.org/10.1016/j.cell.2014.11.021.

3. Nora, E.P., Lajoie, B.R., Schulz, E.G., Giorgetti, L., Okamoto, I., Servant, N., Piolot, T., Van Berkum, N.L., Meisig, J., Sedat, J., et al. (2012). Spatial

Figure 4. Using xNOVA probes to detect non-repetitive loci at kilobase scale
(A) Depiction of the target regions. Two adjacent non-repetitive genomic regions on chr11 (hg19, chr11: 55,810,176–55,816,978, hg19, chr11: 55,817,064–55,821,892) were targeted with 60 xNOVA probes spanning 6.1 or 4.8 kb. In successive experiments, the number of xNOVA probes targeting A was gradually reduced from 60 to 10 probes. 60 xNOVA probes targeting B were used as a reference.
(B) Representative STED images of regions "A" and "B" in two colors. A(1–60) was tagged with ATTO594, and B(1–60) harbored ATTO647N. Scale bar, 500 nm.
(C) Schematic of selective xNOVA probe synthesis. Probe sets are selectively synthesized through the combination of region-specific primers with common template pools.
(D) Detecting kilobase genomic loci using confocal microscopy. 60 probes detecting B were paired with probe sets comprising 60 to 10 individual probes for A. Histograms depict the relative number of detected loci per cell. Venn diagrams depict the number of detected single and co-localizing signals. Scale bars, 5 μm. Number of cells analyzed: A(1–60)B(1–60): $n = 151$; A(1–50)B(1–60): $n = 153$; A(1–40)B(1–60): $n = 172$; A(1–30)B(1–60): $n = 168$; A(1–20)B(1–60): $n = 124$; A(1–10)B(1–60): $n = 101$.
(E) Representative z projections of A paired with B in K562 cells. Scale bars, 200 nm.
(F) 3D distance of A and B. Number of analyzed spot pairs: 1–60: $n = 550$; 1–50: $n = 388$; 1–40: $n = 317$; 1–30: $n = 329$; 1–20: $n = 445$; 1–10: $n = 226$.

partitioning of the regulatory landscape of the X-inactivation centre. Nature *485*, 381–385. https://doi.org/10.1038/nature11049.

4. Jeong, Y., El-Jaick, K., Roessler, E., Muenke, M., and Epstein, D.J. (2006). A functional screen for sonic hedgehog regulatory elements across a 1 Mb interval identifies long-range ventral forebrain enhancers. Development *133*, 761–772. https://doi.org/10.1242/dev.02239.

5. Pombo, A., and Dillon, N. (2015). Three-dimensional genome architecture: players and mechanisms. Nat. Rev. Mol. Cell Biol. *16*, 245–257. https://doi.org/10.1038/nrm3965.

6. Medrano-Fernandez, A., and Barco, A. (2016). Nuclear organization and 3D chromatin architecture in cognition and neuropsychiatric disorders. Mol. Brain *9*, 83. https://doi.org/10.1186/s13041-016-0263-x.

7. Lupiáñez, D.G., Kraft, K., Heinrich, V., Krawitz, P., Brancati, F., Klopocki, E., Horn, D., Kayserili, H., Opitz, J.M., Laxova, R., et al. (2015). Disruptions of topological chromatin domains cause pathogenic rewiring of gene-enhancer interactions. Cell *161*, 1012–1025. https://doi.org/10.1016/j.cell.2015.04.004.

8. Hnisz, D., Weintraub, A.S., Day, D.S., Valton, A.L., Bak, R.O., Li, C.H., Goldmann, J., Lajoie, B.R., Fan, Z.P., Sigova, A.A., et al. (2016). Activation of proto-oncogenes by disruption of chromosome neighborhoods. Science *351*, 1454–1458. https://doi.org/10.1126/science.aad9024.

9. Schuijers, J., Manteiga, J.C., Weintraub, A.S., Day, D.S., Zamudio, A.V., Hnisz, D., Lee, T.I., and Young, R.A. (2018). Transcriptional Dysregulation of MYC Reveals Common Enhancer-Docking Mechanism. Cell Rep. *23*, 349–360. https://doi.org/10.1016/j.celrep.2018.03.056.

10. Dixon, J.R., Jung, I., Selvaraj, S., Shen, Y., Antosiewicz-Bourget, J.E., Lee, A.Y., Ye, Z., Kim, A., Rajagopal, N., Xie, W., et al. (2015). Chromatin architecture reorganization during stem cell differentiation. Nature *518*, 331–336. https://doi.org/10.1038/nature14222.

11. Mateo, L.J., Murphy, S.E., Hafner, A., Cinquini, I.S., Walker, C.A., and Boettiger, A.N. (2019). Visualizing DNA folding and RNA in embryos at single-cell resolution. Nature *568*, 49–54. https://doi.org/10.1038/s41586-019-1035-4.

12. Gizzi, A.M.C., Cattoni, D.I., Fiche, J.-B., Espinola, S.M., Gurgo, J., Messina, O., Houbron, C., Ogiyama, Y., Papadopoulos, G.L., and Cavalli, G. (2019). Microscopy-based chromosome conformation capture enables simultaneous visualization of genome organization and transcription in intact organisms. Mol. Cell *74*, 212–222. https://doi.org/10.1016/j.molcel.2019.01.011.

13. Simonis, M., Klous, P., Splinter, E., Moshkin, Y., Willemsen, R., de Wit, E., van Steensel, B., and de Laat, W. (2006). Nuclear organization of active and inactive chromatin domains uncovered by chromosome conformation capture-on-chip (4C). Nat. Genet. *38*, 1348–1354. https://doi.org/10.1038/ng1896.

14. Dekker, J., Rippe, K., Dekker, M., and Kleckner, N. (2002). Capturing chromosome conformation. Science *295*, 1306–1311. https://doi.org/10.1126/science.1067799.

15. Lieberman-Aiden, E., van Berkum, N.L., Williams, L., Imakaev, M., Ragoczy, T., Telling, A., Amit, I., Lajoie, B.R., Sabo, P.J., Dorschner, M.O., et al. (2009). Comprehensive mapping of long-range interactions reveals folding principles of the human genome. Science *326*, 289–293. https://doi.org/10.1126/science.1181369.

16. Krietenstein, N., Abraham, S., Venev, S.V., Abdennur, N., Gibcus, J., Hsieh, T.H.S., Parsi, K.M., Yang, L., Maehr, R., Mirny, L.A., et al. (2020). Ultrastructural Details of Mammalian Chromosome Architecture. Mol. Cell *78*, 554–565.e7. https://doi.org/10.1016/j.molcel.2020.03.003.

17. Dixon, J.R., Selvaraj, S., Yue, F., Kim, A., Li, Y., Shen, Y., Hu, M., Liu, J.S., and Ren, B. (2012). Topological domains in mammalian genomes identified by analysis of chromatin interactions. Nature *485*, 376–380. https://doi.org/10.1038/nature11082.

18. Jerkovic, I., and Cavalli, G. (2021). Understanding 3D genome organization by multidisciplinary methods. Nat. Rev. Mol. Cell Biol. *22*, 511–528. https://doi.org/10.1038/s41580-021-00362-w.

19. Goel, V.Y., and Hansen, A.S. (2021). The macro and micro of chromosome conformation capture. Wiley Interdiscip. Rev. Dev. Biol. *10*, e395. https://doi.org/10.1002/wdev.395.

20. McCord, R.P., Kaplan, N., and Giorgetti, L. (2020). Chromosome Conformation Capture and Beyond: Toward an Integrative View of Chromosome Structure and Function. Mol. Cell *77*, 688–708. https://doi.org/10.1016/j.molcel.2019.12.021.

21. Nagano, T., Lubling, Y., Stevens, T.J., Schoenfelder, S., Yaffe, E., Dean, W., Laue, E.D., Tanay, A., and Fraser, P. (2013). Single-cell Hi-C reveals cell-to-cell variability in chromosome structure. Nature *502*, 59–64. https://doi.org/10.1038/nature12593.

22. Flyamer, I.M., Gassler, J., Imakaev, M., Brandão, H.B., Ulianov, S.V., Abdennur, N., Razin, S.V., Mirny, L.A., and Tachibana-Konwalski, K. (2017). Single-nucleus Hi-C reveals unique chromatin reorganization at oocyte-to-zygote transition. Nature *544*, 110–114. https://doi.org/10.1038/nature21711.

23. Stevens, T.J., Lando, D., Basu, S., Atkinson, L.P., Cao, Y., Lee, S.F., Leeb, M., Wohlfahrt, K.J., Boucher, W., O'Shaughnessy-Kirwan, A., et al. (2017). 3D structures of individual mammalian genomes studied by single-cell Hi-C. Nature *544*, 59–64. https://doi.org/10.1038/nature21429.

24. Brandstetter, K., Zülske, T., Ragoczy, T., Hörl, D., Guirao-Ortiz, M., Steinek, C., Barnes, T., Stumberger, G., Schwach, J., Haugen, E., et al. (2022). Differences in nanoscale organization of regulatory active and inactive human chromatin. Biophys. J. *121*, 977–990. https://doi.org/10.1016/j.bpj.2022.02.009.

25. Levi, V., Ruan, Q., Plutz, M., Belmont, A.S., and Gratton, E. (2005). Chromatin dynamics in interphase cells revealed by tracking in a two-photon excitation microscope. Biophys. J. *89*, 4275–4285. https://doi.org/10.1529/biophysj.105.066670.

26. Gabriele, M., Brandão, H.B., Grosse-Holz, S., Jha, A., Dailey, G.M., Cattoglio, C., Hsieh, T.-H.S., Mirny, L., Zechner, C., and Hansen, A.S. (2022). Dynamics of CTCF-and cohesin-mediated chromatin looping revealed by live-cell imaging. Science *376*, 496–501. https://doi.org/10.1126/science.abn6583.

27. Giorgetti, L., Galupa, R., Nora, E.P., Piolot, T., Lam, F., Dekker, J., Tiana, G., and Heard, E. (2014). Predictive polymer modeling reveals coupled fluctuations in chromosome conformation and transcription. Cell *157*, 950–963. https://doi.org/10.1016/j.cell.2014.03.025.

28. Bintu, B., Mateo, L.J., Su, J.H., Sinnott-Armstrong, N.A., Parker, M., Kinrot, S., Yamaya, K., Boettiger, A.N., and Zhuang, X. (2018). Super-resolution chromatin tracing reveals domains and cooperative interactions in single cells. Science *362*, eaau1783. https://doi.org/10.1126/science.aau1783.

29. Finn, E.H., Pegoraro, G., Brandao, H.B., Valton, A.L., Oomen, M.E., Dekker, J., Mirny, L., and Misteli, T. (2019). Extensive Heterogeneity and Intrinsic Variation in Spatial Genome Organization. Cell *176*, 1502–1515. https://doi.org/10.1016/j.cell.2019.01.020.

30. Cattoni, D.I., Cardozo Gizzi, A.M., Georgieva, M., Di Stefano, M., Valeri, A., Chamousset, D., Houbron, C., Déjardin, S., Fiche, J.B., González, I., et al. (2017). Single-cell absolute contact probability detection reveals chromosomes are organized by multiple low-frequency yet specific interactions. Nat. Commun. *8*, 1753. https://doi.org/10.1038/s41467-017-01962-x.

31. Bolzer, A., Kreth, G., Solovei, I., Koehler, D., Saracoglu, K., Fauth, C., Müller, S., Eils, R., Cremer, C., Speicher, M.R., and Cremer, T. (2005). Three-dimensional maps of all chromosomes in human male fibroblast nuclei and prometaphase rosettes. PLoS Biol. *3*, e157. https://doi.org/10.1371/journal.pbio.0030157.

32. Kallioniemi, O.P., Kallioniemi, A., Kurisu, W., Thor, A., Chen, L.C., Smith, H.S., Waldman, F.M., Pinkel, D., and Gray, J.W. (1992). ERBB2 amplification in breast cancer analyzed by fluorescence in situ hybridization. Proc. Natl. Acad. Sci. USA *89*, 5321–5325. https://doi.org/10.1073/pnas.89.12.5321.

Cell Reports Methods
Article

CellPress
OPEN ACCESS

33. Cui, C., Shu, W., and Li, P. (2016). Fluorescence In situ Hybridization: Cell-Based Genetic Diagnostic and Research Applications. Front. Cell Dev. Biol. *4*, 89. https://doi.org/10.3389/fcell.2016.00089.

34. Chrzanowska, N.M., Kowalewski, J., and Lewandowska, M.A. (2020). Use of Fluorescence In Situ Hybridization (FISH) in Diagnosis and Tailored Therapies in Solid Tumors. Molecules *25*, 1864. https://doi.org/10.3390/molecules25081864.

35. Pardue, M.L., and Gall, J.G. (1969). Molecular hybridization of radioactive DNA to the DNA of cytological preparations. Proc. Natl. Acad. Sci. USA *64*, 600–604. https://doi.org/10.1073/pnas.64.2.600.

36. Markaki, Y., Smeets, D., Fiedler, S., Schmid, V.J., Schermelleh, L., Cremer, T., and Cremer, M. (2012). The potential of 3D-FISH and super-resolution structured illumination microscopy for studies of 3D nuclear architecture: 3D structured illumination microscopy of defined chromosomal structures visualized by 3D (immuno)-FISH opens new perspectives for studies of nuclear architecture. Bioessays *34*, 412–426. https://doi.org/10.1002/bies.201100176.

37. Wiegant, J., Ried, T., Nederlof, P.M., van der Ploeg, M., Tanke, H.J., and Raap, A.K. (1991). In situ hybridization with fluoresceinated DNA. Nucleic Acids Res. *19*, 3237–3241. https://doi.org/10.1093/nar/19.12.3237.

38. Itzkovitz, S., and van Oudenaarden, A. (2011). Validating transcripts with probes and imaging technology. Nat. Methods *8*, S12–S19. https://doi.org/10.1038/nmeth.1573.

39. Shizuya, H., Birren, B., Kim, U.J., Mancino, V., Slepak, T., Tachiiri, Y., and Simon, M. (1992). Cloning and stable maintenance of 300-kilobase-pair fragments of human DNA in Escherichia coli using an F-factor-based vector. Proc. Natl. Acad. Sci. USA *89*, 8794–8797. https://doi.org/10.1073/pnas.89.18.8794.

40. Burke, D.T., Carle, G.F., and Olson, M.V. (1987). Cloning of large segments of exogenous DNA into yeast by means of artificial chromosome vectors. Science *236*, 806–812. https://doi.org/10.1126/science.3033825.

41. Boettiger, A., and Murphy, S. (2020). Advances in chromatin imaging at kilobase-scale resolution. TiG *36*, 273–287. https://doi.org/10.1016/j.tig.2019.12.010.

42. Huber, D., Voith von Voithenberg, L., and Kaigala, G. (2018). Fluorescence in situ hybridization (FISH): history, limitations and what to expect from micro-scale FISH? Micro Nano Eng. *1*, 15–24. https://doi.org/10.1016/j.mne.2018.10.006.

43. Raj, A., van den Bogaard, P., Rifkin, S.A., van Oudenaarden, A., and Tyagi, S. (2008). Imaging individual mRNA molecules using multiple singly labeled probes. Nat. Methods *5*, 877–879. https://doi.org/10.1038/nmeth.1253.

44. Beliveau, B.J., Joyce, E.F., Apostolopoulos, N., Yilmaz, F., Fonseka, C.Y., McCole, R.B., Chang, Y., Li, J.B., Senaratne, T.N., Williams, B.R., et al. (2012). Versatile design and synthesis platform for visualizing genomes with Oligopaint FISH probes. Proc. Natl. Acad. Sci. USA *109*, 21301–21306. https://doi.org/10.1073/pnas.1213818110.

45. Su, J.H., Zheng, P., Kinrot, S.S., Bintu, B., and Zhuang, X. (2020). Genome-Scale Imaging of the 3D Organization and Transcriptional Activity of Chromatin. Cell *182*, 1641–1659.e26. https://doi.org/10.1016/j.cell.2020.07.032.

46. Takei, Y., Zheng, S., Yun, J., Shah, S., Pierson, N., White, J., Schindler, S., Tischbirek, C.H., Yuan, G.C., and Cai, L. (2021). Single-cell nuclear architecture across cell types in the mouse brain. Science *374*, 586–594. https://doi.org/10.1126/science.abj1966.

47. Szabo, Q., Donjon, A., Jerković, I., Papadopoulos, G.L., Cheutin, T., Bonev, B., Nora, E.P., Bruneau, B.G., Bantignies, F., and Cavalli, G. (2020). Regulation of single-cell genome organization into TADs and chromatin nanodomains. Nat. Genet. *52*, 1151–1157. https://doi.org/10.1038/s41588-020-00716-8.

48. Lizardi, P.M., Huang, X., Zhu, Z., Bray-Ward, P., Thomas, D.C., and Ward, D.C. (1998). Mutation detection and single-molecule counting using isothermal rolling-circle amplification. Nat. Genet. *19*, 225–232. https://doi.org/10.1038/898.

49. Dirks, R.M., and Pierce, N.A. (2004). Triggered amplification by hybridization chain reaction. Proc. Natl. Acad. Sci. USA *101*, 15275–15278. https://doi.org/10.1073/pnas.0407024101.

50. Choi, H.M.T., Beck, V.A., and Pierce, N.A. (2014). Next-generation in situ hybridization chain reaction: higher gain, lower cost, greater durability. ACS Nano *8*, 4284–4294. https://doi.org/10.1021/nn405717p.

51. Rouhanifard, S.H., Mellis, I.A., Dunagin, M., Bayatpour, S., Jiang, C.L., Dardani, I., Symmons, O., Emert, B., Torre, E., Cote, A., et al. (2019). Amendments: Author Correction: ClampFISH detects individual nucleic acid molecules using click chemistry-based amplification. Nat. Biotechnol. *37*, 102. https://doi.org/10.1038/nbt0119-102b.

52. Dardani, I., Emert, B.L., Goyal, Y., Jiang, C.L., Kaur, A., Lee, J., Rouhanifard, S.H., Alicea, G.M., Fane, M.E., Xiao, M., et al. (2022). ClampFISH 2.0 enables rapid, scalable amplified RNA detection in situ. Nat. Methods *19*, 1403–1410. https://doi.org/10.1038/s41592-022-01653-6.

53. Xie, F., Timme, K.A., and Wood, J.R. (2018). Using Single Molecule mRNA Fluorescent in Situ Hybridization (RNA-FISH) to Quantify mRNAs in Individual Murine Oocytes and Embryos. Sci. Rep. *8*, 7930. https://doi.org/10.1038/s41598-018-26345-0.

54. Kishi, J.Y., Lapan, S.W., Beliveau, B.J., West, E.R., Zhu, A., Sasaki, H.M., Saka, S.K., Wang, Y., Cepko, C.L., and Yin, P. (2019). SABER amplifies FISH: enhanced multiplexed imaging of RNA and DNA in cells and tissues. Nat. Methods *16*, 533–544. https://doi.org/10.1038/s41592-019-0404-0.

55. Kropp, H.M., Betz, K., Wirth, J., Diederichs, K., and Marx, A. (2017). Crystal structures of ternary complexes of archaeal B-family DNA polymerases. PLoS One *12*, e0188005. https://doi.org/10.1371/journal.pone.0188005.

56. Pettersen, E.F., Goddard, T.D., Huang, C.C., Couch, G.S., Greenblatt, D.M., Meng, E.C., and Ferrin, T.E. (2004). UCSF Chimera–a visualization system for exploratory research and analysis. J. Comput. Chem. *25*, 1605–1612. https://doi.org/10.1002/jcc.20084.

57. Gardner, A.F., Jackson, K.M., Boyle, M.M., Buss, J.A., Potapov, V., Gehring, A.M., Zatopek, K.M., Corrêa, I.R., Jr., Ong, J.L., and Jack, W.E. (2019). Therminator DNA Polymerase: Modified Nucleotides and Unnatural Substrates. Front. Mol. Biosci. *6*, 28. https://doi.org/10.3389/fmolb.2019.00028.

58. Ichida, J.K., Horhota, A., Zou, K., McLaughlin, L.W., and Szostak, J.W. (2005). High fidelity TNA synthesis by Therminator polymerase. Nucleic Acids Res. *33*, 5219–5225. https://doi.org/10.1093/nar/gki840.

59. Renders, M., Emmerechts, G., Rozenski, J., Krecmerová, M., Holý, A., and Herdewijn, P. (2007). Enzymatic synthesis of phosphonomethyl oligonucleotides by therminator polymerase. Angew. Chem., Int. Ed. Engl. *46*, 2501–2504. https://doi.org/10.1002/anie.200603435.

60. Mohsen, M.G., Ji, D., and Kool, E.T. (2019). Polymerase synthesis of four-base DNA from two stable dimeric nucleotides. Nucleic Acids Res. *47*, 9495–9501. https://doi.org/10.1093/nar/gkz741.

61. Gardner, A.F., and Jack, W.E. (2002). Acyclic and dideoxy terminator preferences denote divergent sugar recognition by archaeon and Taq DNA polymerases. Nucleic Acids Res. *30*, 605–613. https://doi.org/10.1093/nar/30.2.605.

62. Jegou, T., Chung, I., Heuvelman, G., Wachsmuth, M., Görisch, S.M., Greulich-Bode, K.M., Boukamp, P., Lichter, P., and Rippe, K. (2009). Dynamics of telomeres and promyelocytic leukemia nuclear bodies in a telomerase-negative human cell line. Mol. Biol. Cell *20*, 2070–2082. https://doi.org/10.1091/mbc.e08-02-0108.

63. Crabbe, L., Cesare, A.J., Kasuboski, J.M., Fitzpatrick, J.A.J., and Karlseder, J. (2012). Human telomeres are tethered to the nuclear envelope during postmitotic nuclear assembly. Cell Rep. *2*, 1521–1529. https://doi.org/10.1016/j.celrep.2012.11.019.

64. Chuang, T.C.Y., Moshir, S., Garini, Y., Chuang, A.Y.C., Young, I.T., Vermolen, B., van den Doel, R., Mougey, V., Perrin, M., Braun, M., et al.

Cell Reports Methods
Article

(2004). The three-dimensional organization of telomeres in the nucleus of mammalian cells. BMC Biol. *2*, 12. https://doi.org/10.1186/1741-7007-2-12.

65. Adam, N., Degelman, E., Briggs, S., Wazen, R.M., Colarusso, P., Riabowol, K., and Beattie, T. (2019). Telomere analysis using 3D fluorescence microscopy suggests mammalian telomere clustering in hTERT-immortalized Hs68 fibroblasts. Commun. Biol. *2*, 451. https://doi.org/10.1038/s42003-019-0692-z.

66. DeLano, W.L. (2002). Pymol: an open-source molecular graphics tool. CCP4 Newsletter Pro. Crystallogr. *40*, 82–92.

67. Beliveau, B.J., Boettiger, A.N., Avendaño, M.S., Jungmann, R., McCole, R.B., Joyce, E.F., Kim-Kiselak, C., Bantignies, F., Fonseka, C.Y., Erceg, J., et al. (2015). Single-molecule super-resolution imaging of chromosomes and in situ haplotype visualization using Oligopaint FISH probes. Nat. Commun. *6*, 7147. https://doi.org/10.1038/ncomms8147.

68. Willemin, A., Szabó, D., and Pombo, A. (2024). Epigenetic regulatory layers in the 3D nucleus. Mol. Cell *84*, 415–428. https://doi.org/10.1016/j.molcel.2023.12.032.

69. Zheng, H., and Xie, W. (2019). The role of 3D genome organization in development and cell differentiation. Nat. Rev. Mol. Cell Biol. *20*, 535–550. https://doi.org/10.1038/s41580-019-0132-4.

70. Sati, S., and Cavalli, G. (2017). Chromosome conformation capture technologies and their impact in understanding genome function. Chromosoma *126*, 33–44. https://doi.org/10.1007/s00412-016-0593-6.

71. Peng, T., Hou, Y., Meng, H., Cao, Y., Wang, X., Jia, L., Chen, Q., Zheng, Y., Sun, Y., Chen, H., et al. (2023). Mapping nucleolus-associated chromatin interactions using nucleolus Hi-C reveals pattern of heterochromatin interactions. Nat. Commun. *14*, 350. https://doi.org/10.1038/s41467-023-36021-1.

72. Weichenhan, D., Riedel, A., Sollier, E., Toprak, U.H., Hey, J., Breuer, K., Wierzbinska, J.A., Touzart, A., Lutsik, P., Bähr, M., et al. (2023). Altered enhancer-promoter interaction leads to MNX1 expression in pediatric acute myeloid leukemia with t (7; 12)(q36; p13). Preprint at bioRxiv. https://doi.org/10.1101/2023.09.13.557546.

73. Beliveau, B.J., Boettiger, A.N., Nir, G., Bintu, B., Yin, P., Zhuang, X., and Wu, C.T. (2017). In Situ Super-Resolution Imaging of Genomic DNA with OligoSTORM and OligoDNA-PAINT. Methods Mol. Biol. *1663*, 231–252. https://doi.org/10.1007/978-1-4939-7265-4_19.

74. Hottin, A., and Marx, A. (2016). Structural insights into the processing of nucleobase-modified nucleotides by DNA polymerases. Acc. Chem. Res. *49*, 418–427. https://doi.org/10.1021/acs.accounts.5b00544.

75. Tasara, T., Angerer, B., Damond, M., Winter, H., Dörhöfer, S., Hübscher, U., and Amacker, M. (2003). Incorporation of reporter molecule-labeled nucleotides by DNA polymerases. II. High-density labeling of natural DNA. Nucleic Acids Res. *31*, 2636–2646. https://doi.org/10.1093/nar/gkg371.

76. Kropp, H.M., Diederichs, K., and Marx, A. (2019). The Structure of an archaeal B-family DNA polymerase in complex with a chemically modified nucleotide. Angew. Chem., Int. Ed. Engl. *58*, 5457–5461. https://doi.org/10.1002/anie.201900315.

77. Schröder, T., Scheible, M.B., Steiner, F., Vogelsang, J., and Tinnefeld, P. (2019). Interchromophoric Interactions Determine the Maximum Brightness Density in DNA Origami Structures. Nano Lett. *19*, 1275–1281. https://doi.org/10.1021/acs.nanolett.8b04845.

78. Jungmann, R., Avendaño, M.S., Woehrstein, J.B., Dai, M., Shih, W.M., and Yin, P. (2014). Multiplexed 3D cellular super-resolution imaging with DNA-PAINT and Exchange-PAINT. Nat. Methods *11*, 313–318. https://doi.org/10.1038/nmeth.2835.

79. Schnitzbauer, J., Strauss, M.T., Schlichthaerle, T., Schueder, F., and Jungmann, R. (2017). Super-resolution microscopy with DNA-PAINT. Nat. Protoc. *12*, 1198–1228. https://doi.org/10.1038/nprot.2017.024.

80. Solovei, I., Cavallo, A., Schermelleh, L., Jaunin, F., Scasselati, C., Cmarko, D., Cremer, C., Fakan, S., and Cremer, T. (2002). Spatial preservation of nuclear chromatin architecture during three-dimensional fluorescence in situ hybridization (3D-FISH). Exp. Cell Res. *276*, 10–23. https://doi.org/10.1006/excr.2002.5513.

81. Anton, T., Bultmann, S., Leonhardt, H., and Markaki, Y. (2014). Visualization of specific DNA sequences in living mouse embryonic stem cells with a programmable fluorescent CRISPR/Cas system. Nucleus *5*, 163–172. https://doi.org/10.4161/nucl.28488.

82. Ma, H., Naseri, A., Reyes-Gutierrez, P., Wolfe, S.A., Zhang, S., and Pederson, T. (2015). Multicolor CRISPR labeling of chromosomal loci in human cells. Proc. Natl. Acad. Sci. USA *112*, 3002–3007. https://doi.org/10.1073/pnas.1420024112.

83. Xu, Q., Schlabach, M.R., Hannon, G.J., and Elledge, S.J. (2009). Design of 240,000 orthogonal 25mer DNA barcode probes. Proc. Natl. Acad. Sci. USA *106*, 2289–2294. https://doi.org/10.1073/pnas.0812506106.

84. Green, M.R., and Sambrook, J. (2019). Isolation of DNA Fragments from Polyacrylamide Gels by the Crush and Soak Method. Cold Spring Harb. Protoc. *2019*, prot100479. https://doi.org/10.1101/pdb.prot100479.

85. Heine, J., Reuss, M., Harke, B., D'Este, E., Sahl, S.J., and Hell, S.W. (2017). Adaptive-illumination STED nanoscopy. Proc. Natl. Acad. Sci. USA *114*, 9797–9802. https://doi.org/10.1073/pnas.1708304114.

86. Schindelin, J., Arganda-Carreras, I., Frise, E., Kaynig, V., Longair, M., Pietzsch, T., Preibisch, S., Rueden, C., Saalfeld, S., Schmid, B., et al. (2012). Fiji: an open-source platform for biological-image analysis. Nat. Methods *9*, 676–682. https://doi.org/10.1038/nmeth.2019.

87. Bahry, E., Breimann, L., Zouinkhi, M., Epstein, L., Kolyvanov, K., Mamrak, N., King, B., Long, X., Harrington, K.I.S., Lionnet, T., and Preibisch, S. (2022). RS-FISH: precise, interactive, fast, and scalable FISH spot detection. Nat. Methods *19*, 1563–1567. https://doi.org/10.1038/s41592-022-01669-y.

Cell Reports Methods
Article

STAR★METHODS

KEY RESOURCES TABLE

REAGENT or RESOURCE	SOURCE	IDENTIFIER
Chemicals, peptides, and recombinant proteins		
5-Propargylamino-dCTP-ATTO-488 (1 mM)	Jena Bioscience	Cat# NU-809-488
5-Propargylamino-dCTP-ATTO-594 (1 mM)	Jena Bioscience	Cat# NU-809-594
5-Propargylamino-dCTP-ATTO-647N (1 mM)	Jena Bioscience	Cat# NU-809-647N-S/L
5-Propargylamino-dCTP-Cy3	Jena Bioscience	Cat# NU-809-CY3-S/L
Diamond™ Nucleic Acid Dye	Promega	Cat# H1181
DiYO-1	AAT Bioquest	Cat# 17580
dNTP Set (100 mM)	Thermo Fisher Scientific	Cat# R0181
Formaldehyde (16%)	Polysciences	Cat# 18814-10
Formamide ≥99.5%	Sigma Aldrich	Cat# F9037
Klenow Fragment (exo-)	Thermo Fisher Scientific	Cat# EP0421
Lambda exonuclease	Thermo Fisher Scientific	Cat# EN0561
Phusion® High-Fidelity DNA Polymerase (Phusion)	New England BioLabs	Cat# M0530 S/L
Q5® High-Fidelity DNA Polymerase (Q5)	New England BioLabs	Cat# M0491 S/L
RNase A	Thermo Fisher Scientific	Cat# EN0531
Taq DNA Polymerase (Taq)	Thermo Fisher Scientific	Cat# EP0401
Therminator™ DNA Polymeras	New England BioLabs	Cat# M0261 S/L
Critical commercial assays		
Monarch® PCR & DNA Cleanup Kit	New England BioLabs	Cat# T1030 S/L
NucleoSpin Gel and PCR Clean-up Kit	Macherey-Nagel	Cat# 740609
Deposited data		
Uncropped polyacrylamide gels	This paper	https://doi.org/10.17632/nskmtr4h9y.1
Experimental models: Cell lines		
IMR-90	Coriell Biorepository	I90-79
J1	ATCC	SCRC-1010
K562	ATCC	CCL-243
U2OS	ATCC	HTB-96
Oligonucleotides		
See Table S1		
Software and algorithms		
Fiji RRID:SCR_002285	Open Source	https://fiji.sc/
Illustrator CC 2023 RRID:SCR_010279	Adobe	www.adobe.com
ImageJ2 (v.1.54h) RRID:SCR_003070	NIH	www.ImageJ.net/
Microsoft Excel	Microsoft	N/A
Pymol (v.2.5.5) RRID:SCR_000305	Schrödinger	https://pymol.org/2/
UCSF ChimeraX (v.1.17.3) RRID:SCR_015872	UCSF	www.rbvi.ucsf.edu/chimera/

RESOURCE AVAILABILITY

Lead contact

Further information and resource requests can be directed to and will be fulfilled by the lead contact Heinrich Leonhardt (h.leonhardt@lmu.de).

Materials availability

NOVA probes were generated using commercially available reagents and services. Sequences and detailed synthesis instructions for generating the probes reported in this study are listed in Table S1 and the Method Details.

CellPress
OPEN ACCESS

Cell Reports Methods
Article

Data and code availability

- The uncropped polyacrylamide gels have been deposited at Mendeley Data and are publicly available as of the date of publication. An accession number is listed in the Key Resources Table.
- This paper does not report original code.
- Any additional information required to reanalyze the data reported in this paper is available from the lead contact upon request.

METHOD DETAILS

Cell culture

K562 cells were cultivated in Dulbecco's modified Eagle's medium (DMEM), 10% fetal bovine serum (FBS), 100 U/mL penicillin and 100 μg/mL streptomycin. U2OS cells were maintained in McCoy's 5A medium supplemented with 10% FBS, 100 U/ml penicillin, and 100 μg/mL streptomycin at 37 °C in 5% CO$_2$. IMR-90 cells were cultured in DMEM, 20% FBS, 1× MEM Non-essential amino acids, and 100 U/mL penicillin, 100 μg/mL streptomycin.

Mouse embryonic stem cells (ESCs) were maintained on culture dishes treated with 0.2% gelatin in DMEM containing 16% FBS, 0.1 mM β-mercaptoethanol, 2 mM L-glutamine, 1× MEM Non-essential amino acids, 100 U/mL penicillin, 100 μg/mL streptomycin, homemade recombinant LIF, and 2i (1 μM PD032591 and 3 μM CHIR99021). For imaging, ESCs were seeded on plates that have been pre-treated with Geltrex diluted 1:100 in DMEM/F12 overnight at 37 °C in 5% CO$_2$. Cells were passaged every 2–4 days. All cell lines were regularly tested for Mycoplasma contamination by PCR.

Probe design

All generated probe sets are listed in Table S1. NOVA-probes labeling murine major satellites and human repetitive regions (chrX (p11.1) or chr13 (q34), telomeres) were adapted from previously published sequences.[81,82] Target regions ("A": chr11:55810891-55816978 "B": chr11:55817064-55821430) were chosen in hg38 and 60 unique oligonucleotides were selected and filtered, respectively.[24] Barcodes of xNOVA-probes containing repetitive sequences (10-mers) were obtained from previous published data.[28] To generate non-repetitive barcodes, pairs of orthogonal sequences from[83] were merged. Then, the barcodes were filtered for those containing cytosines every 10 bases and trimmed to the required length.

NOVA-FISH Probe synthesis

5′-phosphorylated templates and unlabeled primers were ordered from IDT or Eurofins. Equimolar amounts of 5′-phosphorylated templates and primers (0.10–0.17 nmol each) were combined to a final concentration of 1 μg DNA/μL in 1x ThermoPol Reaction Buffer.

The annealing temperatures were adjusted to the length of the primers. For NOVA-probes (40 nt long templates, 20 nt long primers), the sample was heated up to 95°C for 5 min followed by a stepwise cool-down (1°C/minute) to room temperature. For xNOVA-probes or xNOVA-pools (50–70 nt long templates, 40 nt long primers) the sample was heated up to 95°C for 5 min followed by a stepwise cool-down (1°C/2 min) to 60°C. Complex xNOVA-probe sets were synthesized by adding 2-fold excess of primer sets (e.g., primer 31–40 against "A") to the template pool.

NOVA- and xNOVA-probes were synthesized by adding 2–4 μg annealed DNA (2–4 μL of the solution) to a reaction mixture containing 0.25 mM dATP/dGTP/dTTP each, 0–0.25 mM dCTP, 0–0.25 mM dye-labeled dCTP and 3 U Therminator DNA polymerase in 1x ThermoPol Reaction Buffer (10 μL total volume). The ratios of dye-labeled dCTP to unlabeled dCTP varied depending on the desired labeling density. The reaction was carried out for 60 min at 72°C.

To remove single-stranded DNA, NucleoSpin Gel and PCR Clean-up Kit (Macherey-Nagel) was used according to the manufacturer's instructions. 9 volumes of buffer NTI (provided by the manufacturer) were added to one volume of sample before binding. After washing, the DNA was eluted twice in 22 μL ddH$_2$O (44 μL final volume). In the next step, 5′-phosphorylated strands were removed by adding 1 μL Lambda exonuclease (10 U/μL) and 5 μL Lambda exonuclease reaction buffer (10x) to a final volume of 50 μL and incubating for 30 min at 37°C. The synthesized probes were then purified using the Monarch PCR & DNA Cleanup Kit (New England BioLabs) according to the manufacturer's instructions and the quality was verified on denaturing 12–16% polyacrylamide gels.

Quality control and purification

The absorbance of samples was measured at 260 nm and 488 nm, 596 nm, or 647 nm depending on the incorporated fluorophore using a Nanodrop 2000 spectrophotometer (Thermo Fisher Scientific). To assess the quality of generated probes, samples were denatured in 90% formamide, 0.5% EDTA, 0.1% Xylene cyanol, 0.1% bromophenol blue and loaded onto a 12% polyacrylamide gel containing 6 M urea. The gel was incubated in 1x TBE buffer containing 1x Diamond Nucleic Acid Dye for 30 min at room temperature to visualize single-stranded DNA.

Complex probe sets labeling target region "A" or "B" were further purified following the "crush and soak" method with adaptations.[84] Briefly, segments of the polyacrylamide gel containing the band of interest were cut out and 2 volumes of a buffer containing 10 mM magnesium acetate tetrahydrate, 0.5 M ammonium acetate, 1 mM EDTA (pH 8.0) and 0.1% (w/v) SDS was added followed by incubation at 37°C for 16–24 h. The samples were then centrifuged at 13000 x g for 1 min and the supernatant was once more purified

Cell Reports Methods
Article

using the Monarch PCR & DNA Cleanup Kit (New England BioLabs). We expect the ''crush and soak'' method to improve signal strength if low labeling densities are used during extension.

Polymerase Screens

Polymerases were tested for their ability to incorporate dCTP-ATTO488, dCTP-ATTO594, or dCTP-ATTO647N into oligonucleotides. The maximum number of incorporated dCTP-dye in the probe was eight (CATCCTGAAGGAATGGTCCATG**C**TTA**CC**TGGG **CCC**AT**CC**T).

For detailed information about the reaction conditions see Table S2. 0.1 nmol annealed DNA was added to the recommended reaction mixtures (10 μL final volume) and 5 U of the respective polymerase was added. The following temperatures were used during synthesis: Klenow exo-at 30°C, Taq at 64°C, Q5 at 64°C, Phusion at 64°C, Terminator DNA polymerase at 72°C. All reactions were carried out for 60 min and the reactions were stopped by adding 1 μL 0.5 M EDTA. We did not observe notable differences in incorporation efficiency between the reported results and reactions carried out at higher temperatures (Klenow exo-at 37°C, Taq at 72°C, Q5 at 72°C, Phusion at 72°C, Terminator DNA Polymerase at 75°C) (figure not shown). The absorbance of synthesized products was measured at 200–700 nm on Nanoquant plates using a Tecan Spark microplate reader (Tecan) and choosing the following dye-correction factors: CF_{260}(ATTO488): 0.22, CF_{260}(ATTO594): 0.22, CF_{260}(ATTO647N): 0.04. The depicted data contained at least two measurements per biological replicate.

HPLC

HPLC was used to characterize the number of incorporated fluorophores in NOVA probes with low fluorophore input in synthesis (Figures S3G and S3H). ATTO594-labeled and ATTO647N-labeled probes (0.31 nmol or 0.34 nmol) were analyzed and purified by reverse-phase HPLC using an Agilent Technologies 1260 Infinity II System with a G7165A detector equipped with an EC 250/4 Nucleodur 100-3 C18ec column from Macherey Nagel. A gradient of 0–80% of buffer B in 45 min at 60°C with a flow rate of 1 mL/min was applied. The following buffer system was used: buffer A: 100 mM NEt_3/HOAc, pH 7.0 in H_2O and buffer B: 100 mM NEt_3/HOAc, pH 7.0 in H_2O/MeCN 20/80. The fractions of each signal peak were combined, and the solvents were concentrated by vacuum centrifugation.

Sample preparation and fluorescence *in situ* hybridization

Fluorescence *in situ* hybridization was performed as previously described.[24] Adherent cells were grown overnight on glass coverslips (1.5, 18 × 18 mm, Marienfeld), washed twice with 1x Dulbecco's Phosphate Buffered Saline (PBS), and fixed using osmotically balanced and methanol-free 4% formaldehyde for 10 min at room temperature. Alternatively, PBS-washed suspension cells were resuspended in a small volume of PBS at a density of 1 million cells per mL and applied to poly-L-lysine coated glass coverslips followed by the addition of methanol-free 4% formaldehyde for 10 min at room temperature. The slides were washed twice in 1x PBS for 5 min and the cells were permeabilized in 1X PBS containing 0.5% Triton X-100 for 15 min. After two successive washing steps in 1x PBS, 0.1 M HCl was added to the slides for 5 min. The slides were washed twice with 2 x SSC and were placed onto a solution containing 1 μg/mL RNase for 30 min at 37°C in a wet chamber. Then, adherent or suspension cells were pre-equilibrated in 2x SSC containing 50% formamide for 60 min or overnight, respectively, inverted onto 8 μL of hybridization solution, and sealed with rubber cement (Marabu). The slides were placed on a heat block set to 81°C for 3 min and incubated at 37°C overnight (16–20 h).

On the second day, slides were washed twice with 2x SSC for 15 min followed by two successive 7-min washes in 0.2x SSC containing 0.2% Tween 20 at 56°C. Then, slides were washed with 4x SSC containing 0.2% Tween 20 and with 2x SSC for 5 min, respectively.

For oligoFISH probes, a second hybridization step was performed for 30 min at room temperature. The slides were then washed once with 2x SSC containing 30% formamide for 7 min at 37°C, twice with 2 x SSC for 5 min, once with 0.2X SSC containing 0.2% Tween 20 at 56°C, once with 4x SSC containing 0.2% Tween 20 for 7 min at room temperature and once with 2x SSC for 5 min.

DNA was counterstained with DAPI (1 μg/mL in 2x SSC) for 10 min and washed twice with 2x SSC. For STED microscopy, nuclei were counterstained with or DiYO-1 (12.5 nM in 2x SSC) for 30 min and washed twice with 2x SSC for 5 min, respectively. Coverslips were mounted on microscopic slides with MOWIOL (2.5% DABCO, pH 7.0), dried for 30 min, and sealed with nail polish.

Image acquisition

Confocal images were acquired using a Nikon TiE microscope equipped with a Yokogawa CSU-W1 spinning-disk confocal unit (50 μm pinhole size), an Andor Borealis illumination unit, Andor ALC600 laser beam combiner (405 nm/488 nm/561 nm/640 nm), Andor IXON 888 Ultra EMCCD camera, and a Nikon 100×/1.45 NA oil immersion objective. The microscope was controlled by software from Nikon (NIS Elements, ver. 5.02.00).

Super-resolution was carried out on a 2C STED 775 QUAD Scan microscope (Abberior Instruments) equipped with a 100x 1.4 NA UPlanSApo oil immersion objective lens (Olympus), 3 pulsed excitation lasers (485 nm, 594 nm, 640 nm) and a pulsed depletion laser of 775 nm.

Cell Reports Methods
Article

3D STED microscopy of telomers using adaptive illumination

To avoid photobleaching NOVA-FISH stained telomers of IMR90 cells in 3D, stacks were acquired using adaptive illumination STED microscopy.[85] Cells were recorded using a pixel size of 30 nm, z-steps of 80 nm, a 10 μs dwell time, and a pinhole size of 50 μm.

Automated STED microscopy for two-color NOVA-FISH

Automated STED microscopy was performed according to Brandstetter et al..[24] The acquisition of 3D confocal stacks was automated using home-written Python scripts to control the microscope. Spots within confocal scans were detected using a Laplacian-of-Gaussian blob detector for both channels. Detected spots no further apart than 5 pixels from another spot in the other channel were imaged using 3D STED settings. This process was repeated for each detected spot pair within a confocal scan. Following a spiral pattern, the stage was moved to the next overview to repeat the confocal scan and the subsequent detailed STED acquisition until a specified amount of time elapsed.

Image analysis

For the analysis of the effects of labeling density (Figures 2E–2G), cells in confocal z-stacks of major satellites were segmented first via automatic thresholding in a z-maximum projection of the DAPI channel followed by a second round of thresholding in the 640nm (rel. binding) channel to segment major satellites. In the segmented areas, intensities of both the 488nm (rel. brightness) and the 640nm (rel. binding) channels were measured, background, determined by a manually selected ROI outside the cells, was subtracted, and measurements were averaged (median) per cell. For the plots, measurements were normalized to the intensity at 100% for the binding channel and at 25% for the brightness channel. Analysis was carried out using Fiji.[86]

For analysis of image data of repetitive and non-repetitive loci (in Figures 1D–1F; Figures 3B and 3C, Figures 3F and 3G; Figures 4D; S4C), nuclear segmentation maps of confocal images stained with DAPI or DiYO-1 were obtained using Otsu thresholding. FISH spots within segmentation maps were detected using a Laplacian-of-Gaussian blob detector (Figure 3F and 3G; Figure S4C). Alternatively, FISH spots were detected in each channel using RSFISH[87] and detection threshold parameters were adjusted if necessary (in Figures 1D–1F; Figures 3B and 3C; Figure 4D). Segmentation maps were used to calculate the total number of spots per cell, to obtain the mean background signal within single nuclei to calculate the spot signal over the nucleus background, and the signal-to-noise ratio of single spots. For Figure 4D, distances <500 nm between A and B were considered co-localizing.

Analysis of automated STED measurements of FISH spot pairs was performed as previously described.[24] Automated image acquisition generated large quantities of data requiring an additional quality control step. To filter out low-quality images, we used a machine learning-based classifier (Random Forest) to label images as "good" or "bad". The classifier was trained with a ground truth dataset created by an experienced scientist who manually sorted images.

Detailed spot analysis was performed on images passing this QC step. Subpixel localization of FISH spots in both channels was performed by fitting a multidimensional Gaussian function plus a constant background using the Levenberg-Marquardt algorithm. The peak height of the fitted Gaussians was used to determine spot intensity.

QUANTIFICATION AND STATISTICAL ANALYSIS

The experiments shown in this study were performed as three biologically independent experiments ($n = 3$) and the figures contain pooled data. No statistical methods were used to predetermine the sample size. Images depicted are representative images from the experiments and dotted lines indicate the outlines of the cells. Data plotted as boxplots indicate the 25th and 75th percentiles, with the whiskers showing the minima and maxima (5th and 95th percentiles), black circles indicating the outliers, and the horizontal line showing the median. Some data are plotted in bar graphs as the mean ± SD. Data was normalized by the median of the first depicted condition in the replicates, if not stated otherwise. Significance levels were tested by non-parametric two-sided Wilcoxon tests or pairwise comparisons using the Wilcoxon rank-sum test with Bonferroni's correction for multiple testing (* = $p < 0.05$, ** = $p < 0.01$, *** = $p < 0.001$). Sample sizes for all of the graphs are indicated in the figures or figure legends.

4.2 ALTERED ENHANCER-PROMOTER INTERACTION IN PEDIATRIC AML

Weichenhan, D., Riedel, A., Sollier, E., Toprak, U.H., Hey, J., Breuer, K., Wierzbinska, J.A., Touzart, A., Lutsik, P., Bähr, M. and Östlund, A., Nilsson, T., Jacobsson, S., Edler, M., Waraky, A., Behrens, Y.A., Göhring, G., Schlegelberger, B., **Steinek, C.**, Harz, H., Leonhardt, H., Dolnik, A., Reinhard, D., Bullinger, L., Palmqvist, L., Lipka, D.B., and Plass, C. (Oct. 2024). *Blood Advances* 8 (19), p. 5100–5111.

DOI: 10.1182/bloodadvances.2023012161

blood advances®

REGULAR ARTICLE

Altered enhancer-promoter interaction leads to *MNX1* expression in pediatric acute myeloid leukemia with t(7;12)(q36;p13)

Dieter Weichenhan,[1,*] Anna Riedel,[1,*] Etienne Sollier,[1,*] Umut H. Toprak,[2,*] Joschka Hey,[1] Kersten Breuer,[1] Justyna A. Wierzbinska,[1] Aurore Touzart,[1] Pavlo Lutsik,[1] Marion Bähr,[1] Anders Östlund,[3] Tina Nilsson,[4] Susanna Jacobsson,[4] Marcel Edler,[4] Ahmed Waraky,[3,4] Yvonne Lisa Behrens,[5] Gudrun Göhring,[5] Brigitte Schlegelberger,[5] Clemens Steinek,[6] Hartmann Harz,[6] Heinrich Leonhardt,[6] Anna Dolnik,[7] Dirk Reinhardt,[8] Lars Bullinger,[7] Lars Palmqvist,[3,4] Daniel B. Lipka,[9-11,†] and Christoph Plass[1,10,†]

[1]Division of Cancer Epigenomics and [2]Division of Neuroblastoma Genomics, German Cancer Research Center, Heidelberg, Germany; [3]Department of Laboratory Medicine, University of Gothenburg, Gothenburg, Sweden; [4]Department of Clinical Chemistry, Sahlgrenska University Hospital, Gothenburg, Sweden; [5]Department of Human Genetics, Hannover Medical School, Hannover, Germany; [6]Faculty of Biology, Ludwig-Maximilians-Universität in Munich, Planegg-Martinsried, Germany; [7]Department of Hematology, Oncology, and Tumor Immunology, Charité-Universitätsmedizin Berlin, Corporate Member of Freie Universität Berlin and Humboldt-University Berlin, Berlin, Germany; [8]Department of Pediatric Oncology, University of Duisburg-Essen, Essen, Germany; [9]Section of Translational Cancer Epigenomics, Division of Translational Medical Oncology, German Cancer Research Center, Heidelberg, Germany; [10]German Cancer Consortium, Heidelberg, Germany; and [11]National Center for Tumor Diseases, NCT Heidelberg, a partnership between DKFZ and Heidelberg University Hospital, Heidelberg, Germany

Key Points

- Expression analysis of >1500 pediatric AML samples demonstrates *MNX1* expression as a universal feature of t(7;12)(q36;p13) AML.

- *MNX1* is activated by an enhancer-hijacking event in t(7;12)(q36;p13) AML and not, as previously postulated, by an *MNX1::ETV6* oncofusion.

Acute myeloid leukemia (AML) with the t(7;12)(q36;p13) translocation occurs only in very young children and has a poor clinical outcome. The expected oncofusion between break point partners (*motor neuron and pancreas homeobox 1* [*MNX1*] and *ETS variant transcription factor 6* [*ETV6*]) has only been reported in a subset of cases. However, a universal feature is the strong transcript and protein expression of MNX1, a homeobox transcription factor that is normally not expressed in hematopoietic cells. Here, we map the translocation break points on chromosomes 7 and 12 in affected patients to a region proximal to *MNX1* and either introns 1 or 2 of *ETV6*. The frequency of *MNX1* overexpression in pediatric AML is 2.4% and occurs predominantly in t(7;12)(q36;p13) AML. Chromatin interaction assays in a t(7;12)(q36;p13) induced pluripotent stem cell line model unravel an enhancer-hijacking event that explains *MNX1* overexpression in hematopoietic cells. Our data suggest that enhancer hijacking may be a more widespread consequence of translocations in which no oncofusion product was identified, including t(1;3) or t(4;12) AML.

Introduction

Acute myeloid leukemia (AML) has been successfully investigated in the past using cytogenetic analysis. This led to the discovery of numerous recurrent chromosomal translocations (eg, t(8;21)(q22; q22) or t(15;17)(q22;q12)) generating oncofusion proteins (eg, RUNX1::RUNX1T1 or PML::RARA, respectively) that drive leukemogenesis. For many years, these translocations have served as diagnostic and prognostic

markers and affected patients can now be treated with specific targeted therapies (eg, retinoic acid and arsenic trioxide in t(15;17) cases).[1] In 1998, 2 publications reported the translocation t(7;12)(q36;p13) in AML of infants[2,3] occurring predominantly in children aged <18 months and not in adult AML. A recent meta-analysis of the Nordic Society for Pediatric Hematology and Oncology (NOPHO-AML) determined that t(7;12)(q36;p13) AML constituted 4.3% of all children with AML aged <2 years and found a 3-year event-free survival of 24% (literature-based data) and 43% (NOPHO-AML data).[4] Cytogenetically, t(7;12)(q36;p13) AML is often associated with the occurrence of trisomy 19,[4,5] but no other recurrent aberrations have been described.

Reported break points in t(7;12)(q36;p13) AML have mainly been evaluated by fluorescent in situ hybridization analysis. The break-points on chromosome 12 (chr12) are located within intron 1 or 2 of *ETS variant transcription factor 6* (*ETV6*) and proximal to *motor neuron and pancreas homeobox 1* (*MNX1*) and within the 3' end of *nucleolar protein with MIF4G domain 1* (*NOM1*) on chr7.[6] A *MNX1::ETV6* fusion transcript was described only in a subset of t(7;12)(q36;p13) AML cases.[4-7] However, all AML cases with t(7;12)(q36;p13) have high expression of *MNX1*,[5] suggesting a yet unknown mechanism of *MNX1* activation. Consistent with the activation of a silenced gene locus, a translocation of the *MNX1* locus from the nuclear periphery to the internal nucleus was seen, an observation that is in line with the idea that condensed and silent chromatin is located in the nuclear periphery.[6] Furthermore, interactions of *ETV6* downstream elements with the *MNX1* locus have been postulated as possible mechanisms for *MNX1* activation.[6,8] The first clue for the existence of possible aberrant promoter-enhancer interactions leading to *MNX1* activation came from our investigations of the GDM-1 AML cell line, which harbors a t(6;7)(q23;q36) translocation. In GDM-1, the *MNX1* promoter interacts with an enhancer element from the *MYB* locus on chr6q23.[9]

Recently, Nilsson et al. reported the introduction of a translocation between chr7q36 and chr12p13, modeling the one found in t(7;12)(q36;p13) AML, into the human induced pluripotent stem cell (iPSC) line, ChiPSC22^WT.[8] The derivative line, ChiPSC22^t(7;12), can be differentiated into hematopoietic stem and progenitor cells (HSPCs) and, as such, expresses *MNX1*, suggesting that hematopoietic enhancers play a role in *MNX1* activation. Enhancer hijacking has initially been described as a mechanism for oncogene activation in AML with inv(3)/t(3;3)(q21q26) AML, in which activation of *EVI1*, an isoform encoded from the *MDS and EVI1 complex locus* (*MECOM*), results from the repositioning of a *GATA2* enhancer.[10-12] Enhancer hijacking is also implicated in acute leukemia of ambiguous lineage in which translocated hematopoietic enhancers from different chromosomes are involved in activating *BCL11B*.[13]

Here, we provide a detailed description of the molecular alterations found in 6 patients with t(7;12)(q36;p13) AML and dissect the molecular mechanism leading to *MNX1* activation through the use of CRISPR-engineered ChiPSC22^t(7;12) iPSCs and HSPCs. We identified that a previously proposed[8] enhancer-hijacking event activates the *MNX1* promoter via hematopoietic enhancers from the *ETV6* locus and validated this event in the iPSC/HSPC system. Our data suggest that enhancer hijacking may be a more wide-spread, but so far largely unappreciated, mechanism for gene activation in AML with cytogenetic abnormalities.

Methods

Samples and cell lines

Pediatric leukemia samples T1, T2, and T3 (supplemental Table 1) were obtained at diagnosis after informed consent of patients' legal guardians in accordance with the institution's ethical review board (University Essen and Medical University Hannover, MHH, no. 2899). Sample T4 (supplemental Table 1) came from a pediatric AML cohort in Gothenburg, Sweden, and informed consent was obtained from the legal guardians in accordance with the local ethical review board. Human iPSC line ChiPSC22 (Cellartis/Takara Bio Europe AB) was cultivated in the feeder-free DEF-CS system (Cellartis/Takara Bio Europe) under standard conditions. Before differentiation, cells were transferred to Matrigel (Corning) and mTeSR1 medium (STEMCELL Technologies Inc) for 2 to 3 passages. ChiPSC22 was authenticated; this line and its derivatives were regularly tested for mycoplasma contamination using a commercial test kit (VenorGeM Classic, Minerva Biolabs).

Differentiation to hematopoietic cells

Differentiation of ChiPSC22 was done as previously described.[8]

Whole-genome sequencing (WGS)

Genomic DNA was isolated using the Quick DNA Miniprep kit (Zymo Research), and libraries were sequenced in an Illumina HiSeq X Ten sequencer. FASTQ files were aligned with the Burrows-Wheeler Aligner (maximal exact match option) to the hg19 reference genome. Single nucleotide variants (SNVs) were called using mutect2. Because of the lack of matched germ line sequences, only 52 known AML driver genes (supplemental Table 2) were screened for mutations. Structural variants (SVs) and somatic copy number alterations (SCNAs) were called using the Hartwig Medical Foundation (HMF) pipeline (https://github.com/hartwigmedical/hmftools). HMF tools were used in tumor-only mode, and putative germ line SVs were filtered out using a large panel of HMF-provided normals. SVs <20 kb were filtered out. Processed data of 2 samples of the TARGET-AML data set (supplemental Table 1; database of Genotypes and Phenotypes (dbGaP) accession: phs000465.v22.p8) was downloaded using the Globus platform.[14]

RNA isolation, sequencing, and quantitative Reverse Transcriptase-Polymerase Chain Reaction (qRT-PCR)

Total RNA was isolated using the RNeasy Plus Mini kit (Qiagen). After library preparation, RNA was sequenced on NOVASEQ 6000 with 100-bp paired end. The FASTQ files were processed using the nf-core[15] RNA-sequencing (RNAseq) v3.9 pipeline, with alignment performed using Spliced Transcripts Alignment to a Reference (STAR)[16] and quantification performed using Salmon.[17] Allele-specific expression was examined by first detecting heterozygous single-nucleotide polymorphisms in exons using the genomic analysis toolkit (GATK) HaplotypeCaller and then counting the allelic expression in RNA using GATK ASEReadCounter.[18] Differential expression analysis was performed using limma for Affymetrix array data and pydeseq2 for RNAseq data.

qRT-PCR was performed as previously described using TaqMan Universal Master Mix II with uracil-N-glycosylase (ThermoFisher Scientific, Applied Biosystems) and TaqMan gene expression assays

(ThermoFisher Scientific, Applied Biosystems; supplemental Table 3).[8]

Detection of fusion transcripts

For our own samples, fusion transcripts were detected using STAR-Fusion v1.10.1.[19] For the TARGET-AML cohort, we downloaded the processed STAR-Fusion results from the Genomic Data Commons data portal.

Protein extraction, western blotting, and protein detection

Protein extraction, western blotting, and protein detection with antibodies (supplemental Table 4) was done as described previously.[9]

Expression screens

RNAseq expression data were downloaded from the TARGET cohort[20] (both TARGET-NCI (Therapeutically Applicable Research to Generate Effective Treatments, National Cancer Institute) and TARGET-FHCRC (Fred Hutchinson Cancer Research Center); https://target-data.nci.nih.gov/Public/AML/mRNA-seq/L3/expression/BCCA/). *MNX1* is not expressed in normal hematopoietic cells; hence, in RNAseq, a *MNX1* expression >0.5 transcripts per million was considered overexpression. Gene expression data files of the Balgobind cohort[21] were downloaded from Gene Expression Omnibus (GSE17855) and normalized using the affy R package (https://bioconductor.org/packages/release/bioc/html/affy.html). Log-expression values of microarray data were assumed to be normally distributed. We computed the mean and standard deviation for *MNX1* expression across all samples; those whose *MNX1* expression was higher than the mean plus 3 standard deviations were considered to express *MNX1* (3-sigma rule).

4C

Circular chromosome conformation capture (4C) with 2 million cells was done and analyzed as described[9] using *Hin*dIII in combination with *Dpn*II (supplemental Table 5).

High-throughput chromosome conformation capture (Hi-C)

Hi-C libraries were prepared and analyzed as previously described[22] with minor modifications. One million cells were fixed at a final concentration of 1% formaldehyde in RPMI 1640 medium. Digestion was performed using *Dpn*II. Two to 3 Hi-C library replicates per sample were sequenced with 240 million reads per replicate. The FASTQ files were processed using the nf-core/hic v.2.1.0 pipeline. Hi-C figures were generated using figeno (https://github.com/CompEpigen/figeno)[23].

Two-color fluorescence in situ hybridization (FISH)

Two NOVA-probe sets targeting *MNX1* (chr7:156802250-156807250) and *ETV6* (chr12:11949500-11954500) carrying multiple ATTO594 or ATTO647N dyes were synthesized as described previously[24] (supplemental Table 6). Two-color FISH was conducted as previously described with minor adaptations.[25,26] ChiPSC22[t(7;12)] iPSCs were seeded on DEF-CS COAT-1–coated coverslips (Cellartis, Takara BioSciences) and

ChiPSC22[t(7;12)] HSPCs on poly-L-lysine–coated coverslips. After washing and fixation steps, coverslips were mounted on microscopic slides with Mowiol (2.5% 1,4-Diazabicyclo[2.2.2]octane and pH 7.0; Carl Roth), dried for 30 minutes, and sealed with nail polish.[27] Automated Stimulated Emission Depletion (STED) microscopy was performed according to Brandstetter et al.[25] FISH signals within confocal scans were detected using a Laplacian-of-Gaussian blob detector and subsequently imaged using 3-dimensional (3D) STED settings. Subpixel localization of FISH spots in both channels was performed by fitting a multidimensional Gaussian function plus a constant background using the Levenberg-Marquardt algorithm. The peak height of the fitted Gaussians was used to determine spot intensity. Only distances <600 nm were considered.

ACT-seq and ATAC-seq

Genome-wide targeting and mapping of histone modifications (supplemental Table 4) and mapping of open chromatin were done by antibody-guided chromatin tagmentation sequencing (ACT-seq) and assay for transposase-accessible chromatin by sequencing (ATAC-seq), respectively, as described previously.[9] For read normalization using spiked-in yeast DNA in ACT-seq, trimmed reads were additionally aligned against the *Saccharomyces cerevisiae* R64 reference genome followed by postalignment filtering. An ACT-seq library–specific scaling factor was obtained by calculating the multiplicative inverse of the number of filtered alignments against the yeast genome.[9] ACT-seq peak calling was done applying MACS v.2.2.6 (https://pypi.org/project/MACS2/) with a q-value cutoff of 0.05 and default parameters using a wrapper script with settings narrowPeak and broadPeak for acetylated lysine 27 of histone 3 (H3K27ac) and (monomethylated lysine 4 of histone 3) H3K4me1, respectively. To facilitate visualization of hematopoietic-specific enhancers in the Integrative Genomics Viewer (version 2.11.7),[28] we generated HSPC-specific H3K27ac and H3K4me1 bw-tracks with callpeaks using corresponding iPSC data as internal reference.

Deletion of the enhancer region

A region of 213.5 kb (chr12:11951022-12164578, GRCh37/hg19) covering the 4 enhancers located closest to the break point in ChiPSC22[t(7;12)] was deleted by CRISPR/Cas9 editing as described previously[8] using CRISPR RNAs designed with the Alt-R Custom Cas9 crRNA Design Tool (Integrated DNA Technologies). To join the 2 ends by homology-directed repair, a 150 single-stranded deoxynucleotide was designed with 75 bases sequence homology on each side. Deletion was done in ChiPSC22[WT] and ChiPSC22[t(7;12)] sublines 14D7 and 24C7.[8] The presence of the deletion on the translocated and the wild-type allele was validated by PCR using the Terra PCR Direct Polymerase Mix (Takara Bio Europe; supplemental Table 7). From line 14D7, cell line 2304B4 was generated, and from 24C7, lines 2305B10 and 2305C9 were generated.

Phenotypic characterization of enhancer deletion clones

For flow cytometry analysis, cells were resuspended in phosphate-buffered saline plus EDTA and incubated with the mix of antibodies for 15 to 20 minutes in the dark at room temperature. Cells were washed once and resuspended in phosphate-buffered saline plus
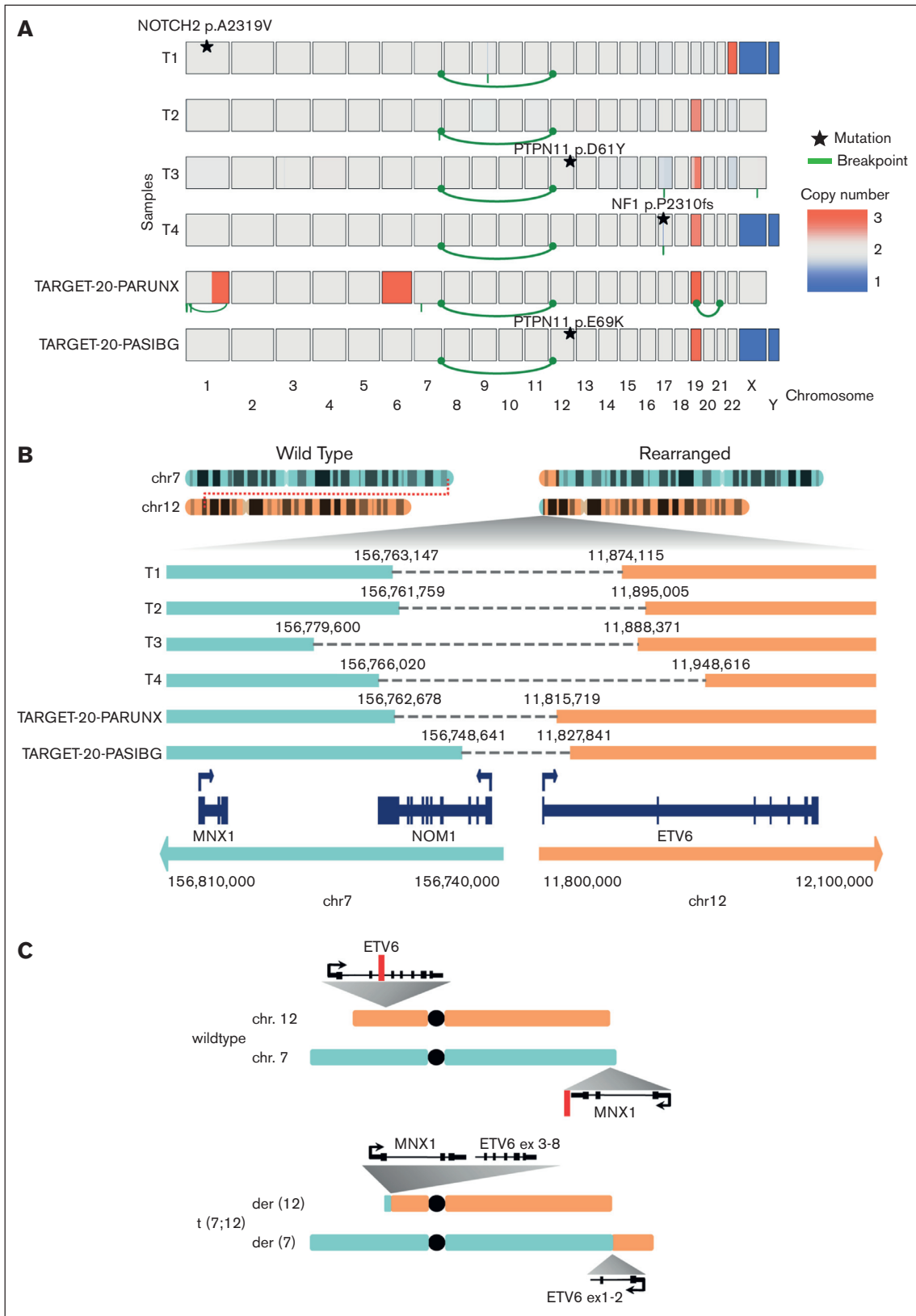
Figure 1.
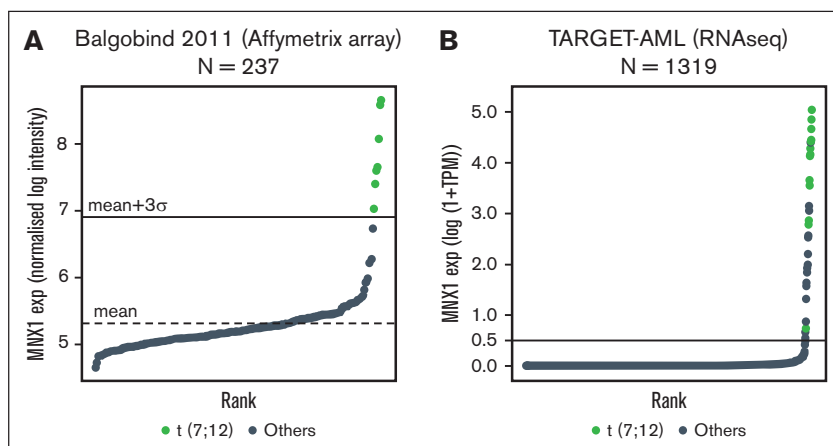
Figure 2. *MNX1* expression in pediatric AML with t(7;12)(q36;p13) translocation. (A-B) *MNX1* expression in 2 different pediatric AML cohorts. (A) Balgobind et al[31]; 237 samples profiled with Affymetrix arrays. The mean expression level is shown with a dashed line, and the mean plus 3 standard deviations is shown with a horizontal line. (B) TARGET-AML[29]; 1319 samples profiled with RNAseq (cutoff, 0.5 TPM). Samples with cytogenetically detected t(7;12)(q36;p13) translocation are shown in green and other samples in gray. exp, expression; TPM, transcripts per million.

EDTA. Data were collected on BD FACS Aria (BD Biosciences) and analyzed using BD FACSDiva. The colony-forming unit assay was done using MethoCult H4034 Optimum (STEMCELL Technologies) following the manufacturer's protocol. Proliferation was analyzed by continuous culture of the HSPCs in StemSpan SFEM II + CC100 (STEMCELL Technologies) for 14 days. Cells were counted every 48 hours, centrifuged, and 75% fresh medium was added to 25% old medium. Cell division was calculated as follows: ln(B/A)/(ln2), in which A = number of seeded cells and B = number of cells after 48 hours.

Results

WGS of t(7;12)(q36;p13) AML

To precisely map structural rearrangements, SCNAs, and genetic mutations in t(7;12)(q36;p13) AML, we performed WGS of 4 t(7;12)(q36;p13) AML cases, T1, T2, T3, and T4 (Figure 1A; supplemental Table 1). We additionally used published WGS data from 2 samples with t(7;12)(q36;p13) from the TARGET cohort[29] (supplemental Table 1). The presence of t(7;12)(q36;p13) as a reciprocal balanced translocation was verified in all 6 samples (Figure 1A). The break point on chr12 is located in 5 samples in intron 1 and in 1 sample in intron 2 of ETV6. On chr7, all break points are located proximal to *MNX1*; in 4 cases within *NOM1*, located next to *MNX1*; and in 2 cases, between *MNX1* and *NOM1* (Figure 1B). In none of these cases, an oncofusion gene between *MNX1* and *ETV6* is supported by the observed translocation break points, leaving the main *MNX1* variant (RefSeq: NM_005515) unaffected by the genomic rearrangements (Figure 1C). Accompanying cytogenetic data (supplemental Table 1) revealed trisomy 19 in all cases, a result confirmed by SCNA analysis for all cases except for T1, for which SCNA analysis identified a trisomy 22 but no trisomy 19 (Figure 1A). We found mutations in common leukemia genes (supplemental Table 2), namely in *NOTCH2*

(p.A2319V), *NF1* (p.P2310fs), and *PTPN11* (p.D61Y and p.E69K; Figure 1A).

T1, T2, and T3 were profiled with RNAseq, but no fusion transcript *MNX1::ETV6* could be identified. The TARGET-AML cohort contains 14 t(7;12) samples, and of these, only 1 has an *MNX1::ETV6* fusion detected by STAR-Fusion (TARGET-20-PAWNHH), and 1 has an *ETV6::LMBR1* fusion (TARGET-20-PAWNYK). Therefore, fusion transcripts do not appear to be the driving factor behind t(7;12)(q36;p13).

MNX1 is highly expressed in all t(7;12)(q36;p13) AML and is associated with a characteristic gene expression signature

Although normally not expressed in the hematopoietic lineage, *MNX1* is highly expressed in all analyzed t(7;12)(q36;p13) AML.[5,6,30] In line with this, AML cases T1 to T4 showed high *MNX1* expression (supplemental Table 1). We additionally evaluated *MNX1* expression in 2 pediatric AML cohorts with available expression data: Balgobind et al (237 samples profiled with Affymetrix array[31]; Figure 2A) and TARGET-AML (1319 samples profiled with RNAseq[29]; Figure 2B). *MNX1* was expressed in 7 of 237 samples (2.9%) of the Balgobind cohort and in 31 of 1319 (2.3%; including resample for samples TARGET-20-PARUNX and TARGET-21-PASVJS) samples of the TARGET-AML cohort. All t(7;12) samples showed *MNX1* expression but also some samples without 7q36-rearrangements. Accordingly, there might be alternative mechanisms leading to *MNX1* activation. Most t(7;12)(q36;p13) samples were diagnosed at younger than 2 years; however, most *MNX1*-overexpressing samples without t(7;12) were diagnosed at an older age (supplemental Table 1). A characteristic gene expression signature for t(7;12)(q36;p13) AML compared with other cytogenetic subgroups in pediatric AML has been described.[31] The majority of these genes are either

---

Figure 1. WGS analysis of t(7;12)(q36;p13) AML. (A) Copy numbers (blue, loss; red, gain), structural rearrangements (green bow connecting 2 chromosomes), and mutations in known AML driver genes for 6 t(7;12)(q36;p13) AML samples based on WGS. Samples T1, T2, T3, and T4 were profiled in this study, whereas TARGET-20-PARUNX and TARGET-20-PASIBG are from the TARGET-AML cohort 15. (B) Sketch of the rearranged chr7 and chr12 and zoom-in on the region around the break points. (C) Schematic overview of chr7 (turquoise), chr12 (orange), and derivative chromosomes der(12) and der(7) resulting from the reciprocal t(7;12) translocation involving *MNX1* on chr7 and *ETV6* on chr12. Red lines indicate positions of break/fusion points.

consistently downregulated in t(7;12)(q36;p13) AML (eg, *TP53BP2*) or upregulated together with *MNX1* (*EDIL3, LIN28B, BAMBI, MAF, FAM171B, AGR2, CRISP3, KRT72,* and *MMP9*). These do not lie on the translocated piece of chr7; and, hence, their expression change might be a secondary effect of the translocation. We performed differential expression analysis between the t(7;12)(q36;p13) and the other cases from each the Balgobind and the TARGET-AML cohort (supplemental Table 8; supplemental Figure 1). Our lists of upregulated and downregulated genes include the genes identified by Balgobind et al,[31] which are indeed consistently deregulated in t(7;12)(q36;p13) across several cohorts, as well as other genes not reported before. The samples with *MNX1* expression but without genomic rearrangement close to *MNX1* did not exhibit this typical gene signature (supplemental Figures 1 and 2). Several experimental systems have recently been developed to model t(7;12): an HSPC system with a t(7;12) translocation[8,32] and a mouse model of leukemia induced by *MNX1* overexpression.[33] The HSPC system partially recapitulated the patients' gene expression signature, whereas in the mouse model, most genes of the t(7;12) signature were not differentially expressed (supplemental Figure 2).

The break points on chr12 in the t(7;12)(q36;p13) samples led to a corrupted *ETV6* allele and reduced *ETV6* expression compared with other samples (supplemental Figure 3), but this was not significant due to the low number of t(7;12) cases and the high *ETV6* expression variability even in the absence of rearrangements. Heterozygous single-nucleotide polymorphisms in exons of *ETV6* were found in T1 and T3, and the allele frequency in RNA suggested monoallelic expression of ETV6 in the leukemic cells (supplemental Figure 3).

A t(7;12)(q36;p13) cell line model exhibits *MNX1* protein expression and chromatin interactions between the *MNX1* and *ETV6* regions

Previously, Nilsson et al engineered an iPSC line harboring a balanced translocation t(7;12)(q36;p13) (ChiPSC22$^{t(7;12)}$) with a break point in *ETV6* intron 2 and a second one ~21 kb proximal to *MNX1* in the common break point region.[8,32] Upon differentiation of ChiPSC22$^{t(7;12)}$ cells to HSPCs, *MNX1* became activated. We confirmed this result at the protein level in 3 ChiPSC22$^{t(7;12)}$ sublines, 14D7, 23G8, and 24C7; the *MNX1* protein was only expressed in the ChiPSC22$^{t(7;12)}$ HSPCs but not in the ChiPSC22$^{t(7;12)}$ iPSCs, ChiPSC22^{WT} iPSCs or ChiPSC22^{WT} HSPCs (Figure 3A). WGS of the 3 sublines did not reveal any relevant changes to the original line ChiPSC22, except for the presence of the heterozygous t(7;12). To examine whether the t(7;12)(q36;p13) translocation juxtaposes enhancers from the *ETV6* region with the *MNX1* promoter, we profiled the iPSCs and HSPCs of both ChiPSC22^{WT} and ChiPSC22$^{t(7;12)}$ lines with Hi-C. No interactions were seen between chr7 and chr12 in the ChiPSC22^{WT} (supplemental Figure 4), but we observed a new topologically associating domain (neo-TAD) around the break point in both iPSC and HSPC ChiPSC22$^{t(7;12)}$ (Figure 3B). The neo-TAD extends up to chr12:12200000, meaning that enhancers located between the break point and the end of the neo-TAD could interact with the *MNX1* promoter. Public ChIPseq data from K562 cells revealed binding of CCCTC-Binding Factor (CTCF) and

Radiation Gene 21 (RAD21) at the extremities of the neo-TAD, which would explain its formation (Figure 3B). For an independent proof of interaction, we performed 4C using an *MNX1* viewpoint (chr7:156805780-156806574) and a viewpoint located in the neo-TAD, close to the *ETV6* break point (chr12:11953871-11954315; supplemental Table 5). Reciprocal 4C confirmed the interaction between the *MNX1* and *ETV6* regions in HSPCs and, less strongly, in 1 iPSC sample (supplemental Figure 5).

We further performed 2-color FISH targeting the *MNX1* promoter and a neo-TAD region located close to the *ETV6* break point and observed a significantly decreased 3D distance between the targeted regions in ChiPSC22$^{t(7;12)}$ HSPCs compared with the corresponding iPSCs (Figure 3C). This suggests a reinforced contact between an enhancer from the *ETV6* neo-TAD region and the *MNX1* promoter upon differentiation.

Identification of hematopoietic enhancers in *ETV6* and its vicinity

We next searched for hematopoietic enhancers located in the chr12 part of the neo-TAD. Active enhancers reside in open chromatin; hence, we profiled accessible chromatin by ATAC in AML-T1 and -T2 and in HSPCs of our cell line model. The patient samples clustered with the HSPCs, separately from the iPSCs, and had similar peaks as HSPCs (supplemental Figure 6A-B). We found 4 consistent open chromatin sites common to the patient samples and to the ChiPSC22$^{t(7;12)}$ and ChiPSC22^{WT} cells within the ETV6 neo-TAD (Figure 4). Additionally, we mapped peaks of enhancer marks H3K27ac and H3K4me1 in both iPSCs and HSPCs. To facilitate the identification of hematopoietic enhancers in ChiPSC22$^{t(7;12)}$ and ChiPSC22^{WT} HSPCs, we applied MACS2 peak calling using the corresponding iPSC data as internal reference. The 4 open chromatin regions were also marked by HSPC-specific H3K27ac and H3K4me1 peaks. In addition, we used public chromatin immunoprecipitation followed by sequencing (ChIPseq) data sets for the same enhancer marks (Gene Expression Omnibus: GSM772885 and GSM621451) and the histone acetyltransferase P300, generated from CD34$^+$ cells and the chronic myeloid leukemia–derived cell line MOLM-1.[10] Again, the 4 ATAC/H3K27ac/H3K4me1 peaks were found as well in MOLM-1 and CD34$^+$ cells (Figure 4). Two of these peaks coincide in addition with p300 peaks (Figure 4). In conclusion, we identified 4 strong enhancer candidates in the *ETV6* neo-TAD region, 2 of which coincide with p300 peaks and may drive *MNX1* activation in t(7;12)(q36;p13) AML.

Deletion of enhancers in the *ETV6* region abrogates *MNX1* expression in ChiPSC22$^{t(7;12)}$ HSPCs

As a further layer of experimental evidence for de novo promoter-enhancer interactions in t(7;12)(q36;p13) AML, we examined *MNX1* expression levels in 3 ChiPSC22$^{t(7;12)}$ sublines carrying a deletion of 213.5 kb, which removed the 4 enhancer candidates (ChiPSC22$^{t(7;12)ΔEn}$; Figure 5A; supplemental Figure 7A). We performed WGS of the ChiPSC22$^{t(7;12)ΔEn}$ derivatives 2304B4 and 2305C9, could confirm the enhancer deletion in both, and found no other rearrangements in 2304B4 but an inversion in the nontranslocated *ETV6* allele of 2305B9 (supplemental Figure 8). Consequently, clone 2305B9 was omitted from further analyses. In the other 2 ChiPSC22$^{t(7;12)ΔEn}$ lines, HSPC-specific *MNX1*
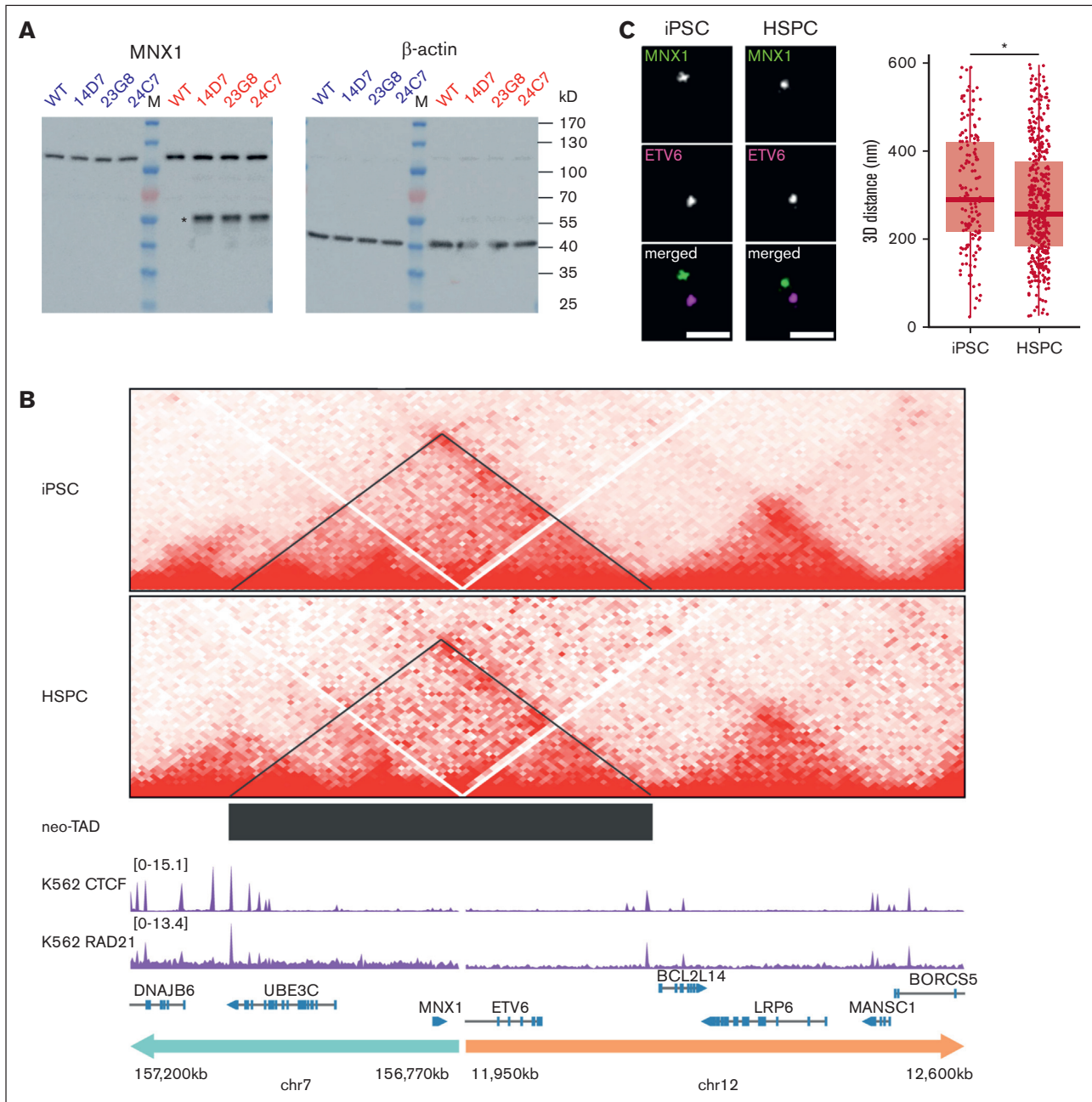
Figure 3. MNX1 protein expression and chromatin interaction of the *MNX1* gene with the *ETV6* region in ChiPSC22$^{t(7;12)}$ cells. (A) Western blot with an *MNX1* antibody (left) and iPSC (blue) and HSPC (red) protein extracts from ChiPSC22^{WT} and ChiPSC22$^{t(7;12)}$ sublines 14D7, 23G8, and 24C7. The *MNX1* protein (asterisk) is only detected in HSPCs of ChiPSC22$^{t(7;12)}$ sublines 14D7, 23G8, and 24C7. The common band at ~120 kD results from an unknown protein cross-reacting with the *MNX1* antibody. To demonstrate loading of equal protein amounts, the unstripped blot was reincubated with an antibody against β-actin (right). (B) Chromatin interactions analyzed by Hi-C seq in the genomic region flanking the translocation break point in the ChiPSC22$^{t(7;12)}$ subline 24C7, either as iPSCs (top) or HSPCs (below). The neo-TAD is indicated by a black bar. ChIPseq data for CTCF and RAD21 in K562 were retrieved from the encode project (IDs ENCFF468HJA and ENCFF000YXZ). (C) Increased proximity between *MNX1* and *ETV6* in ChiPSC22t(7;12) subline 14D7−derived HSPCs compared with iPSCs. Representative STED images of FISH spots in 2 colors targeting *MNX1* and *ETV6* in iPSCs and HSPCs (left). Scale bars, 500 nm. 3D distances between the *MNX1* and *ETV6* signals (right). Red horizontal lines within boxes indicate medians; box limits indicate upper and lower quartiles. iPSCs, n = 154; HSPCs, n = 409, across 3 independent replicates. *$P < .05$, Wilcoxon rank-sum test.
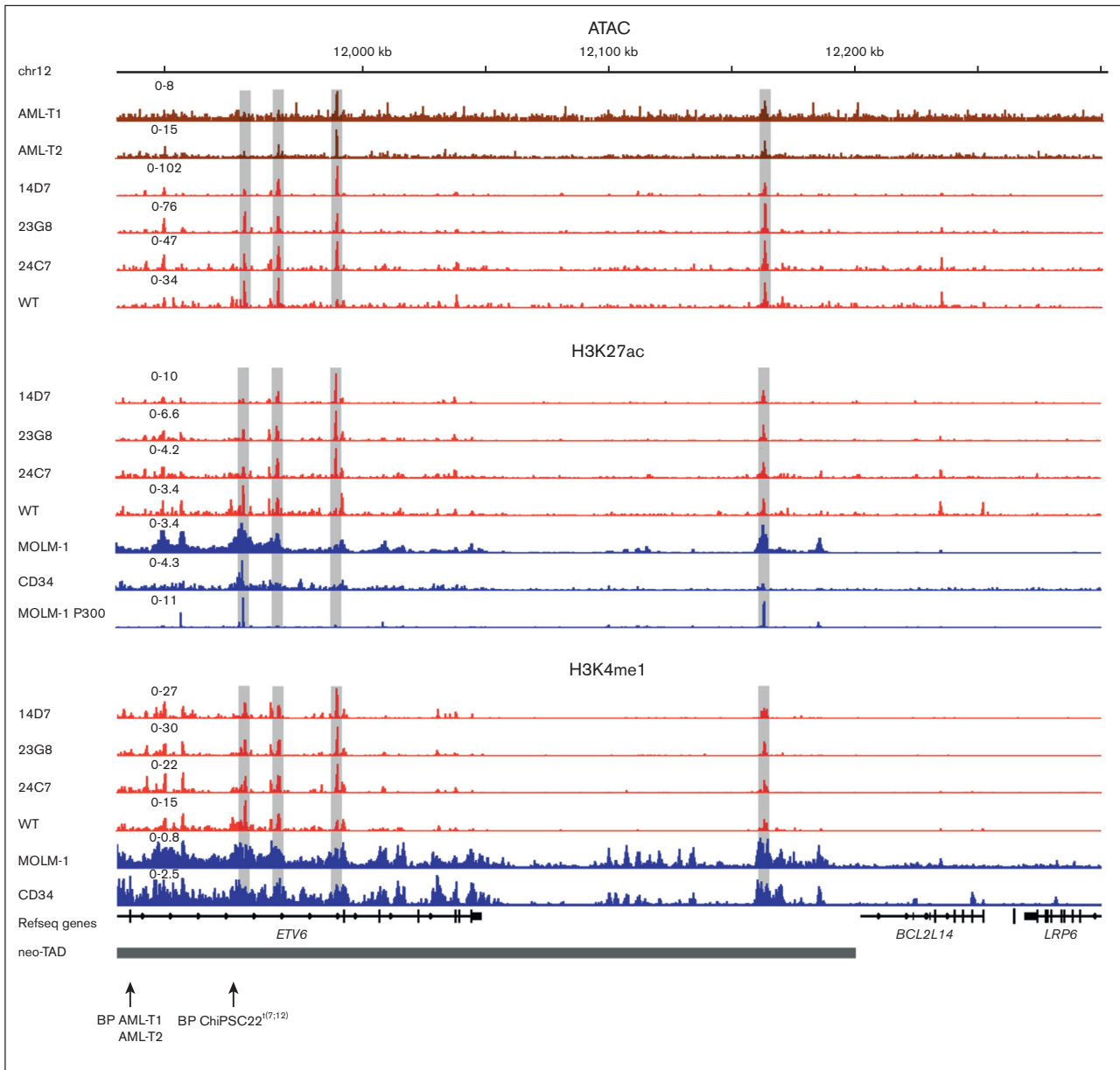
Figure 4. Open chromatin and enhancer mark profiles in the *ETV6* neo-TAD region of patient and cell line samples. Open chromatin profiles (ATAC) of patients with AML , T1 and T2, and of HSPCs from ChiPSC22[WT] and ChiPSC22[t(7;12)] sublines 14D7, 23G8, and 24C7 in the *ETV6* neo-TAD region. HSPC-specific enhancer mark H3K27ac and H3K4me1 profiles and publicly available[10] p300, H3K27ac, and H3K4me1 profiles from MOLM-1 and CD34^{+}. Relevant common peak positions are highlighted by a gray shading. The chr12 break point (BP) position in T1 and T2 and in the ChiPSC22[t(7;12)] sublines are indicated.

expression was abrogated (Figure 5B), whereas the expression of *LRP6* and *BCL2L14* near the deletion was not changed (supplemental Figure 7B). This supports the hypothesis that *MNX1* activation in ChiPSC22[t(7;12)] is the result of interactions between the *MNX1* promoter and 1 or multiple enhancers located in or close to *ETV6*. We also observed downregulation of genes that are upregulated together with *MNX1* in t(7;12)(q36;p13), such as *AGR2, MMP9, MAF*, and *CRISP3* (Figure 5B), suggesting that they are regulated by *MNX1*. Similar to differentiated ChiPSC22[WT], *ETV6* was upregulated, which might be explained by

MNX1 regulation as well. Further phenotypic characterization of the ChiPSC22[t(7;12)ΔEn] sublines 2304B4 and 2305B10 revealed that there is no difference in differentiation capacity compared with the parental ChiPSC22[t(7;12)] (supplemental Figure 7C). The HSPCs derived from both groups also show similar proliferation rates and give rise to similar colony-forming units (supplemental Figure 7D-E).

In conclusion, we provide experimental evidence for a previously proposed enhancer-hijacking event[8] rather than the creation of an oncofusion protein in pediatric AML with t(7;12)(q36;p13). Using
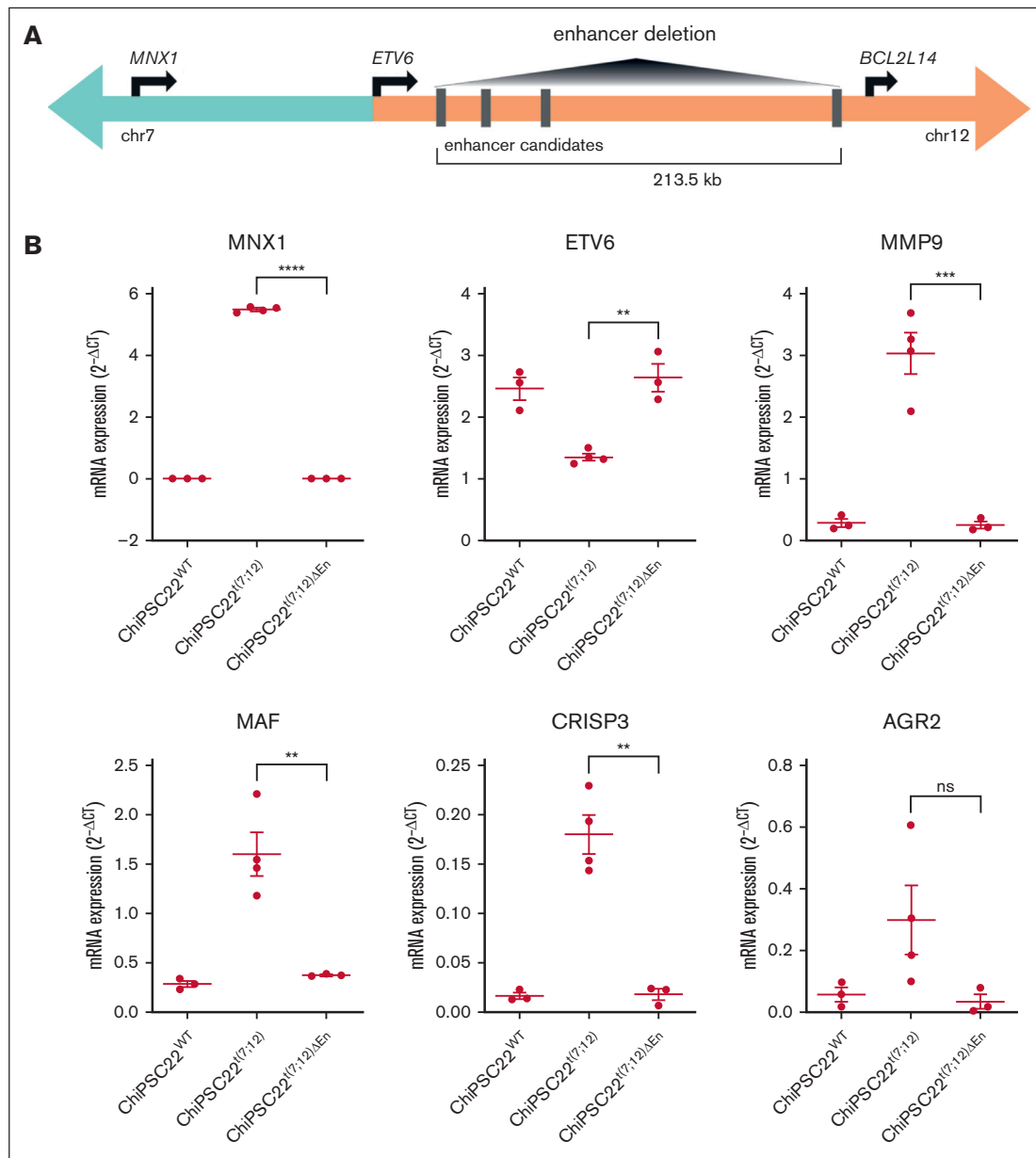
Figure 5. Molecular validation of enhancer-promoter interaction in ChiPSC22$^{t(7;12)}$ upon differentiation. (A) Scheme of the enhancer deletion experiment performed to validate the interaction between the *MNX1* promoter and enhancers distal to the BP. (B) Gene expression in HSPCs derived from ChiPSC22^{WT} (n = 3), ChiPSC22$^{t(7;12)}$ (n = 4, from 2 independent cell lines), and ChiPSC22$^{t(7;12)\Delta En}$ (n = 3, from 2 independent cell lines) measured via qRT-PCR and shown as $2^{-\Delta Ct}$ vs *GUSB* as endogenous reference. ****$P < .0001$; ***$P < .001$; **$P < .01$; *$P < .05$. ns, not significant.

an in vitro iPSC/HSPC cell system, we demonstrate that 1 or several enhancers in the *ETV6* region interact with *MNX1* to regulate its expression.

Discussion

In this manuscript, we describe enhancer hijacking and activation of *MNX1* as a novel molecular mechanism resulting from a translocation between chr7 and chr12 [t(7;12)(q36;p13)] in pediatric AML. Our study shifts the focus from a putative *MNX1::ETV6*

oncofusion transcript[42] to the activation of *MNX1* as the unifying putative leukemia-driving event. Overexpression of *MNX1* is accompanied by monoallelic inactivation of *ETV6* on the translocated chromosome, putatively resulting in haploinsufficiency. Our observation has important implications for the diagnosis of this subgroup of patients, as well as novel therapeutic approaches. As shown in the expression reanalysis, all t(7;12)(q36;p13) AML demonstrate overexpression of *MNX1*. Only few AML cases without t(7;12)(q36;p13) show *MNX1* overexpression; but although t(7;12)(q36;p13) AML is diagnosed at a very young age

(<20 months), *MNX1* overexpression in the absence of this translocation occurs predominantly at a later age, suggesting different, yet unexplained, molecular pathways converging in *MNX1* expression. Considering that *MNX1* is not expressed in the normal hematopoietic system, quantitative *MNX1* expression analysis could be used as a diagnostic marker for this subgroup of pediatric AML.

Enhancer-hijacking events resulting in the activation of proto-oncogenes have been described also in other human malignancies including translocations resulting in the activation of oncogenes *MYC, BCL2,* or *CCND1* in B-cell lymphoma[34-36] or rearrangements in medulloblastoma.[37] Subtype-specific 3D genomic alterations were recently discovered in AML leading to enhancer-promoter or enhancer-silencer loops.[38] We demonstrated that the t(7;12)(q36;p13) translocation results in a neo-TAD, in which the *MNX1* promoter is able to interact with the *ETV6* region.

Initial evidence for an oncogenic role of *MNX1* in leukemogenesis comes from a study by Nagel et al characterizing the *MNX1*-overexpressing cell line GDM-1.[20] Knockdown of *MNX1* led to a reduction of cell viability and cell adhesion. In vitro overexpression of *MNX1* in HT1080 and NIH3T3 cells leads to premature, oncogene-induced senescence mediated by the induction of p53 signaling.[39] In vivo, ectopic *MNX1* expression in murine HSPCs resulted in strong differentiation arrest and accumulation at the megakaryocyte/erythrocyte progenitor stage.[39] Overall, this phenotype is in line with reports on t(7;12)(q36;p13) AML blast cells that are less differentiated (French-American-British subtype M0 or M2) and demonstrate expression of the stem cell markers CD34 and CD117.[5,40] Waraky et al used retroviral transduction of *MNX1*-expressing constructs into murine fetal HSPCs and were able to induce AML.[33] A possible link to leukemogenesis was described with the observation that *MNX1* activation resulted in reduced H3K4me1/2/3 and H3K27me3 levels providing increased chromatin accessibility.[33]

Our study challenges the concept in AML that all reciprocal translocations lead to oncofusion proteins as an overestimated molecular mechanism in AML for gene activation. Future studies unraveling the molecular defects of t(7;12)(q36;p13) AML should focus on the targets of homeobox transcription factor *MNX1* rather than the oncofusion, as already initiated in some reports.[21,30,39] Furthermore, copy number alterations of genes such as *DNA methyltransferase 1* (*DNMT1*) or *RNA polymerase II transcriptional elongation factor* (*ELL*) on chr19, coupregulation of genes such as *EDIL3* and *LIN28B*, or haploinsufficiency of *ETV6* might contribute to the leukemogenic process. ETV6 is a strong transcriptional repressor, and haploinsufficiency could result in reactivation of its target genes.[41] Moreover, the study of a potential therapeutic benefit by epigenetic drug treatment targeting *MNX1* promoter-*ETV6* enhancer interaction in the ChiPSC22^(t(7;12)) iPSC/HSPC model is warranted.

We recognize that this study has several limitations that could be overcome in future studies. Due to the rarity of the disease and the limitations in obtaining primary leukemic samples, multiple (epi) genomic studies on a single patient sample are currently not possible but may become possible with improved biobanking, international collaboration, and the development of low-input profiling assays. A step in this direction is the survival analysis in pediatric AML by the NOPHO-AML.[4] Another limitation is the

mapping of responsible enhancers in the 213 kb ETV6 region, including at least 4 potential hematopoietic enhancers that could drive *MNX1* expression. Individual enhancer knockout experiments will determine whether a single enhancer or multiple enhancers are required to activate *MNX1*.

Acknowledgments

Authorship

Contribution: Y.L.B., G.G., B.S., D.R., and L.B. provided the clinical specimens; A.R., A.T., M.B., A.Ö., T.N., S.J., M.E., A.W., A.D., C.S., H.H., and H.L. performed the experimental procedures; E.S., U.H.T., J.H., J.A.W., K.B., J.A.W., P.L., and D.W. performed the bioinformatics and statistical analyses; E.S. was responsible for the sequence data upload to the public databases; D.B.L., L.P., D.W., and C.P. designed the study and supervised the experimental and bioinformatics work; D.W., A.R., E.S., and C.P. wrote the paper; and all authors provided feedback on the report.

Conflict-of-interest disclosure: L.B. has received honoraria from AbbVie, Amgen, Astellas, Bristol Myers Squibb, Celgene, Daiichi Sankyo, Gilead, Hexal, Janssen, Jazz Pharmaceuticals, Menarini, Novartis, Pfizer, Roche, and Sanofi; and research support from Bayer and Jazz Pharmaceuticals. D.B.L. receives honoraria from Infectopharm GmbH. The remaining authors declare no competing financial interests.

ORCID profiles: D.W., 0000-0002-7915-412X; A.R., 0000-0002-0626-3894; E.S., 0000-0002-3612-8562; U.H.T., 0009-0009-6923-6816; J.H., 0000-0003-2842-764X; K.B., 0000-0003-3716-7739; P.L., 0000-0001-9383-8555; A.W., 0000-0003-4635-021X; B.S., 0000-0001-5256-1270; C.S., 0000-0003-3590-2103; H.H., 0000-0003-1218-2107; H.L., 0000-0002-5086-6449; D.R., 0000-0002-7027-4483; L.P., 0000-0001-9274-360X; D.B.L., 0000-0001-5081-7869; C.P., 0000-0003-2554-3952.

Correspondence: Christoph Plass, Division of Cancer Epigenomics, German Cancer Research Center, INF 280, 69120 Heidelberg, Germany; email: c.plass@dkfz.de; and Daniel B. Lipka, Section of Translational Cancer Epigenomics, Division of Translational Medical Oncology, German Cancer Research Center, Im Neuenheimer Feld 581, 69120 Heidelberg, Germany; email: d.lipka@dkfz.de.

References

1. de Thé H, Pandolfi PP, Chen Z. Acute promyelocytic leukemia: a paradigm for oncoprotein-targeted cure. *Cancer Cell*. 2017;32(5):552-560.

2. Tosi S, Giudici G, Mosna G, et al. Identification of new partner chromosomes involved in fusions with the ETV6 (TEL) gene in hematologic malignancies. *Genes Chromosomes Cancer*. 1998;21(3):223-229.

3. Wlodarska I, La Starza R, Baens M, et al. Fluorescence in situ hybridization characterization of new translocations involving TEL (ETV6) in a wide spectrum of hematologic malignancies. *Blood*. 1998;91(4):1399-1406.

4. Espersen ADL, Noren-Nyström U, Abrahamsson J, et al. Acute myeloid leukemia (AML) with t(7;12)(q36;p13) is associated with infancy and trisomy 19: data from Nordic Society for Pediatric Hematology and Oncology (NOPHO-AML) and review of the literature. *Genes Chromosomes Cancer*. 2018; 57(7):359-365.

5. von Bergh ARM, van Drunen E, van Wering ER, et al. High incidence of t(7;12)(q36;p13) in infant AML but not in infant ALL, with a dismal outcome and ectopic expression of HLXB9. *Genes Chromosomes Cancer*. 2006;45(8):731-739.

6. Ballabio E, Cantarella CD, Federico C, et al. Ectopic expression of the HLXB9 gene is associated with an altered nuclear position in t(7;12) leukaemias. *Leukemia*. 2009;23(6):1179-1182.

7. Beverloo HB, Panagopoulos I, Isaksson M, et al. Fusion of the homeobox gene HLXB9 and the ETV6 gene in infant acute myeloid leukemias with the t(7; 12)(q36;p13). *Cancer Res*. 2001;61(14):5374-5377.

8. Nilsson T, Waraky A, Östlund A, et al. An induced pluripotent stem cell t(7;12)(q36;p13) acute myeloid leukemia model shows high expression of MNX1 and a block in differentiation of the erythroid and megakaryocytic lineages. *Int J Cancer*. 2022;151(5):770-782.

9. Weichenhan D, Riedel A, Meinen C, et al. Translocation t(6;7) in AML-M4 cell line GDM-1 results in MNX1 activation through enhancer-hijacking. *Leukemia*. 2023;37(5):1147-1150.

10. Gröschel S, Sanders MA, Hoogenboezem R, et al. A single oncogenic enhancer rearrangement causes concomitant EVI1 and GATA2 deregulation in leukemia. *Cell*. 2014;157(2):369-381.

11. Ottema S, Mulet-Lazaro R, Beverloo HB, et al. Atypical 3q26/MECOM rearrangements genocopy inv(3)/t(3;3) in acute myeloid leukemia. *Blood*. 2020; 136(2):224-234.

12. Ottema S, Mulet-Lazaro R, Erpelinck-Verschueren C, et al. The leukemic oncogene EVI1 hijacks a MYC super-enhancer by CTCF-facilitated loops. *Nat Commun*. 2021;12(1):5679.

13. Montefiori LE, Bendig S, Gu Z, et al. Enhancer hijacking drives oncogenic BCL11B expression in lineage-ambiguous stem cell leukemia. *Cancer Discov*. 2021;11(11):2846-2867.

14. Foster I. Globus online: accelerating and democratizing science through cloud-based services. *IEEE Internet Comput*. 2011;15(3):70-73.

15. Ewels PA, Peltzer A, Fillinger S, et al. The nf-core framework for community-curated bioinformatics pipelines. *Nat Biotechnol*. 2020;38(3):276-278.

16. Dobin A, Davis CA, Schlesinger F, et al. STAR: ultrafast universal RNA-seq aligner. *Bioinformatics*. 2013;29(1):15-21.

17. Patro R, Duggal G, Love MI, Irizarry RA, Kingsford C. Salmon provides fast and bias-aware quantification of transcript expression. *Nat Methods*. 2017; 14(4):417-419.

18. McKenna A, Hanna M, Banks E, et al. The Genome Analysis Toolkit: a MapReduce framework for analyzing next-generation DNA sequencing data. *Genome Res*. 2010;20(9):1297-1303.

19. Haas BJ, Dobin A, Li B, Stransky N, Pochet N, Regev A. Accuracy assessment of fusion transcript detection via read-mapping and de novo fusion transcript assembly-based methods. *Genome Biol*. 2019;20(1):213.

20. Nagel S, Kaufmann M, Scherr M, Drexler HG, MacLeod RAF. Activation of HLXB9 by juxtaposition with MYB via formation of t(6;7)(q23;q36) in an AML-M4 cell line (GDM-1). *Genes Chromosomes Cancer*. 2005;42(2):170-178.

21. Thompson N, Gésina E, Scheinert P, Bucher P, Grapin-Botton A. RNA profiling and chromatin immunoprecipitation-sequencing reveal that PTF1a stabilizes pancreas progenitor identity via the control of MNX1/HLXB9 and a network of other transcription factors. *Mol Cell Biol*. 2012;32(6): 1189-1199.

22. Rao SSP, Huntley MH, Durand NC, et al. A 3D map of the human genome at kilobase resolution reveals principles of chromatin looping. *Cell*. 2014; 159(7):1665-1680.

23. Sollier E, Heilmann J, Gerhauser C, Scherer M, Plass C, Lutsik P. Figeno: multi-region genomic figures with long-read support. *Bioinformatics*. 2024; 40(6).

24. Steinek C, Ortiz MG, Stumberger G, et al. Generation of densely labeled oligonucleotides for the detection of small genomic elements. *bioRxiv*. Preprint posted online 15 March 2024. https://doi.org/10.1101/2024.03.15.583980

25. Brandstetter K, Zülske T, Ragoczy T, et al. Differences in nanoscale organization of regulatory active and inactive human chromatin. *Biophys J*. 2022; 121(6):977-990.

26. Bintu B, Mateo LJ, Su J-H, et al. Super-resolution chromatin tracing reveals domains and cooperative interactions in single cells. *Science*. 2018; 362(6413):eaau1783.

27. Wurm CA, Neumann D, Schmidt R, Egner A, Jakobs S. Sample preparation for STED microscopy. *Methods Mol Biol*. 2010;591:185-199.

28. Robinson JT, Thorvaldsdóttir H, Winckler W, et al. Integrative genomics viewer. *Nat Biotechnol*. 2011;29(1):24-26.

29. Bolouri H, Farrar JE, Triche T Jr, et al. The molecular landscape of pediatric acute myeloid leukemia reveals recurrent structural alterations and age-specific mutational interactions. *Nat Med*. 2018;24(1):103-112.

30. Schwaller J. Novel insights into the role of aberrantly expressed MNX1 (HLXB9) in infant acute myeloid leukemia. *Haematologica*. 2019;104(1):1-3.

31. Balgobind BV, Van den Heuvel-Eibrink MM, De Menezes RX, et al. Evaluation of gene expression signatures predictive of cytogenetic and molecular subtypes of pediatric acute myeloid leukemia. *Haematologica*. 2011;96(2):221-230.

32. Tosi S, Hughes J, Scherer SW, et al. Heterogeneity of the 7q36 breakpoints in the t(7;12) involving ETV6 in infant leukemia. *Genes Chromosomes Cancer*. 2003;38(2):191-200.

33. Waraky A, Östlund A, Nilsson T, et al. Aberrant MNX1 expression associated with t(7;12)(q36;p13) pediatric acute myeloid leukemia induces the disease through altering histone methylation. *Haematologica*. 2024;109(3):725-739.

34. Dalla-Favera R, Lombardi L, Pelicci PG, Lanfrancone L, Cesarman E, Neri A. Mechanism of activation and biological role of the c-myc oncogene in B-cell lymphomagenesis. *Ann N Y Acad Sci*. 1987;511:207-218.

35. Duan H, Xiang H, Ma L, Boxer LM. Functional long-range interactions of the IgH 3' enhancers with the bcl-2 promoter region in t(14;18) lymphoma cells. *Oncogene*. 2008;27(53):6720-6728.

36. Ryan RJH, Drier Y, Whitton H, et al. Detection of enhancer-associated rearrangements reveals mechanisms of oncogene dysregulation in B-cell lymphoma. *Cancer Discov*. 2015;5(10):1058-1071.

37. Northcott PA, Lee C, Zichner T, et al. Enhancer hijacking activates GFI1 family oncogenes in medulloblastoma. *Nature*. 2014;511(7510):428-434.

38. Xu J, Song F, Lyu H, et al. Subtype-specific 3D genome alteration in acute myeloid leukaemia. *Nature*. 2022;611(7935):387-398.

39. Ingenhag D, Reister S, Auer F, et al. The homeobox transcription factor HB9 induces senescence and blocks differentiation in hematopoietic stem and progenitor cells. *Haematologica*. 2019;104(1):35-46.

40. Wildenhain S, Ingenhag D, Ruckert C, et al. Homeobox protein HB9 binds to the prostaglandin E receptor 2 promoter and inhibits intracellular cAMP mobilization in leukemic cells. *J Biol Chem*. 2012;287(48):40703-40712.

41. Kodgule R, Goldman JW, Monovich AC, et al. ETV6 deficiency unlocks ERG-dependent microsatellite enhancers to drive aberrant gene activation in B-lymphoblastic leukemia. *Blood Cancer Discov*. 2023;4(1):34-53.

42. Ragusa D, Dijkhuis L, Pina C, Tosi S. Mechanisms associated with t(7;12) acute myeloid leukaemia: from genetics to potential treatment targets. *Biosci Rep*. 2023;43(1).

4.3 NANOSCALE ORGANIZATION OF ACTIVE AND INACTIVE CHROMATIN

Brandstetter, K., Zülske, T., Ragoczy, T., Hörl, D., Guirao-Ortiz, M., **Steinek, C.**, Barnes, T., Stumberger, G., Schwach, J., Haugen, E. and Rynes, E., Korber, P., Stamatoyannopoulos, J.A., Leonhardt, H., Wedemann, G., and Harz, H. (Mar. 2022). *Biophysical Journal* 121, pp. 977-990.
  DOI: 10.1016/j.bpj.2022.02.009

Article

Differences in nanoscale organization of regulatory active and inactive human chromatin

Katharina Brandstetter,[1,7] Tilo Zülske,[2,7] Tobias Ragoczy,[3] David Hörl,[1] Miguel Guirao-Ortiz,[1] Clemens Steinek,[1] Toby Barnes,[4] Gabriela Stumberger,[1] Jonathan Schwach,[1] Eric Haugen,[3] Eric Rynes,[3] Philipp Korber,[4] John A. Stamatoyannopoulos,[3,5,6] Heinrich Leonhardt,[1] Gero Wedemann,[2,*] and Hartmann Harz[1,*]

[1]Human Biology & BioImaging, Faculty of Biology, Ludwig-Maximilians-Universität München, Munich, Germany; [2]Competence Center Bioinformatics, Institute for Applied Computer Science, Hochschule Stralsund, Stralsund, Germany; [3]Altius Institute for Biomedical Sciences, Seattle, Washington; [4]Biomedical Center (BMC), Molecular Biology, Faculty of Medicine, Ludwig-Maximilians-Universität München, Martinsried, Germany; [5]Department of Genome Sciences, University of Washington, Seattle, Washington; and [6]Department of Medicine, Division of Oncology, University of Washington, Seattle, Washington

ABSTRACT   Methodological advances in conformation capture techniques have fundamentally changed our understanding of chromatin architecture. However, the nanoscale organization of chromatin and its cell-to-cell variance are less studied. Analyzing genome-wide data from 733 human cell and tissue samples, we identified 2 prototypical regions that exhibit high or absent hypersensitivity to deoxyribonuclease I, respectively. These regulatory active or inactive regions were examined in the lymphoblast cell line K562 by using high-throughput super-resolution microscopy. In both regions, we systematically measured the physical distance of 2 fluorescence in situ hybridization spots spaced by only 5 kb of DNA. Unexpectedly, the resulting distance distributions range from very compact to almost elongated configurations of more than 200-nm length for both the active and inactive regions. Monte Carlo simulations of a coarse-grained model of these chromatin regions based on published data of nucleosome occupancy in K562 cells were performed to understand the underlying mechanisms. There was no parameter set for the simulation model that can explain the microscopically measured distance distributions. Obviously, the chromatin state given by the strength of internucleosomal interaction, nucleosome occupancy, or amount of histone H1 differs from cell to cell, which results in the observed broad distance distributions. This large variability was not expected, especially in inactive regions. The results for the mechanisms for different distance distributions on this scale are important for understanding the contacts that mediate gene regulation. Microscopic measurements show that the inactive region investigated here is expected to be embedded in a more compact chromatin environment. The simulation results of this region require an increase in the strength of internucleosomal interactions. It may be speculated that the higher density of chromatin is caused by the increased internucleosomal interaction strength.

SIGNIFICANCE   Conformation capture techniques are limited to measuring contact probability. Here, we focused on a complementary aspect by measuring physical distances of loci, with a genomic distance of ∼5 kb in single cells. This range of distances of approximately 100 nm is crucial for mediating the physical contact of transcription factors and other regulatory elements. Microscopy data delivered the complete distance distribution of two prototypic regions with regulatory active and inactive chromatin, respectively. Unexpectedly, we found very broad distributions of distances in both regions. Computer simulations of a coarse-grained model of these regions showed that the variance of the single-cell measurements can be explained only by the combinations of different influencing factors. This emphasizes the large cell-to-cell variance in the processes regulating chromatin compaction even in inactive regions.

INTRODUCTION

For almost 100 years, it has been known that interphase chromatin can be distinguished by means of light microscopy into less dense euchromatin and denser packed heterochromatin (1,2). Later, it became clear that nucleosomes are the basic building blocks organizing DNA packaging and are therefore central to the organization

Brandstetter et al.

of chromatin (3). Groundbreaking electron microscopic studies showed the tight interaction between histones and DNA, forming an 11-nm-thick fiber (4,5). Methodological advances have led to the view that chromatin has a rather irregular, heterogeneous organization (6–8). This view is supported by electron microscopic studies and super-resolution fluorescence microscopy that show interphase chromatin to be organized in a flexible and disordered structure in which regions with higher nucleosome density are interspersed with nucleosome-depleted regions (9–14).

The landscape of chromatin states is much more diverse than the originally described euchromatin and heterochromatin suggest. By analyzing genome-wide distribution patterns of chromatin-associated proteins, posttranslational histone modifications and DNase I hypersensitivity with algorithms such as ChromHMM and Segway, investigators have proposed up to 51 chromatin classes (15–21). DNase I hypersensitivity is a criterion that can also be used alone to subdivide chromatin in regulatory or active DNA with a high number of DNase I hypersensitive sites (DHS) as opposed to inactive regions with a low density of DHS (22,23).

Posttranslational histone modifications of the active chromatin classes, such as acetylation, may reduce nucleosome interaction strength and thus participate, among other mechanisms such as through ATP-dependent remodelers, in producing an open, less densely packed chromatin (24–28). Inactive classes are often characterized by methylation marks on histone 3 (e.g., H3K9me2/3), which can be bound by the heterochromatic protein 1, thereby compacting chromatin (29). However, large parts of inactive and more densely packed chromatin do not carry significant amounts of posttranslational histone modifications (15). Other mechanisms, such as the amount of linker histone H1, must therefore be responsible for the compaction (14).

A remarkable feature of chromatin is its dynamic nature, which has been observed in several fluorescence imaging studies (30–40) and is the reason for the large cell-to-cell variability in the structure of chromatin domains (41). Changes in nucleosome occupancy are actively regulated and can drastically affect the 3-dimensional (3D) genome architecture as it has been shown, for example, by the effects of tumor necrosis factor alpha on human endothelial cells (42). Even at the level of single nucleosomes, a significant and dynamic cell-to-cell variability can be found (43). The recently developed Fiber-seq method reveals that regulatory elements are actuated in an all-or-none fashion, thereby replacing a canonical nucleosome (44). Some ATP-dependent chromatin remodelers, and probably also some pioneer transcription factors, are known to exhibit nucleosome eviction activity (45–47). Together, these examples show that, depending on the regulatory context, the number and exact position of nucleosomes in active chromatin of eukaryotes can dynamically change.

Computational studies show a close link between nucleosome positions and the spatial organization of chromatin

(48), which was explored by applying computer simulations of a coarse-grained model by many groups (e.g., (49–51)). These studies demonstrate, for example, that different nucleosome repeat lengths are responsible for more open or closed chromatin configurations (14,52). Moving even a single nucleosome can strongly influence the spatial organization (53). Thus, including the real length of the different linker DNA into coarse-grained models is required to obtain realistic results (14,53).

In our research, we investigated structural differences between active and inactive 5-kb chromatin segments of prototypical chromatin regions, selected on the basis of the presence or absence of DNase I hypersensitivity, using oligonucleotide-based fluorescence in situ hybridization (oligoFISH). By measuring the distance between labeled endpoints with systematic 3D stimulated emission depletion (STED) microscopy and comparing these data with Monte Carlo simulations of a coarse-grained model (53,54), we aimed to find underlying organizational principles. In active chromatin, simulated data match the microscopic data well, assuming cell-to-cell variability in nucleosomal occupancy. For inactive chromatin, variability of the maximal strength of the internucleosomal interaction and the binding of the linker histone H1 must be assumed to match the width of the distribution. Regardless of whether chromatin is active or inactive, our results reveal two striking features for 5-kb segments: (1) all distance distributions are right-tailed, and simulations indicate an underlying cell-to-cell variance in chromatin organization, and (2) distributions cover a wide range of distances from less than 50 nm to more than 200 nm.

MATERIALS AND METHODS

For a more detailed description of the methods and procedures described in this section, please refer to the supporting material's and methods.

Cell culture

Human erythroleukemia K562 cells (ATCC: CCL243) received from the Stamatoyannopoulos lab were grown in RPMI 1640 medium (Sigma, USA) supplemented with 10% fetal bovine serum (Sigma, USA) and 1% v/v penicillin/streptomycin (Sigma, USA) in cell culture flasks. Cells were cultured at 37°C in a humidified atmosphere containing 5% CO_2 and regularly tested for mycoplasma contamination.

Selection criteria for genomic regions

Universally active and inactive genomic regions were assessed by using the index of consensus DHSs of Meuleman et al. (22) derived from DNase I hypersensitive regions in 733 human biosamples encompassing 438 human cell and tissue types and states. We identified genomic regions with statistically significant enrichments of cleavage activity in DNase-seq experiments by using the program hotspot2 (55). The selected active region (chr11: 119,075,000–119,125,000) is spanned by a diverse set of genes, whereas the inactive region (chr11: 55,810,260–55,840,940) has a minimal number of elements overlapped by RepeatMasker.

Sample preparation and microscopy

Oligonucleotide probes for STED microscopy: We tiled 30 non-overlapping oligonucleotides (40-mers) across each target region (1.5–2 kb), selected for uniqueness and a higher density than afforded by other published design tools optimized for whole-genome coverage or chromosome walking (56–58). Oligonucleotides were labeled with ATTO 594 or ATTO 647N (LGC Biosearch Technologies, USA). A list of all of the oligonucleotides used is provided in Table S1 in the supporting material's and methods. FISH of formaldehyde-fixed K562 cells was carried out as previously published (41) with adaptations.

STED microscopy was carried out on a 3D STED microscope (Abberior Instruments, Germany) equipped with 2 pulsed excitation lasers (594 nm, 0.3 mW and 640 nm, 1.2 mW), 1 pulsed depletion laser (775 nm, 1.2 W), and Avalanche photodiodes for detection. A 100× UPlanSApo 1.4 NA oil immersion objective (Olympus, Japan) was used for all of the acquisitions. Pairs of FISH spots labeled with different dyes were detected in confocal scans, and high-resolution STED detail stacks were acquired only around these points of interest.

Image data analysis

Supervised machine learning was used as a quality control step to automatically classify STED stacks into "good" or "bad." Detailed spot analysis was performed on the analyzable good data to determine the coordinates of both FISH spots in their respective STED channels. The algorithm searched for the spot pair with the brightest signal by using a Laplacian-of-Gaussian blob detector and saved their subpixel coordinates derived from fitting a multidimensional Gaussian using the Levenberg-Marquardt algorithm for further statistical analysis. For measurements with 2D depletion, 3D coordinates were transformed into projected 2D coordinates by omitting the z coordinate.

Coarse-grained modeling

Simulation software: The software was developed in the Wedemann group in the last few decades and used in many studies. It was written in C++ and was adapted for the use of shared-memory parallel architectures according to the OpenMP standard. The replica exchange algorithm was implemented for distributed memory architectures using Message Passing Interface. The software cannot be made public at the moment, since it contains code under copyright by other parties.

Simulation protocol: A Monte Carlo (MC) algorithm was used to create a statistically relevant set of configurations satisfying the Boltzmann distribution (59). To overcome local energy minima (54), we applied a replica exchange procedure introduced by Swendsen and Wang (60). Here, M replicas of the system were simulated with Metropolis MC simultaneously, each at a different temperature, T_i. After a fixed number of MC simulation step replicas with adjacent temperatures (T_i, T_{i+1}), the temperature is swapped with the probability (Eq. 1):

$$\min[1, \exp(-(\beta_i - \beta_{i+1})(E_{i+1} - E_i))], \tag{1}$$

with $\beta_i = 1/(k_B T_i)$, k_B being the Boltzmann constant and E_i the energy (e.g., elastic energies), of the system i. Before the simulations, the set of temperatures was determined using a feedback-optimized approach (61). This algorithm optimizes the distribution of temperatures iteratively, such that the diffusion of replicas from the highest to the lowest temperature and vice versa is improved in each iteration. The procedure is more efficient when starting with a system that is pre-relaxed using a simulated annealing approach (54). Simulation parameters and constants are given in Table S2.

We chose 16–60 replicas, depending on the system. For systems with 4 kT as a maximum value of internucleosomal interaction energy, we computed at least 10×10^6 MC steps and 90×10^6 steps for 6 kT per replica

after simulated annealing. For checking the convergence, we analyzed the end-to-end distance and the energy as parameters. To determine the point when equilibrium was reached, we analyzed visually the plots with the number of steps on a logarithmic scale. Only configurations after that point were used in the analysis. From analysis of the autocorrelation of energy and end-to-end distance, we estimated that configurations are uncorrelated after 10×10^3 steps for systems with 4-kT maximum interaction strength and 20×10^3 steps for 6 kT (see supporting material's and methods). This leads to 1000–2000 uncorrelated configurations. See Table S3 for all of these values of every simulation in the supporting material.

Modeling of 3D configurations: Since atomistic modeling of chains with many nucleosomes is not possible, coarse-grained models are widely used. We applied the simulation procedure as described in Muller et al. and followed the description given there (53). Chromatin is modeled as a chain of segments, in which spherocylindrical units describing the nucleosomes are connected by cylindrical segments describing the linker DNA. Each segment i possesses a position and a local coordinate system consisting of three perpendicular unit vectors ($\hat{u}_i$, $\hat{v}_i$, $\hat{f}_i$) that describe its torsional orientation (Fig. S1). Vector $\hat{u}_i$ is parallel to the direction of the segment (i.e., the vector $\vec{s}_i$ from its position to the position of the next segment). The position of the center of the nucleosome and its orientation is computed from the center of the nucleosome segment by the length d and six angles describing the relative orientation (Fig. S2). Systems without linker histone and with linker histone differ by the set of angles (62). The length of each individual linker DNA was computed from the positions of the nucleosomes in the studied region. The number of base pairs of a linker length is converted to nanometers by a factor of 0.34 nm/bp. Each linker DNA is modeled by at least 2 segments. If the linker length is larger than 20 nm, then the number of segments is calculated by rounding up (linker length/10 nm).

Statistical analysis

A mixture histogram (Fig. 4 H) was calculated by minimizing the squared differences between the bins of a histogram of the microscopically measured FISH spot distances (Fig. 4 A) and a linear combination of the histograms of simulation results with varying nucleosome occupancies (Fig. 4 B–G). Quadratic programming (via the quadprog package in R) was used to find a solution in which the contributions of the individual simulations are non-negative and equal 1.

2D and 3D distance data were cut off at the maximum length of a theoretical beads-on-a-string fiber, since it is very unlikely that genomic regions more elongated than a fully stretched beads-on-a-string fiber are present in the nucleus. To calculate the length of a beads-on-a-string fiber, the following formula was used: genomic length [bp] * 0.34 nm (size of 1 base)/7 (63). For 5-kb genomic distances, the cutoff for measured distances was at 250 nm.

Data availability

All of the data are available through the public Open Science Framework repository: https://doi.org/10.17605/OSF.IO/ZJWXM. Simulation trajectories are in an easily readable XML format (64). Analysis and visualization scripts are available as a directly runnable code ocean capsule: https://codeocean.com/capsule/8421512/tree/v2.

RESULTS

Chromatin organization of active and inactive chromatin was analyzed in K562 cells using systematic super-resolution microscopy of DNA sequences labeled with oligoFISH probes and comparison with simulated 3D chromatin configurations generated by a coarse-grained model. The

Brandstetter et al.
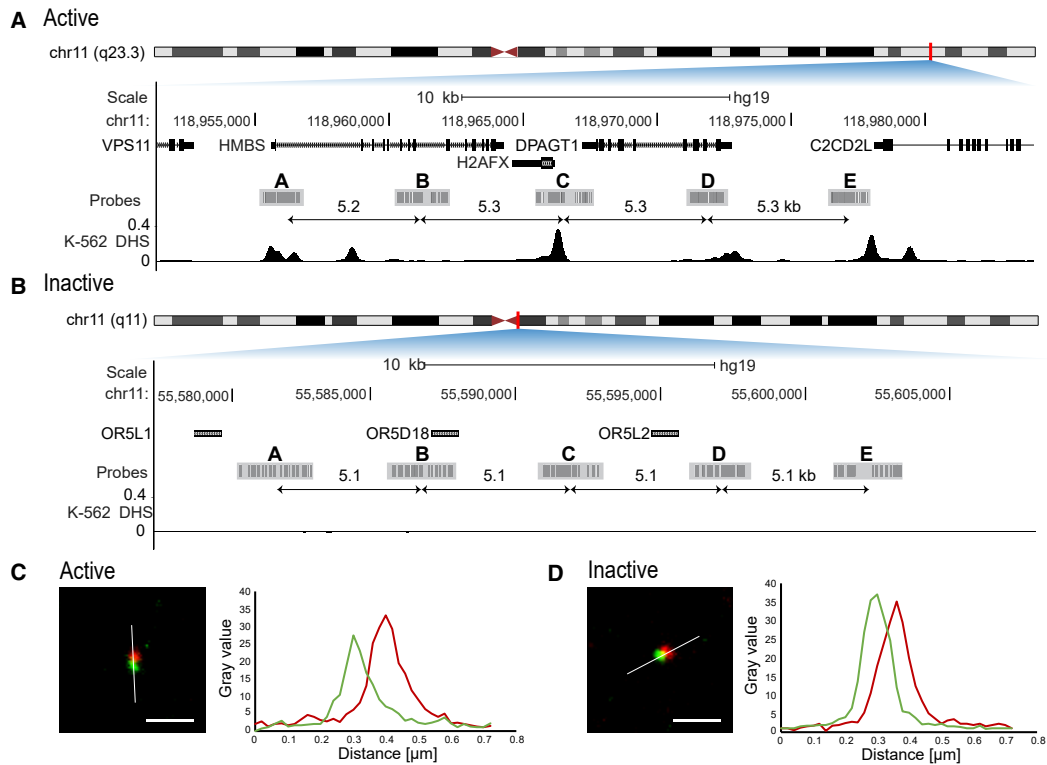
FIGURE 1   FISH probe design for active and inactive region. (*A*) The active region contains the genes *HMBS*, *H2AFX*, and *DPAGT1*. The probe sets are almost equally spaced (5.2, 5.3, 5.3, and 5.3 kb midpoint to midpoint) and mostly cover DHS sites. (*B*) The inactive region contains genes for olfactory receptors. The region shows no DNase I hypersensitivity, and the probe sets are equally spaced (5.1 kb midpoint to midpoint). Modified University of California, Santa Cruz genome browser plot (68); the data for the DNase I track are from GEO: GSM816655. (*C* and *D*) Representative STED detail images of FISH spots in 2 colors for active (*C*) and inactive (*D*) (target 1 in green, target 2 in red). Line plots depict intensity values for both colors along lines of interest (*white lines*). Scale bar, 500 nm. To see this figure in color, go online.

K562 cell line is well suited to computer simulations as a wealth of information such as genome-wide chromatin immunoprecipitation sequencing data, comprehensive maps of posttranslational nucleosome modifications, and nucleosome positioning generated by the ENCODE project are available (21,65).

STED microscopy as a tool to study prototypic chromatin regions on the kilobase scale

By using data from Meuleman et al. (22), we selected a 20-kb region on chromosome 11 (hg19, chr11: 118955404–118977871), which exhibits very high density of DHSs, not only in K562 (Fig. 1 *A*) but also in more than 730 samples from human cells and tissues. Moreover, this region is flanked upstream and downstream by highly active chromatin. For inactive chromatin, the selection criteria were a minimal number of repetitive elements and missing DHS over 30 kb in more than 730 human samples. In K562 cells, the region without DHSs spans over 2 Mb. The selected 20-kb inactive region is also located on chromosome 11 (hg19, chr11: 55580425–55603312) (Fig. 1 *B*).

For each of these 20-kb regions, 5 oligoFISH probe sets (A, B, C, D, E; Fig. 1, *A* and *B*) were designed, dividing the 20 kb into 4 approximately 5-kb-long segments from midpoint to midpoint of the respective probe set (probe set combinations: AB, BC, CD, DE). Each oligoFISH probe set consisted of 30 oligonucleotides (directly fluorescently labeled 40mers) covering a region of approximately 1.5–2 kb (Fig. 1, *A* and *B*). These small genomic distances are expected to result in spatial distances falling below the resolution limit of light microscopy (66), which is more than 200 nm in the x- and y-dimensions and >500 nm in the z dimension (67). Using STED microscopy, we achieved a root mean square precision for the distance measurements between two spots with a different spectral behavior of approximately 7.5 nm in 3D (supporting material's and methods) (Fig. 1, *C* and *D*). By using reconstituted chromatin, we showed that STED microscopy can resolve distances between the ends of chromatin consisting of ~5 kb DNA and up to 25 nucleosomes (Fig. S3). The distances measured microscopically were in the range of a simulated distance distribution of the same system.
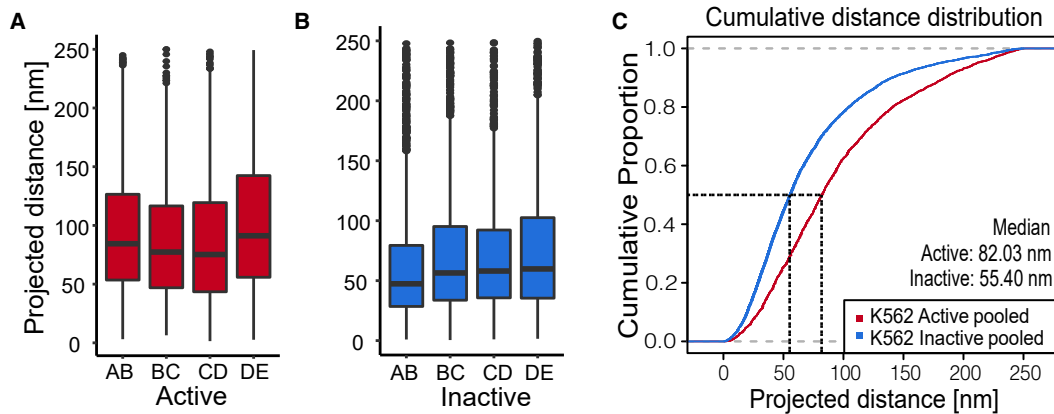
FIGURE 2 2D STED distance measurements showed increased compaction in the inactive region versus the active region. (*A*) Boxplot for the active region for all 4 measured intervals (AB: n = 672, BC: n = 540, CD: n = 484, DE: n = 566; n = number of single-cell measurements pooled from 3 independent replicates). (*B*) Boxplot for the inactive region for all 4 measured intervals (AB: n = 1585, BC: n = 1621, CD: n = 1200, DE: n = 1395; n = single-cell measurements from 3 independent replicates). (*C*) All of the data from active (*A*) and inactive (*B*) regions were pooled to generate a cumulative distribution. The cumulative distribution of measured distances showed differences in distributions between active (*red*) and inactive (*blue*). The median is the value at the 50% proportion (*black dashed line*). For the active region, the median is 82 nm and for the inactive region, it is 55 nm. To see this figure in color, go online.

Inactive regions are more compact than active regions

Recent studies reveal a high cell-to-cell variance of the spatial genome organization (69–71). To study the chosen regions, we applied high-throughput 2D STED microscopy to generate data with high statistical power characterizing the nanoscale organization of 5-kb segments of active and inactive chromatin. For each of the 8 investigated 5-kb segments, between 484 and 1621 single-cell measurements were analyzed. The four measured intervals in the active chromatin region differ from one another. We found some significant deviations, with the maximum difference in the median projected distance of 16 nm (p = 0.00053, BC versus DE and CD versus DE, Wilcoxon rank-sum test) (Fig. 2 *A*; Table S4). In active chromatin, variability of the nanoscale organization is expected since each 5-kb segment is composed of different proportions of exons, introns, enhancers, and other regulatory sequences. Surprisingly, we also found highly significant differences between the investigated intervals in inactive chromatin. We expected much less difference in compaction because inactive chromatin is expected to be more uniform as it does not harbor active regulatory elements and nucleosome occupancy is not modified by transcriptional activity (Figs. 2 *B* and S4). The maximum difference in the median projected distance was 12 nm within the inactive chromatin group (p < 0.0001, AB versus DE, Wilcoxon rank-sum test; Table S4).

However, since the differences within the active and inactive regions are small, they were pooled to show the overall length distribution of each chromatin class. The median projected distance between 2 FISH spots flanking a typical 5-kb interval of active chromatin is 82 nm and 55 nm in inactive chromatin (Fig. 2 *C*). Shorter double spot distances indicate

a higher degree of chromatin compaction, whereas larger distances suggest less compaction. Thus, data from our measurements are in line with published data showing active chromatin to be less compacted compared to inactive chromatin (11). As expected, the distributions of the FISH spot distances of active and inactive chromatin differ significantly as shown in a cumulative distribution plot (Fig. 2 *C*, p < 2 × 10^{-16}, Wilcoxon rank-sum test; Table S4).

For a more in-depth analysis, we selected a 5-kb segment for both the active and inactive regions, which are representative of the respective group in 2D STED measurements. We chose interval AB for the active region and CD for the inactive region (Fig. 2, *A* and *B*). Both regions do not show CCCTC-binding factor (CTCF) binding sites and are therefore not anchors for chromatin loops.

Assigning the input parameters for coarse-grained modeling

The exact position of nucleosomes is an important input parameter for coarse-grained models and strongly affects simulated configurations (14,53). Nucleosomal positioning can be determined by micrococcal nuclease digestion followed by deep sequencing (MNase-seq) (72). Here, we used ENCODE MNase-seq tracks of K562 cells, which are derived from cell populations and therefore often show a seemingly overlapping nucleosome pattern (University of California, Santa Cruz accession: wgEncodeEH000921, GEO accession: GSM920557). These data are unsuitable for our coarse-grained model, as it requires non-overlapping unique nucleosome positions as input. Therefore, we computed the most probable non-overlapping nucleosome populations by applying the NucPosSimulator (73).

Brandstetter et al.
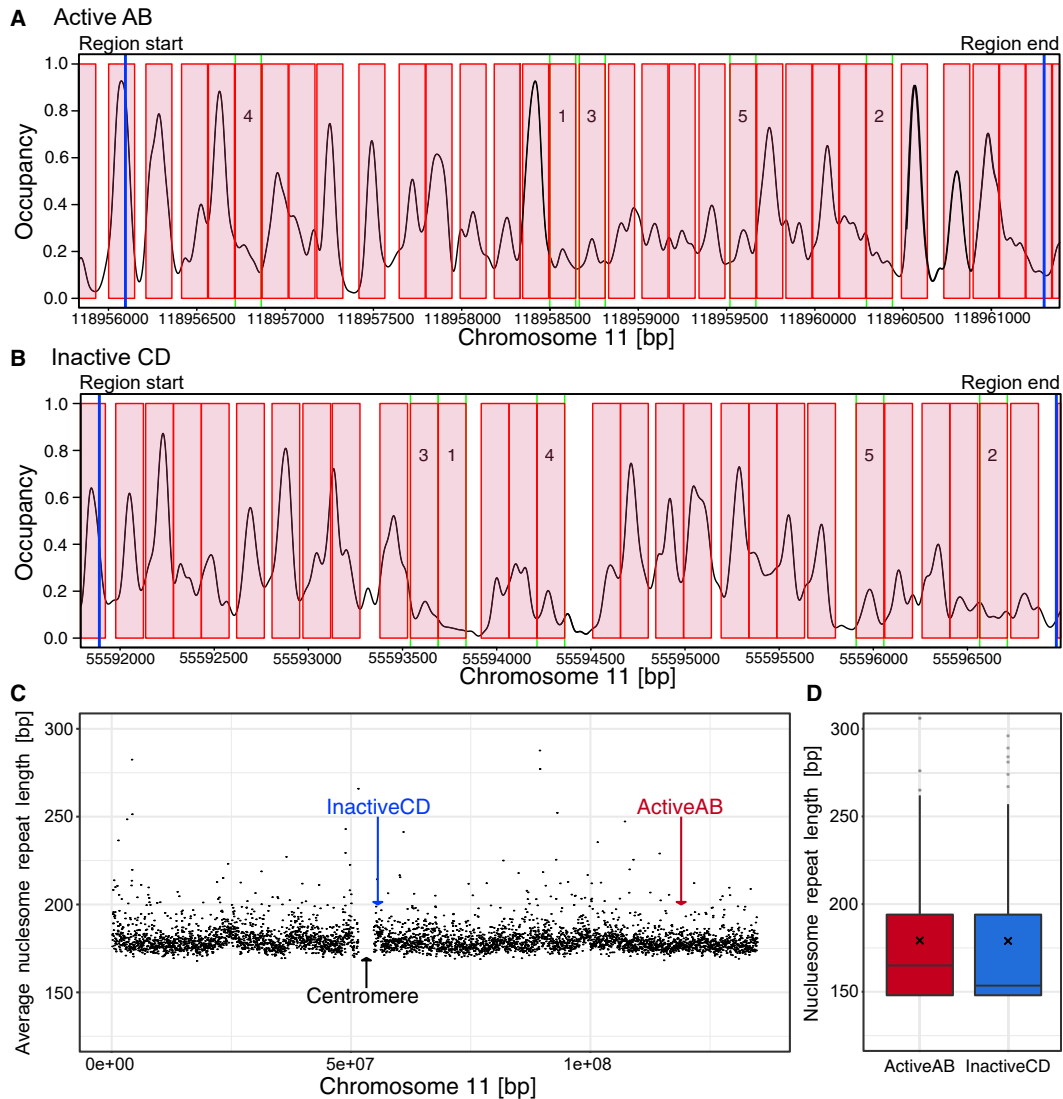
FIGURE 3   Nucleosome positions and nucleosome repeat lengths were calculated using the NucPosSimulator. Nucleosome positions (*red boxes*) for active AB (*A*) and inactive CD (*B*) were based on MNase-seq occupancy tracks (*black line*). The blue lines indicate the start and end of the investigated region. Numbers in boxes indicate the ranking of the 5 nucleosomes with the lowest nucleosome occupancy signal. (*C*) The mean values of the NRL of a sliding window of 30,000 bp. Values larger than 300 and windows with fewer than 3 nucleosomes were omitted. The mean NRL for chromosome 11 was 183.4 ± 66.3 bp. (*D*) Investigated active and inactive regions as marked in the plot (*arrows in C*) have a mean of 179.6 and 179.1 bp, respectively (black x). To see this figure in color, go online.

Experimentally derived nucleosome occupancy and the computed most probable nucleosome positions of active region AB and inactive region CD are shown in Fig. 3, *A* and *B*. Nucleosome positions of the respective flanking regions can be found in Fig. S4. We identified 28 nucleosomes in the active region and 29 nucleosomes in the inactive region. The flanking regions contain approximately 110 nucleosomes on each side. A list of the lengths of all linker DNA can be found in the Open Science Framework repository. For the nucleosomal repeat length (NRL) of chromosome 11, we calculated a mean value of 183.4

± 66.3 bp applying NucPosSimulator (Fig. 3 *C*) (for calculation details, see the Materials and methods section). The mean NRL of the active (AB) and inactive (CD) region studied in detail is 179.6 and 179.1 bp, respectively (Fig. 3 *D*). Both values are in the range of the NRL of chromosome 11. To cross-check the effects of possible inaccuracies in the positions of the nucleosomes, additionally we determined the nucleosome positions for both regions and flanking regions from lymphoblastoid cell lines (74) and used them for control simulations.

The strength of the internucleosomal energy is another important parameter in all coarse-grained models and depends on the solvent (75) and histone modification (71). Literature values for this energy typically range from 3 to 10 kT (71,76,77). Nucleosomes containing unmodified histones have a higher interaction energy, whereas modifications such as acetylation weaken internucleosomal interactions (71). Since the inactive chromatin examined here does not exhibit significant histone modifications (Fig. S4 B), we have used a value from the upper range of the literature values (6 kT) to simulate this chromatin type. Conversely, the active region features many posttranslational histone modifications (Fig. S4 A), and we thus used a lower value (4 kT) to compute the respective configurations.

The nucleosome occupancy varies from cell to cell in active chromatin

The microscopic data shown so far are 2D data, which underestimate the real 3D distances between the FISH spots since the cells are expected to be rotated randomly relative to the optical axis of the microscope. Only 3D single-cell microscopy allows the study of real distances between 2 spots on a single-cell level and to compare data between microscopy and simulation. Therefore, we performed 3D STED measurements, which require careful correction for refractive index mismatch between the immersion fluid of the objective lens and the embedding medium (see supporting material's and methods).

The 3D STED measurements for the 5-kb AB interval in the active chromatin region revealed distances ranging from <50 to 250 nm, with a mean distance of 115 nm (n = 762; Fig. 4 A; data of all other segments Fig. S5; statistical data in Table S5). Remarkably, in active chromatin, elongated configurations can be found, which results in a right-tailed distribution of the microscopic distance measurements. To understand this phenomenon better, we performed coarse-grained computer modeling of the nucleosome chain with the most probable nucleosome positions. We sampled a statistically relevant ensemble of independent 3D configurations in the active region by applying our coarse-grained model, which included elastic and electrostatic properties as well as excluded volume effects. To compare the simulated data with the microscopic data, the distances between the simulated sequence segments that correspond to those of the microscopic measurements were determined. In this way, a distance histogram was generated from the simulated data, which can be directly compared to the microscopic data (Fig. 4, B–G). The computed distribution was narrower, and the mean distance was approximately a standard deviation shorter than the microscopically measured distribution (Fig. 4 B).

We hypothesized that in the cell population used for the microscopy experiment, the number of bound nucleosomes varies from cell to cell. This hypothesis was tested by computer simulations, in which the least probable nucleosomes were removed. To find the nucleosomes with the lowest occupancy signal, we analyzed the mean value from the occupancy data calculated by NucPosSimulator (nucleosomes with lowest occupancy signal are indicated in Figs. 3 A and S4). Next, we computed statistically relevant ensembles of 3D configurations by replacing the nucleosome with the lowest occupancy signal by naked DNA (−1, Fig. 4 C). The same was done by replacing two (Fig. 4 D), three (Fig. 4 E), four (Fig. 4 F), and five (Fig. 4 G) nucleosomes according to the rank order of the nucleosome occupancy signal. In fact, a reduction of the total nucleosome number resulted in increasingly larger mean distances, but none of the individual distributions were comparable with the microscopically measured distribution. By applying a least squares fit, the different distance distributions were combined and resulted in a mixed distance histogram that mimics the microscopic data better than each of the underlying histograms, as indicated by a reduction in the root mean square error (Fig. 4 H) (see Materials and methods). Visualizations of simulated chromatin configurations show that both fibers with all nucleosomes and with a reduced nucleosome number (−5) can have short and long end-to-end distances (Fig. 4, I and J). These configurations show local accumulations of a few nucleosomes connected by stretches with low nucleosome occupancy. These structures are remarkably similar to recently published light and electron microscopic data of interphase chromatin (12,14,78). These results from the models are robust against possible inaccuracies in the nucleosome positions since computer simulations with nucleosome positions derived from lymphoblastoid cell lines deliver nearly identical results (Fig. S6, K and L). Linker histone H1 does not change the distance distributions in this case either (Fig. S6, I and J).

A process that is obviously accompanied by major changes in chromatin structure and in which nucleosomes are also temporarily removed from the chromatin structure is DNA replication in the S phase of the cell cycle. Fluorescence-activated cell sorting of cells with fluorescently labeled DNA was used to generate G1, S, and G2 phase fractions for further analysis (Fig. S7). Microscopically measured distance distributions of G1 and S phase cells resemble the data of the unsorted population.

Inactive region is compacted by various mechanisms

Microscopic data of the inactive region CD show the expected shift of the histogram to shorter distances, indicating more condensed chromatin (Fig. 5 A). Similar to the active chromatin, the histogram of the inactive region also contains large distances that cannot be explained by replicating DNA (Fig. S7). 3D STED distance histograms of the inactive

Brandstetter et al.
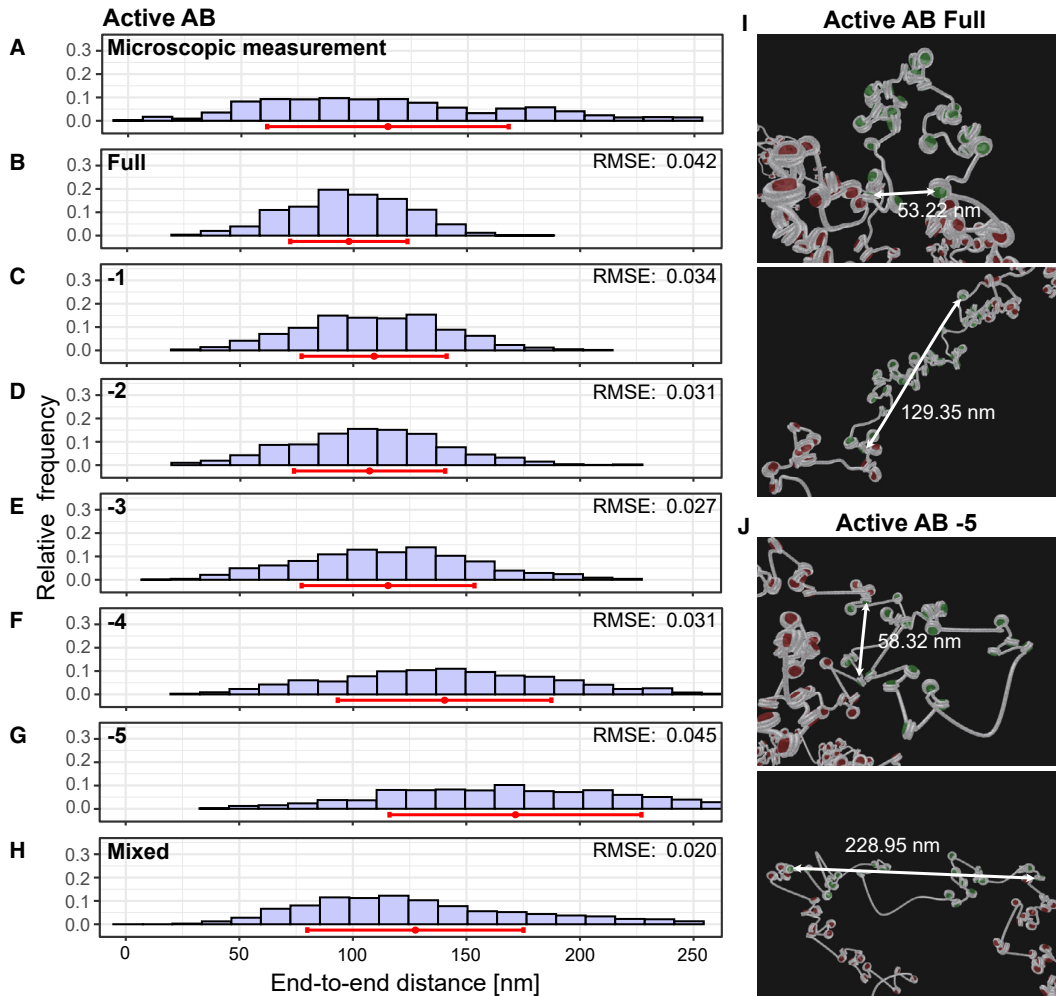
FIGURE 4   Distance distributions from microscopic experiments and from computer simulations of the active region. (*A*) 3D STED measurements of active AB result in a distance distribution ranging from <50 to 250 nm, with a mean of 115 ± 53 nm (n = 762 single-cell measurements from 3 independent replicates). (*B–H*) For computer simulations, results are shown for the region active AB with all nucleosomes (*full*) (*B*), with 1–5 nucleosomes replaced by naked DNA (*C–G*) and a combined plot (*H*). The mean value (*red dot*) and standard deviation (*red line*) are shown for each distribution. In the combined plot (*H*), the distributions have a weight of 0.45, 0.00, 0.00, 0.00, 0.31, and 0.24 (from all nucleosomes to −5 nucleosomes). (*I* and *J*) Example images of simulated chromatin fibers for active region AB (*green nucleosomes*), with all nucleosomes (*I*) and with −5 nucleosomes (*J*) and the adjacent sequences (*red nucleosomes*). The upper image in (*I*) and (*J*) shows a configuration resulting in a short end-to-end distance indicated by a white arrow; the lower image depicts a large end-to-end distance. RMSE, root mean square error of simulated histogram bins in comparison to the measured data. To see this figure in color, go online.

region CD were compared with simulated data by the same strategy as above. The comparison showed that the computed mean distance was ∼40 nm larger than the microscopically measured distance when a maximal attractive internucleosomal energy of 4 kT was used for the simulation (Fig. 5, *A* and *B*). As argued earlier, an increase in the interaction energy to 6 kT seems to be more realistic for simulating inactive chromatin. This approach delivered configurations with the mean value of the simulated distance distribution in the correct range but symmetrical and not skewed to smaller values (Fig. 5 *C*). Obviously, additional

mechanisms compact the inactive chromatin of the investigated region.

Genome-wide data on the level of H3K9me3 (GEO: GSM733776) and H3K27me3 (GEO: GSM733658) histone modifications show in the inactive region CD only background levels, which can be found throughout the genome. Also, repetitive DNA sequences (RepeatMasker) are not enriched. The levels of these markers are significantly lower than in regions known to be compacted by heterochromatinization or by binding the Polycomb group proteins. Therefore, other mechanisms must be considered,
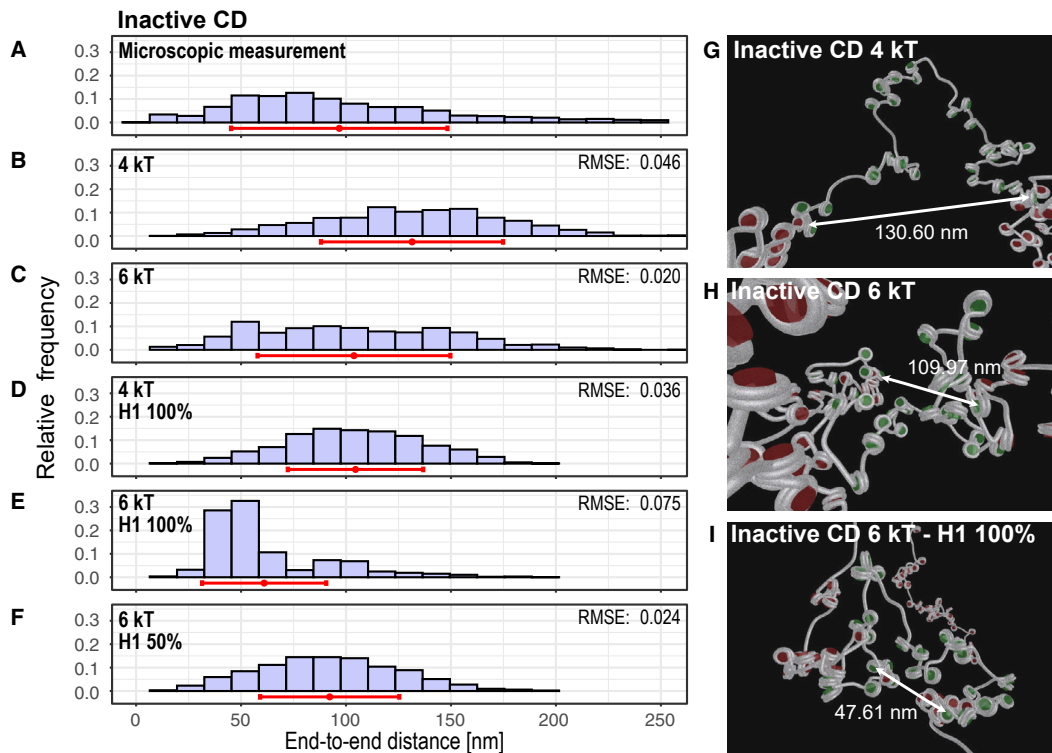
FIGURE 5 Distance distributions from microscopic experiments and from computer simulations of the inactive region. (*A*) 3D STED measurement of inactive CD results in a right-tailed distance distribution, with the mass of the distribution toward shorter distances and a mean of 97 ± 52 nm (n = 1320 single-cell measurements from 3 independent replicates). (*B–F*) Computed distance distributions with different maximal internucleosomal interactions (4 kT [*B, D*] and 6 kT [*C, E, F*]), without (*B, C*) linker histone H1 or with (*D, E*) H1 (100% of nucleosomes occupied), and a random distribution of binding of 50% H1 (*F*). The mean value (*red dot*) and standard deviation (*red line*) are shown for each distribution. (*G–I*) Visualizations of simulated configurations. RMSE, root-mean-square error of simulated histogram bins in comparison to the measured data. To see this figure in color, go online.

such as the binding of linker histone 1 (H1), which has long been known to have a chromatin-compacting effect (14,79). H1 is included in the computer model by different angles of the attached linker DNA at the nucleosomes (52). These angles were derived by a systematic analysis of data from reconstituted fibers (62). It can be expected that details of the angles vary since the chicken linker histone H5, for example, causes different angles than human H1 (62). However, all of the variants of H1 lead to higher chromatin compaction.

In fact, simulations with a stochiometric H1 to nucleosome ratio of 1:1 led to more compact configurations, with a mean value of 27 nm less for 4 kT (Fig. 5 *D*) and 43 nm less for 6 kT (Fig. 5 *E*). To explore the effects of different stoichiometry of H1, we performed computer simulations of a random 50% nucleosome binding (1:2). Here, the compaction is less pronounced, and the mean is approximately 12 nm smaller than without H1 (Fig. 5 *F*). Visualizations of exemplary simulated configurations are shown in Fig. 5, *G–I*.

In summary, similar to the active region the experimental data of the inactive region can only be explained by a cell-

to-cell variability but including a stronger internucleosomal interaction and binding of H1.

DISCUSSION

By using high-throughput super-resolution microscopy, we studied the nanoscale organization of 5-kb chromatin segments that are located in regulatory active and inactive chromatin. The data shown here contain information that differs for fundamental reasons from that of published conformation capture data sets such as Hi-C. While microscopy measures the physical distances between genomic loci, conformation capture methods assess how often direct contacts between genomic elements occur (80). Most conformation capture data sets represent a population average, whereas we provide here statistically robust data on the chromatin configuration in single cells that can be directly compared with data from simulations. The selected areas are prototypic for active and inactive chromatin because patterns of prominent or absent DHSs spread over hundreds of kilobases around the selected region and can be found in more than 730 different human cell and tissue samples. Both regions have an NRL close to the average

Brandstetter et al.

of the entire chromosome, which is another indication that representative regions were selected. For these reasons, we assume that the structural principles described apply to other parts of the genome.

In both active and inactive chromatin, 3D spatial distances between the endpoints of the 5-kb segments differ from cell to cell, resulting in a broad distance distribution, with the mass of the distribution shifted more to shorter values in inactive chromatin. In contrast, simulations with different nucleosome occupancies, changed strength of the internucleosomal energies, or deviations from stoichiometric H1 binding led to far narrower distance distributions. Therefore, the large width of the distance distribution seems to be a feature that is caused by the summation of cell-to-cell differences in the resulting histogram.

Unexpectedly, we found very elongated chromatin configurations with 5-kb exhibiting lengths of over 200 nm in both active and inactive chromatin. For comparison, a stretched beads-on-a-string chromatin fiber of 5 kb has a length of 243 nm (63). Replication cannot account for the majority of these elongated configurations as we have shown by measurements on cells in G1 phase. Replication is a fast process, occurring at ~16 bp/s (81), so the probability of fixing a cell at the moment a 5-kb segment is currently replicated is low. The same is true for other active mechanisms such as loop extrusion by cohesion (82). In simulations with our coarse-grained model, elongated chromatin configurations are more probable if a number of nucleosomes are replaced by naked DNA. Therefore, it is important to investigate which nucleosomes have the weakest occupancy in our model. In fact, 8 of the 10 nucleosomes with the lowest occupancy in the active region are localized within DHSs (Fig. S4 A), a result that is consistent with genome-wide measurements (44).

The perspective of cell-to-cell differences in nucleosome occupancy in active DNA is supported by different lines of evidence: (1) While at certain positions nucleosomes are positioned with high precision (83), nucleosome positions can vary substantially from cell to cell (43,73), (2) pioneer transcription factors and chromatin remodeling complexes can change nucleosome occupancy (84,85), (3) the upregulation of genes is known to reduce the number of bound nucleosomes (42) and increases H2B mobility (14), (4) transcription factors compete cooperatively with nucleosomes for access to DNA (86,87), and (5) regulatory elements are actuated in an all-or-none fashion by the cooperative binding of transcriptional factors in place of a canonical nucleosome (44,88).

For most of the 1600 known transcription factors (89), there are no models to estimate the DNA structure after binding. We simulated regions without nucleosomes as linker DNA with the corresponding elastic and electrostatic properties, since 92% of the transcription factors studied have a DNA footprint between 7 and 30 nt (90), while nucleosomes have a footprint of 146–147 nt and the DNA is $1.65\times$ wrapped around them (5). Therefore, we can neglect bound transcription factors in the model without limiting the conclusions.

As described earlier, the microscopic measurements of inactive chromatin revealed a compaction that can be explained by an increase in the strength of internucleosomal interactions and by the additional introduction of the linker histone H1. Microscopic measurements showed that the inactive region investigated here is expected to be embedded in a more compact chromatin environment (Fig. S8). It can be speculated that this higher density is caused by the increased internucleosomal interaction strength as found in the model. This result is in line with the current discussion of phase separation in the nucleus (91).

Similar to the active regions, microscopic data of the inactive region also show elongated chromatin configurations (>200 nm) in individual cells. In analogy to active chromatin, this could indicate variable nucleosome occupancy in inactive chromatin as well. In fact, the data shown in Fig. 3 B also show weakly bound nucleosomes in this chromatin class, but this does not exclude further mechanisms causing elongated chromatin configurations. Regardless, the large variation in physical distances between spots with a genomic distance of 5 kb from cell to cell suggests that inactive chromatin is also subject to continuous reorganization.

In each computer simulation, a system has a certain number of nucleosomes, amount of bound H1, and internucleosomal interaction strength. It can be expected that *in vivo* more variety exists (e.g., in the active region, one or two nucleosome are missing and a varying stoichiometry of linker histone is present). The properties of these systems are expected to be in the range of the already-broad range of different simulated systems presented here.

An extensive body of literature (for a review, see Schoenfelder and Fraser (92)) on chromatin architecture focuses on the formation of chromatin loops, bringing regulatory elements into close contact and thus regulating gene expression. Distances below which an enhancer is thought to activate a promotor range from less than 150 nm (66) to 300 nm (93). Here, we show by high-throughput microscopy of human chromatin that in active regions more than 45% of the 5-kb endpoints approach to less than 100 nm, whereas in inactive chromatin, this is the case in more than 60% of the cells (value derived from data of Figs. 4 A and 5 A). Apparently, thermodynamically driven spontaneous movements can bring regulatory elements into close contact with their promoters that are only a few kilobases distant from one another. Considering that in the human genome, 142,000 enhancer-like elements fall within 2 kb from the nearest transcription start site (21), such spontaneous movements of chromatin could significantly influence gene regulation.

SUPPORTING MATERIAL

Supporting material can be found online at https://doi.org/10.1016/j.bpj.2022.02.009.

AUTHOR CONTRIBUTIONS

This study was conceived and supervised by H.H., G.W., J.A.S., and H.L. K.B. performed all of the microscopic experiments, including sample preparation and STED imaging shown in Figs. 1, 2, 4 A, 5 A, S5, and S8. Work on reconstituted chromatin (Fig. S3) was completed by C.S., who was responsible for the molecular biology; T.B. prepared the salt gradient dialysis chromatin under the supervision of P.K.; D.H., M.G.-O. and C.S. performed the imaging. Cell-cycle measurements (Fig. S7) were performed by M.G.-O. and G.S. (imaging) and J.S. (fluorescence-activated cell sorting). E.R. selected the investigated genomic regions, and E.H. provided the computational tools for the oligo probe design. T.R. designed the oligo probes and supervised the FISH experiments. K.B. analyzed and interpreted the published ENCODE genome browser data, with the assistance of T.R. (Fig. S4). D.H. provided the computational tools for microscope automation and image analysis. T.Z. performed the computational modeling, with input from G.W. T.Z. analyzed the nucleosome position from MNase data, prepared and executed all of the simulations, and analyzed the simulation data as 3D visualizations and histograms (Figs. 3; 4, *B–J*; 5, *B–I*; S1; S2; S3, *D*; and S6, *B–L*). The manuscript was written by H.H. and G.W., with support from all of the authors.

ACKNOWLEDGMENTS

SUPPORTING CITATIONS

References (94–110) appear in the supporting material.

REFERENCES

1. Trojer, P., and D. Reinberg. 2007. Facultative heterochromatin: is there a distinctive molecular signature? *Mol. Cell.* 28:1–13.

2. Heitz, E. 1928. Das heterochromatin der Moose. *Jahrb. Wiss. Bot.* 69:762–818.

3. Kornberg, R. D. 1974. Chromatin structure: a repeating unit of histones and DNA. *Science.* 184:868–871. https://doi.org/10.1126/science.184.4139.868.

4. Olins, A. L., and D. E. Olins. 1974. Spheroid chromatin units (v bodies). *Science.* 183:330–332.

5. Luger, K., A. W. Mader, …, T. J. Richmond. 1997. Crystal structure of the nucleosome core particle at 2.8 A resolution. *Nature.* 389:251–260. https://doi.org/10.1038/38444.

6. Lakadamyali, M., and M. P. Cosma. 2020. Visualizing the genome in high resolution challenges our textbook understanding. *Nat. Methods.* 17:371–379. https://doi.org/10.1038/s41592-020-0758-3.

7. Maeshima, K., S. Ide, and M. Babokhov. 2019. Dynamic chromatin organization without the 30-nm fiber. *Curr. Opin. Cell Biol.* 58:95–104. https://doi.org/10.1016/j.ceb.2019.02.003.

8. Mirny, L. A. 2011. The fractal globule as a model of chromatin architecture in the cell. *Chromosome Res.* 19:37–51. https://doi.org/10.1007/s10577-010-9177-0.

9. Konig, P., M. B. Braunfeld, …, D. A. Agard. 2007. The three-dimensional structure of in vitro reconstituted Xenopus laevis chromosomes by EM tomography. *Chromosoma.* 116:349–372. https://doi.org/10.1007/s00412-007-0101-0.

10. Fussner, E., M. Strauss, …, D. P. Bazett-Jones. 2012. Open and closed domains in the mouse genome are configured as 10-nm chromatin fibres. *EMBO Rep.* 13:992–996. https://doi.org/10.1038/embor.2012.139.

11. Boettiger, A. N., B. Bintu, …, X. Zhuang. 2016. Super-resolution imaging reveals distinct chromatin folding for different epigenetic states. *Nature.* 529:418–422. https://doi.org/10.1038/nature16496.

12. Ou, H. D., S. Phan, …, C. C. O'Shea. 2017. ChromEMT: visualizing 3D chromatin structure and compaction in interphase and mitotic cells. *Science.* 357:eaag0025. https://doi.org/10.1126/science.aag0025.

13. Nir, G., I. Farabella, …, C. T. Wu. 2018. Walking along chromosomes with super-resolution imaging, contact maps, and integrative modeling. *PLoS Genet.* 14:e1007872. https://doi.org/10.1371/journal.pgen.1007872.

14. Gomez-Garcia, P. A., S. Portillo-Ledesma, …, M. Lakadamyali. 2021. Mesoscale modeling and single-nucleosome tracking reveal remodeling of clutch folding and dynamics in stem cell differentiation. *Cell Rep.* 34:108614. https://doi.org/10.1016/j.celrep.2020.108614.

15. Ernst, J., and M. Kellis. 2010. Discovery and characterization of chromatin states for systematic annotation of the human genome. *Nat. Biotechnol.* 28:817–825. https://doi.org/10.1038/nbt.1662.

16. Ernst, J., P. Kheradpour, …, B. E. Bernstein. 2011. Mapping and analysis of chromatin state dynamics in nine human cell types. *Nature.* 473:43–49. https://doi.org/10.1038/nature09906.

17. Filion, G. J., J. G. van Bemmel, …, B. van Steensel. 2010. Systematic protein location mapping reveals five principal chromatin types in Drosophila cells. *Cell.* 143:212–224. https://doi.org/10.1016/j.cell.2010.09.009.

18. Ram, O., A. Goren, …, B. E. Bernstein. 2011. Combinatorial patterning of chromatin regulators uncovered by genome-wide location analysis in human cells. *Cell.* 147:1628–1639. https://doi.org/10.1016/j.cell.2011.09.057.

19. Hoffman, M. M., O. J. Buske, …, W. S. Noble. 2012. Unsupervised pattern discovery in human chromatin structure through genomic segmentation. *Nat. Methods.* 9:473–476. https://doi.org/10.1038/nmeth.1937.

20. Hoffman, M. M., J. Ernst, …, W. S. Noble. 2013. Integrative annotation of chromatin elements from ENCODE data. *Nucleic Acids Res.* 41:827–841. https://doi.org/10.1093/nar/gks1284.

21. ENCODE Project Consortium, Moore, J. E., …, Z. Weng 2020. Expanded encyclopaedias of DNA elements in the human and mouse genomes. *Nature.* 583:699–710. https://doi.org/10.1038/s41586-020-2493-4.

22. Meuleman, W., A. Muratov, …, J. Stamatoyannopoulos. 2020. Index and biological spectrum of human DNase I hypersensitive sites. *Nature.* 584:244–251. https://doi.org/10.1038/s41586-020-2559-3.

23. Gross, D. S., and W. T. Garrard. 1988. Nuclease hypersensitive sites in chromatin. *Annu. Rev. Biochem.* 57:159–197. https://doi.org/10.1146/annurev.bi.57.070188.001111.

24. Gorisch, S. M., M. Wachsmuth, …, K. Rippe. 2005. Histone acetylation increases chromatin accessibility. *J. Cell Sci.* 118 (Pt 24):5825–5834. https://doi.org/10.1242/jcs.02689.

25. Moller, J., J. Lequieu, and J. J. de Pablo. 2019. The free energy landscape of internucleosome interactions and its relation to chromatin fiber structure. *ACS Cent. Sci.* 5:341–348. https://doi.org/10.1021/acscentsci.8b00836.

26. Nozaki, T., R. Imai, …, K. Maeshima. 2017. Dynamic organization of chromatin domains revealed by super-resolution live-cell imaging.

Brandstetter et al.

Mol. Cell. 67:282–293 e287. https://doi.org/10.1016/j.molcel.2017.06.018.

27. Zhang, R., J. Erler, and J. Langowski. 2017. Histone acetylation regulates chromatin accessibility: role of H4K16 in inter-nucleosome interaction. *Biophys. J.* 112:450–459. https://doi.org/10.1016/j.bpj.2016.11.015.

28. Otterstrom, J., A. Castells-Garcia, …, M. Lakadamyali. 2019. Super-resolution microscopy reveals how histone tail acetylation affects DNA compaction within nucleosomes in vivo. *Nucleic Acids Res.* 47:8470–8484.

29. Allshire, R. C., and H. D. Madhani. 2018. Ten principles of heterochromatin formation and function. *Nat. Rev. Mol. Cell Biol.* 19:229–244. https://doi.org/10.1038/nrm.2017.119.

30. Heun, P., T. Laroche, …, S. M. Gasser. 2001. Chromosome dynamics in the yeast interphase nucleus. *Science.* 294:2181–2186. https://doi.org/10.1126/science.1065366.

31. Marshall, W. F., A. Straight, …, J. W. Sedat. 1997. Interphase chromosomes undergo constrained diffusional motion in living cells. *Curr. Biol.* 7:930–939. https://doi.org/10.1016/s0960-9822(06)00412-x.

32. Levi, V., Q. Ruan, …, E. Gratton. 2005. Chromatin dynamics in interphase cells revealed by tracking in a two-photon excitation microscope. *Biophys. J.* 89:4275–4285. https://doi.org/10.1529/biophysj.105.066670.

33. Hajjoul, H., J. Mathon, …, A. Bancaud. 2013. High-throughput chromatin motion tracking in living yeast reveals the flexibility of the fiber throughout the genome. *Genome Res.* 23:1829–1838. https://doi.org/10.1101/gr.157008.113.

34. Lucas, J. S., Y. Zhang, …, C. Murre. 2014. 3D trajectories adopted by coding and regulatory DNA elements: first-passage times for genomic interactions. *Cell.* 158:339–352. https://doi.org/10.1016/j.cell.2014.05.036.

35. Germier, T., S. Kocanova, …, K. Bystricky. 2017. Real-time imaging of a single gene reveals transcription-initiated local confinement. *Biophys. J.* 113:1383–1394. https://doi.org/10.1016/j.bpj.2017.08.014.

36. Chen, B., L. A. Gilbert, …, B. Huang. 2013. Dynamic imaging of genomic loci in living human cells by an optimized CRISPR/Cas system. *Cell.* 155:1479–1491. https://doi.org/10.1016/j.cell.2013.12.001.

37. Gu, B., T. Swigut, …, J. Wysocka. 2018. Transcription-coupled changes in nuclear mobility of mammalian cis-regulatory elements. *Science.* 359:1050–1055. https://doi.org/10.1126/science.aao3136.

38. Ma, H., L. C. Tu, …, T. Pederson. 2019. Cell cycle- and genomic distance-dependent dynamics of a discrete chromosomal region. *J. Cell Biol.* 218:1467–1477. https://doi.org/10.1083/jcb.201807162.

39. Shaban, H. A., R. Barth, and K. Bystricky. 2018. Formation of correlated chromatin domains at nanoscale dynamic resolution during transcription. *Nucleic Acids Res.* 46:e77.

40. Zidovska, A., D. A. Weitz, and T. J. Mitchison. 2013. Micron-scale coherence in interphase chromatin dynamics. *Proc. Natl. Acad. Sci. U S A.* 110:15555–15560. https://doi.org/10.1073/pnas.1220313110.

41. Bintu, B., L. J. Mateo, …, X. Zhuang. 2018. Super-resolution chromatin tracing reveals domains and cooperative interactions in single cells. *Science.* 362:eaau1783. https://doi.org/10.1126/science.aau1783.

42. Diermeier, S., P. Kolovos, …, R. Merkl. 2014. TNFα signalling primes chromatin for NF-κB binding and induces rapid and widespread nucleosome repositioning. *Genome Biol.* 15:536.

43. Lai, B., W. Gao, …, K. Zhao. 2018. Principles of nucleosome organization revealed by single-cell micrococcal nuclease sequencing. *Nature.* 562:281–285.

44. Stergachis, A. B., B. M. Debo, …, J. A. Stamatoyannopoulos. 2020. Single-molecule regulatory architectures captured by chromatin fiber sequencing. *Science.* 368:1449–1454. https://doi.org/10.1126/science.aaz1646.

45. Becker, P. B., and J. L. Workman. 2013. Nucleosome remodeling and epigenetics. *Cold Spring Harb Perspect. Biol.* 5:a017905. https://doi.org/10.1101/cshperspect.a017905.

46. Hargreaves, D. C., and G. R. Crabtree. 2011. ATP-dependent chromatin remodeling: genetics, genomics and mechanisms. *Cell Res.* 21:396–420. https://doi.org/10.1038/cr.2011.32.

47. Dultz, E., R. Mancini, …, K. Weis. 2018. Quantitative imaging of chromatin decompaction in living cells. *Mol. Biol. Cell.* 29:1763–1777. https://doi.org/10.1091/mbc.E17-11-0648.

48. Parmar, J. J., and R. Padinhateeri. 2020. Nucleosome positioning and chromatin organization. *Curr. Opin. Struct. Biol.* 64:111–118. https://doi.org/10.1016/j.sbi.2020.06.021.

49. Collepardo-Guevara, R., and T. Schlick. 2014. Chromatin fiber polymorphism triggered by variations of DNA linker lengths. *Proc. Natl. Acad. Sci. U S A.* 111:8061–8066. https://doi.org/10.1073/pnas.1315872111.

50. Clauvelin, N., P. Lo, …, W. K. Olson. 2015. Nucleosome positioning and composition modulate in silico chromatin flexibility. *J. Phys. Condens Matter.* 27:064112. https://doi.org/10.1088/0953-8984/27/6/064112.

51. Nordenskiöld, L., A. P. Lyubartsev, and N. Korolev. 2017. Coarse-grained Modeling of Nucleosomes and Chromatin. CRC Press, pp. 297–340.

52. Kepper, N., D. Foethke, …, K. Rippe. 2008. Nucleosome geometry and internucleosomal interactions control the chromatin fiber conformation. *Biophys. J.* 95:3692–3705. https://doi.org/10.1529/biophysj.107.121079.

53. Muller, O., N. Kepper, …, G. Wedemann. 2014. Changing chromatin fiber conformation by nucleosome repositioning. *Biophys. J.* 107:2141–2150. https://doi.org/10.1016/j.bpj.2014.09.026.

54. Stehr, R., N. Kepper, …, G. Wedemann. 2008. The effect of internucleosomal interaction on folding of the chromatin fiber. *Biophys. J.* 95:3677–3691. https://doi.org/10.1529/biophysj.107.120543.

55. John, S., P. J. Sabo, …, J. A. Stamatoyannopoulos. 2011. Chromatin accessibility pre-determines glucocorticoid receptor binding patterns. *Nat. Genet.* 43:264–268. https://doi.org/10.1038/ng.759.

56. Beliveau, B. J., J. Y. Kishi, …, P. Yin. 2018. OligoMiner provides a rapid, flexible environment for the design of genome-scale oligonucleotide in situ hybridization probes. *Proc. Natl. Acad. Sci. U S A.* 115:E2183–E2192. https://doi.org/10.1073/pnas.1714530115.

57. Gelali, E., G. Girelli, …, M. Bienko. 2019. iFISH is a publically available resource enabling versatile DNA FISH to study genome architecture. *Nat. Commun.* 10:1636. https://doi.org/10.1038/s41467-019-09616-w.

58. Beliveau, B. J., E. F. Joyce, …, C. T. Wu. 2012. Versatile design and synthesis platform for visualizing genomes with Oligopaint FISH probes. *Proc. Natl. Acad. Sci. U S A.* 109:21301–21306. https://doi.org/10.1073/pnas.1213818110.

59. Metropolis, N., A. W. Rosenbluth, …, E. Teller. 1953. Equation of state calculations by fast computing machines. *J. Chem. Phys.* 21:1087–1092.

60. Swendsen, R. H., and J. S. Wang. 1986. Replica Monte Carlo simulation of spin glasses. *Phys. Rev. Lett.* 57:2607–2609. https://doi.org/10.1103/PhysRevLett.57.2607.

61. Katzgraber, H. G., S. Trebst, …, M. Troyer. 2006. Feedback-optimized parallel tempering Monte Carlo. *J. Stat. Mech. Theor. Exp.* 2006:P03018.

62. Stehr, R., R. Schopflin, …, G. Wedemann. 2010. Exploring the conformational space of chromatin fibers and their stability by numerical dynamic phase diagrams. *Biophys. J.* 98:1028–1037. https://doi.org/10.1016/j.bpj.2009.11.040.

63. Carlson, R. D., and D. E. Olins. 1976. Chromatin model calculations: arrays of spherical nu bodies. *Nucleic Acids Res.* 3:89–100. https://doi.org/10.1093/nar/3.1.89.

64. Mörl, M.-C., T. Zülske, …, G. Wedemann. 2019. Data formats for modelling the spatial structure of chromatin based on experimental positions of nucleosomes. *AIMS Biophys.* 6:83.

65. Davis, C. A., B. C. Hitz, …, J. M. Cherry. 2018. The Encyclopedia of DNA elements (ENCODE): data portal update. *Nucleic Acids Res.* 46:D794–D801. https://doi.org/10.1093/nar/gkx1081.

66. Mateo, L. J., S. E. Murphy, …, A. N. Boettiger. 2019. Visualizing DNA folding and RNA in embryos at single-cell resolution. *Nature.* 568:49–54. https://doi.org/10.1038/s41586-019-1035-4.

67. Sahl, S. J., S. W. Hell, and S. Jakobs. 2017. Fluorescence nanoscopy in cell biology. *Nat. Rev. Mol. Cell Biol.* 18:685–701. https://doi.org/10.1038/nrm.2017.71.

68. Kent, W. J., C. W. Sugnet, …, D. Haussler. 2002. The human genome browser at UCSC. *Genome Res.* 12:996–1006. https://doi.org/10.1101/gr.229102.

69. Finn, E. H., G. Pegoraro, …, T. Misteli. 2019. Extensive heterogeneity and intrinsic variation in spatial genome organization. *Cell.* 176:1502–1515 e1510. https://doi.org/10.1016/j.cell.2019.01.020.

70. Ashwin, S. S., K. Maeshima, and M. Sasai. 2020. Heterogeneous fluid-like movements of chromatin and their implications to transcription. *Biophys. Rev.* 12:461–468. https://doi.org/10.1007/s12551-020-00675-8.

71. Funke, J. J., P. Ketterer, …, H. Dietz. 2016. Uncovering the forces between nucleosomes using DNA origami. *Sci. Adv.* 2:e1600974.

72. Cui, K., and K. Zhao. 2012. Genome-wide approaches to determining nucleosome occupancy in metazoans using MNase-Seq. *Methods Mol. Biol.* 833:413–419. https://doi.org/10.1007/978-1-61779-477-3_24.

73. Schopflin, R., V. B. Teif, …, G. Wedemann. 2013. Modeling nucleosome position distributions from experimental nucleosome positioning maps. *Bioinformatics.* 29:2380–2386. https://doi.org/10.1093/bioinformatics/btt404.

74. Gaffney, D. J., G. McVicker, …, J. K. Pritchard. 2012. Controls of nucleosome positioning in the human genome. *PLoS Genet.* 8:e1003036. https://doi.org/10.1371/journal.pgen.1003036.

75. Mangenot, S., A. Leforestier, …, F. Livolant. 2002. Salt-induced conformation and interaction changes of nucleosome core particles. *Biophys. J.* 82 (1 Pt 1):345–356. https://doi.org/10.1016/S0006-3495(02)75399-X.

76. Kepper, N., R. Ettig, …, K. Rippe. 2011. Force spectroscopy of chromatin fibers: extracting energetics and structural information from Monte Carlo simulations. *Biopolymers.* 95:435–447. https://doi.org/10.1002/bip.21598.

77. Norouzi, D., and V. B. Zhurkin. 2018. Dynamics of chromatin fibers: comparison of Monte Carlo simulations with force spectroscopy. *Biophys. J.* 115:1644–1655. https://doi.org/10.1016/j.bpj.2018.06.032.

78. Ricci, M. A., C. Manzo, …, M. P. Cosma. 2015. Chromatin fibers are formed by heterogeneous groups of nucleosomes in vivo. *Cell.* 160:1145–1158. https://doi.org/10.1016/j.cell.2015.01.054.

79. Van Holde, K. E. 1989. Chromatin. Springer Science & Business Media, Heidelberg.

80. Fudenberg, G., and M. Imakaev. 2017. FISH-ing for captured contacts: towards reconciling FISH and 3C. *Nat. Methods.* 14:673–678. https://doi.org/10.1038/nmeth.4329.

81. Maya-Mendoza, A., P. Moudry, …, J. Bartek. 2018. High speed of fork progression induces DNA replication stress and genomic instability. *Nature.* 559:279–284. https://doi.org/10.1038/s41586-018-0261-5.

82. Davidson, I. F., B. Bauer, …, J. M. Peters. 2019. DNA loop extrusion by human cohesin. *Science.* 366:1338–1345. https://doi.org/10.1126/science.aaz3418.

83. Baldi, S., P. Korber, and P. B. Becker. 2020. Beads on a string-nucleosome array arrangements and folding of the chromatin fiber. *Nat. Struct. Mol. Biol.* 27:109–118. https://doi.org/10.1038/s41594-019-0368-x.

84. Zaret, K. S. 2020. Pioneer transcription factors initiating gene network changes. *Annu. Rev. Genet.* 54:367–385. https://doi.org/10.1146/annurev-genet-030220-015007.

85. Bartholomew, B. 2014. Regulating the chromatin landscape: structural and mechanistic perspectives. *Annu. Rev. Biochem.* 83:671–696. https://doi.org/10.1146/annurev-biochem-051810-093157.

86. Svaren, J., E. Klebanow, …, R. Chalkley. 1994. Analysis of the competition between nucleosome formation and transcription factor binding. *J. Biol. Chem.* 269:9335–9344.

87. Mirny, L. A. 2010. Nucleosome-mediated cooperativity between transcription factors. *Proc. Natl. Acad. Sci. U S A.* 107:22534–22539.

88. Thurman, R. E., E. Rynes, …, J. A. Stamatoyannopoulos. 2012. The accessible chromatin landscape of the human genome. *Nature.* 489:75–82. https://doi.org/10.1038/nature11232.

89. Lambert, S. A., A. Jolma, …, M. T. Weirauch. 2018. The human transcription factors. *Cell.* 172:650–665. https://doi.org/10.1016/j.cell.2018.01.029.

90. Vierstra, J., J. Lazar, …, J. A. Stamatoyannopoulos. 2020. Global reference mapping of human transcription factor footprints. *Nature.* 583:729–736. https://doi.org/10.1038/s41586-020-2528-x.

91. Rippe, K. 2021. Liquid-Liquid phase separation in chromatin. *Cold Spring Harb Perspect. Biol.* 14:a040683. https://doi.org/10.1101/cshperspect.a040683.

92. Schoenfelder, S., and P. Fraser. 2019. Long-range enhancer-promoter contacts in gene expression control. *Nat. Rev. Genet.* 20:437–455. https://doi.org/10.1038/s41576-019-0128-0.

93. Chen, H., M. Levo, …, T. Gregor. 2018. Dynamic interplay between enhancer–promoter topology and gene activity. *Nat. Genet.* 50:1296–1303.

94. Wurm, C. A., D. Neumann, …, S. Jakobs. 2010. Sample preparation for STED microscopy. *In* Live Cell Imaging. Springer, pp. 185–199.

95. Markaki, Y., D. Smeets, …, M. Cremer. 2012. The potential of 3D-FISH and super-resolution structured illumination microscopy for studies of 3D nuclear architecture: 3D structured illumination microscopy of defined chromosomal structures visualized by 3D (immuno)-FISH opens new perspectives for studies of nuclear architecture. *Bioessays.* 34:412–426. https://doi.org/10.1002/bies.201100176.

96. Solovei, I., A. Cavallo, …, T. Cremer. 2002. Spatial preservation of nuclear chromatin architecture during three-dimensional fluorescence in situ hybridization (3D-FISH). *Exp. Cell Res.* 276:10–23. https://doi.org/10.1006/excr.2002.5513.

97. Branco, M. R., and A. Pombo. 2006. Intermingling of chromosome territories in interphase suggests role in translocations and transcription-dependent associations. *PLoS Biol.* 4:e138. https://doi.org/10.1371/journal.pbio.0040138.

98. Göttfert, F., C. A. Wurm, …, S. W. Hell. 2013. Coaligned dual-channel STED nanoscopy and molecular diffusion analysis at 20 nm resolution. *Biophysical J.* 105:L01–L03.

99. Esa, A., P. Edelmann, …, C. Cremer. 2000. Three-dimensional spectral precision distance microscopy of chromatin nanostructures after triple-colour DNA labelling: a study of the BCR region on chromosome 22 and the Philadelphia chromosome. *J. Microsc.* 199 (Pt 2):96–105. https://doi.org/10.1046/j.1365-2818.2000.00707.x.

100. Lieleg, C., P. Ketterer, …, P. Korber. 2015. Nucleosome spacing generated by ISWI and CHD1 remodelers is constant regardless of nucleosome density. *Mol. Cell Biol.* 35:1588–1605. https://doi.org/10.1128/MCB.01070-14.

101. Oberbeckmann, E., N. Krietenstein, …, S. Eustermann. 2021. Genome information processing by the INO80 chromatin remodeler positions nucleosomes. *Nat. Commun.* 12:3231. https://doi.org/10.1038/s41467-021-23016-z.

102. Van Rossum, G., and F. L. Drake. 2009. Python 3 Reference Manual. Create Space, Scotts Valley, CA.

103. Klenin, K., H. Merlitz, and J. Langowski. 1998. A Brownian dynamics program for the simulation of linear and circular DNA and

Brandstetter et al.

other wormlike chain polyelectrolytes. *Biophys. J.* 74:780–788. https://doi.org/10.1016/S0006-3495(98)74003-2.

104. Zewdie, H. 1998. Computer simulation studies of liquid crystals: a new Corner potential for cylindrically symmetric particles. *J. Chem. Phys.* 108:2117–2133.

105. Hess, B., C. Kutzner, …, E. Lindahl. 2008. GROMACS 4: algorithms for highly efficient, load-balanced, and scalable molecular simulation. *J. Chem. Theory Comput.* 4:435–447. https://doi.org/10.1021/ct700301q.

106. Levin, Y. 2002. Electrostatic correlations: from plasma to biology. *Rep. Prog. Phys.* 65:1577.

107. Walker, D. A., B. Kowalczyk, …, B. A. Grzybowski. 2011. Electrostatics at the nanoscale. *Nanoscale.* 3:1316–1344. https://doi.org/10.1039/c0nr00698j.

108. Maffeo, C., R. Schopflin, …, R. Seidel. 2010. DNA-DNA interactions in tight supercoils are described by a small effective charge density. *Phys. Rev. Lett.* 105:158101. https://doi.org/10.1103/PhysRevLett.105.158101.

109. RStudioTeam. 2020. RStudio: Integrated Development for R. RStudio, PBC.

110. Rippe, K., R. Stehr, and G. Wedemann. 2012. Monte Carlo simulations of nucleosome chains to identify factors that control DNA compaction and access. *Rsc Biomol. Sci.* 198–235. https://doi.org/10.1039/9781849735056-00198.

DISCUSSION

5.1 TOWARDS SUB-KILOBASE IMAGING OF THE GENOME

Recent advances in sample preparation, bioinformatics analysis, and data processing have enabled the development of high-throughput sequencing- and imaging-based techniques that probe complex DNA-DNA interaction patterns in the genome. However, the detection of sub-kilobase genomic targets, such as regulatory elements, in single cells remains challenging. Current 3C-based methods can identify genome-wide pairwise chromatin contacts with a resolution down to 1 kilobase but require millions of cells to generate high-quality datasets (Bonev et al., 2017; Rao et al., 2014). Single-cell Hi-C has confirmed variability in large-scale genomic interactions, but the current resolution restricts the investigation of small genomic targets (Flyamer et al., 2017; Nagano et al., 2013; Nagano et al., 2017; Stevens et al., 2017). While live-cell imaging probes the spatiotemporal dynamics between selected genomic regions, experimental preparations often involve laborious genetic perturbations and typically allow for the visualization of only a few targets (Amiad-Pavlov et al., 2021; Gabriele et al., 2022; Nozaki et al., 2017).

We aimed to develop FISH-based strategies to probe small genomic elements in the three-dimensional context of the nucleus. Previous approaches often used large FISH probes derived from BACs, YACs, cosmids, or PCR, but the length of these probes limited the minimum target size to several tens of kilobases (Burke et al., 1987; Nath and Johnson, 1998; Shizuya et al., 1992). Oligonucleotide-based FISH probes enable multiplexed imaging of genomic targets, but current state-of-the-art methods are typically limited to probing regions in the range of several kilobases (Bintu et al., 2018; Mateo et al., 2019; Nir et al., 2018). While signal amplification methods increase signal strength through multiple rounds of probe hybridization, DNA accessibility and nonspecific background signals complicate the visualization of sub-kilobase genomic loci (Choi et al., 2014; Dardani et al., 2022; Dirks and Pierce, 2004; Kishi et al., 2019; Lizardi et al., 1998; Rouhanifard et al., 2019; Xie et al., 2018). We focused our efforts on generating densely labeled primary probes (NOVA probes) to amplify FISH signals without the need for multiple hybridization steps.

DNA is typically labeled through the chemical attachment of dyes or the enzymatic incorporation of modified nucleotides. However, covalent conjugation of fluorophores to probes is usually restricted to their 3'-end and does not yield densely labeled probes (Ishizuka et al.,

2016; Kolb et al., 2001; Raddaoui et al., 2020; Raj et al., 2008; Raj and Tyagi, 2010). Therefore, we chose an enzymatic approach to produce probes that carry multiple fluorophores in the genome-binding or in an overhang region. To this end, we screened family A and family B polymerases for their ability to incorporate modified nucleotides into short probes. Family A polymerases, such as Klenow exo-, Taq, or DNA polI, are routinely used in nick translation or random priming to generate large, labeled DNA fragments (Mathew, 1984; Ried et al., 1992). However, our screening showed that engineered family B polymerases (Q5, Phusion, Therminator) are better suited than family A polymerases for creating short, densely labeled probes. This observation is supported by structural data showing that family B polymerases have a larger channel volume and phosphate backbone-mediated protein-DNA interactions, which are less likely to be disturbed by modified nucleotides (Hottin and Marx, 2016; Kropp et al., 2017, 2019; Tasara et al., 2003). Point mutations in the exonuclease domain (D141A, E143A) and the finger domain (A485L) of Therminator DNA polymerase may further enhance the incorporation efficiency of dye-labeled nucleotides, similar to the Klenow exo- mutant (Gardner et al., 2019; Lieu et al., 2005). In our study, we successfully generated ATTO488-, Cy3-, ATTO594-, and ATTO647N-labeled NOVA-probes and expect that Therminator DNA polymerase can also incorporate other dye-labeled nucleotides into probes. We note that chemical and physical properties of dyes, such as lipophilicity, photostability, and fluorescence lifetime, can impact image quality and may render certain dyes unsuitable for detecting small genomic loci (Hughes et al., 2014; Schirripa Spagnolo and Luin, 2022).

Having established a workflow that allows for the flexible incorporation of dye-labeled nucleotides into probes, we generated densely labeled probes but observed that high labeling density reduces signal strength. Through systemic analysis, we found that the observed decrease in signal intensity is caused by distance-dependent dye-dye interactions rather than a reduction in probe binding. Consistent with the characteristics of homo-FRET, these dye-dye interactions diminish as the distance between dye molecules increases (Jun et al., 2020). In the case of ATTO647N, the optimal distance between two dyes was 7 nucleotides, which is consistent with in silico studies performed with DNA origami (Kessler et al., 2023). Similarly, Schröder et al. observed that contact quenching between two ATTO647N molecules can be avoided when the dyes are spaced 7 nucleotides apart (Schroder et al., 2019). However, we also found that the fluorescence of two ATTO488 molecules did not saturate at a 10-nucleotide distance, indicating that the optimal spacing between dyes may vary between fluorophores.

Since NOVA -probes enable the robust detection of sub-kilobase genomic loci, they are ideally suited for several applications: (i) Interactions between regulatory elements can be mapped with high

precision. This may be particularly advantageous in genomic regions where regulatory elements are positioned near each other or their targets (Uyehara and Apostolou, 2023). Additionally, this capability has allowed us to detect small genomic loci near breakpoints in AML models. (ii) Short repetitive DNA motifs can be visualized. The human genome contains numerous transcription factor binding sites that modulate gene expression (Lambert et al., 2018). NOVA-probes may enable the detection of repetitive DNA motifs and, when combined with immunostaining, provide insights into the binding and unbinding of transcription factors. This could be valuable for investigating the activity of transcription factors during development, such as the binding of pioneer transcription factors during zygotic genome activation or interactions between pluripotency factors in embryonic stem cells (Gassler et al., 2022; Sandoval-Villegas et al., 2021). (iii) Semi-quantitative analysis of gene copy number variation can be facilitated. Since copy number variations of certain genes are involved in cancer formation, the development of sensitive tools that probe these variations may support cancer diagnostics and research (Shao et al., 2019). (iv) The integration of genetic elements into cell lines can be validated. While genome-editing tools enable the generation of transgenic cell lines, detecting desired and undesired integration sites often require labor-intensive genome sequencing (Janik et al., 2020; Sandoval-Villegas et al., 2021). NOVA-probes can determine the number and organization of integrated DNA sequences and may become especially useful for detecting integrated elements that span less than 1 kb, such as fluorescent reporter genes.

We also anticipate that our NOVA workflow will find applications beyond FISH, such as in DNA-PAINT, DNA origami synthesis, and protein labeling (Jungmann et al., 2014; Schnitzbauer et al., 2017). Specifically, the enzymatic synthesis of bright, densely labeled probes can reduce imaging acquisition time, lower the cost of probe labeling, and facilitate detailed studies of dye-dye interactions. However, our probe design is limited to applications that require a small number of targets. Unlike barcoded probes, NOVA-probes are incompatible with multiplexed imaging, limiting their use to pairwise imaging of regulatory elements. Nonetheless, NOVA-probes could be adapted for multiplexed imaging by serving as enhanced readout probes that facilitate the detection of unlabeled barcoded probes.

5.2 DETECTING ENHANCER HIJACKING EVENTS IN CANCER

In recent years, numerous genetic rearrangements have been identified in cancer cells that impact cell proliferation, survival, and function (Boveri, 2008; Spielmann et al., 2018; Yi and Ju, 2018). It is widely accepted that genetic rearrangements can lead to gene amplification, truncation, deletion, or fusion and alter the properties of a cell (Mertens et al., 2015). Promoter insertion and gene fusion events at the breakpoints of reciprocal translocations have been extensively studied due to their simple identification and impact on patient prognosis (Canoy et al., 2022; Fritz et al., 2019; Neves et al., 1999; Roix et al., 2003). The advent of high-throughput sequencing technologies has accelerated the characterization of chromosomal rearrangements and identified dysregulated transcription in numerous genes located near breakpoints (Claringbould and Zaugg, 2021; Helmsauer et al., 2020; Northcott et al., 2014, 2017; Spielmann et al., 2018). Since the DNA sequences of these genes often remain unchanged, transcriptional changes may result from local reconfigurations in genome architecture.

We focused our efforts on the characterization of three-dimensional chromatin reconfigurations and enhancer hijacking events in acute myeloid leukemia (AML) with t(7;12)(q36;p13), a pediatric cancer with poor prognosis (Bergh et al., 2006). Previously, it was hypothesized that the high occurrence of t(7;12)(q36;p13) in pediatric AML could be attributed to the formation of a MNX1::ETV6 oncofusion gene (De Braekeleer et al., 2012; Li, 2022; Taketani et al., 2008). Motor neuron and pancreas homeobox 1 (MNX1) is a transcription factor that is involved in motor neuron and pancreas development and its overexpression is associated with differentiation arrest in hematopoietic stem and progenitor cells (Harrison et al., 1999; Ingenhag et al., 2019; Thaler et al., 1999). Furthermore, MNX1 overexpression results in reduced levels of H3K4me1/2/3 and H3K27me3 and increased chromatin accessibility (Waraky et al., 2024). However, the precise mechanisms by which MNX1::ETV6 oncofusions drive AML formation remain unclear (Taketani et al., 2008).

In this study, we used whole-genome sequencing to analyze structural rearrangements in six AML patients, but did not detect any MNX1::ETV6 oncofusions among these cases. Based on the expression analysis of over 1500 pediatric AML samples, we hypothesized that MNX1 upregulation, rather than MNX1::ETV6 oncofusions, may drive cancer progression in pediatric AML. We used a combined approach of Hi-C, 4C, ATAC-seq, and FISH to characterize MNX1 activation in CRISPR-engineered t(7;12)(q36;p13) differentiation models (Nilsson et al., 2022). The induced pluripotent stem cell (iPSC) model used in this study carried t(7;12)(q36;p13) and expressed MNX1 upon differentiation into human hematopoietic stem and progenitor cells (HSPC),

comparable to AML with t(7;12)(q36;p13) (Ballabio et al., 2009; Bergh et al., 2006).

We detected a neo-TAD in t(7;12)(q36;p13) cells that contains MNX1 and the ETV6 locus and novel interactions between MNX1 and ETV6 enhancers. This is consistent with previous studies that have linked neo-TAD formation to altered gene expression in developmental disorders and cancer (Bruijn et al., 2020; Cova et al., 2023; Dixon et al., 2018; Franke et al., 2016; Melo et al., 2020; Northcott et al., 2017). For example, the translocation of Kcnj2 into a neo-TAD caused its overexpression and a limb malformation phenotype in mice (Franke et al., 2016). Moreover, structural rearrangements resulted in the relocation of RCOR2 into a neo-TAD and its activation in a subgroup of ependymoma patients (Okonechnikov et al., 2023). However, it is unclear whether the impact of neo-TADs on gene expression is caused by the formation of an active genomic region or the establishment of specific enhancer hijacking events (Benabdallah et al., 2019; Williamson et al., 2014). In our study, 4C, ATAC-seq, and ACT-seq identified four enhancer candidates (ETV6enh1 – ETV6enh4) in the neo-TAD that may upregulate MNX1. Given that two enhancer candidates (ETV6-enh1, ETV6-enh4) coincided with p300 peaks, we probed their interactions with MNX1 using FISH.

The distance between our enhancer candidates and the promoter spans 29 kb for MNX1-ETV6-enh1 and 240 kb for MNX1-ETV6-enh4. Given the proximity of ETV6-enh1 to MNX1 and the breaking point, it is crucial to minimize the target size covered by FISH probes to enable accurate detection of enhancer-promoter interactions. Therefore, we synthesized xNOVA-probe sets targeting 5-kilobase segments of MNX1, ETV6enh1, or ETV6enh4. Consistent with 4C datasets, we found a significant increase in contact frequency between MNX1 and ETV6enh1 or MNX1 and ETV6enh4 in HSPCs but not iPSCs. However, the statistical significance of MNX1-ETV6enh1 proximity was higher than that of MNX1-ETV6enh4, and CRISPR-induced deletion experiments confirmed a crucial role of MNX1-ETV6enh1 interaction in MNX1 regulation. Therefore, we hypothesize that MNX1-ETV6enh1 interactions drive MNX1 expression, while other regulatory elements in the neo-TAD exhibit smaller effects.

As described in chapter 3.2.1, different models have been formulated to characterize proximal and distal enhancer-promoter interactions. Although long-range enhancer-promoter interactions are often mapped in the three-dimensional context of the nucleus, it remains a subject of debate if physical contact between enhancers and promoters is necessary to drive gene expression. For example, activation of the ssh locus during neural differentiation is accompanied by increased distances between enhancers and promoters (Benabdallah et al., 2019). Similarly, an enhancer sequence variant in PHACTR1 seems to regulate EDN1 expression without increased enhancer-promoter contact

frequency in endothelial cells (Gupta et al., 2017). Nevertheless, an increasing number of studies have detected spatial proximity and increased enhancer-promoter contact frequency upon gene activation (Bartman et al., 2016; Bonev et al., 2017; Chen et al., 2024; Deng et al., 2014; Deng et al., 2012; Zhou et al., 2022). Our findings are consistent with models that use physical proximity of regulatory elements as an indicator of gene activity.

We observed that slight increases in MNX1-ETV6enh1 contact frequency led to a strong upregulation of MNX1 in t(7;12)(q36;p13) HSPCs. This raises the question of how occasional enhancer-promoter contacts can exert such profound effects on gene expression. Several models have been proposed to explain the nonlinear relationship between enhancer-promoter contact frequency and gene expression, including bistability, hysteresis, and transient enhancer-promoter interactions (Xiao et al., 2021; Zuin et al., 2022). According to these models, physical enhancer-promoter interactions are dynamic, short-lived, and cause strong increases in transcription (Xiao et al., 2021). These models are also compatible with transcriptional bursting, which describes eukaryotic transcription as occurring in discontinuous bursts with subsequent refractory periods (Raj et al., 2006).

The unexplored roles of neo-TAD formation and enhancer hijacking events have broader implications for cancer research. Whole-genome sequencing data from 268 cancer patients revealed that enhancer hijacking events occur more frequently than protein fusions (Yun et al., 2020). Furthermore, analysis of 1200 cancer genomes identified hundreds of dysregulated genes that may be activated by enhancer hijacking and neo-TAD formation (Zhang et al., 2020b). As enhancer hijacking emerges as a common mechanism in cancer formation, new opportunities arise for the diagnosis, prognosis, and treatment of patients (Wang and Yue, 2024). Especially the identification of enhancer hijacking events across multiple cancer types could refine cancer classification and improve the assessment of treatment options.

While we demonstrate that structural rearrangements in pediatric AML lead to neo-TAD formation and enhancer-hijacking events, our study is limited to the pairwise analysis of enhancer-promoter interactions. Multiple studies have revealed additive, synergistic, or hierarchical contributions of multiple enhancers to the activation of single genes (Blinka et al., 2016; Hay et al., 2016; Huang et al., 2018, 2016; Uyehara and Apostolou, 2023). For example, alpha-globin is regulated by multiple enhancers that have additive effects on its expression (Hay et al., 2016). Given that 4C detected interactions between MNX1 and four ETV6 enhancers, it may be possible that these regulatory elements exert additive effects on MNX1 expression. Moreover, the extent to which ETV6 function is compromised in t(7;12)(q36;p13) cells has yet to be determined. ETV6 encodes a transcriptional repressor that plays a crucial role in embryonic development and hematopoiesis

and regulates genes that are involved in signaling pathways (Hock and Shimamura, n.d.; Neveu et al., 2022). Neo-TAD formation and enhancer hijacking in t(7;12)(q36;p13) cells may alter ETV6 expression and impact cell properties independently of MNX1 activation (Kodgule et al., 2023; Nilsson et al., 2022).

5.3 NANOSCALE VARIATION OF ACTIVE AND INACTIVE CHROMATIN

DNA is compacted by several orders of magnitude to fit into the confined space of the nucleus. The nucleosome is the fundamental unit of DNA compaction and nucleosome arrays organize into heterogeneous clutches and fibers to create regions with high nucleosome density interspersed with nucleosome-depleted regions (Baldi et al., 2020; Chen et al., 2021; Fussner et al., 2012; Narlikar et al., 2013; Ou et al., 2017; Ricci et al., 2015; Segal and Widom, 2009). While population-averaged nucleosome mapping methods suggest a defined pattern of nucleosome occupancy across the genome, single-cell methods reveal cell-to-cell variability down to the placement of individual nucleosomes. (Lai et al., 2018; Mavrich et al., 2008; Schones et al., 2008). Furthermore, simulations suggest that nucleosome positioning can impact 3D chromatin conformations, with even the repositioning of single nucleosomes affecting local compaction (Kepper et al., 2008; Muller et al., 2014). However, it is not clear how the placement of nucleosomes impacts the organization of kilobase genomic loci in cells. In this study, we combined super-resolution microscopy with simulation models to investigate structural differences between active and inactive kilobase genomic loci (Brandstetter et al., 2022).

To this end, we identified two targets representing open ('Active') and closed ('Inactive') chromatin regions through publicly available ChIP-seq, MNase-seq, and DNase-seq databases (Consortium et al., 2020; Davis et al., 2018; Meuleman et al., 2020). Since the selected genomic loci contain DNase I hypersensitive sites and nucleosome repeat lengths representative of the human genome, we expect that measurements in these regions are applicable to other parts of the genome. 'Active' and 'Inactive' regions were subdivided into five sub-regions with intervals of approximately 5 kb between them and distances were measured using FISH. In accordance with previous studies, we overall measured longer distances between 'Active' (82 nm) sub-regions comparted to 'Inactive' (55 nm) regions (Mateo et al., 2019; Strom et al., 2017; Xu and Liu, 2021), However, we also observed broad distance distributions and elongated configurations for both regions, with maximum lengths exceeding 200 nm. Since a fully stretched chromatin fiber can theoretically be elongated to roughly 240 nm, we hypothesized that differences in nucleosome occupancy could account for our measurements (Carlson and Olins, 1976). We used simulations

with a coarse-grained model to identify nucleosomes that exhibit the lowest occupancy and found that the same nucleosomes coincide with DNase I hypersensitive sites. Therefore, we concluded that both 'Active' and 'Inactive' regions exhibit nucleosome positions that vary in occupancy across different cells in a population. However, we also speculate that the binding of H1-linker histones may contribute to the broad distribution of distances observed (Gomez-Garcia et al., 2021; Izzo and Schneider, 2016).

We further validated the simulated distance distribution through chromatin reconstitution using linearized Widom 601 arrays that have been end-labeled using our NOVA workflow (Lieleg et al., 2015). Although the average end-to-end distance of reconstituted chromatin (70 nm) was similar to that of 'Inactive' chromatin (55 nm), our in silico measurements only consider the presence of histones and do not account for other proteins that may influence chromatin compaction. Nonetheless, the striking concordance between simulated, in silico, and in vivo measurements highlights the impact of nucleosome occupancy on the nanoscale organization of chromatin.

Our study demonstrates considerable cell-to-cell variability in nucleosome occupancy in selected genomic regions. Nucleosomes can be deposited, repositioned, or removed by a variety of proteins, including chromatin remodeling complexes, pioneer transcription factors, or through competitive interactions with other transcription factors (Baldi et al., 2020; Bartholomew, 2014; Mirny, 2010; Zaret, 2020). For 'Active' sub-regions, the observed variation in compaction may also be attributed to transcription, as gene expression is associated with histone displacement (Diermeier et al., 2014; Kotova et al., 2022). We expect histone modifications, such as histone acetylation, to play a minor role as they are comparatively sparse at this scale (Ernst and Kellis, 2010; Talbert and Henikoff, 2021). Cumulatively, these factors influence the local positioning of nucleosomes and may especially affect the assembly and dissociation of nucleosomes with the lowest occupancy observed in our simulations.

The human genome contains more than 142,000 enhancer-like elements that are situated within two kilobases of the nearest promoter (Consortium et al., 2020). Proximal enhancer-promoter interactions are typically described using one-dimensional models that involve the enhancer-dependent recruitment and activity of RNA Pol II, chromatin remodelers, or transcription factors (Bulger and Groudine, 1999; Moreau et al., 1981; Travers, 1999; Yang and Hansen, 2024). While these models provide mechanistic insights into gene expression, they neglect three-dimensional chromatin conformations and DNA-DNA contacts. Fluctuations in distances between remote genomic loci have been detected using 3C-based methods or FISH, and directly observed through live-cell imaging (Chen et al., 2018a; Flyamer et al., 2017; Gabriele et al., 2022; Nagano et al., 2017; Stevens et al., 2017; Szabo

et al., 2020, 2018). We provide evidence that nucleosome occupancy impacts the three-dimensional organization of 'active' and 'inactive' chromatin down to the kilobase level. Given that nucleosome eviction is linked to changes in gene expression, it is plausible to assume that dynamic changes in the placement of individual nucleosomes impact the flexibility of local chromatin, binding of DNA-protein factors, and enhancer-promoter communication (Baldi et al., 2020; Nizovtseva et al., 2017; Singh and Mueller-Planitz, 2021). Consequently, the deposition, repositioning, and removal of nucleosomes may help to fine-tune gene expression over time (Buenrostro et al., 2015; Lai et al., 2018; Tang et al., 2009).

We systematically measured and simulated distances between 'Active' and 'Inactive' genomic loci representative of the human genome but cannot exclude the possibility that unstudied factors may impact nanoscale compaction. Our simulations included a defined number of nucleosomes, H1-linker proteins, and internucleosomal interaction strength but did not account for other DNA-binding proteins or transcription factors. Therefore, future studies may probe the effects of other proteins on nucleosome occupancy and local chromatin compaction. Similar to other studies that use cancer cells, we cannot rule out that the pseudo-triploid karyotype and aberrant gene expression in K562 cells affect cell-to-cell variability in nucleosome occupancy (Karagiannis et al., 2023). Lastly, the effects of fixation, permeabilization and heat denaturation on fine chromatin structures remain a subject of debate (Markaki et al., 2012; Solovei et al., 2002). While we chose a comparatively mild FISH protocol that has been shown to preserve chromatin structures larger than 100 nm, we cannot accurately estimate the extent to which smaller chromatin structures are altered by chemical fixation and heat treatment (Markaki et al., 2012; Schnell et al., 2012; Thavarajah et al., 2012).

In conclusion, we employ super-resolution microscopy to explore the nanoscopic organization of chromatin. Previous imaging-based methodologies have delineated large genomic regions in the three-dimensional space, but the detection of small genomic elements has remained challenging. In this thesis, we established a novel workflow for the enzymatic synthesis of densely-labeled FISH probes and demonstrated their capability to detect sub-kilobase genomic loci. With these probes, we characterized enhancer hijacking events in cancer and expect that our workflow will facilitate the detection of other small genomic elements, including TAD boundaries, short repetitive DNA motifs, gene copy number variation, or reporter genes. With advancements in sensitivity, accuracy, and throughput of microscopy-based methods, we may soon be able to investigate the spatial relationships of numerous small genomic elements in single cells and dissect their roles in the activation and repression of genes.

BIBLIOGRAPHY

Abbe, E. (1873). "Beiträge zur Theorie des Mikroskops und der mikroskopischen Wahrnehmung." *Arch Mikr Anat* 9, pp. 413–468. DOI: 10.1007/BF02956173.

Aguilar, R., C. K. Camplisson, Q. Lin, K. H. Miga, W. S. Noble, and B. J. Beliveau (2024). "Tigerfish designs oligonucleotide-based in situ hybridization probes targeting intervals of highly repetitive DNA at the scale of genomes." *Nat Commun* 15, p. 1027. DOI: 10.1038/s41467-024-45385-x.

Alexander, J. M., J. Guan, B. Li, L. Maliskova, M. Song, Y. Shen, B. Huang, S. Lomvardas, and O. D. Weiner (2019). "Live-cell imaging reveals enhancer-dependent Sox2 transcription in the absence of enhancer proximity." *Elife* 8, p. e41769. DOI: 10.7554/eLife.41769.

Allawi, H. T. and J. SantaLucia J. (1997). "Thermodynamics and NMR of internal G.T mismatches in DNA." *Biochemistry* 36, pp. 10581–10594. DOI: 10.1021/bi962590c.

Allen, B. L. and D. J. Taatjes (2015). "The Mediator complex: a central integrator of transcription." *Nat Rev Mol Cell Biol* 16, pp. 155–166. DOI: 10.1038/nrm3951.

Allfrey, V. G., R Faulkner, and A. Mirsky (1964). "Acetylation and methylation of histones and their possible role in the regulation of RNA synthesis." *Proc Natl Acad Sci U S A* 51, pp. 786–794. DOI: 10.1073/pnas.51.5.786.

Altschul, S. F., W. Gish, W. Miller, E. W. Myers, and D. J. Lipman (1990). "Basic local alignment search tool." *J Mol Biol* 215, pp. 403–410. DOI: 10.1016/S0022-2836(05)80360-2.

Amiad-Pavlov, D., D. Lorber, G. Bajpai, A. Reuveny, F. Roncato, R. Alon, S. Safran, and T. Volk (2021). "Live imaging of chromatin distribution reveals novel principles of nuclear architecture and chromatin compartmentalization." *Sci Adv* 7, eabf6251. DOI: 10.1126/sciadv.abf6251.

Anand, R., A. Villasante, and C. Tyler-Smith (1989). "Construction of yeast artificial chromosome libraries with large inserts using fractionation by pulsed-field gel electrophoresis." *Nucleic Acids Res* 17, pp. 3425–3433. DOI: 10.1093/nar/17.9.3425.

Andersson, R. and A. Sandelin (2020). "Determinants of enhancer and promoter activities of regulatory elements." *Nat Rev Genet* 21, pp. 71–87. DOI: 10.1038/s41576-019-0173-8.

Avery, O. T., C. M. MacLeod, and M. McCarty (1943). "Studies on the chemical nature of the substance inducing transformation of pneumococcal types: induction of transformation by a desoxyribonucleic acid fraction isolated from pneumococcus type III." In: *Die Entdeckung der Doppelhelix: Die grundlegenden Arbeiten von Watson, Crick und anderen*. Springer, pp. 97–120. DOI: 10.1084/jem.79.2.137.

Axelrod, D., D. E. Koppel, J. Schlessinger, E. Elson, and W. W. Webb (1976). "Mobility measurement by analysis of fluorescence photobleaching recovery kinetics." *Biophys J* 16, pp. 1055–1069. DOI: 10.1016/S0006-3495(76)85755-4.

Bader, A. N., E. G. Hofman, J. Voortman, P. M. en Henegouwen, and H. C. Gerritsen (2009). "Homo-FRET imaging enables quantification of protein cluster sizes with subcellular resolution." *Biophys J* 97, pp. 2613–2622. DOI: 10.1016/j.bpj.2009.07.059.

Bader, A. N., S. Hoetzl, E. G. Hofman, J. Voortman, P. M. van Bergen en Henegouwen, G. van Meer, and H. C. Gerritsen (2011). "Homo-FRET imaging as a tool to quantify protein and lipid clustering." *Chem Phys Chem* 12, pp. 475–483. DOI: 10.1002/cphc.201000801.

Baldi, S., P. Korber, and P. B. Becker (2020). "Beads on a string-nucleosome array arrangements and folding of the chromatin fiber." *Nat Struct Mol Biol* 27, pp. 109–118. DOI: 10.1038/s41594-019-0368-x.

Ballabio, E, C. Cantarella, C Federico, P Di Mare, G Hall, J Harbott, J Hughes, S Saccone, and S Tosi (2009). "Ectopic expression of the HLXB9 gene is associated with an altered nuclear position in t (7; 12) leukaemias." *Leukemia* 23, pp. 1179–1182. DOI: 10.1038/leu.2009.15.

Banerji, J., S. Rusconi, and W. Schaffner (1981). "Expression of a -globin gene is enhanced by remote SV40 DNA sequences." *Cell* 27, pp. 299–308. DOI: 10.1016/0092-8674(81)90413-X.

Banigan, E. J. and L. A. Mirny (2020). "Loop extrusion: theory meets single-molecule experiments." *Curr Opin Cell Biol* 64, pp. 124–138. DOI: 10.1016/j.ceb.2020.04.011.

Bantignies, F., V. Roure, I. Comet, B. Leblanc, B. Schuettengruber, J. Bonnet, V. Tixier, A. Mas, and G. Cavalli (2011). "Polycomb-dependent regulatory contacts between distant Hox loci in Drosophila." *Cell* 144, pp. 214–226. DOI: 10.1016/j.cell.2010.12.026.

Bartholomew, B. (2014). "Regulating the chromatin landscape: structural and mechanistic perspectives." *Annu Rev Biochem* 83, pp. 671–696. DOI: 10.1146/annurev-biochem-051810-093157.

Bartman, C. R., S. C. Hsu, C. C. Hsiung, A. Raj, and G. A. Blobel (2016). "Enhancer Regulation of Transcriptional Bursting Parameters Revealed by Forced Chromatin Looping." *Mol Cell* 62, pp. 237–247. DOI: 10.1016/j.molcel.2016.03.007.

Baum, B. and A. Spang (2023). "On the origin of the nucleus: a hypothesis." *Microbiol Mol Biol Rev* 87, p. e0018621. DOI: 10.1128/mmbr.00186-21.

Bauman, J. G., J. Wiegant, P. Borst, and P. van Duijn (1980). "A new method for fluorescence microscopical localization of specific DNA sequences by in situ hybridization of fluorochrome-labelled RNA." *Exp Cell Res* 128, pp. 485–490. DOI: 10.1016/0014-4827(80)90087-7.

Baylin, S. B. and P. A. Jones (2016). "Epigenetic Determinants of Cancer." *Cold Spring Harb Perspect Biol* 8, p. a019505. DOI: 10.1101/cshperspect.a019505.

Beliveau, B. J., E. F. Joyce, N. Apostolopoulos, F. Yilmaz, C. Y. Fonseka, R. B. McCole, Y. Chang, J. B. Li, T. N. Senaratne, B. R. Williams, J. M. Rouillard, and C. T. Wu (2012). "Versatile design and synthesis platform for visualizing genomes with Oligopaint FISH probes." *Proc Natl Acad Sci U S A* 109, pp. 21301–21306. DOI: 10.1073/pnas.1213818110.

Beliveau, B. J., J. Y. Kishi, G. Nir, H. M. Sasaki, S. K. Saka, S. C. Nguyen, C. T. Wu, and P. Yin (2018). "OligoMiner provides a rapid, flexible environment for the design of genome-scale oligonucleotide in situ hybridization probes." *Proc Natl Acad Sci U S A* 115, E2183–E2192. DOI: 10.1073/pnas.1714530115.

Beliveau, B. J. et al. (2015). "Single-molecule super-resolution imaging of chromosomes and in situ haplotype visualization using Oligopaint FISH probes." *Nat Commun* 6, p. 7147. DOI: 10.1038/ncomms8147.

Belmont, A. S. (2022). "Nuclear Compartments: An Incomplete Primer to Nuclear Compartments, Bodies, and Genome Organization Relative to Nuclear Architecture." *Cold Spring Harb Perspect Biol* 14, p. a041268. DOI: 10.1101/cshperspect.a041268.

Benabdallah, N. S., I. Williamson, R. S. Illingworth, S. Boyle, G. R. Grimes, P. Therizols, and W. A. Bickmore (2019). "Decreased Enhancer-Promoter Proximity Accompanying Enhancer Activation." *Mol Cell*, pp. 473–484. DOI: 10.1016/j.molcel.2019.07.038.

Bergh, A. R. von, E. van Drunen, E. R. van Wering, L. J. van Zutven, I. Hainmann, G. Lonnerholm, J. P. Meijerink, R. Pieters, and H. B. Beverloo (2006). "High incidence of t(7;12)(q36;p13) in infant AML but not in infant ALL, with a dismal outcome and ectopic expression of HLXB9." *Genes Chromosomes Cancer* 45, pp. 731–739. DOI: 10.1002/gcc.20335.

Bintu, B., L. J. Mateo, J. H. Su, N. A. Sinnott-Armstrong, M. Parker, S. Kinrot, K. Yamaya, A. N. Boettiger, and X. Zhuang (2018). "Super-resolution chromatin tracing reveals domains and cooperative interactions in single cells." *Science* 362, p. eaau1783. DOI: 10.1126/science.aau1783.

Blinka, S., M. H. Reimer, K. Pulakanti, and S. Rao (2016). "Super-enhancers at the Nanog locus differentially regulate neighboring pluripotency-associated genes." *Cell Rep* 17, pp. 19–28. DOI: 10.1016/j.celrep.2016.09.002.

Boettiger, A. and S. Murphy (2020). "Advances in Chromatin Imaging at Kilobase-Scale Resolution." *Trends Genet* 36, pp. 273–287. DOI: 10.1016/j.tig.2019.12.010.

Boija, A., I. A. Klein, B. R. Sabari, A. Dall'Agnese, E. L. Coffey, A. V. Zamudio, C. H. Li, K. Shrinivas, J. C. Manteiga, and N. M. Hannett (2018). "Transcription factors activate genes through the phase-separation capacity of their activation domains." *Cell* 175, pp. 1842–1855. DOI: 10.1016/j.cell.2018.10.042.

Bolland, D. J., M. R. King, W. Reik, A. E. Corcoran, and C. Krueger (2013). "Robust 3D DNA FISH using directly labeled probes." *J Vis Exp*, p. e50587. DOI: 10.3791/50587.

Bolzer, A., G. Kreth, I. Solovei, D. Koehler, K. Saracoglu, C. Fauth, S. Muller, R. Eils, C. Cremer, M. R. Speicher, and T. Cremer (2005). "Three-dimensional maps of all chromosomes in human male fibroblast nuclei and prometaphase rosettes." *PLoS Biol* 3, p. e157. DOI: 10.1371/journal.pbio.0030157.

Bommarito, S., N. Peyret, and J. SantaLucia J. (2000). "Thermodynamic parameters for DNA sequences with dangling ends." *Nucleic Acids Res* 28, pp. 1929–1934. DOI: 10.1093/nar/28.9.1929.

Bonev, B., N. Mendelson Cohen, Q. Szabo, L. Fritsch, G. L. Papadopoulos, Y. Lubling, X. Xu, X. Lv, J. P. Hugnot, A. Tanay, and G. Cavalli (2017). "Multiscale 3D Genome Rewiring during Mouse Neural Development." *Cell* 171, pp. 557–572. DOI: 10.1016/j.cell.2017.09.043.

Bonev, B. and G. Cavalli (2016). "Organization and function of the 3D genome." *Nat Rev Genet* 17, pp. 661–678. DOI: 10.1038/nrg.2016.112.

Boveri, T. (2008). "Concerning the origin of malignant tumours by Theodor Boveri. Translated and annotated by Henry Harris." *J Cell Sci* 121 Suppl 1, pp. 1–84. DOI: 10.1242/jcs.025742.

Boveri, T. (1909). "Die Blastomerenkerne von Ascaris megalocephala und die Theorie der Chromosomenindividualitat." *Arch Zellf* 3, pp. 181–268.

Brandstetter, K. et al. (2022). "Differences in nanoscale organization of regulatory active and inactive human chromatin." *Biophys J* 121, pp. 977–990. DOI: 10.1016/j.bpj.2022.02.009.

Breslauer, K. J., R. Frank, H. Blocker, and L. A. Marky (1986). "Predicting DNA duplex stability from the base sequence." *Proc Natl Acad Sci U S A* 83, pp. 3746–3750. DOI: 10.1073/pnas.83.11.3746.

Brown, J. M., S. De Ornellas, E. Parisi, L. Schermelleh, and V. J. Buckle (2022). "RASER-FISH: non-denaturing fluorescence in situ hybridization for preservation of three-dimensional

interphase chromatin structure." *Nat Protoc* 17, pp. 1306–1331. DOI: 10.1038/s41596-022-00685-8.

Brown, J. M., N. A. Roberts, B. Graham, D. Waithe, C. Lagerholm, J. M. Telenius, S. De Ornellas, A. M. Oudelaar, C. Scott, I. Szczerbal, C. Babbs, M. T. Kassouf, J. R. Hughes, D. R. Higgs, and V. J. Buckle (2018). "A tissue-specific self-interacting chromatin domain forms independently of enhancer-promoter interactions." *Nat Commun* 9, p. 3849. DOI: 10.1038/s41467-018-06248-4.

Bruijn, S. E. de et al. (2020). "Structural Variants Create New Topological-Associated Domains and Ectopic Retinal Enhancer-Gene Contact in Dominant Retinitis Pigmentosa." *Am J Hum Genet* 107, pp. 802–814. DOI: 10.1016/j.ajhg.2020.09.002.

Buchwalter, A., J. M. Kaneshiro, and M. W. Hetzer (2019). "Coaching from the sidelines: the nuclear periphery in genome regulation." *Nat Rev Genet* 20, pp. 39–50. DOI: 10.1038/s41576-018-0063-5.

Buenrostro, J. D., B. Wu, U. M. Litzenburger, D. Ruff, M. L. Gonzales, M. P. Snyder, H. Y. Chang, and W. J. Greenleaf (2015). "Single-cell chromatin accessibility reveals principles of regulatory variation." *Nature* 523, pp. 486–490. DOI: 10.1038/nature14590.

Bulger, M. and M. Groudine (1999). "Looping versus linking: toward a model for long-distance gene activation." *Genes Dev* 13, pp. 2465–2477. DOI: 10.1101/gad.13.19.2465.

Burke, D. T., G. F. Carle, and M. V. Olson (1987). "Cloning of large segments of exogenous DNA into yeast by means of artificial chromosome vectors." *Science* 236, pp. 806–812. DOI: 10.1126/science.3033825.

Canoy, R. J., A. Shmakova, A. Karpukhina, M. Shepelev, D. Germini, and Y. Vassetzky (2022). "Factors that affect the formation of chromosomal translocations in cells." *Cancers* 14, p. 5110. DOI: 10.3390/cancers14205110.

Cardozo Gizzi, A. M., D. I. Cattoni, J. B. Fiche, S. M. Espinola, J. Gurgo, O. Messina, C. Houbron, Y. Ogiyama, G. L. Papadopoulos, G. Cavalli, M. Lagha, and M. Nollmann (2019). "Microscopy-Based Chromosome Conformation Capture Enables Simultaneous Visualization of Genome Organization and Transcription in Intact Organisms." *Mol Cell* 74, 212–222 e5. DOI: 10.1016/j.molcel.2019.01.011.

Carlson, R. D. and D. E. Olins (1976). "Chromatin model calculations: Arrays of spherical nu bodies." *Nucleic Acids Res* 3, pp. 89–100. DOI: 10.1093/nar/3.1.89.

Cattoni, D. I. et al. (2017). "Single-cell absolute contact probability detection reveals chromosomes are organized by multiple low-frequency yet specific interactions." *Nat Commun* 8, p. 1753. DOI: 10.1038/s41467-017-01962-x.

Ceze, L., J. Nivala, and K. Strauss (2019). "Molecular digital data storage using DNA." *Nat Rev Genet* 20, pp. 456–466. DOI: 10.1038/s41576-019-0125-3.

Chambeyron, S. and W. A. Bickmore (2004). "Chromatin decondensation and nuclear reorganization of the HoxB locus upon induction of transcription." *Genes Dev* 18, pp. 1119–1130. DOI: 10.1101/gad.292104.

Chargaff, E. (1950). "Chemical specificity of nucleic acids and mechanism of their enzymatic degradation." *Experientia* 6, pp. 201–209. DOI: 10.1007/BF02173653.

Chen, F., P. W. Tillberg, and E. S. Boyden (2015a). "Optical imaging. Expansion microscopy." *Science* 347, pp. 543–548. DOI: 10.1126/science.1260088.

Chen, H., M. Levo, L. Barinov, M. Fujioka, J. B. Jaynes, and T. Gregor (2018a). "Dynamic interplay between enhancer–promoter topology and gene activity." *Nat Genet* 50, pp. 1296–1303. DOI: 10.1038/s41588-018-0175-z.

Chen, K. H., A. N. Boettiger, J. R. Moffitt, S. Wang, and X. Zhuang (2015b). "RNA imaging. Spatially resolved, highly multiplexed RNA profiling in single cells." *Science* 348, p. aaa6090. DOI: 10.1126/science.aaa6090.

Chen, P., W. Li, and G. Li (2021). "Structures and Functions of Chromatin Fibers." *Annu Rev Biophys* 50, pp. 95–116. DOI: 10.1146/annurev-biophys-062920-063639.

Chen, Y., Y. Zhang, Y. Wang, L. Zhang, E. K. Brinkman, S. A. Adam, R. Goldman, B. Van Steensel, J. Ma, and A. S. Belmont (2018b). "Mapping 3D genome organization relative to nuclear compartments using TSA-Seq as a cytological ruler." *JCB* 217, pp. 4025–4048. DOI: 10.1083/jcb.201807108.

Chen, Z., V. Snetkova, G. Bower, S. Jacinto, B. Clock, A. Dizehchi, I. Barozzi, B. J. Mannion, A. Alcaina-Caro, J. Lopez-Rios, D. E. Dickel, A. Visel, L. A. Pennacchio, and E. Z. Kvon (2024). "Increased enhancer-promoter interactions during developmental enhancer activation in mammals." *Nat Genet* 56, pp. 675–685. DOI: 10.1038/s41588-024-01681-2.

Choi, H. M., V. A. Beck, and N. A. Pierce (2014). "Next-generation in situ hybridization chain reaction: higher gain, lower cost, greater durability." *ACS nano* 8, pp. 4284–4294. DOI: 10.1021/nn405717p.

Choi, K. J., M. D. Quan, C. Qi, J. H. Lee, P. S. Tsoi, M. Zahabiyon, A. Bajic, L. Hu, B. V. V. Prasad, S. J. Liao, W. Li, A. C. M. Ferreon, and J. C. Ferreon (2022). "NANOG prion-like assembly mediates DNA bridging to facilitate chromatin reorganization and activation of pluripotency." *Nat Cell Biol* 24, pp. 737–747. DOI: 10.1038/s41556-022-00896-x.

Chong, S., T. G. W. Graham, C. Dugast-Darzacq, G. M. Dailey, X. Darzacq, and R. Tjian (2022). "Tuning levels of low-complexity domain interactions to modulate endogenous oncogenic transcription." *Mol Cell* 82, pp. 2084–2097. DOI: 10.1016/j.molcel.2022.04.007.

Ciosk, R., M. Shirayama, A. Shevchenko, T. Tanaka, A. Toth, A. Shevchenko, and K. Nasmyth (2000). "Cohesin's binding to chromosomes depends on a separate complex consisting of Scc2 and Scc4 proteins." *Mol Cell* 5, pp. 243–254. DOI: 10.1016/s1097-2765(00)80420-7.

Cisse, I., I. Izeddin, S. Z. Causse, L. Boudarene, A. Senecal, L. Muresan, C. Dugast-Darzacq, B. Hajj, M. Dahan, and X. Darzacq (2013). "Real-time dynamics of RNA polymerase II clustering in live human cells." *Science* 341, pp. 664–647. DOI: 10.1126/science.1239053.

Claringbould, A. and J. B. Zaugg (2021). "Enhancers in disease: molecular basis and emerging treatment strategies." *Trends Mol Med* 27, pp. 1060–1073. DOI: 10.1016/j.molmed.2021.07.012.

Clowney, E. J., M. A. LeGros, C. P. Mosley, F. G. Clowney, E. C. Markenskoff-Papadimitriou, M. Myllys, G. Barnea, C. A. Larabell, and S. Lomvardas (2012). "Nuclear aggregation of olfactory receptor genes governs their monogenic expression." *Cell* 151, pp. 724–737. DOI: 10.1016/j.cell.2012.09.043.

Consortium, E. P. et al. (2020). "Expanded encyclopaedias of DNA elements in the human and mouse genomes." *Nature* 583, pp. 699–710. DOI: 10.1038/s41586-020-2493-4.

Consortium, I. H. G. S. (2001). "Initial sequencing and analysis of the human genome." *Nature* 409, pp. 860–921. DOI: 10.1038/35057062.

Core, L. J., A. L. Martins, C. G. Danko, C. T. Waters, A. Siepel, and J. T. Lis (2014). "Analysis of nascent RNA identifies a unified architecture of initiation regions at mammalian promoters and enhancers." *Nat Genet* 46, pp. 1311–1320. DOI: 10.1038/ng.3142.

Correns, C. (1900). "G. Mendel's Regel über das Verhalten der Nachkommenschaft der Rassenbastarde." *Ber Dtsch Bot Ges* 18, 158–167. DOI: 10.1007/978-3-642-52587-2_2.

Cova, G., J. Glaser, R. Schöpflin, C. A. Prada-Medina, S. Ali, M. Franke, R. Falcone, M. Federer, E. Ponzi, and R. Ficarella (2023). "Combinatorial effects on gene expression at the Lbx1/Fgf8 locus resolve split-hand/foot malformation type 3." *Nat Commun* 14, p. 1475. DOI: 10.1038/s41467-023-37057-z.

Cremer, M., K. Brandstetter, A. Maiser, S. S. P. Rao, V. J. Schmid, M. Guirao-Ortiz, N. Mitra, S. Mamberti, K. N. Klein, D. M. Gilbert, H. Leonhardt, M. C. Cardoso, E. L. Aiden, H. Harz, and T. Cremer (2020). "Cohesin depleted cells rebuild functional nuclear compartments after endomitosis." *Nat Commun* 11, p. 6146. DOI: 10.1038/s41467-020-19876-6.

Cremer, T. and M. Cremer (2010). "Chromosome territories." *Cold Spring Harb Perspect Biol* 2, a003889. DOI: 10.1101/cshperspect.a003889.

Cremer, T., C. Cremer, H Baumann, E. Luedtke, K Sperling, V Teuber, and C. Zorn (1982). "Rabl's model of the interphase chromosome arrangement tested in Chinise hamster cells by premature chromosome condensation and laser-UV-microbeam experiments." *Hum Genet* 60, pp. 46–56. DOI: 10.1007/BF00281263.

Cremer, T., S. P. Peterson, C. Cremer, and M. W. Berns (1981). "Laser microirradiation of Chinese hamster cells at wavelength 365 nm: effects of psoralen and caffeine." *Radiat Res* 85, pp. 529–543. DOI: 10.2307/3575423.

Creyghton, M. P., A. W. Cheng, G. G. Welstead, T. Kooistra, B. W. Carey, E. J. Steine, J. Hanna, M. A. Lodato, G. M. Frampton, P. A. Sharp, L. A. Boyer, R. A. Young, and R. Jaenisch (2010). "Histone H3K27ac separates active from poised enhancers and predicts developmental state." *Proc Natl Acad Sci U S A* 107, pp. 21931–21936. DOI: 10.1073/pnas.1016071107.

Crick, F. (1970). "Central dogma of molecular biology." *Nature* 227, pp. 561–563. DOI: 10.1038/227561a0.

Crick, F. H. (1958). "On protein synthesis." In: *Symp Soc Exp Biol*. Vol. 12, p. 8.

Crosetto, N. and M. Bienko (2020). "Radial Organization in the Mammalian Nucleus." *Front Genet* 11, p. 33. DOI: 10.3389/fgene.2020.00033.

Crump, N. T., C. A. Hazzalin, E. M. Bowers, R. M. Alani, P. A. Cole, and L. C. Mahadevan (2011). "Dynamic acetylation of all lysine-4 trimethylated histone H3 is evolutionarily conserved and mediated by p300/CBP." *Proc Natl Acad Sci U S A* 108, pp. 7814–7819. DOI: 10.1073/pnas.1100099108.

Dahm, R. (2005). "Friedrich Miescher and the discovery of DNA." *Dev Biol* 278, pp. 274–288. DOI: 10.1016/j.ydbio.2004.11.028.

Dahm, R. (2008). "Discovering DNA: Friedrich Miescher and the early years of nucleic acid research." *Hum Genet* 122, pp. 565–581. DOI: 10.1007/s00439-007-0433-0.

Dao, L. T. M. et al. (2017). "Genome-wide characterization of mammalian promoters with distal enhancer functions." *Nat Genet* 49, pp. 1073–1081. DOI: 10.1038/ng.3884.

Dardani, I., B. L. Emert, Y. Goyal, C. L. Jiang, A. Kaur, J. Lee, S. H. Rouhanifard, G. M. Alicea, M. E. Fane, and M. Xiao (2022). "ClampFISH 2.0 enables rapid, scalable amplified RNA detection in situ." *Nat Methods* 19, pp. 1403–1410. DOI: 10.1038/s41592-022-01653-6.

Davidson, I. F., B. Bauer, D. Goetz, W. Tang, G. Wutz, and J. M. Peters (2019). "DNA loop extrusion by human cohesin." *Science* 366, pp. 1338–1345. DOI: 10.1126/science.aaz3418.

Davis, C. A. et al. (2018). "The Encyclopedia of DNA elements (ENCODE): data portal update." *Nucleic Acids Res* 46, pp. D794–D801. DOI: 10.1093/nar/gkx1081.

De Braekeleer, E., N. Douet-Guilbert, F. Morel, M. J. Le Bris, A. Basinko, and M. De Braekeleer (2012). "ETV6 fusion genes in hematological malignancies: a review." *Leuk Res* 36, pp. 945–961. DOI: 10.1016/j.leukres.2012.04.010.

De Santa, F., I. Barozzi, F. Mietton, S. Ghisletti, S. Polletti, B. K. Tusi, H. Muller, J. Ragoussis, C. L. Wei, and G. Natoli (2010). "A large fraction of extragenic RNA pol II transcription sites overlap enhancers." *PLoS Biol* 8, p. e1000384. DOI: 10.1371/journal.pbio.1000384.

De Vries, H. (1900). "Das Spaltungsgesetz der Bastarde. Ber. d." *Dtsch Bot Ges* 29, pp. 83–90. DOI: 10.1007/978-3-642-52587-2_6.

Deaven, L., M. Van Dilla, M. Bartholdi, A. Carrano, L. Cram, J. Fuscoe, J. Gray, C. Hildebrand, R. Moyzis, and J Perlman (1986). "Construction of human chromosome-specific DNA libraries from flow-sorted chromosomes." In: *Cold Spring Harb Symp Quant Biol*. Vol. 51. Cold Spring Harbor Laboratory Press, pp. 159–167. DOI: 10.1101/SQB.1986.051.01.019.

Dekker, J., K. Rippe, M. Dekker, and N. Kleckner (2002). "Capturing chromosome conformation." *Science* 295, pp. 1306–11. DOI: 10.1126/science.1067799.

Dekker, J. and L. Mirny (2016). "The 3D genome as moderator of chromosomal communication." *Cell* 164, pp. 1110–1121. DOI: 10.1016/j.cell.2016.02.007.

Demchenko, A. P. (2020). "Photobleaching of organic fluorophores: quantitative characterization, mechanisms, protection." *Methods Appl Fluoresc* 8, p. 022001. DOI: 10.1088/2050-6120/ab7365.

Deng, W., J. W. Rupon, I. Krivega, L. Breda, I. Motta, K. S. Jahn, A. Reik, P. D. Gregory, S. Rivella, A. Dean, and G. A. Blobel (2014). "Reactivation of developmentally silenced globin genes by forced chromatin looping." *Cell* 158, pp. 849–860. DOI: 10.1016/j.cell.2014.05.050.

Deng, W., X. Shi, R. Tjian, T. Lionnet, and R. H. Singer (2015). "CASFISH: CRISPR/Cas9-mediated in situ labeling of genomic loci in fixed cells." *Proc Natl Acad Sci U S A* 112, pp. 11870–11875. DOI: 10.1073/pnas.1515692112.

Deng, W., J. Lee, H. Wang, J. Miller, A. Reik, P. D. Gregory, A. Dean, and G. A. Blobel (2012). "Controlling long-range genomic interactions at a native locus by targeted tethering of a looping factor." *Cell* 149, pp. 1233–1244. DOI: 10.1016/j.cell.2012.03.051.

Deschout, H., K. Raemdonck, J. Demeester, S. C. De Smedt, and K. Braeckmans (2014). "FRAP in pharmaceutical research: practical guidelines and applications in drug delivery." *Pharm Res* 31, pp. 255–270. DOI: 10.1007/s11095-013-1146-9.

Di Giammartino, D. C., A. Polyzos, and E. Apostolou (2020). "Transcription factors: building hubs in the 3D space." *Cell Cycle* 19, pp. 2395–2410. DOI: 10.1080/15384101.2020.1805238.

Di Giulio, M. (2021). "The late appearance of DNA, the nature of the LUCA and ancestors of the domains of life." *Biosystems* 202, p. 104330. DOI: 10.1016/j.biosystems.2020.104330.

Diermeier, S., P. Kolovos, L. Heizinger, U. Schwartz, T. Georgomanolis, A. Zirkel, G. Wedemann, F. Grosveld, T. A. Knoch, R. Merkl, P. R. Cook, G. Langst, and A. Papantonis (2014). "TNFalpha signalling primes chromatin for NF-kappaB binding and induces rapid and widespread nucleosome repositioning." *Genome Biol* 15, p. 536. DOI: 10.1186/s13059-014-0536-6.

Dirks, R. M. and N. A. Pierce (2004). "Triggered amplification by hybridization chain reaction." *Proc Natl Acad Sci U S A* 101, pp. 15275–15278. DOI: 10.1073/pnas.0407024101.

Dixon, J. R., S. Selvaraj, F. Yue, A. Kim, Y. Li, Y. Shen, M. Hu, J. S. Liu, and B. Ren (2012). "Topological domains in mammalian genomes identified by analysis of chromatin interactions." *Nature* 485, pp. 376–380. DOI: 10.1038/nature11082.

Dixon, J. R. et al. (2018). "Integrative detection and analysis of structural variation in cancer genomes." *Nat Genet* 50, pp. 1388–1398. DOI: 10.1038/s41588-018-0195-8.

Dorighi, K. M., T. Swigut, T. Henriques, N. V. Bhanu, B. S. Scruggs, N. Nady, n. Still C. D., B. A. Garcia, K. Adelman, and J. Wysocka (2017). "Mll3 and Mll4 Facilitate Enhancer RNA Synthesis and Transcription from Promoters Independently of H3K4 Monomethylation." *Mol Cell* 66, pp. 568–576. DOI: 10.1016/j.molcel.2017.04.018.

Dostie, J., T. A. Richmond, R. A. Arnaout, R. R. Selzer, W. L. Lee, T. A. Honan, E. D. Rubio, A. Krumm, J. Lamb, and C. Nusbaum (2006). "Chromosome Conformation Capture Carbon Copy (5C): a massively parallel solution for mapping interactions between genomic elements." *Genome Res* 16, pp. 1299–1309. DOI: 10.1101/gr.5571506.

Doyle, B., G. Fudenberg, M. Imakaev, and L. A. Mirny (2014). "Chromatin loops as allosteric modulators of enhancer-promoter interactions." *PLoS Comput Biol* 10, p. e1003867. DOI: 10.1371/journal.pcbi.1003867.

Du, M., S. H. Stitzinger, J.-H. Spille, W.-K. Cho, C. Lee, M. Hijaz, A. Quintana, and I. I. Cissé (2024). "Direct observation of a condensate effect on super-enhancer controlled gene bursting." *Cell* 187, pp. 331–344. DOI: 10.1016/j.cell.2023.12.005.

Dupont, S. and S. A. Wickstrom (2022). "Mechanical regulation of chromatin and transcription." *Nat Rev Genet* 23, pp. 624–643. DOI: 10.1038/s41576-022-00493-6.

Ehrlich, M., M. A. Gama-Sosa, L. H. Huang, R. M. Midgett, K. C. Kuo, R. A. McCune, and C. Gehrke (1982). "Amount and distribution of 5-methylcytosine in human DNA from different types of tissues of cells." *Nucleic Acids Res* 10, pp. 2709–2721. DOI: 10.1093/nar/10.8.2709.

Elgin, S. C. and G. Reuter (2013). "Position-effect variegation, heterochromatin formation, and gene silencing in Drosophila." *Cold Spring Harb Perspect Biol* 5, p. a017780. DOI: `10.1101/cshperspect.a017780`.

Elimelech, A. and R. Y. Birnbaum (2020). "From 3D organization of the genome to gene expression." *Curr Opin Syst Biol* 22, pp. 22–31. DOI: `10.1016/j.coisb.2020.07.006`.

Elliott, A. D. (2020). "Confocal Microscopy: Principles and Modern Practices." *Curr Protoc Cytom* 92, p. e68. DOI: `10.1002/cpcy.68`.

Engreitz, J. M., J. E. Haines, E. M. Perez, G. Munson, J. Chen, M. Kane, P. E. McDonel, M. Guttman, and E. S. Lander (2016). "Local regulation of gene expression by lncRNA promoters, transcription and splicing." *Nature* 539, pp. 452–455. DOI: `10.1038/nature20149`.

Eres, I. E. and Y. Gilad (2021). "A TAD skeptic: is 3D genome topology conserved?" *tiG* 37, pp. 216–223. DOI: `10.1016/j.tig.2020.10.009`.

Ernst, J. and M. Kellis (2010). "Discovery and characterization of chromatin states for systematic annotation of the human genome." *Nat Biotechnol* 28, pp. 817–825. DOI: `10.1038/nbt.1662`.

Eskeland, R., M. Leeb, G. R. Grimes, C. Kress, S. Boyle, D. Sproul, N. Gilbert, Y. Fan, A. I. Skoultchi, A. Wutz, and W. A. Bickmore (2010). "Ring1B compacts chromatin structure and represses gene expression independent of histone ubiquitination." *Mol Cell* 38, pp. 452–464. DOI: `10.1016/j.molcel.2010.02.032`.

Fabre, P. J., M. Leleu, B. H. Mormann, L. Lopez-Delisle, D. Noordermeer, L. Beccari, and D. Duboule (2017). "Large scale genomic reorganization of topological domains at the HoxD locus." *Genome Biol* 18, pp. 1–15. DOI: `10.1186/s13059-017-1278-z`.

Finn, E. H. and T. Misteli (2019). "Molecular basis and biological function of variability in spatial genome organization." *Science* 365, p. eaaw9498. DOI: `10.1126/science.aaw9498`.

Finn, E. H., G. Pegoraro, H. B. Brandao, A. L. Valton, M. E. Oomen, J. Dekker, L. Mirny, and T. Misteli (2019). "Extensive Heterogeneity and Intrinsic Variation in Spatial Genome Organization." *Cell* 176, pp. 1502–1515. DOI: `10.1016/j.cell.2019.01.020`.

Fiorillo, L., F. Musella, M. Conte, R. Kempfer, A. M. Chiariello, S. Bianco, A. Kukalev, I. Irastorza-Azcarate, A. Esposito, and A. Abraham (2021). "Comparison of the Hi-C, GAM and SPRITE methods using polymer models of chromatin." *Nat methods* 18, pp. 482–490. DOI: `10.1038/s41592-021-01251-y`.

Flemming, W. (1882). *Zellsubstanz, kern und zelltheilung*. FCW Vogel, Leipzig. DOI: `10.5962/bhl.title.168645`.

Flyamer, I. M., J. Gassler, M. Imakaev, H. B. Brandao, S. V. Ulianov, N. Abdennur, S. V. Razin, L. A. Mirny, and K. Tachibana-Konwalski (2017). "Single-nucleus Hi-C reveals unique chromatin reorganization at oocyte-to-zygote transition." *Nature* 544, pp. 110–114. DOI: `10.1038/nature21711`.

Franke, M. et al. (2016). "Formation of new chromatin domains determines pathogenicity of genomic duplications." *Nature* 538, pp. 265–269. DOI: `10.1038/nature19800`.

Franklin, R. E. and R. G. Gosling (1953). "Molecular configuration in sodium thymonucleate." *Nature* 171, pp. 740–741. DOI: `10.1038/171740a0`.

Freier, S. M., R. Kierzek, J. A. Jaeger, N. Sugimoto, M. H. Caruthers, T. Neilson, and D. H. Turner (1986). "Improved free-energy parameters for predictions of RNA duplex stability." *Proc Natl Acad Sci U S A* 83, pp. 9373–9377. DOI: `10.1073/pnas.83.24.9373`.

Fritz, A. J., N. Sehgal, A. Pliss, J. Xu, and R. Berezney (2019). "Chromosome territories and the global regulation of the genome." *Genes Chromosom Cancer* 58, pp. 407–426. DOI: `10.1002/gcc.22732`.

Frixione, E. and L. Ruiz-Zamarripa (2019). "The "scientific catastrophe" in nucleic acids research that boosted molecular biology." *Journal of Biological Chemistry* 294, pp. 2249–2255. DOI: `10.1074/jbc.CL119.007397`.

Fudenberg, G., M. Imakaev, C. Lu, A. Goloborodko, N. Abdennur, and L. A. Mirny (2016). "Formation of Chromosomal Domains by Loop Extrusion." *Cell Rep* 15, pp. 2038–49. DOI: `10.1016/j.celrep.2016.04.085`.

Fukaya, T., B. Lim, and M. Levine (2016). "Enhancer Control of Transcriptional Bursting." *Cell* 166, pp. 358–368. DOI: `10.1016/j.cell.2016.05.025`.

Fussner, E., M. Strauss, U. Djuric, R. Li, K. Ahmed, M. Hart, J. Ellis, and D. P. Bazett-Jones (2012). "Open and closed domains in the mouse genome are configured as 10-nm chromatin fibres." *EMBO Rep* 13, pp. 992–996. DOI: `10.1038/embor.2012.139`.

Gabriele, M., H. B. Brandao, S. Grosse-Holz, A. Jha, G. M. Dailey, C. Cattoglio, T. S. Hsieh, L. Mirny, C. Zechner, and A. S. Hansen (2022). "Dynamics of CTCF- and cohesin-mediated chromatin looping revealed by live-cell imaging." *Science* 376, pp. 496–501. DOI: `10.1126/science.abn6583`.

Galbraith, C. G. and J. A. Galbraith (2011). "Super-resolution microscopy at a glance." *J Cell Sci* 124, pp. 1607–1611. DOI: `10.1242/jcs.080085`.

Gall, J. G. (1968). "Differential synthesis of the genes for ribosomal RNA during amphibian oogenesis." *Proc Natl Acad Sci U S A* 60, pp. 553–560. DOI: `10.1073/pnas.60.2.553`.

Gall, J. G. and M. L. Pardue (1969). "Formation and detection of RNA-DNA hybrid molecules in cytological preparations." *Proc Natl Acad Sci U S A* 63, pp. 378–383. DOI: 10.1073/pnas.63.2.378.

Gandhi, R., P. J. Gillespie, and T. Hirano (2006). "Human Wapl is a cohesin-binding protein that promotes sister-chromatid resolution in mitotic prophase." *Curr Biol* 16, pp. 2406–2417. DOI: 10.1016/j.cub.2006.10.061.

Ganji, M., I. A. Shaltiel, S. Bisht, E. Kim, A. Kalichava, C. H. Haering, and C. Dekker (2018). "Real-time imaging of DNA loop extrusion by condensin." *Science* 360, pp. 102–105. DOI: 10.1126/science.aar7831.

Gardner, A. F., K. M. Jackson, M. M. Boyle, J. A. Buss, V. Potapov, A. M. Gehring, K. M. Zatopek, J. Correa I. R., J. L. Ong, and W. E. Jack (2019). "Therminator DNA Polymerase: Modified Nucleotides and Unnatural Substrates." *Front Mol Biosci* 6, p. 28. DOI: 10.3389/fmolb.2019.00028.

Garimberti, E. and S. Tosi (2010). "Fluorescence in situ hybridization (FISH), basic principles and methodology." *Methods Mol Biol* 659, pp. 3–20. DOI: 10.1007/978-1-60761-789-1_1.

Garini, Y., I. T. Young, and G. McNamara (2006). "Spectral imaging: principles and applications." *Cytometry A* 69, pp. 735–47. DOI: 10.1002/cyto.a.20311.

Gasperini, M., A. J. Hill, J. L. McFaline-Figueroa, B. Martin, S. Kim, M. D. Zhang, D. Jackson, A. Leith, J. Schreiber, and W. S. Noble (2019). "A genome-wide framework for mapping gene regulation via cellular genetic screens." *Cell* 176, pp. 377–390. DOI: 10.1016/j.cell.2018.11.029.

Gassler, J., W. Kobayashi, I. Gáspár, S. Ruangroengkulrith, A. Mohanan, L. Gómez Hernández, P. Kravchenko, M. Kümmecke, A. Lalic, N. Rifel, et al. (2022). "Zygotic genome activation by the totipotency pioneer factor Nr5a2." *Science* 378, pp. 1305–1315. DOI: 10.1126/science.abn7478.

Gates, L. A., C. E. Foulds, and B. W. O'Malley (2017). "Histone Marks in the 'Driver's Seat': Functional Roles in Steering the Transcription Cycle." *Trends Biochem Sci* 42, pp. 977–989. DOI: 10.1016/j.tibs.2017.10.004.

Gavrilov, A. A., A. K. Golov, and S. V. Razin (2013). "Actual ligation frequencies in the chromosome conformation capture procedure." *PLoS One* 8, p. e60403. DOI: 10.1371/journal.pone.0060403.

Gelali, E., G. Girelli, M. Matsumoto, E. Wernersson, J. Custodio, A. Mota, M. Schweitzer, K. Ferenc, X. Li, and R. Mirzazadeh (2019). "iFISH is a publically available resource enabling versatile DNA FISH to study genome architecture." *Nat Commun* 10, p. 1636. DOI: 10.1038/s41467-019-09616-w.

Gerlich, D., J. Beaudouin, B. Kalbfuss, N. Daigle, R. Eils, and J. Ellenberg (2003). "Global chromosome positions are transmitted through mitosis in mammalian cells." *Cell* 112, pp. 751–764. DOI: 10.1016/S0092-8674(03)00189-2.

Gervasio, J., H. da Costa Oliveira, A. G. da Costa Martins, J. B. Pesquero, B. M. Verona, and N. N. P. Cerize (2024). "How close are we to storing data in DNA?" *Trends Biotechnol* 42, pp. 156–167. DOI: 10.1016/j.tibtech.2023.08.001.

Giorgetti, L. and E. Heard (2016). "Closing the loop: 3C versus DNA FISH." *Genome Biol* 17, p. 215. DOI: 10.1186/s13059-016-1081-2.

Goehring, N. W., D. Chowdhury, A. A. Hyman, and S. W. Grill (2010). "FRAP analysis of membrane-associated proteins: lateral diffusion and membrane-cytoplasmic exchange." *Biophys J* 99, pp. 2443–2452. DOI: 10.1016/j.bpj.2010.08.033.

Goel, V. Y. and A. S. Hansen (2021). "The macro and micro of chromosome conformation capture." *Wiley Interdiscip Rev Dev Biol* 10, p. e395. DOI: 10.1002/wdev.395.

Gomez-Garcia, P. A., S. Portillo-Ledesma, M. V. Neguembor, M. Pesaresi, W. Oweis, T. Rohrlich, S. Wieser, E. Meshorer, T. Schlick, M. P. Cosma, and M. Lakadamyali (2021). "Mesoscale Modeling and Single-Nucleosome Tracking Reveal Remodeling of Clutch Folding and Dynamics in Stem Cell Differentiation." *Cell Rep* 34, p. 108614. DOI: 10.1016/j.celrep.2020.108614.

Grimm, J. B. and L. D. Lavis (2022). "Caveat fluorophore: an insiders' guide to small-molecule fluorescent labels." *Nat Methods* 19, pp. 149–158. DOI: 10.1038/s41592-021-01338-6.

Guelen, L., L. Pagie, E. Brasset, W. Meuleman, M. B. Faza, W. Talhout, B. H. Eussen, A. de Klein, L. Wessels, W. de Laat, and B. van Steensel (2008). "Domain organization of human chromosomes revealed by mapping of nuclear lamina interactions." *Nature* 453, pp. 948–951. DOI: 10.1038/nature06947.

Gupta, R. M., J. Hadaya, A. Trehan, S. M. Zekavat, C. Roselli, D. Klarin, C. A. Emdin, C. R. Hilvering, V. Bianchi, and C. Mueller (2017). "A genetic variant associated with five vascular diseases is a distal regulator of endothelin-1 gene expression." *Cell* 170, 522–533. e15. DOI: 10.1016/j.cell.2017.06.049.

Gustafsson, M. G. (2000). "Surpassing the lateral resolution limit by a factor of two using structured illumination microscopy." *J Microsc* 198, pp. 82–87. DOI: 10.1046/j.1365-2818.2000.00710.x.

Haarhuis, J. H. I., R. H. van der Weide, V. A. Blomen, J. O. Yanez-Cuna, M. Amendola, M. S. van Ruiten, P. H. L. Krijger, H. Teunissen, R. H. Medema, B. van Steensel, T. R. Brummelkamp,

E. de Wit, and B. D. Rowland (2017). "The Cohesin Release Factor WAPL Restricts Chromatin Loop Extension." *Cell* 169, pp. 693–707. DOI: 10.1016/j.cell.2017.04.013.

Haberle, V. and A. Stark (2018). "Eukaryotic core promoters and the functional basis of transcription initiation." *Nat Rev Mol Cell Biol* 19, pp. 621–637. DOI: 10.1038/s41580-018-0028-8.

Halfon, M. S. (2020). "Silencers, Enhancers, and the Multifunctional Regulatory Genome." *Trends Genet* 36, pp. 149–151. DOI: 10.1016/j.tig.2019.12.005.

Hanahan, D. (2022). "Hallmarks of Cancer: New Dimensions." *Cancer Discov* 12, pp. 31–46. DOI: 10.1158/2159-8290.CD-21-1059.

Harrison, K. A., J. Thaler, S. L. Pfaff, H. Gu, and J. H. Kehrl (1999). "Pancreas dorsal lobe agenesis and abnormal islets of Langerhans in Hlxb9-deficient mice." *Nat Genet* 23, pp. 71–75. DOI: 10.1038/12674.

Hausmann, M., R. Winkler, G. Hildenbrand, J. Finsterle, A. Weisel, A. Rapp, E. Schmitt, S. Janz, and C. Cremer (2003). "COMBO-FISH: specific labeling of nondenatured chromatin targets by computer-selected DNA oligonucleotide probe combinations." *Biotechniques* 35, pp. 564–70. DOI: 10.2144/03353rr03.

Hay, D. et al. (2016). "Genetic dissection of the alpha-globin super-enhancer in vivo." *Nat Genet* 48, pp. 895–903. DOI: 10.1038/ng.3605.

Hell, S. W. (2007). "Far-field optical nanoscopy." *Science* 316, pp. 1153–1158. DOI: 10.1126/science.1137395.

Hell, S. W. and M. Kroug (1995). "Ground-state-depletion fluorscence microscopy: A concept for breaking the diffraction resolution limit." *Applied Physics B* 60, pp. 495–497. DOI: 10.1007/BF01081333.

Helmsauer, K. et al. (2020). "Enhancer hijacking determines extrachromosomal circular MYCN amplicon architecture in neuroblastoma." *Nat Commun* 11, p. 5823. DOI: 10.1038/s41467-020-19452-y.

Hernandez, M. R., M. B. Davis, J. Jiang, E. A. Brouhard, A. F. Severson, and G. Csankovszki (2018). "Condensin I protects meiotic cohesin from WAPL-1 mediated removal." *PLoS Genet* 14, p. e1007382. DOI: 10.1371/journal.pgen.1007382.

Hershberg, E. A., C. K. Camplisson, J. L. Close, S. Attar, R. Chern, Y. Liu, S. Akilesh, P. R. Nicovich, and B. J. Beliveau (2021). "PaintSHOP enables the interactive design of transcriptome- and genome-scale oligonucleotide FISH experiments." *Nat Methods* 18, pp. 937–944. DOI: 10.1038/s41592-021-01273-6.

Hershey, A. D. and M. Chase (1952). "Independent functions of viral protein and nucleic acid in growth of bacteriophage." *J Gen Physiol* 36, pp. 39–56. DOI: 10.1085/jgp.36.1.39.

Hess, S. T., T. P. Girirajan, and M. D. Mason (2006). "Ultra-high resolution imaging by fluorescence photoactivation localization microscopy." *Biophys J* 91, pp. 4258–4272. DOI: 10.1529/biophysj.106.091116.

Hickey, S. M., B. Ung, C. Bader, R. Brooks, J. Lazniewska, I. R. D. Johnson, A. Sorvina, J. Logan, C. Martini, C. R. Moore, L. Karageorgos, M. J. Sweetman, and D. A. Brooks (2021). "Fluorescence Microscopy-An Outline of Hardware, Biological Handling, and Fluorophore Considerations." *Cells* 11, p. 35. DOI: 10.3390/cells11010035.

Hilton, I. B., A. M. D'Ippolito, C. M. Vockley, P. I. Thakore, G. E. Crawford, T. E. Reddy, and C. A. Gersbach (2015). "Epigenome editing by a CRISPR-Cas9-based acetyltransferase activates genes from promoters and enhancers." *Nat Biotechnol* 33, pp. 510–7. DOI: 10.1038/nbt.3199.

Hock, H. and A. Shimamura (n.d.). "ETV6 in hematopoiesis and leukemia predisposition." In: *Semin Hematol*. Vol. 54. Elsevier, pp. 98–104. DOI: 10.1053/j.seminhematol.2017.04.005.

Hoetelmans, R. W., F. A. Prins, I. Cornelese-ten Velde, J. van der Meer, C. J. van de Velde, and J. H. van Dierendonck (2001). "Effects of acetone, methanol, or paraformaldehyde on cellular structure, visualized by reflection contrast microscopy and transmission and scanning electron microscopy." *Appl Immunohistochem Mol Morphol* 9, pp. 346–351. DOI: 10.1097/00129039-200112000-00010.

Holliday, R. and J. E. Pugh (1975). "DNA Modification Mechanisms and Gene Activity During Development: Developmental clocks may depend on the enzymic modification of specific bases in repeated DNA sequences." *Science* 187, pp. 226–232. DOI: 10.1126/science.187.4173.226.

Hotchkiss, R. D. (1948). "The quantitative separation of purines, pyrimidines, and nucleosides by paper chromatography." *J Biol Chem* 175, pp. 315–332. DOI: 10.1016/S0021-9258(18)57261-6.

Hottin, A. and A. Marx (2016). "Structural Insights into the Processing of Nucleobase-Modified Nucleotides by DNA Polymerases." *Acc Chem Res* 49, pp. 418–27. DOI: 10.1021/acs.accounts.5b00544.

Hsieh, T. H., A. Weiner, B. Lajoie, J. Dekker, N. Friedman, and O. J. Rando (2015). "Mapping Nucleosome Resolution Chromosome Folding in Yeast by Micro-C." *Cell* 162, pp. 108–119. DOI: 10.1016/j.cell.2015.05.048.

Hsieh, T. S., C. Cattoglio, E. Slobodyanyuk, A. S. Hansen, O. J. Rando, R. Tjian, and X. Darzacq (2020). "Resolving the 3D Landscape of Transcription-Linked Mammalian Chromatin Folding." *Mol Cell* 78, pp. 539–553. DOI: 10.1016/j.molcel.2020.03.002.

Hu, M., B. Yang, Y. Cheng, J. S. Radda, Y. Chen, M. Liu, and S. Wang (2020). "ProbeDealer is a convenient tool for designing probes for highly multiplexed fluorescence in situ hybridization." *Sci Rep* 10, p. 22031. DOI: 10.1038/s41598-020-76439-x.

Huang, J., K. Li, W. Cai, X. Liu, Y. Zhang, S. H. Orkin, J. Xu, and G. C. Yuan (2018). "Dissecting super-enhancer hierarchy based on chromatin interactions." *Nat Commun* 9, p. 943. DOI: 10.1038/s41467-018-03279-9.

Huang, J., X. Liu, D. Li, Z. Shao, H. Cao, Y. Zhang, E. Trompouki, T. V. Bowman, L. I. Zon, G. C. Yuan, S. H. Orkin, and J. Xu (2016). "Dynamic Control of Enhancer Repertoires Drives Lineage and Stage-Specific Transcription during Hematopoiesis." *Dev Cell* 36, pp. 9–23. DOI: 10.1016/j.devcel.2015.12.014.

Huber, D., L. V. Von Voithenberg, and G. V. Kaigala (2018). "Fluorescence in situ hybridization (FISH): History, limitations and what to expect from micro-scale FISH?" *MNE* 1, pp. 15–24. DOI: 10.1016/j.mne.2018.10.006.

Hughes, L. D., R. J. Rawle, and S. G. Boxer (2014). "Choose your label wisely: water-soluble fluorophores often interact with lipid bilayers." *PloS one* 9, p. e87649. DOI: 10.1371/journal.pone.0087649.

Hughes, R. A. and A. D. Ellington (2017). "Synthetic DNA Synthesis and Assembly: Putting the Synthetic in Synthetic Biology." *Cold Spring Harb Perspect Biol* 9, p. a023812. DOI: 10.1101/cshperspect.a023812.

Humbel, B. M., H. Schwarz, E. M. Tranfield, and R. A. Fleck (2019). *Chemical fixation*. Vol. 2. Biological Field Emission Scanning Electron Microscopy. John Wiley Sons, Chichester. DOI: 10.1002/9781118663233.ch10.

Ingenhag, D., S. Reister, F. Auer, S. Bhatia, S. Wildenhain, D. Picard, M. Remke, J. I. Hoell, A. Kloetgen, D. Sohn, R. U. Janicke, G. Koegler, A. Borkhardt, and J. Hauer (2019). "The home-obox transcription factor HB9 induces senescence and blocks differentiation in hematopoietic stem and progenitor cells." *Haematologica* 104, pp. 35–46. DOI: 10.3324/haematol.2018.189407.

Ishizuka, T., H. S. Liu, K. Ito, and Y. Xu (2016). "Fluorescence imaging of chromosomal DNA using click chemistry." *Sci Rep* 6, p. 33217. DOI: 10.1038/srep33217.

Izzo, A. and R. Schneider (2016). "The role of linker histone H1 modifications in the regulation of gene expression and chromatin dynamics." *Biochim Biophys Acta* 1859, pp. 486–495. DOI: 10.1016/j.bbagrm.2015.09.003.

Jabłoński, A. (1935). "Über den mechanismus der photolumineszenz von farbstoffphosphoren." *Z Phys* 94, pp. 38–46. DOI: 10.1007/BF01330795.

Jamur, M. C. and C. Oliver (2010). "Permeabilization of cell membranes." *Methods Mol Biol* 588, pp. 63–66. DOI: 10.1007/978-1-59745-324-0_9.

Janik, E., M. Niemcewicz, M. Ceremuga, L. Krzowski, J. Saluk-Bijak, and M. Bijak (2020). "Various aspects of a gene editing system—crispr-cas9." *Int J Mol Sci* 21, p. 9604. DOI: 10.1007/978-1-59745-324-0_9.

Jares-Erijman, E. A. and T. M. Jovin (2003). "FRET imaging." *Nat Biotechnol* 21, pp. 1387–1395. DOI: 10.1038/nbt896.

Jiang, G., H. Liu, H. Liu, G. Ke, T. B. Ren, B. Xiong, X. B. Zhang, and L. Yuan (2024). "Chemical Approaches to Optimize the Properties of Organic Fluorophores for Imaging and Sensing." *Angew Chem Int Ed Engl* 63, p. e202315217. DOI: 10.1002/anie.202315217.

Jonkman, J., C. M. Brown, G. D. Wright, K. I. Anderson, and A. J. North (2020). "Tutorial: guidance for quantitative confocal microscopy." *Nat Protoc* 15, pp. 1585–1611. DOI: 10.1038/s41596-020-0313-9.

Jun, J. V., D. M. Chenoweth, and E. J. Petersson (2020). "Rational design of small molecule fluorescent probes for biological applications." *Org Biomol Chem* 18, pp. 5747–5763. DOI: 10.1039/d0ob01131b.

Jungmann, R., M. S. Avendano, J. B. Woehrstein, M. Dai, W. M. Shih, and P. Yin (2014). "Multiplexed 3D cellular super-resolution imaging with DNA-PAINT and Exchange-PAINT." *Nat Methods* 11, pp. 313–318. DOI: 10.1038/nmeth.2835.

Kalhor, R., H. Tjong, N. Jayathilaka, F. Alber, and L. Chen (2012). "Genome architectures revealed by tethered chromosome conformation capture and population-based modeling." *Nature Biotechnol* 30, pp. 90–98. DOI: 10.1038/nbt.2057.

Kane, L., I. Williamson, I. M. Flyamer, Y. Kumar, R. E. Hill, L. A. Lettice, and W. A. Bickmore (2022). "Cohesin is required for long-range enhancer action at the Shh locus." *Nat Struct Mol Biol* 29, pp. 891–897. DOI: 10.1038/s41594-022-00821-8.

Kang, J., O. Kaczmarek, J. Liebscher, and L. Dähne (2010). "Prevention of H-aggregates formation in Cy5 labeled macromolecules." *Int J Polym Sci* 2010, p. 264781. DOI: 10.1155/2010/264781.

Karagiannis, T. C., M. Wall, K. Ververis, E. Pitsillou, S. M. Tortorella, P. A. Wood, H. Rafehi, I. Khurana, S. S. Maxwell, A. Hung, J. Vongsvivut, and A. El-Osta (2023). "Characterization of K562 cells: uncovering novel chromosomes, assessing transferrin receptor expression, and probing pharmacological therapies." *Cell Mol Life Sci* 80, p. 248. DOI: 10.1007/s00018-023-04905-6.

Kasha, M., H. R. Rawls, and M Ashraf El-Bayoumi (1965). "The exciton model in molecular spectroscopy." *Pure Appl Chem* 11, pp. 371–392. DOI: 10.1351/pac196511030371.

Kempfer, R. and A. Pombo (2020). "Methods for mapping 3D chromosome architecture." *Nat Rev Genet* 21, pp. 207–226. DOI: 10.1038/s41576-019-0195-2.

Kepper, N., D. Foethke, R. Stehr, G. Wedemann, and K. Rippe (2008). "Nucleosome geometry and internucleosomal interactions control the chromatin fiber conformation." *Biophys J* 95, pp. 3692–3705. DOI: 10.1529/biophysj.107.121079.

Keshava, N. and J. F. Mustard (2002). "Spectral unmixing." *IEEE Signal Process Mag* 19, pp. 44–57. DOI: 10.1109/79.974727.

Kessler, L. F., A. Balakrishnan, N. S. Deussner-Helfmann, Y. Li, M. Mantel, M. Glogger, H. D. Barth, M. S. Dietz, and M. Heilemann (2023). "Self-quenched Fluorophore Dimers for DNA-PAINT and STED Microscopy." *Angew Chem Int Ed Engl* 62, p. e202307538. DOI: 10.1002/anie.202307538.

Kim, I. H., J. Nagel, S. Otten, B. Knerr, R. Eils, K. Rohr, and S. Dietzel (2007). "Quantitative comparison of DNA detection by GFP-lac repressor tagging, fluorescence in situ hybridization and immunostaining." *BMC Biotechnol* 7, p. 92. DOI: 10.1186/1472-6750-7-92.

Kim, T.-K., M. Hemberg, and J. M. Gray (2015). "Enhancer RNAs: a class of long noncoding RNAs synthesized at enhancers." *Cold Spring Harb Perspect Biol* 7, p. a018622. DOI: 10.1101/cshperspect.a018622.

Kim, T.-K., M. Hemberg, J. M. Gray, A. M. Costa, D. M. Bear, J. Wu, D. A. Harmin, M. Laptewicz, K. Barbara-Haley, and S. Kuersten (2010). "Widespread transcription at neuronal activity-regulated enhancers." *Nature* 465, pp. 182–187. DOI: 10.1038/nature09033.

Kim, Y., Z. Shi, H. Zhang, I. J. Finkelstein, and H. Yu (2019). "Human cohesin compacts DNA by loop extrusion." *Science* 366, pp. 1345–1349. DOI: 10.1126/science.aaz4475.

Kind, J. et al. (2015). "Genome-wide maps of nuclear lamina interactions in single human cells." *Cell* 163, pp. 134–147. DOI: 10.1016/j.cell.2015.08.040.

Kishi, J. Y., S. W. Lapan, B. J. Beliveau, E. R. West, A. Zhu, H. M. Sasaki, S. K. Saka, Y. Wang, C. L. Cepko, and P. Yin (2019). "SABER amplifies FISH: enhanced multiplexed imaging of RNA and DNA in cells and tissues." *Nat Methods* 16, pp. 533–544. DOI: 10.1038/s41592-019-0404-0.

Kloetgen, A. et al. (2020). "Three-dimensional chromatin landscapes in T cell acute lymphoblastic leukemia." *Nat Genet* 52, pp. 388–400. DOI: 10.1038/s41588-020-0602-9.

Kner, P., B. B. Chhun, E. R. Griffis, L. Winoto, and M. G. Gustafsson (2009). "Super-resolution video microscopy of live cells by structured illumination." *Nat Methods* 6, pp. 339–342. DOI: 10.1038/nmeth.1324.

Kodgule, R. et al. (2023). "ETV6 Deficiency Unlocks ERG-Dependent Microsatellite Enhancers to Drive Aberrant Gene Activation in B-Lymphoblastic Leukemia." *Blood Cancer Discov* 4, pp. 34–53. DOI: 10.1158/2643-3230.BCD-21-0224.

Kolb, H. C., M. G. Finn, and K. B. Sharpless (2001). "Click Chemistry: Diverse Chemical Function from a Few Good Reactions." *Angew Chem Int Ed Engl* 40, pp. 2004–2021. DOI: 10.1002/1521-3773(20010601)40:11<2004::AID-ANIE2004>3.0.CO;2-5.

Kolovos, P., T. A. Knoch, F. G. Grosveld, P. R. Cook, and A. Papantonis (2012). "Enhancers and silencers: an integrated and simple model for their function." *Epigenet Chromatin* 5, pp. 1–8. DOI: 10.1186/1756-8935-5-1.

Kornberg, R. D. (1974). "Chromatin Structure: A Repeating Unit of Histones and DNA: Chromatin structure is based on a repeating unit of eight histone molecules and about 200 DNA base pairs." *Science* 184, pp. 868–871. DOI: 10.1126/science.184.4139.868.

Kosak, S., J. Skok, L Kay, K. Medina, R Riblet, M. Le Beau, C Schildkraut, A. Fisher, and H Singh (2002). "Immunoglobulin loci undergo lineage-specific subnuclear compartmentalisation." *Science* 296, pp. 158–162. DOI: 10.1126/science.1068768.

Kossel, A. (1884). "Ueber einen peptonartigen Bestandtheil des Zellkerns." *Physiol Chem*, Physiol Chem. DOI: 10.1515/bchm1.1884.8.6.511.

Kotova, E. Y., F.-K. Hsieh, H.-W. Chang, N. V. Maluchenko, M.-F. Langelier, J. M. Pascal, D. S. Luse, A. V. Feofanov, and V. M. Studitsky (2022). "Human PARP1 facilitates transcription through a nucleosome and histone displacement by Pol II in vitro." *Int J Mol Sci* 23, p. 7107. DOI: 10.3390/ijms23137107.

Krijger, P. H. and W. de Laat (2016). "Regulation of disease-associated gene expression in the 3D genome." *Nat Rev Mol Cell Biol* 17, pp. 771–782. DOI: 10.1038/nrm.2016.138.

Kropp, H. M., K. Betz, J. Wirth, K. Diederichs, and A. Marx (2017). "Crystal structures of ternary complexes of archaeal B-family DNA polymerases." *PLoS One* 12, p. e0188005. DOI: 10.1371/journal.pone.0188005.

Kropp, H. M., K. Diederichs, and A. Marx (2019). "The Structure of an Archaeal B-Family DNA Polymerase in Complex with a Chemically Modified Nucleotide." *Angew Chem Int Ed Engl* 58, pp. 5457–5461. DOI: 10.1002/anie.201900315.

Krufczik, M., A. Sievers, A. Hausmann, J.-H. Lee, G. Hildenbrand, W. Schaufler, and M. Hausmann (2017). "Combining low temperature fluorescence DNA-hybridization, immunostaining, and super-resolution localization microscopy for nano-structure analysis of ALU

elements and their influence on chromatin structure." *Int J Mol Sci* 18, p. 1005. DOI: 10.3390/ijms18051005.

Kubo, N. et al. (2021). "Promoter-proximal CTCF binding promotes distal enhancer-dependent gene activation." *Nat Struct Mol Biol* 28, pp. 152–161. DOI: 10.1038/s41594-020-00539-5.

Kucho, K., H. Yoneda, M. Harada, and M. Ishiura (2004). "Determinants of sensitivity and specificity in spotted DNA microarrays with unmodified oligonucleotides." *Genes Genet Syst* 79, pp. 189–97. DOI: 10.1266/ggs.79.189.

Kurz, A., S. Lampel, J. E. Nickolenko, J. Bradl, A. Benner, R. M. Zirbel, T. Cremer, and P. Lichter (1996). "Active and inactive genes localize preferentially in the periphery of chromosome territories." *J Cell Biol* 135, pp. 1195–1205. DOI: 10.1083/jcb.135.5.1195.

Lai, B., W. Gao, K. Cui, W. Xie, Q. Tang, W. Jin, G. Hu, B. Ni, and K. Zhao (2018). "Principles of nucleosome organization revealed by single-cell micrococcal nuclease sequencing." *Nature* 562, pp. 281–285. DOI: 10.1038/s41586-018-0567-3.

Lambert, S. A., A. Jolma, L. F. Campitelli, P. K. Das, Y. Yin, M. Albu, X. Chen, J. Taipale, T. R. Hughes, and M. T. Weirauch (2018). "The human transcription factors." *Cell* 172, pp. 650–665. DOI: 10.1016/j.cell.2018.01.029.

Langmead, B. and S. L. Salzberg (2012). "Fast gapped-read alignment with Bowtie 2." *Nat Methods* 9, pp. 357–359. DOI: 10.1038/nmeth.1923.

Lansdorp, P. M., N. P. Verwoerd, F. M. van de Rijke, V. Dragowska, M. T. Little, R. W. Dirks, A. K. Raap, and H. J. Tanke (1996). "Heterogeneity in telomere length of human chromosomes." *Hum Mol Genet* 5, pp. 685–691. DOI: 10.1093/hmg/5.5.685.

Lettice, L. A., S. J. Heaney, L. A. Purdie, L. Li, P. De Beer, B. A. Oostra, D. Goode, G. Elgar, R. E. Hill, and E. de Graaff (2003). "A long-range Shh enhancer regulates expression in the developing limb and fin and is associated with preaxial polydactyly." *Hum Mol Genet* 12, pp. 1725–1735. DOI: 10.1093/hmg/ddg180.

Levene, P. A. and J. A. Mandel (1908). "Über die Konstitution der Thymo-nucleinsäure." *Dtsch Chem Ges* 41, pp. 1905–1909. DOI: 10.1002/cber.19080410266.

Li, W. (2022). *The 5th Edition of the World Health Organization Classification of Hematolymphoid Tumors*. Exon Publications, pp. 1–21. DOI: 10.36255/exon-publications-leukemia-who-5th-edition-hematolymphoid-tumors.

Lieberman-Aiden, E. et al. (2009). "Comprehensive mapping of long-range interactions reveals folding principles of the human genome." *Science* 326, pp. 289–293. DOI: 10.1126/science.1181369.

Lieleg, C., P. Ketterer, J. Nuebler, J. Ludwigsen, U. Gerland, H. Dietz, F. Mueller-Planitz, and P. Korber (2015). "Nucleosome spacing generated by ISWI and CHD1 remodelers is constant regardless of nucleosome density." *MCB* 35, pp. 1588–1605. DOI: 10.1128/MCB.01070-14.

Lieu, P. T., P. Jozsi, P. Gilles, and T. Peterson (2005). "Development of a DNA-labeling system for array-based comparative genomic hybridization." *J Biomol Tech* 16, pp. 104–111.

Liu, G. and T. Zhang (2021). "Single Copy Oligonucleotide Fluorescence In Situ Hybridization Probe Design Platforms: Development, Application and Evaluation." *Int J Mol Sci* 22, p. 7124. DOI: 10.3390/ijms22137124.

Liu, M., Y. Lu, B. Yang, Y. Chen, J. S. D. Radda, M. Hu, S. G. Katz, and S. Wang (2020). "Multiplexed imaging of nucleome architectures in single cells of mammalian tissue." *Nat Commun* 11, p. 2907. DOI: 10.1038/s41467-020-16732-5.

Lizardi, P. M., X. Huang, Z. Zhu, P. Bray-Ward, D. C. Thomas, and D. C. Ward (1998). "Mutation detection and single-molecule counting using isothermal rolling-circle amplification." *Nat Genet* 19, pp. 225–232. DOI: 10.1038/898.

Lorén, N., J. Hagman, J. K. Jonasson, H. Deschout, D. Bernin, F. Cella-Zanacchi, A. Diaspro, J. G. McNally, M. Ameloot, and N. Smisdom (2015). "Fluorescence recovery after photobleaching in material and life sciences: putting theory into practice." *Q Rev Biophys* 48, pp. 323–387. DOI: 10.1017/S0033583515000013.

Lu, C. M., J. Kwan, A. Baumgartner, J. F. Weier, M. Wang, T. Escudero, S. Munne, H. F. Zitzelsberger, and H. U. Weier (2009). "DNA probe pooling for rapid delineation of chromosomal breakpoints." *J Histochem Cytochem* 57, pp. 587–597. DOI: 10.1369/jhc.2009.953638.

Luger, K., A. W. Mäder, R. K. Richmond, D. F. Sargent, and T. J. Richmond (1997). "Crystal structure of the nucleosome core particle at 2.8 Å resolution." *Nature* 389, pp. 251–260. DOI: 10.1038/38444.

Lupianez, D. G. et al. (2015). "Disruptions of topological chromatin domains cause pathogenic rewiring of gene-enhancer interactions." *Cell* 161, pp. 1012–1025. DOI: 10.1016/j.cell.2015.04.004.

Luu, D. T. and C. Maurel (2013). "Aquaporin trafficking in plant cells: an emerging membrane-protein model." *Traffic* 14, pp. 629–635. DOI: 10.1111/tra.12062.

Ma, W., F. Ay, C. Lee, G. Gulsoy, X. Deng, S. Cook, J. Hesson, C. Cavanaugh, C. B. Ware, A. Krumm, J. Shendure, C. A. Blau, C. M. Disteche, W. S. Noble, and Z. Duan (2015). "Fine-scale chromatin interaction maps reveal the cis-regulatory landscape of human lincRNA genes." *Nat Methods* 12, pp. 71–78. DOI: 10.1038/nmeth.3205.

Magana-Acosta, M. and V. Valadez-Graham (2020). "Chromatin Remodelers in the 3D Nuclear Compartment." *Front Genet* 11, p. 600615. DOI: 10.3389/fgene.2020.600615.

Marcais, G. and C. Kingsford (2011). "A fast, lock-free approach for efficient parallel counting of occurrences of k-mers." *Bioinformatics* 27, pp. 764–70. DOI: 10.1093/bioinformatics/btr011.

Markaki, Y., D. Smeets, S. Fiedler, V. J. Schmid, L. Schermelleh, T. Cremer, and M. Cremer (2012). "The potential of 3D-FISH and super-resolution structured illumination microscopy for studies of 3D nuclear architecture: 3D structured illumination microscopy of defined chromosomal structures visualized by 3D (immuno)-FISH opens new perspectives for studies of nuclear architecture." *Bioessays* 34, pp. 412–426. DOI: 10.1002/bies.201100176.

Maslova, A. and A. Krasikova (2021). "FISH Going Meso-Scale: A Microscopic Search for Chromatin Domains." *Front Cell Dev Biol* 9, p. 753097. DOI: 10.3389/fcell.2021.753097.

Mateo, L. J., S. E. Murphy, A. Hafner, I. S. Cinquini, C. A. Walker, and A. N. Boettiger (2019). "Visualizing DNA folding and RNA in embryos at single-cell resolution." *Nature* 568, pp. 49–54. DOI: 10.1038/s41586-019-1035-4.

Mathew, C. (1984). *Radiolabeling of DNA by nick translation*. Vol. 2. Nucleic Acids. Humana Press, pp. 257–261. DOI: 10.1385/0-89603-064-4:257.

Matsuda, Y. and V. M. Chapman (1995). "Application of fluorescence in situ hybridization in genome analysis of the mouse." *Electrophoresis* 16, pp. 261–272. DOI: 10.1002/elps.1150160142.

Mattei, A. L., N. Bailly, and A. Meissner (2022). "DNA methylation: a historical perspective." *Trends Genet* 38, pp. 676–707. DOI: 10.1016/j.tig.2022.03.010.

Mavrich, T. N., C. Jiang, I. P. Ioshikhes, X. Li, B. J. Venters, S. J. Zanton, L. P. Tomsho, J. Qi, R. L. Glaser, S. C. Schuster, D. S. Gilmour, I. Albert, and B. F. Pugh (2008). "Nucleosome organization in the Drosophila genome." *Nature* 453, pp. 358–362. DOI: 10.1038/nature06929.

McCord, R. P., N. Kaplan, and L. Giorgetti (2020). "Chromosome Conformation Capture and Beyond: Toward an Integrative View of Chromosome Structure and Function." *Mol Cell* 77, pp. 688–708. DOI: 10.1016/j.molcel.2019.12.021.

McGinnis, W., M. S. Levine, E. Hafen, A. Kuroiwa, and W. J. Gehring (1984). "A conserved DNA sequence in homoeotic genes of the Drosophila Antennapedia and bithorax complexes." *Nature* 308, pp. 428–433. DOI: 10.1038/308428a0.

Meaburn, K. J. and T. Misteli (2007). "Cell biology: chromosome territories." *Nature* 445, pp. 379–781. DOI: 10.1038/445379a.

Mello, M. L. S. and B. C. Vidal (2017). "The Feulgen reaction: A brief review and new perspectives." *Acta Histochem* 119, pp. 603–609. DOI: 10.1016/j.acthis.2017.07.002.

Melo, U. S. et al. (2020). "Hi-C Identifies Complex Genomic Rearrangements and TAD-Shuffling in Developmental Diseases." *Am J Hum Genet* 106, pp. 872–884. DOI: 10.1016/j.ajhg.2020.04.016.

Mendel, G. (1866). "Versuche über pflanzenhybriden." *Verh. Naturforsch. Ver. Brünn*, 3–47. DOI: 10.1007/978-3-663-19714-0_4.

Mertens, F., B. Johansson, T. Fioretos, and F. Mitelman (2015). "The emerging complexity of gene fusions in cancer." *Nat Rev Cancer* 15, pp. 371–381. DOI: 10.1038/nrc3947.

Meuleman, W., D. Peric-Hupkes, J. Kind, J. B. Beaudry, L. Pagie, M. Kellis, M. Reinders, L. Wessels, and B. van Steensel (2013). "Constitutive nuclear lamina-genome interactions are highly conserved and associated with A/T-rich sequence." *Genome Res* 23, pp. 270–280. DOI: 10.1101/gr.141028.112.

Meuleman, W. et al. (2020). "Index and biological spectrum of human DNase I hypersensitive sites." *Nature* 584, pp. 244–251. DOI: 10.1038/s41586-020-2559-3.

Miescher, J. F. (1871). "Ueber die chemische Zusammensetzung der Eiterzellen." *Med-Chem Unters*, pp. 441–460.

Mirny, L. A. (2010). "Nucleosome-mediated cooperativity between transcription factors." *Proc Natl Acad Sci U S A* 107, pp. 22534–22539. DOI: 10.1073/pnas.0913805107.

Mizuguchi, T., G. Fudenberg, S. Mehta, J. M. Belton, N. Taneja, H. D. Folco, P. FitzGerald, J. Dekker, L. Mirny, J. Barrowman, and S. I. S. Grewal (2014). "Cohesin-dependent globules and heterochromatin shape 3D genome architecture in S. pombe." *Nature* 516, pp. 432–435. DOI: 10.1038/nature13833.

Moffitt, J. R. and X. Zhuang (2016). "RNA imaging with multiplexed error-robust fluorescence in situ hybridization (MERFISH)." In: *Methods Enzymol*. Vol. 572. Elsevier, pp. 1–49. DOI: 10.1016/bs.mie.2016.03.020.

Monfils, K. and T. S. Barakat (2021). "Models behind the mystery of establishing enhancer-promoter interactions." *Eur J Cell Biol* 100, p. 151170. DOI: 10.1016/j.ejcb.2021.151170.

Moreau, P, R Hen, B Wasylyk, R Everett, M. Gaub, and P Chambon (1981). "The SV40 72 base repair repeat has a striking effect on gene expression both in SV40 and other chimeric recombinants." *Nucleic Acids Res* 9, pp. 6047–6068. DOI: 10.1093/nar/9.22.6047.

Morgan, T. H. (1910). "Sex Limited Inheritance in Drosophila." *Science* 32, pp. 120–122. DOI: 10.1126/science.32.812.120.

Muller, H. J. (1927). "Artificial Transmutation of the Gene." *Science* 66, pp. 84–87. DOI: 10.1126/science.66.1699.84.

Muller, O., N. Kepper, R. Schopflin, R. Ettig, K. Rippe, and G. Wedemann (2014). "Changing chromatin fiber conformation by nucleosome repositioning." *Biophys J* 107, pp. 2141–2150. DOI: 10.1016/j.bpj.2014.09.026.

Murgha, Y. E., J. M. Rouillard, and E. Gulari (2014). "Methods for the preparation of large quantities of complex single-stranded oligonucleotide libraries." *PLoS One* 9, p. e94752. DOI: 10.1371/journal.pone.0094752.

Murphy, D. B. and M. W. Davidson (2012). *Fundamentals of light microscopy and electronic imaging*. John Wiley Sons. DOI: 10.1117/1.JBO.18.2.029901.

Nagano, T., Y. Lubling, T. J. Stevens, S. Schoenfelder, E. Yaffe, W. Dean, E. D. Laue, A. Tanay, and P. Fraser (2013). "Single-cell Hi-C reveals cell-to-cell variability in chromosome structure." *Nature* 502, pp. 59–64. DOI: 10.1038/nature12593.

Nagano, T., Y. Lubling, C. Várnai, C. Dudley, W. Leung, Y. Baran, N. Mendelson Cohen, S. Wingett, P. Fraser, and A. Tanay (2017). "Cell-cycle dynamics of chromosomal organization at single-cell resolution." *Nature* 547, pp. 61–67. DOI: 10.1038/nature23001.

Narlikar, G. J., R. Sundaramoorthy, and T. Owen-Hughes (2013). "Mechanisms and functions of ATP-dependent chromatin-remodeling enzymes." *Cell* 154, pp. 490–503. DOI: 10.1016/j.cell.2013.07.011.

Nath, J. and K. L. Johnson (1998). "Fluorescence in situ hybridization (FISH): DNA probe production and hybridization criteria." *Biotech Histochem* 73, pp. 6–22. DOI: 10.3109/10520299809140502.

Nelson, D. E. et al. (2004). "Oscillations in NF-kappaB signaling control the dynamics of gene expression." *Science* 306, pp. 704–708. DOI: 10.1126/science.1099962.

Neves, H., C. Ramos, M. G. da Silva, A. Parreira, and L. Parreira (1999). "The Nuclear Topography of ABL, BCR, PML, and RAR Genes: Evidence for Gene Proximity in Specific Phases of the Cell Cycle and Stages of Hematopoietic Differentiation." *Blood* 93, pp. 1197–1207. DOI: 10.1182/blood.V93.4.1197.

Neveu, B., C. Richer, P. Cassart, M. Caron, C. Jimenez-Cortes, P. St-Onge, C. Fuchs, N. Garnier, S. Gobeil, and D. Sinnett (2022). "Identification of new ETV6 modulators through a high-throughput functional screening." *iScience* 25, p. 103858. DOI: 10.1016/j.isci.2022.103858.

Nguyen, H. Q., S. Chattoraj, D. Castillo, S. C. Nguyen, G. Nir, A. Lioutas, E. A. Hershberg, N. M. C. Martins, P. L. Reginato, M. Hannan, B. J. Beliveau, G. M. Church, E. R. Daugharthy, M. A. Marti-Renom, and C. T. Wu (2020). "3D mapping and accelerated super-resolution imaging of the human genome using in situ sequencing." *Nat Methods* 17, pp. 822–832. DOI: 10.1038/s41592-020-0890-0.

Ni, Y., B. Cao, T. Ma, G. Niu, Y. Huo, J. Huang, D. Chen, Y. Liu, B. Yu, M. Q. Zhang, and H. Niu (2017). "Super-resolution imaging of a 2.5 kb non-repetitive DNA in situ in the nuclear genome using molecular beacon probes." *Elife* 6, p. e21660. DOI: 10.7554/eLife.21660.

Nielsen, P. E., M. Egholm, R. H. Berg, and O. Buchardt (1991). "Sequence-selective recognition of DNA by strand displacement with a thymine-substituted polyamide." *Science* 254, pp. 1497–500. DOI: 10.1126/science.1962210.

Nilsson, T., A. Waraky, A. Östlund, S. Li, A. Staffas, J. Asp, L. Fogelstrand, J. Abrahamsson, and L. Palmqvist (2022). "An induced pluripotent stem cell t (7; 12)(q36; p13) acute myeloid leukemia model shows high expression of MNX1 and a block in differentiation of the erythroid and megakaryocytic lineages." *Int J Cancer* 151, pp. 770–782. DOI: 10.1002/ijc.34122.

Nir, G. et al. (2018). "Walking along chromosomes with super-resolution imaging, contact maps, and integrative modeling." *PLoS Genet* 14, p. e1007872. DOI: 10.1371/journal.pgen.1007872.

Nizovtseva, E. V., N. Clauvelin, S. Todolli, Y. S. Polikanov, O. I. Kulaeva, S. Wengrzynek, W. K. Olson, and V. M. Studitsky (2017). "Nucleosome-free DNA regions differentially affect distant communication in chromatin." *Nucleic Acids Res* 45, pp. 3059–3067. DOI: 10.1093/nar/gkw1240.

Nora, E. P., A. Goloborodko, A. L. Valton, J. H. Gibcus, A. Uebersohn, N. Abdennur, J. Dekker, L. A. Mirny, and B. G. Bruneau (2017). "Targeted Degradation of CTCF Decouples Local Insulation of Chromosome Domains from Genomic Compartmentalization." *Cell* 169, 930–944 e22. DOI: 10.1016/j.cell.2017.05.004.

Nora, E. P., B. R. Lajoie, E. G. Schulz, L. Giorgetti, I. Okamoto, N. Servant, T. Piolot, N. L. van Berkum, J. Meisig, J. Sedat, J. Gribnau, E. Barillot, N. Bluthgen, J. Dekker, and E. Heard (2012). "Spatial partitioning of the regulatory landscape of the X-inactivation centre." *Nature* 485, pp. 381–385. DOI: 10.1038/nature11049.

Northcott, P. A. et al. (2014). "Enhancer hijacking activates GFI1 family oncogenes in medulloblastoma." *Nature* 511, pp. 428–434. DOI: 10.1038/nature13379.

Northcott, P. A. et al. (2017). "The whole-genome landscape of medulloblastoma subtypes." *Nature* 547, pp. 311–317. DOI: 10.1038/nature22973.

Nozaki, T., R. Imai, M. Tanbo, R. Nagashima, S. Tamura, T. Tani, Y. Joti, M. Tomita, K. Hibino, M. T. Kanemaki, K. S. Wendt, Y. Okada, T. Nagai, and K. Maeshima (2017). "Dynamic

Organization of Chromatin Domains Revealed by Super-Resolution Live-Cell Imaging." *Mol Cell* 67, pp. 282–293. DOI: 10.1016/j.molcel.2017.06.018.

O'Connor, C. and I. Miko (2008). "Developing the chromosome theory." *Nat Educ* 1, p. 44.

Okonechnikov, K. et al. (2023). "3D genome mapping identifies subgroup-specific chromosome conformations and tumor-dependency genes in ependymoma." *Nat Commun* 14, p. 2300. DOI: 10.1038/s41467-023-38044-0.

Oreopoulos, J., R. Berman, and M. Browne (2014). "Spinning-disk confocal microscopy: present technology and future trends." *Methods Cell Biol* 123, pp. 153–175. DOI: 10.1016/B978-0-12-420138-5.00009-4.

Osoegawa, K., A. G. Mammoser, C. Wu, E. Frengen, C. Zeng, J. J. Catanese, and P. J. de Jong (2001). "A bacterial artificial chromosome library for sequencing the complete human genome." *Genome Res* 11, pp. 483–496. DOI: 10.1101/gr.169601.

Ou, H. D., S. Phan, T. J. Deerinck, A. Thor, M. H. Ellisman, and C. C. O'Shea (2017). "ChromEMT: Visualizing 3D chromatin structure and compaction in interphase and mitotic cells." *Science* 357, p. eaag0025. DOI: 10.1126/science.aag0025.

Palikyras, S. et al. (2024). "Rapid and synchronous chemical induction of replicative-like senescence via a small molecule inhibitor." *Aging Cell* 23, p. e14083. DOI: 10.1111/acel.14083.

Pardue, M. L. and J. G. Gall (1969). "Molecular hybridization of radioactive DNA to the DNA of cytological preparations." *Proc Natl Acad Sci U S A* 64, pp. 600–604. DOI: 10.1073/pnas.64.2.600.

Passaro, M., M. Martinovic, V. Bevilacqua, E. A. Hershberg, G. Rossetti, B. J. Beliveau, R. J. Bonnal, and M. Pagani (2020). "OligoMinerApp: a web-server application for the design of genome-scale oligonucleotide in situ hybridization probes through the flexible OligoMiner environment." *Nucleic Acids Res* 48, W332–W339. DOI: 10.1093/nar/gkaa251.

Pederson, T. (2011). "The nucleus introduced." *Cold Spring Harb Perspect Biol* 3, p. a000521. DOI: 10.1101/cshperspect.a000521.

Pellestor, F., B. Andreo, K. Taneja, and B. Williams (2003). "PNA on human sperm: a new approach for in situ aneuploidy estimation." *Eur J Hum Genet* 11, pp. 337–341. DOI: 10.1038/sj.ejhg.5200958.

Peng, Y., S. Li, D. Landsman, and A. R. Panchenko (2021). "Histone tails as signaling antennas of chromatin." *Curr Opin Struct Biol* 67, pp. 153–160. DOI: 10.1016/j.sbi.2020.10.018.

Peyret, N., P. A. Seneviratne, H. T. Allawi, and J. SantaLucia (1999). "Nearest-Neighbor Thermodynamics and NMR of DNA Sequences with Internal A A, C C, G G, and T T Mismatches." *Biochemistry* 38, pp. 3468–3477. DOI: 10.1021/bi9803729.

Phillips-Cremins, J. E. et al. (2013). "Architectural protein subclasses shape 3D organization of genomes during lineage commitment." *Cell* 153, pp. 1281–1295. DOI: 10.1016/j.cell.2013.04.053.

Pichugin, A., O. V. Iarovaia, A. Gavrilov, I. Sklyar, N. Barinova, A. Barinov, E. Ivashkin, G. Caron, S. Aoufouchi, and S. V. Razin (2017). "The IGH locus relocalizes to a "recombination compartment" in the perinucleolar region of differentiating B-lymphocytes." *Oncotarget* 8, p. 40079. DOI: 10.18632/oncotarget.16941.

Piovesan, A., M. C. Pelleri, F. Antonaros, P. Strippoli, M. Caracausi, and L. Vitale (2019). "On the length, weight and GC content of the human genome." *BMC Res Notes* 12, p. 106. DOI: 10.1186/s13104-019-4137-z.

Pope, B. D. et al. (2014). "Topologically associating domains are stable units of replication-timing regulation." *Nature* 515, pp. 402–405. DOI: 10.1038/nature13986.

Pradeepa, M. M. (2017). "Causal role of histone acetylations in enhancer function." *Transcription* 8, pp. 40–47. DOI: 10.1080/21541264.2016.1253529.

Quinodoz, S. A. et al. (2018). "Higher-Order Inter-chromosomal Hubs Shape 3D Genome Organization in the Nucleus." *Cell* 174, pp. 744–757. DOI: 10.1016/j.cell.2018.05.024.

Rabl, C. (1885). "Über Zellteilung." 10, pp. 214–330.

Rada-Iglesias, A., R. Bajpai, T. Swigut, S. A. Brugmann, R. A. Flynn, and J. Wysocka (2011). "A unique chromatin signature uncovers early developmental enhancers in humans." *Nature* 470, pp. 279–283. DOI: 10.1038/nature09692.

Raddaoui, N., S. Croce, F. Geiger, A. Borodavka, L. Mockl, S. Stazzoni, B. Viverge, C. Brauchle, T. Frischmuth, H. Engelke, and T. Carell (2020). "Supersensitive Multifluorophore RNA-FISH for Early Virus Detection and Flow-FISH by Using Click Chemistry." *Chembiochem* 21, pp. 2214–2218. DOI: 10.1002/cbic.202000081.

Raj, A., P. van den Bogaard, S. A. Rifkin, A. van Oudenaarden, and S. Tyagi (2008). "Imaging individual mRNA molecules using multiple singly labeled probes." *Nat Methods* 5, pp. 877–879. DOI: 10.1038/nmeth.1253.

Raj, A., C. S. Peskin, D. Tranchina, D. Y. Vargas, and S. Tyagi (2006). "Stochastic mRNA synthesis in mammalian cells." *PLoS Biol* 4, p. e309. DOI: 10.1371/journal.pbio.0040309.

Raj, A. and S. Tyagi (2010). "Detection of individual endogenous RNA transcripts in situ using multiple singly labeled probes." In: *Methods Enzymol*. Vol. 472. Elsevier, pp. 365–386. DOI: 10.1016/S0076-6879(10)72004-8.

Rajagopal, N., S. Srinivasan, K. Kooshesh, Y. Guo, M. D. Edwards, B. Banerjee, T. Syed, B. J. Emons, D. K. Gifford, and R. I. Sherwood (2016). "High-throughput mapping of regulatory DNA." *Nat Biotechnol* 34, pp. 167–174. DOI: 10.1038/nbt.3468.

Rao, S. S. P. et al. (2017). "Cohesin Loss Eliminates All Loop Domains." *Cell* 171, pp. 305–320. DOI: 10.1016/j.cell.2017.09.026.

Rao, S. S., M. H. Huntley, N. C. Durand, E. K. Stamenova, I. D. Bochkov, J. T. Robinson, A. L. Sanborn, I. Machol, A. D. Omer, E. S. Lander, and E. L. Aiden (2014). "A 3D map of the human genome at kilobase resolution reveals principles of chromatin looping." *Cell* 159, pp. 1665–1680. DOI: 10.1016/j.cell.2014.11.021.

Reindl, J., S. Girst, D. W. Walsh, C. Greubel, B. Schwarz, C. Siebenwirth, G. A. Drexler, A. A. Friedl, and G. Dollinger (2017). "Chromatin organization revealed by nanostructure of irradiation induced gammaH2AX, 53BP1 and Rad51 foci." *Sci Rep* 7, p. 40616. DOI: 10.1038/srep40616.

Reinhardt, S. C. M., L. A. Masullo, I. Baudrexel, P. R. Steen, R. Kowalewski, A. S. Eklund, S. Strauss, E. M. Unterauer, T. Schlichthaerle, M. T. Strauss, C. Klein, and R. Jungmann (2023). "Angstrom-resolution fluorescence microscopy." *Nature* 617, pp. 711–716. DOI: 10.1038/s41586-023-05925-9.

Ricci, M. A., C. Manzo, M. F. Garcia-Parajo, M. Lakadamyali, and M. P. Cosma (2015). "Chromatin fibers are formed by heterogeneous groups of nucleosomes in vivo." *Cell* 160, pp. 1145–1158. DOI: 10.1016/j.cell.2015.01.054.

Ried, T., G. Landes, W. Dackowski, K. Klinger, and D. C. Ward (1992). "Multicolor fluorescence in situ hybridization for the simultaneous detection of probe sets for chromosomes 13, 18, 21, X and Y in uncultured amniotic fluid cells." *Hum Mol Genet* 1, pp. 307–313. DOI: 10.1093/hmg/1.5.307.

Rodríguez-Carballo, E., L. Lopez-Delisle, Y. Zhan, P. J. Fabre, L. Beccari, I. El-Idrissi, T. H. N. Huynh, H. Ozadam, J. Dekker, and D. Duboule (2017). "The HoxD cluster is a dynamic and resilient TAD boundary controlling the segregation of antagonistic regulatory landscapes." *Genes Dev* 31, pp. 2264–2281. DOI: 10.1101/gad.307769.117.

Roix, J. J., P. G. McQueen, P. J. Munson, L. A. Parada, and T. Misteli (2003). "Spatial proximity of translocation-prone gene loci in human lymphomas." *Nat Genet* 34, pp. 287–291. DOI: 10.1038/ng1177.

Rost, F. W. (1991). *Quantitative fluorescence microscopy*. Cambridge University Press. DOI: 10.1002/sca.4950180810.

Rothbart, S. B. and B. D. Strahl (2014). "Interpreting the language of histone and DNA modifications." *Biochim Biophys Acta* 1839, pp. 627–643. DOI: 10.1016/j.bbagrm.2014.03.001.

Rouhanifard, S. H., I. A. Mellis, M. Dunagin, S. Bayatpour, C. L. Jiang, I. Dardani, O. Symmons, B. Emert, E. Torre, A. Cote, A. Sullivan, J. A. Stamatoyannopoulos, and A. Raj (2019). "Amendments: Author Correction: ClampFISH detects individual nucleic acid molecules using click chemistry-based amplification." *Nat Biotechnol* 37, 84–89. DOI: 10.1038/nbt0119-102b.

Rouillard, J. M., C. J. Herbert, and M. Zuker (2002). "OligoArray: genome-scale oligonucleotide design for microarrays." *Bioinformatics* 18, pp. 486–487. DOI: 10.1093/bioinformatics/18.3.486.

Rouillard, J. M., M. Zuker, and E. Gulari (2003). "OligoArray 2.0: design of oligonucleotide probes for DNA microarrays using a thermodynamic approach." *Nucleic Acids Res* 31, pp. 3057–3062. DOI: 10.1093/nar/gkg426.

Rudan, M. V., C. Barrington, S. Henderson, C. Ernst, D. T. Odom, A. Tanay, and S. Hadjur (2015). "Comparative Hi-C reveals that CTCF underlies evolution of chromosomal domain architecture." *Cell Rep* 10, pp. 1297–1309. DOI: 10.1016/j.celrep.2015.02.004.

Rudkin, G. T. and B. D. Stollar (1977). "High resolution detection of DNA-RNA hybrids in situ by indirect immunofluorescence." *Nature* 265, pp. 472–473. DOI: 10.1038/265472a0.

Rust, M. J., M. Bates, and X. Zhuang (2006). "Sub-diffraction-limit imaging by stochastic optical reconstruction microscopy (STORM)." *Nat Methods* 3, pp. 793–795. DOI: 10.1038/nmeth929.

Sabari, B. R., A. Dall'Agnese, A. Boija, I. A. Klein, E. L. Coffey, K. Shrinivas, B. J. Abraham, N. M. Hannett, A. V. Zamudio, and J. C. Manteiga (2018). "Coactivator condensation at super-enhancers links phase separation and gene control." *Science* 361, p. eaar3958. DOI: 10.1126/science.aar3958.

Sahl, S. J., S. W. Hell, and S. Jakobs (2017). "Fluorescence nanoscopy in cell biology." *Nat Rev Mol Cell Biol* 18, pp. 685–701. DOI: 10.1038/nrm.2017.71.

Sahoo, H. (2011). "Förster resonance energy transfer–A spectroscopic nanoruler: Principle and applications." *J Photochem Photobiol* 12, pp. 20–30. DOI: 10.1016/j.jphotochemrev.2011.05.001.

Sailem, H. Z., S. Cooper, and C. Bakal (2016). "Visualizing quantitative microscopy data: History and challenges." *Crit Rev Biochem Mol Biol* 51, pp. 96–101. DOI: 10.3109/10409238.2016.1146222.

Sanborn, A. L. et al. (2015). "Chromatin extrusion explains key features of loop and domain formation in wild-type and engineered genomes." *Proc Natl Acad Sci U S A* 112, E6456–E6465. DOI: 10.1073/pnas.1518552112.

Sandoval-Villegas, N., W. Nurieva, M. Amberger, and Z. Ivics (2021). "Contemporary transposon tools: a review and guide through mechanisms and applications of sleeping beauty, piggyBac and Tol2 for genome engineering." *Int J Mol Sci* 22, p. 5084. DOI: 10.3390/ijms22105084.

Schermelleh, L., A. Ferrand, T. Huser, C. Eggeling, M. Sauer, O. Biehlmaier, and G. P. C. Drummen (2019). "Super-resolution microscopy demystified." *Nat Cell Biol* 21, pp. 72–84. DOI: 10.1038/s41556-018-0251-8.

Schermelleh, L., A. Haemmer, F. Spada, N. Rosing, D. Meilinger, U. Rothbauer, M. C. Cardoso, and H. Leonhardt (2007). "Dynamics of Dnmt1 interaction with the replication machinery and its role in postreplicative maintenance of DNA methylation." *Nucleic Acids Res* 35, pp. 4301–4312. DOI: 10.1093/nar/gkm432.

Schermelleh, L., R. Heintzmann, and H. Leonhardt (2010). "A guide to super-resolution fluorescence microscopy." *J Cell Biol* 190, pp. 165–175. DOI: 10.1083/jcb.201002018.

Schirripa Spagnolo, C. and S. Luin (2022). "Choosing the Probe for Single-Molecule Fluorescence Microscopy." *Int J Mol Sci* 23, p. 14949. DOI: 10.3390/ijms232314949.

Schlessinger, J., D. E. Koppel, D. Axelrod, K. Jacobson, W. W. Webb, and E. L. Elson (1976). "Lateral transport on cell membranes: mobility of concanavalin A receptors on myoblasts." *Proc Natl Acad Sci U S A* 73, pp. 2409–2413. DOI: 10.1073/pnas.73.7.2409.

Schneider, K., C. Fuchs, A. Dobay, A. Rottach, W. Qin, P. Wolf, J. M. Alvarez-Castro, M. M. Nalaskowski, E. Kremmer, V. Schmid, H. Leonhardt, and L. Schermelleh (2013). "Dissection of cell cycle-dependent dynamics of Dnmt1 by FRAP and diffusion-coupled modeling." *Nucleic Acids Res* 41, pp. 4860–4876. DOI: 10.1093/nar/gkt191.

Schnell, U., F. Dijk, K. A. Sjollema, and B. N. Giepmans (2012). "Immunolabeling artifacts and the need for live-cell imaging." *Nat Methods* 9, pp. 152–158. DOI: 10.1038/nmeth.1855.

Schnitzbauer, J., M. T. Strauss, T. Schlichthaerle, F. Schueder, and R. Jungmann (2017). "Super-resolution microscopy with DNA-PAINT." *Nat Protoc* 12, pp. 1198–1228. DOI: 10.1038/nprot.2017.024.

Schones, D. E., K. Cui, S. Cuddapah, T. Y. Roh, A. Barski, Z. Wang, G. Wei, and K. Zhao (2008). "Dynamic regulation of nucleosome positioning in the human genome." *Cell* 132, pp. 887–898. DOI: 10.1016/j.cell.2008.02.022.

Schroder, T., M. B. Scheible, F. Steiner, J. Vogelsang, and P. Tinnefeld (2019). "Interchromophoric Interactions Determine the Maximum Brightness Density in DNA Origami Structures." *Nano Lett* 19, pp. 1275–1281. DOI: 10.1021/acs.nanolett.8b04845.

Schultz, J. (1936). "Variegation in Drosophila and the Inert Chromosome Regions." *Proc Natl Acad Sci U S A* 22, pp. 27–33. DOI: 10.1073/pnas.22.1.27.

Schwarzer, W., N. Abdennur, A. Goloborodko, A. Pekowska, G. Fudenberg, Y. Loe-Mie, N. A. Fonseca, W. Huber, C. H. Haering, L. Mirny, and F. Spitz (2017). "Two independent modes of chromatin organization revealed by cohesin removal." *Nature* 551, pp. 51–56. DOI: 10.1038/nature24281.

Sealey, P. G., P. A. Whittaker, and E. M. Southern (1985). "Removal of repeated sequences from hybridisation probes." *Nucleic Acids Res* 13, pp. 1905–1922. DOI: 10.1093/nar/13.6.1905.

Segal, E. and J. Widom (2009). "What controls nucleosome positions?" *TiG* 25, pp. 335–343. DOI: 10.1016/j.tig.2009.06.002.

Sekar, R. B. and A. Periasamy (2003). "Fluorescence resonance energy transfer (FRET) microscopy imaging of live cell protein localizations." *J Cell Biol* 160, pp. 629–633. DOI: 10.1083/jcb.200210140.

Sexton, T., E. Yaffe, E. Kenigsberg, F. Bantignies, B. Leblanc, M. Hoichman, H. Parrinello, A. Tanay, and G. Cavalli (2012). "Three-dimensional folding and functional organization principles of the Drosophila genome." *Cell* 148, pp. 458–472. DOI: 10.1016/j.cell.2012.01.010.

Shah, S., Y. Takei, W. Zhou, E. Lubeck, J. Yun, C. L. Eng, N. Koulena, C. Cronin, C. Karp, E. J. Liaw, M. Amin, and L. Cai (2018). "Dynamics and Spatial Genomics of the Nascent Transcriptome by Intron seqFISH." *Cell* 174, pp. 363–376. DOI: 10.1016/j.cell.2018.05.035.

Shao, X., N. Lv, J. Liao, J. Long, R. Xue, N. Ai, D. Xu, and X. Fan (2019). "Copy number variation is highly correlated with differential gene expression: a pan-cancer study." *BMC Med Genet* 20, pp. 1–14. DOI: 10.1186/s12881-019-0909-5.

Shizuya, H., B. Birren, U. J. Kim, V. Mancino, T. Slepak, Y. Tachiiri, and M. Simon (1992). "Cloning and stable maintenance of 300-kilobase-pair fragments of human DNA in Escherichia coli using an F-factor-based vector." *Proc Natl Acad Sci U S A* 89, pp. 8794–8797. DOI: 10.1073/pnas.89.18.8794.

Shogren-Knaak, M., H. Ishii, J. M. Sun, M. J. Pazin, J. R. Davie, and C. L. Peterson (2006). "Histone H4-K16 acetylation controls chromatin structure and protein interactions." *Science* 311, pp. 844–847. DOI: 10.1126/science.1124000.

Shopland, L. S., C. R. Lynch, K. A. Peterson, K. Thornton, N. Kepper, J. Hase, S. Stein, S. Vincent, K. R. Molloy, G. Kreth, C. Cremer, C. J. Bult, and T. P. O'Brien (2006). "Folding and organization of a contiguous chromosome region according to the gene distribution pattern in primary genomic sequence." *J Cell Biol* 174, pp. 27–38. DOI: 10.1083/jcb.200603083.

Simonis, M., P. Klous, E. Splinter, Y. Moshkin, R. Willemsen, E. de Wit, B. van Steensel, and W. de Laat (2006). "Nuclear organization of active and inactive chromatin domains uncovered by chromosome conformation capture-on-chip (4C)." *Nat Genet* 38, pp. 1348–1354. DOI: 10.1038/ng1896.

Singh, A. K. and F. Mueller-Planitz (2021). "Nucleosome Positioning and Spacing: From Mechanism to Function." *J Mol Biol* 433, p. 166847. DOI: 10.1016/j.jmb.2021.166847.

Solovei, I., A. Cavallo, L. Schermelleh, F. Jaunin, C. Scasselati, D. Cmarko, C. Cremer, S. Fakan, and T. Cremer (2002). "Spatial preservation of nuclear chromatin architecture during three-dimensional fluorescence in situ hybridization (3D-FISH)." *Exp Cell Res* 276, pp. 10–23. DOI: 10.1006/excr.2002.5513.

Solovei, I., M. Kreysing, C. Lanctot, S. Kosem, L. Peichl, T. Cremer, J. Guck, and B. Joffe (2009). "Nuclear architecture of rod photoreceptor cells adapts to vision in mammalian evolution." *Cell* 137, pp. 356–68. DOI: 10.1016/j.cell.2009.01.052.

Spielmann, M., D. G. Lupianez, and S. Mundlos (2018). "Structural variation in the 3D genome." *Nat Rev Genet* 19, pp. 453–467. DOI: 10.1038/s41576-018-0007-0.

Stack, S. M., D. B. Brown, and W. C. Dewey (1977). "Visualization of interphase chromosomes." *J Cell Sci* 26, pp. 281–299. DOI: 10.1242/jcs.26.1.281.

Stadhouders, R., G. J. Filion, and T. Graf (2019). "Transcription factors and 3D genome conformation in cell-fate decisions." *Nature* 569, pp. 345–354. DOI: 10.1038/s41586-019-1182-7.

Steensel, B. van and A. S. Belmont (2017). "Lamina-Associated Domains: Links with Chromosome Architecture, Heterochromatin, and Gene Repression." *Cell* 169, pp. 780–791. DOI: 10.1016/j.cell.2017.04.022.

Stevens, T. J. et al. (2017). "3D structures of individual mammalian genomes studied by single-cell Hi-C." *Nature* 544, pp. 59–64. DOI: 10.1038/nature21429.

Strom, A. R., A. V. Emelyanov, M. Mir, D. V. Fyodorov, X. Darzacq, and G. H. Karpen (2017). "Phase separation drives heterochromatin domain formation." *Nature* 547, pp. 241–245. DOI: 10.1038/nature22989.

Su, J.-H., P. Zheng, S. S. Kinrot, B. Bintu, and X. Zhuang (2020). "Genome-scale imaging of the 3D organization and transcriptional activity of chromatin." *Cell* 182, pp. 1641–1659. DOI: 10.1016/j.cell.2020.07.032.

Sugimoto, N., S. Nakano, M. Yoneyama, and K. Honda (1996). "Improved thermodynamic parameters and helix initiation factor to predict stability of DNA duplexes." *Nucleic Acids Res* 24, pp. 4501–4505. DOI: 10.1093/nar/24.22.4501.

Symmons, O., V. V. Uslu, T. Tsujimura, S. Ruf, S. Nassari, W. Schwarzer, L. Ettwiller, and F. Spitz (2014). "Functional and topological characteristics of mammalian regulatory domains." *Genome Res* 24, pp. 390–400. DOI: 10.1101/gr.163519.113.

Szabo, Q., A. Donjon, I. Jerkovic, G. L. Papadopoulos, T. Cheutin, B. Bonev, E. P. Nora, B. G. Bruneau, F. Bantignies, and G. Cavalli (2020). "Regulation of single-cell genome organization into TADs and chromatin nanodomains." *Nat Genet* 52, pp. 1151–1157. DOI: 10.1038/s41588-020-00716-8.

Szabo, Q., D. Jost, J. M. Chang, D. I. Cattoni, G. L. Papadopoulos, B. Bonev, T. Sexton, J. Gurgo, C. Jacquier, M. Nollmann, F. Bantignies, and G. Cavalli (2018). "TADs are 3D structural units of higher-order chromosome organization in Drosophila." *Sci Adv* 4, p. eaar8082. DOI: 10.1126/sciadv.aar8082.

Takei, Y., S. Zheng, J. Yun, S. Shah, N. Pierson, J. White, S. Schindler, C. H. Tischbirek, G.-C. Yuan, and L. Cai (2021). "Single-cell nuclear architecture across cell types in the mouse brain." *Science* 374, pp. 586–594. DOI: 10.1126/science.abj1966.

Taketani, T., T. Taki, M. Sako, T. Ishii, S. Yamaguchi, and Y. Hayashi (2008). "MNX1-ETV6 fusion gene in an acute megakaryoblastic leukemia and expression of the MNX1 gene in leukemia and normal B cell lines." *Cancer Genet Cytogenet* 186, pp. 115–159. DOI: 10.1016/j.cancergencyto.2008.06.009.

Talbert, P. B. and S. Henikoff (2021). "The Yin and Yang of Histone Marks in Transcription." *Annu Rev Genomics Hum Genet* 22, pp. 147–170. DOI: 10.1146/annurev-genom-120220-085159.

Tanabe, H., F. A. Habermann, I. Solovei, M. Cremer, and T. Cremer (2002). "Non-random radial arrangements of interphase chromosome territories: evolutionary considerations and functional implications." *Mutat Res* 504, pp. 37–45. DOI: 10.1016/s0027-5107(02)00077-5.

Tang, F., C. Barbacioru, Y. Wang, E. Nordman, C. Lee, N. Xu, X. Wang, J. Bodeau, B. B. Tuch, A. Siddiqui, K. Lao, and M. A. Surani (2009). "mRNA-Seq whole-transcriptome analysis of a single cell." *Nat Methods* 6, pp. 377–382. DOI: 10.1038/nmeth.1315.

Tasara, T., B. Angerer, M. Damond, H. Winter, S. Dorhofer, U. Hubscher, and M. Amacker (2003). "Incorporation of reporter molecule-labeled nucleotides by DNA polymerases. II.

High-density labeling of natural DNA." *Nucleic Acids Res* 31, pp. 2636–2646. DOI: `10.1093/nar/gkg371`.

Tedeschi, A., G. Wutz, S. Huet, M. Jaritz, A. Wuensche, E. Schirghuber, I. F. Davidson, W. Tang, D. A. Cisneros, and V. Bhaskara (2013). "Wapl is an essential regulator of chromatin structure and chromosome segregation." *Nature* 501, pp. 564–568. DOI: `10.1038/nature12471`.

Terai, T. and T. Nagano (2013). "Small-molecule fluorophores and fluorescent probes for bioimaging." *Pflugers Arch* 465, pp. 347–359. DOI: `10.1007/s00424-013-1234-z`.

Thaler, J., K. Harrison, K. Sharma, K. Lettieri, J. Kehrl, and S. L. Pfaff (1999). "Active suppression of interneuron programs within developing motor neurons revealed by analysis of homeodomain factor HB9." *Neuron* 23, pp. 675–687. DOI: `10.1016/s0896-6273(01)80027-1`.

Thavarajah, R., V. K. Mudimbaimannar, J. Elizabeth, U. K. Rao, and K. Ranganathan (2012). "Chemical and physical basics of routine formaldehyde fixation." *J Oral Maxillofac Pathol* 16, pp. 400–405. DOI: `10.4103/0973-029X.102496`.

Thomson, I., S. Gilchrist, W. A. Bickmore, and J. R. Chubb (2004). "The radial positioning of chromatin is not inherited through mitosis but is established de novo in early G1." *Curr Biol* 14, pp. 166–172. DOI: `10.1016/j.cub.2003.12.024`.

Travers, A. (1999). "Chromatin modification by DNA tracking." *Proc Natl Acad Sci U S A* 96, pp. 13634–13637. DOI: `10.1073/pnas.96.24.13634`.

Trojanowski, J., L. Frank, A. Rademacher, N. Mücke, P. Grigaitis, and K. Rippe (2022). "Transcription activation is enhanced by multivalent interactions independent of phase separation." *Mol Cell* 82, pp. 1878–1893. DOI: `10.1016/j.molcel.2022.04.017`.

Tschermak, E. (1900). "Über künstliche Kreuzung bei Pisum sativum." *Ber Dtsch Bot Ges* 18, pp. 232–239. DOI: `10.1111/j.1438-8677.1900.tb04903.x`.

Uyehara, C. M. and E. Apostolou (2023). "3D enhancer-promoter interactions and multi-connected hubs: Organizational principles and functional roles." *Cell Rep* 42, p. 112068. DOI: `10.1016/j.celrep.2023.112068`.

Valeur, B. and M. N. Berberan-Santos (2013). *Molecular fluorescence: principles and applications*. John Wiley Sons. DOI: `10.1002/9783527650002`.

Vielkind, U and S. Swierenga (1989). "A simple fixation procedure for immunofluorescent detection of different cytoskeletal components within the same cell." *Histochemistry* 91, pp. 81–88. DOI: `10.1007/BF00501916`.

Voss, A. K. and T. Thomas (2018). "Histone Lysine and Genomic Targets of Histone Acetyltransferases in Mammals." *Bioessays* 40, p. e1800078. DOI: `10.1002/bies.201800078`.

Waldeyer, W. (1888). "Über Karyokinese und ihre Beziehungen zu den Befruchtungsvorgängen." *Arch Mikrosk Anat Entwickl* 32, pp. 1–122. DOI: `10.1007/BF02956988`.

Walter, J., L. Schermelleh, M. Cremer, S. Tashiro, and T. Cremer (2003). "Chromosome order in HeLa cells changes during mitosis and early G1, but is stably maintained during subsequent interphase stages." *JCB* 160, pp. 685–697. DOI: `10.1083/jcb.200211103`.

Wang, S., J.-H. Su, B. J. Beliveau, B. Bintu, J. R. Moffitt, C.-t. Wu, and X. Zhuang (2017). "Spatial organization of chromatin domains and compartments in single chromosomes." *Biophys J* 112, pp. 598–602. DOI: `10.3390/ijms18051005`.

Wang, X. and F. Yue (2024). "Hijacked enhancer-promoter and silencer-promoter loops in cancer." *Curr Opin Genet Dev* 86, p. 102199. DOI: `10.1016/j.gde.2024.102199`.

Wang, Y., W. T. Cottle, H. Wang, X. A. Feng, J. Mallon, M. Gavrilov, S. Bailey, and T. Ha (2021). "Genome oligopaint via local denaturation fluorescence in situ hybridization." *Mol Cell* 81, pp. 1566–1577. DOI: `10.1016/j.molcel.2021.02.011`.

Waraky, A., A. Östlund, T. Nilsson, D. Weichenhan, P. Lutsik, M. Bähr, J. Hey, G. Tunali, J. Adamsson, and S. Jacobsson (2024). "Aberrant MNX1 expression associated with t (7; 12)(q36; p13) pediatric acute myeloid leukemia induces the disease through altering histone methylation." *Haematologica* 109, pp. 725–739. DOI: `10.3324/haematol.2022.282255`.

Watson, J. D. and F. H. Crick (1953). "Molecular structure of nucleic acids; a structure for deoxyribose nucleic acid." *Nature* 171, pp. 737–738. DOI: `10.1038/171737a0`.

Wegel, E. and P. Shaw (2005). "Gene activation and deactivation related changes in the three-dimensional structure of chromatin." *Chromosoma* 114, pp. 331–337. DOI: `10.1007/s00412-005-0015-7`.

Weintraub, A. S., C. H. Li, A. V. Zamudio, A. A. Sigova, N. M. Hannett, D. S. Day, B. J. Abraham, M. A. Cohen, B. Nabet, and D. L. Buckley (2017). "YY1 is a structural regulator of enhancer-promoter loops." *Cell* 171, pp. 1573–1588. DOI: `10.1016/j.cell.2017.11.008`.

Weischenfeldt, J. et al. (2017). "Pan-cancer analysis of somatic copy-number alterations implicates IRS4 and IGF2 in enhancer hijacking." *Nat Genet* 49, pp. 65–74. DOI: `10.1038/ng.3722`.

Weiss, M. C., M. Preiner, J. C. Xavier, V. Zimorski, and W. F. Martin (2018). "The last universal common ancestor between ancient Earth chemistry and the onset of genetics." *PLoS Genet* 14, p. e1007518. DOI: `10.1371/journal.pgen.1007518`.

Wiegant, J., T. Ried, P. M. Nederlof, M. van der Ploeg, H. J. Tanke, and A. K. Raap (1991). "In situ hybridization with fluoresceinated DNA." *Nucleic Acids Res* 19, pp. 3237–3241. DOI: `10.1093/nar/19.12.3237`.

Wilkins, M. H., W. E. Seeds, A. R. Stokes, and H. R. Wilson (1953). "Helical structure of crystalline deoxypentose nucleic acid." *Nature* 172, pp. 759–762. DOI: 10.1038/172759b0.

Williamson, I., S. Berlivet, R. Eskeland, S. Boyle, R. S. Illingworth, D. Paquette, J. Dostie, and W. A. Bickmore (2014). "Spatial genome organization: contrasting views from chromosome conformation capture and fluorescence in situ hybridization." *Genes Dev* 28, pp. 2778–2791. DOI: 10.1101/gad.251694.114.

Woodcock, C. L., A. I. Skoultchi, and Y. Fan (2006). "Role of linker histone in chromatin structure and function: H1 stoichiometry and nucleosome repeat length." *Chromosome Res* 14, pp. 17–25. DOI: 10.1007/s10577-005-1024-3.

Wurm, C. A., D. Neumann, R. Schmidt, A. Egner, and S. Jakobs (2010). "Sample preparation for STED microscopy." *Methods Mol Biol* 591, pp. 185–199. DOI: 10.1007/978-1-60761-404-3_11.

Wutz, G. et al. (2017). "Topologically associating domains and chromatin loops depend on cohesin and are regulated by CTCF, WAPL, and PDS5 proteins." *EMBO J* 36, pp. 3573–3599. DOI: 10.15252/embj.201798004.

Xiao, J. Y., A. Hafner, and A. N. Boettiger (2021). "How subtle changes in 3D structure can create large changes in transcription." *Elife* 10, p. e64320. DOI: 10.7554/eLife.64320.

Xie, F., K. A. Timme, and J. R. Wood (2018). "Using single molecule mRNA fluorescent in situ hybridization (RNA-FISH) to quantify mRNAs in individual murine oocytes and embryos." *Sci Rep* 8, p. 7930. DOI: 10.1038/s41598-018-26345-0.

Xu, J. and Y. Liu (2021). "Probing Chromatin Compaction and Its Epigenetic States in situ With Single-Molecule Localization-Based Super-Resolution Microscopy." *Front Cell Dev Biol* 9, p. 653077. DOI: 10.3389/fcell.2021.653077.

Yang, J. H. and A. S. Hansen (2024). "Enhancer selectivity in space and time: from enhancer-promoter interactions to promoter activation." *Nat Rev Mol Cell Biol* 25, pp. 574–591. DOI: 10.1038/s41580-024-00710-6.

Yang, Y., F. Gao, Y. Wang, H. Li, J. Zhang, Z. Sun, and Y. Jiang (2022). "Fluorescent Organic Small Molecule Probes for Bioimaging and Detection Applications." *Molecules* 27, p. 8421. DOI: 10.3390/molecules27238421.

Yi, K. and Y. S. Ju (2018). "Patterns and mechanisms of structural variations in human cancer." *Exp Mol Med* 50, pp. 1–11. DOI: 10.1038/s12276-018-0112-3.

Yilmaz, L. S., S. Parnerkar, and D. R. Noguera (2011). "mathFISH, a web tool that uses thermodynamics-based mathematical models for in silico evaluation of oligonucleotide probes for fluorescence in situ hybridization." *Appl Environ Microbiol* 77, pp. 1118–1122. DOI: 10.1128/AEM.01733-10.

York, A. G., S. H. Parekh, D. Dalle Nogare, R. S. Fischer, K. Temprine, M. Mione, A. B. Chitnis, C. A. Combs, and H. Shroff (2012). "Resolution doubling in live, multicellular organisms via multifocal structured illumination microscopy." *Nat Methods* 9, pp. 749–754. DOI: 10.1038/nmeth.2025.

Yun, J. W., L. Yang, H. Y. Park, C. W. Lee, H. Cha, H. T. Shin, K. W. Noh, Y. L. Choi, W. Y. Park, and P. J. Park (2020). "Dysregulation of cancer genes by recurrent intergenic fusions." *Genome Biol* 21, p. 166. DOI: 10.1186/s13059-020-02076-2.

Zamudio, A. V. et al. (2019). "Mediator Condensates Localize Signaling Factors to Key Cell Identity Genes." *Mol Cell* 76, pp. 753–766. DOI: 10.1016/j.molcel.2019.08.016.

Zaret, K. S. (2020). "Pioneer Transcription Factors Initiating Gene Network Changes." *Annu Rev Genet* 54, pp. 367–385. DOI: 10.1146/annurev-genet-030220-015007.

Zhang, L. F., K. D. Huynh, and J. T. Lee (2007). "Perinucleolar targeting of the inactive X during S phase: evidence for a role in the maintenance of silencing." *Cell* 129, pp. 693–706. DOI: 10.1016/j.cell.2007.03.036.

Zhang, M., S. W. Eichhorn, B. Zingg, Z. Yao, K. Cotter, H. Zeng, H. Dong, and X. Zhuang (2021a). "Spatially resolved cell atlas of the mouse primary motor cortex by MERFISH." *Nature* 598, pp. 137–143. DOI: 10.1038/s41586-021-03705-x.

Zhang, T., Z. Zhang, Q. Dong, J. Xiong, and B. Zhu (2020a). "Histone H3K27 acetylation is dispensable for enhancer activity in mouse embryonic stem cells." *Genome Biol* 21, pp. 1–7. DOI: 10.1186/s13059-020-01957-w.

Zhang, Y., F. Chen, N. A. Fonseca, Y. He, M. Fujita, H. Nakagawa, Z. Zhang, A. Brazma, P. T. W. Group, P. S. V. W. Group, C. J. Creighton, and P. Consortium (2020b). "High-coverage whole-genome analysis of 1220 cancers reveals hundreds of genes deregulated by rearrangement-mediated cis-regulatory alterations." *Nat Commun* 11, p. 736. DOI: 10.1038/s41467-019-13885-w.

Zhang, Y., Z. Sun, J. Jia, T. Du, N. Zhang, Y. Tang, Y. Fang, and D. Fang (2021b). "Overview of Histone Modification." *Adv Exp Med Biol* 1283, pp. 1–16. DOI: 10.1007/978-981-15-8104-5_1.

Zhao, Z., G. Tavoosidana, M. Sjolinder, A. Gondor, P. Mariano, S. Wang, C. Kanduri, M. Lezcano, K. S. Sandhu, U. Singh, V. Pant, V. Tiwari, S. Kurukuti, and R. Ohlsson (2006). "Circular chromosome conformation capture (4C) uncovers extensive networks of epigenetically regulated intra- and interchromosomal interactions." *Nat Genet* 38, pp. 1341–1347. DOI: 10.1038/ng1891.

Zhegalova, N. G., S. He, H. Zhou, D. M. Kim, and M. Y. Berezin (2014). "Minimization of self-quenching fluorescence on dyes conjugated to biomolecules with multiple labeling sites via asymmetrically charged NIR fluorophores." *Contrast Media Mol Imaging* 9, pp. 355–362. DOI: 10.1002/cmmi.1585.

Zheng, H. and W. Xie (2019). "The role of 3D genome organization in development and cell differentiation." *Nat Rev Mol Cell Biol* 20, pp. 535–550. DOI: 10.1038/s41580-019-0132-4.

Zhou, Y., J. Petrovic, J. Zhao, W. Zhang, A. Bigdeli, Z. Zhang, S. L. Berger, W. S. Pear, and R. B. Faryabi (2022). "EBF1 nuclear repositioning instructs chromatin refolding to promote therapy resistance in T leukemic cells." *Mol Cell* 82, pp. 1003–1020. DOI: 10.1016/j.molcel.2022.01.015.

Zink, D., T. Cremer, R. Saffrich, R. Fischer, M. F. Trendelenburg, W. Ansorge, and E. H. Stelzer (1998). "Structure and dynamics of human interphase chromosome territories in vivo." *Hum Genet* 102, pp. 241–251. DOI: 10.1007/s004390050686.

Znosko, B. M., S. B. Silvestri, H. Volkman, B. Boswell, and M. J. Serra (2002). "Thermodynamic parameters for an expanded nearest-neighbor model for the formation of RNA duplexes with single nucleotide bulges." *Biochemistry* 41, pp. 10406–10417. DOI: 10.1021/bi025781q.

Zuin, J., G. Roth, Y. Zhan, J. Cramard, J. Redolfi, E. Piskadlo, P. Mach, M. Kryzhanovska, G. Tihanyi, and H. Kohler (2022). "Nonlinear control of transcription through enhancer–promoter interactions." *Nature* 604, pp. 571–577. DOI: 10.1038/s41586-022-04570-y.

A

ANNEX

A.1 ACKNOWLEDGMENTS

PUBLICATIONS

Steinek, C., Guirao Ortiz, M., Stumberger, G., Toelke, A. J., Hoerl, D., Carell, T., Harz, H. and Leonhardt, H. (2024). Generation of densely labeled oligonucleotides for the detection of small genomic elements. Cell Reports Methods 4, 100840.

Weichenhan, D., Riedel, A., Sollier, E., Toprak, U. H., Hey, J., Breuer, K., Wierzbinska, JA., Touzart, A., Lutsik, P., Bähr, M., Östlund, A., Nilsson T., Jacobsson, S., Edler, M., Waraky, A., Behrens YL., Göhring G., Schlegelberger B., **Steinek, C.**, Harz, H., Leonhardt, H., Dolnik, A., Reinhard, D., Bullinger, L., Palmqvist, L., Lipka, DB., Plass, C., 2023. Altered enhancer-promoter interaction leads to MNX1 expression in pediatric acute myeloid leukemia with t (7; 12)(q36; p13). Blood Advances. [Accepted]

Qin, W., **Steinek, C**., Kolobynina, K., Forné, I., Imhof, A., Cardoso, M.C. and Leonhardt, H., 2022. Probing protein ubiquitination in live cells. Nucleic Acids Research, 50(21), pp.e125-e125.

Brandstetter, K., Zülske, T., Ragoczy, T., Hörl, D., Guirao-Ortiz, M., **Steinek, C.**, Barnes, T., Stumberger, G., Schwach, J., Haugen, E. and Rynes, E., 2022. Differences in nanoscale organization of regulatory active and inactive human chromatin. Biophysical Journal, 121(6), pp.977-990.